Universidade do Minho

EROSION MECHANISMS IN MARINE SEDIMENTS

Maria Amélia Vieira da Costa Araújo

PhD Thesis

Guimarães, 2004

ABSTRACT

Erosion of intertidal sediments may be influenced by several factors. In this study, the influence on sediment erosion of some physical mechanisms such as the sediment bed roughness, suspended particles and surface waves was investigated. Because of the complexity of the phenomena involved, careful experiments have been planed in order to make each mechanism dominant and to assess its contribution.

Experiments were carried out in laboratory in a circular mini flume, 131 *mm* in diameter using the laser Doppler anemometry (LDA) technique. Simultaneous measurements of the tangential and axial velocity components and the Reynolds stresses were obtained by the use of two colours (blue and green) of a 6 *W* Argon ion laser operating on a backscatter mode. The fluid is driven on a tangential flow at controllable speeds by a circular flat lid on the top of the flume, which is linked to the shaft of a rheometer. A comprehensive physical and chemical analysis of the sediment enabled the accurate definition of the laboratory test conditions.

Tests were made in natural sediments collected in two estuaries and in artificial (simulated) beds at various Reynolds numbers. For artificial beds, both rigid and deformable (either fluid or grain) surfaces were investigated. For the fixed bed option, three different alternatives were considered: a smooth surface was set as a basis for subsequent comparisons with more complex structures; an exact reproduction of the sediment morphology on a gypsum mould; a sand roughness bed, using a range of glass beads. The deformable bed consisted of a two-fluid layer or by the use of a set of glass and polymer beads, to investigate the influence of entrained particles upon the turbulence. From this analysis, the surface topology proved to be a key factor in the flow field. Therefore, the use of solid replica of marine sediments appears to be an appropriate method to generate a simulated bed.

The influence of surface waves upon the flow patterns in the vicinity of the sediment surface, and its contribution to the turbulence, was investigated using special rings with a wavy shape, in which the wave amplitude and wavelength were controlled.

The use of LDA in natural sediments enables the direct measurement of the shear stress at the sediment interface. By comparing the changes on the fluid velocity profiles, the sediment critical shear stress was determined. The occurrence of bed deformation in erosion was identified by discontinuities of the shear stress.

It was concluded that the suspended particles concentration is the most important factor affecting the fluid turbulence close to the interface. Results also showed that the bed deformation plays an important role in controlling the wall shear stress.

The flow inside the mini flume was characterised experimental and numerically, using the CFX code. It was observed the existence of secondary flows near the outer wall, which affect erosion in such mini flumes. It was also found that the numerical models employed cannot predict exactly the flow in channels with strong curvature, as the mini flume, in which the turbulent flow is non isotropic.

RESUMO

A erosão de sedimentos costeiros pode ser influenciada por diversos factores. No presente estudo, será avaliada a influência na erosão de alguns mecanismos físicos tais como, a rugosidade da superfície, a presença de partículas suspensas no fundo e de ondas superficiais. Devido à complexidade dos fenómenos envolvidos, foi planeado um conjunto de experiências por forma a estudar individualmente cada um dos referidos mecanismos.

O programa experimental foi executado em laboratório sobre um canal toroidal de 131 *mm* de diâmetro externo, usando anemometria por efeito Doppler (LDA). Os dois canais (azul e verde) de um laser de 6*W* de potência operando em rectrodifusão, permitiu a medição simultânea das componentes tangencial e axial da velocidade, bem assim com as tensões de Reynolds. O fluido é movimentado tangencialmente por um disco no topo do canal, sendo accionado a velocidade controlada por um reómetro. Uma detalhada análise física e química dos sedimentos possibilitou a definição das condições laboratoriais.

Foram conduzidos testes em sedimentos naturais e em leitos simulados a vários números de Reynolds. Nestes foram testados leitos rígidos e deformáveis. Quanto aos primeiros, foram consideradas três opções: fundo liso, reprodução exacta da superfície do sedimento, fundo de areia. O leito deformado consistiu num sistema de dois fluidos imiscíveis e no uso de partículas esféricas de vidro. Esta configuração permitiu ainda a avaliação da influência na turbulência de partículas arrastadas pelo fluido.

Da análise dos resultados, concluiu-se que a reprodução da topografia de um sedimento parece ser uma metodologia apropriada para a simulação, em laboratório, de um sedimento.

A influência das ondas superficiais no escoamento foi avaliada pela aplicação de anéis no disco de accionamento do escoamento.

O uso do LDA em sedimentos naturais permitiu a medição directa da tensão de corte na interface. Comparando as alterações no perfil de velocidades, determinou-se a tensão crítica de corte do sedimento. A ocorrência de deformação do leito foi identificada pela presença de descontinuidades no valor da tensão de corte.

Dos resultados, concluiu-se que a concentração de partículas suspensas no escoamento é o principal factor que afecta a turbulência junto da interface. Os resultados mostraram ainda que a deformação do leito desempenha um papel importante na tensão de corte na parede.

O escoamento no interior do canal foi caracterizado experimental e numericamente, usando o código CFX. Observou-se a ocorrência de escoamentos secundários junto à parede exterior, o que afecta a erosão em canais com esta configuração. Concluiu-se que os modelos de turbulência demonstram alguma dificuldade em prever o escoamento em canais de forte curvatura nos quais o escoamento é extremamente anisotrópico.

This PhD thesis was partially funded through a scholarship (Ref. SFRH/BD/6951/2001) sponsored by the **F**undação para a **C**iência e **T**ecnologia (FCT) under the POCTI programme.

"Human subtlety will never devise an invention more beautiful, more simple or more direct than does Nature, because in her inventions, nothing is lacking and nothing is superfluous."

Leonardo da Vinci

ACKNOWLEDGEMENTS

I am deeply grateful to my supervisors, Professors José Carlos Fernandes Teixeira and Senhorinha de Fátima Capela Fortunas Teixeira, whose advice and encouragement have guided me throughout this research.

I am thankful to the Portuguese Foundation for the Science and Technology (FCT) for scholarship funding. Also, the opportunity to be part of the CLIMEROD project "The Influence of Climate Change on Coastal Sediment Erosion", MAST III (contract MAS3-CT98-0166) was a deeply rewarding experience. Most of the experimental work was carried out in the framework of this project. I would like to thank all the partners of this project for their fruitful collaboration and friendship.

In addition, I acknowledge the University of Plymouth (UK), where part of the work was carried out, specially to Professors T. E. R. Jones and P. W. James for their training on CFD techniques, and Dr. J. P. Hughes for his assistance.

I wish to express my appreciation to University of Minho and all persons who direct or indirectly were involved in this research. In particular, the departments of Mechanical Engineering, Production and Systems, Polymer Engineering and Biological Engineering, and also to the FEUP (Mechanical Engineering department) for their collaboration.

I also would like to thank my colleagues at the university, for the friendly atmosphere at work.

Last, but not the least, I would like to thank my family for their constant encouragement. Specially to my husband, Billy, I wish to express my gratitude in two ways: for the development of a customized software (Flume 3D, V. 1.0; 2003) with the purpose of my research for 3D plots generation, and for his love, patience and understanding during the course of this work.

CONTENTS

1 INTRODUCTION 1

1.1 The importance of erosion studies 1

1.2 Research objectives 2

1.3 Thesis outline 3

2 LITERATURE REVIEW 5

2.1 Sediments characterisation 5

2.2 Factors affecting the sediments erosion 7

2.3 Flow characterisation 16

2.4 Interface shear stress 19

2.5 Conclusions 25

3 THE LDA TECHNIQUE FOR FLOW MEASUREMENTS 27

3.1 Measurement of fluid velocity 27

3.2 Basic principles 29

3.3 Operation technique 33

3.3.1 Directional discrimination and frequency shift 33

3.3.2 Signal 34

3.3.3 Selection of a suitable tracer 36

3.4 Data processing 38

3.5 Turbulence analysis 40

3.6 LDA configuration 43

4 EXPERIMENTAL TECHNIQUES 47

4.1 Laser diffraction technique 47

4.1.1 The Malvern 2600 48

4.1.2 Particle size distribution 50

4.1.3 Measuring procedure 52

4.1.4 Accuracy and limitations 52

4.2 High speed video camera 53

4.3 Sample collection 54

4.4 Sediment analysis 56

4.4.1 Chemical composition 56

4.4.2 Water content 56

4.4.3 Salinity 56

4.5 Rheology 56

5 EXPERIMENTAL DETAILS 59

5.1 Experimental apparatus 59
5.1.1 The mini flume 61
5.1.2 Refractive index compensation 62
5.1.3 Optical configuration of the LDA 66

5.2 Flow seeding 69

5.3 Experimental procedures 72

5.4 Accuracy and uncertainty analysis in LDA 73
5.4.1 Accuracy 73
5.4.2 Uncertainty analysis of the velocities 74
5.4.3 Uncertainty analysis of the shear stresses 80

5.5 Construction of test beds 80
5.5.1 Sediment interface reproduction 80
5.5.2 Surface waves generator 81

5.6 Field surveys 83
5.6.1 Gironde estuary 83
5.6.2 Westerschelde estuary 83
5.6.3 Cávado estuary 84

5.7 Physical and chemical characterisation 86
5.7.1 Water salinity in estuaries 87
5.7.2 Erosion tests 87
5.7.3 Fluids characterisation 88
5.7.4 Characterisation of the mud samples 90

5.8 Tests conditions 96
5.8.1 Tests in simulated beds 96
5.8.2 Tests in natural sediments 104

6 FLOW CHARACTERISATION IN A SMALL DIAMETER FLUME 109

6.1 Velocity profiles in turbulent flows 109
6.1.1 Velocity profiles near a smooth wall 109
6.1.2 Velocity profiles near rough walls 113

6.2 Experimental results in smooth beds 116

6.3 Numerical simulation 126
6.3.1 Governing equations of fluid flow 127
6.3.2 Turbulence models 127
6.3.3 Simulation conditions 132
6.3.4 Results and discussion 135

7 FACTORS AFFECTING THE TURBULENCE -EXPERIMENTAL RESULTS 145

7.1 Influence of surface roughness 145
7.1.1 Experimental results 146

7.1.2 Boundary layer analysis 155
7.2 Influence of entrained particles 173
7.2.1 Flow over a deforming particle layer 173
7.2.2 Velocity data 176
7.2.3 Discussion 184
7.2.4 Summary 195
7.3 Influence of surface waves 196
7.3.1 Multiple factors 206
7.3.2 Discussion 214
7.4 Two-fluid bed 215
7.5 Concluding remarks 218

8 FLOW OVER NATURAL SEDIMENTS: RESULTS AND DISCUSSION 219

8.1 Seasonal effects 219
8.2 Sampling site effects 225
8.3 Comparison between different estuaries 228
8.4 Comparison of simulated and natural beds 231
8.4.1 Rigid and deformable beds 232
8.4.2 Presence of surface waves 235
8.4.3 Final discussions 240

9 CONCLUSIONS AND FUTURE WORK 243

9.1 Conclusions 243
9.2 Suggestions for future work 244

ANNEX A - RHEOMETER CHARACTERISTICS 247

ANNEX B - REFRACTIVE INDEX COMPENSATION FOR LDA CROSSING ANGLES 249

ANNEX C - PHYSICAL AND CHEMICAL SAMPLE CHARACTERISATION 257

ANNEX D - VISCOSITY OF WATER 265

APPENDIX - INFLUENCE OF GAP IN THE FLUME 267

LIST OF REFERENCES 271

LIST OF TABLES

Table 4.1- Particle size ranges and correspondent lens 49

Table 4.2- Mean diameters 51

Table 5.1- Refractive index of the different media 64

Table 5.2- Corrections of the vertical beams (blue) full crossing angle 65

Table 5.3- Optical properties of the system 67

Table 5.4- Equivalent beam spacing at the transmitting optics for the various experiments 67

Table 5.5- Output properties referent to the solution of glycerine 67

Table 5.6- Output properties referent to ethyl alcohol 68

Table 5.7- Output properties referent to oil 68

Table 5.8- Output properties referent to natural sediment beds 68

Table 5.9- Physical properties of the fluids 70

Table 5.10- *Particle/fluid* density ratio 71

Table 5.11- Fluid eddy frequency using different conditions estimated from Hutchinson and Hewitt (1971) 71

Table 5.12- Mean velocity gradient broadening bias related to the mean velocity 76

Table 5.13- Mean velocity gradient broadening bias related to the RMS velocity 77

Table 5.14- Total uncertainty to the mean and RMS velocities and to the cross moments 79

Table 5.15- Total uncertainty to the position at 10 *mm* from the wall 79

Table 5.16- Uncertainty to the shear stress to both study cases 80

Table 5.17- Samples identification and respective tests carried out 84

Table 5.18- Samples identification at different seasons 85

Table 5.19- Physical aspect of each sample 86

Table 5.20- Sediment temperature and pH 91

Table 5.21- Temperature of water and air in each season 91

Table 5.22- Sauter mean diameter: samples close the water 93

Table 5.23- Sauter mean diameter: samples away from the water 93

Table 5.24- Mud percentage to Cávado samples 93

Table 5.25- Ranges of particle size and density 99

Table 5.26- Density ratio of the beads and the fluids 100

Table 5.27- Geometric characteristics of the lids 102

Table 5.28- Experimental plan with simulated beds 104

Table 5.29- Reynolds numbers referent at each sediment sample 106

Table 5.30- Gap size for the Cávado samples 106

Table 6.1- Simulation tests using CFX 135

Table 8.1- Critical shear stress; samples near the water line 222

Table 8.2- Percentage of diatoms per season and sampling site (Soares, 2004) 222

Table 8.3- Critical shear stress; samples far from the water line 224

LIST OF FIGURES

Figure 3.1- Dual beam mode of LDA 29

Figure 3.2- Fringe model for laser-Doppler signals 31

Figure 3.3- Types of signal from particles crossing a region of intersection of laser light beams 32

Figure 3.4- Filtered signal with the DC-component removed 35

Figure 3.5- Steady and unsteady turbulent flow 40

Figure 3.6- a) Schematic layout of the LDA instrumentation; b) Transmitting/receiving optics 45

Figure 4.1- Layout of the Malvern 2600 48

Figure 4.2- Malvern during a measurement 49

Figure 4.3- High speed video system 53

Figure 4.4- The Cávado estuary 55

Figure 4.5- Sampling natural sediments at the estuary 55

Figure 5.1- Basic experimental rig 59

Figure 5.2- Test rig 60

Figure 5.3- Traverse mechanism with the transmitting/receiving optics 61

Figure 5.4- The laser source 61

Figure 5.5- The mini flume 62

Figure 5.6- Light ray through an interface 63

Figure 5.7- Effect of the incidence angle on the refraction angle 63

Figure 5.8- Corrected horizontal cross angles to the glycerine solution 66

Figure 5.9- Influence of the fluid eddy frequency on the amplitude ratio for two seeding media 69

Figure 5.10- Influence of the fluid eddy frequency on the amplitude ratio for the various fluids 70

Figure 5.11- Effect of the seeding diameter upon the amplitude ratio 72

Figure 5.12- Sediment model (rough surface) 81

Figure 5.13- The making the prototype for a wavy lid..... 82

Figure 5.14- View of a wavy lid..... 82

Figure 5.15- Water salinity results 87

Figure 5.16- Torque *versus* velocity..... 88

Figure 5.17- Viscosity of the fluid 89

Figure 5.18- Chemical composition of the sediments for different seasons..... 91

Figure 5.19- Particle size of the sediments (close to the water) 92

Figure 5.20- Particle size of the sediments (away from the water) 92

Figure 5.21- Sediment water content 95

Figure 5.22- Sediment salinity 96

Figure 5.23- Surface map (RB1) 97

Figure 5.24- Surface map (RB2) 98

Figure 5.25- Grid used for measurements 98

Figure 5.26- Measuring positions along the dune length 100

Figure 5.27- Amplitude ratio for the different beads 101

Figure 5.28- Effects of the beads P1 size on the amplitude ratio 101

Figure 5.29- Grid points for measurements in natural samples..... 105

Figure 5.30- Effects of particle diameter on the amplitude ratio..... 107

Figure 6.1- Velocity distribution near a solid wall in a turbulent boundary layer (Clauser, 1956) 110

Figure 6.2- Variation of parameter B_S with roughness Reynolds number (Schlichting, 1979) 115

Figure 6.3- Flume and velocity profile representation 116

Figure 6.4- Tangential velocity field; smooth bed 117

Figure 6.5- Axial velocity field; smooth bed..... 118

Figure 6.6- Recirculation pattern in a flume 119

Figure 6.7- Tangential velocity turbulence field; smooth bed..... 120

Figure 6.8- Axial velocity turbulence field; smooth bed..... 121

Figure 6.9- Isotropic ratio; smooth bed 122

Figure 6.10- Cross-moments field; smooth bed 123
Figure 6.11- Turbulence intensity field; smooth bed 124
Figure 6.12- Shear stress field; smooth bed 125
Figure 6.13- Sketch of the flume 133
Figure 6.14- Numerical velocity profiles at different Re 135
Figure 6.15- Numerical profiles in the entire flume section 136
Figure 6.16- Experimental and numerical data; Re=2,000 137
Figure 6.17- Numerical results; Re=2,000 138
Figure 6.18- Experimental data; smooth bed; Re=2,000 139
Figure 6.19- Experimental and numerical data; Re=10,000 139
Figure 6.20- Numerical results; Re=10,000 141
Figure 6.21- Experimental and numerical data; Re=40,000 141
Figure 6.22- Numerical results; Re=40,000 142
Figure 6.23- Experimental and numerical data (at radial distance x=13.14 *mm*) 143
Figure 7.1- Erosion of a sediment bed 146
Figure 7.2- Tangential velocity field; RB1 147
Figure 7.3- Tangential velocity field; RB2; Re=20,000 147
Figure 7.4- Tangential velocity field; RB3; Re=10,000 148
Figure 7.5- Axial velocity field; RB1 149
Figure 7.6- Axial velocity field; RB2; Re=20,000 149
Figure 7.7- Axial velocity field; RB3; Re=10,000 150
Figure 7.8- Tangential velocity turbulence field; RB1 150
Figure 7.9- Tangential velocity turbulence field; RB2; Re=20,000 151
Figure 7.10- Tangential velocity turbulence field; RB3; Re=10,000 151
Figure 7.11- Isotropic ratio; RB1 152
Figure 7.12- Isotropic ratio; RB3; Re=10,000 153
Figure 7.13- Shear stress field; RB1 154
Figure 7.14- Shear stress field; RB2; Re=20,000 154

Figure 7.15- Shear stress field; RB3; Re=10,000 155
Figure 7.16- Normalised mean tangential velocity; Re=10,000 155
Figure 7.17- Normalised mean tangential velocity; Re=20,000 156
Figure 7.18- Normalised mean tangential velocity; Re=40,000 156
Figure 7.19- Shear stress on a smooth and rough beds; Re=20,000 157
Figure 7.20- Axial velocity field truncating the scale; Re=20,000 157
Figure 7.21- Mean velocity profiles; Re=10,000 158
Figure 7.22- Mean velocity profiles; Re=20,000 158
Figure 7.23- Mean velocity profiles; Re=40,000 158
Figure 7.24- Mean velocity-defect; Re=10,000 160
Figure 7.25- Mean velocity-defect; Re=20,000 160
Figure 7.26- Mean velocity-defect; Re=40,000 161
Figure 7.27- Streamwise Reynolds normal stresses; $\overline{u'^{+2}}$; Re=10,000 162
Figure 7.28- Streamwise Reynolds normal stresses; $\overline{u'^{+2}}$; Re=20,000 163
Figure 7.29- Streamwise Reynolds normal stresses; $\overline{u'^{+2}}$; Re=40,000 163
Figure 7.30- Crosswise Reynolds normal stresses; $\overline{v'^{+2}}$; Re=10,000 163
Figure 7.31- Crosswise Reynolds normal stresses; $\overline{v'^{+2}}$; Re=20,000 164
Figure 7.32- Crosswise Reynolds normal stresses; $\overline{v'^{+2}}$; Re=40,000 164
Figure 7.33- Reynolds shear stresses; $-\overline{u'^{+}v'^{+}}$; Re=10,000 165
Figure 7.34- Reynolds shear stresses; $-\overline{u'^{+}v'^{+}}$; Re=20,000 165
Figure 7.35- Reynolds shear stresses; $-\overline{u'^{+}v'^{+}}$; Re=40,000 165
Figure 7.36- Turbulent kinetic energy; Re=10,000 166
Figure 7.37- Turbulent kinetic energy; Re=20,000 167
Figure 7.38- Turbulent kinetic energy; Re=40,000 167
Figure 7.39- Rate of production of mean turbulent energy; Re=10,000 168
Figure 7.40- Rate of dissipation of mean turbulent energy; Re=10,000 168

Figure 7.41- Rate of production of mean turbulent energy; Re=20,000 169

Figure 7.42- Rate of dissipation of mean turbulent energy; Re=20,000 169

Figure 7.43- Rate of production/dissipation of mean turbulent energy; RB2 170

Figure 7.44- Rate of production of mean turbulent energy; Re=40,000 170

Figure 7.45- Rate of dissipation of mean turbulent energy; Re=40,000 171

Figure 7.46- Skewness; Re=10,000.....172

Figure 7.47- Flatness; Re=10,000 172

Figure 7.48- Typical deforming bed 174

Figure 7.49- Mean tangential velocity along the time.....175

Figure 7.50- Mean tangential velocity profiles at different positions 175

Figure 7.51- Mean tangential velocity; beads P1; Re=20,000 176

Figure 7.52- Tangential velocity turbulence; beads P1; Re=20,000 177

Figure 7.53- Shear stress; beads P1; Re=20,000.....177

Figure 7.54- Mean tangential velocity; beads P2; Re=20,000 178

Figure 7.55- Tangential velocity turbulence; beads P2; Re=20,000 178

Figure 7.56- Mean tangential velocity; beads P2; Re=40,000 179

Figure 7.57- Tangential velocity turbulence; beads P2; Re=40,000 179

Figure 7.58- Shear stress; beads P2; Re=40,000.....179

Figure 7.59- Mean tangential velocity; beads P3; Re=20,000 180

Figure 7.60- Tangential velocity turbulence; beads P3; Re=20,000 180

Figure 7.61- Shear stress; beads P3; Re=20,000.....181

Figure 7.62- Mean tangential velocity; beads P3; Re=40,000 182

Figure 7.63- Tangential velocity turbulence; beads P3; Re=40,000 182

Figure 7.64- Shear stress; beads P3; Re=40,000.....182

Figure 7.65- Variation of the local shear stress over a sandy dune; Re=20,000 183

Figure 7.66- Variation of the local shear stress over a sandy dune; Re=40,000 184

Figure 7.67- Tangential velocity turbulence; beads P1, P2, P3 and P4; Re=20,000.....185

Figure 7.68- Tangential velocity turbulence; beads P2, P3 and P4; Re=40,000.....185

Figure 7.69- Tangential velocity turbulence; effect of Reynolds number; beads P3 186

Figure 7.70- Normalised mean tangential velocity at position A; beads P1, P2 and P3; Re=20,000 186

Figure 7.71- Normalised mean tangential velocity at position B; beads P1, P2 and P3; Re=20,000 187

Figure 7.72- Normalised mean tangential velocity at position C; beads P1, P2 and P3; Re=20,000 187

Figure 7.73- Normalised mean tangential velocity at position D; beads P1, P2 and P3; Re=20,000 188

Figure 7.74- Tangential velocity turbulence at position D; beads P1, P2 and P3; Re=20,000 189

Figure 7.75- Shear stress at position D; beads P1 and P3; Re=20,000..... 189

Figure 7.76- Normalised mean tangential velocity at position A; beads P3 190

Figure 7.77- Normalised mean tangential velocity at position B; beads P3..... 190

Figure 7.78- Normalised mean tangential velocity at position C; beads P3..... 191

Figure 7.79- Normalised mean tangential velocity at position D; beads P3 191

Figure 7.80- Shear stress at position D; beads P3 192

Figure 7.81- Normalised mean tangential velocity; SB, RB2 and beads P1; Re=20,000 192

Figure 7.82- Tangential velocity turbulence; SB, RB2 and beads P1; Re=20,000 193

Figure 7.83- Shear stress; SB, RB2 and beads P1; Re=20,000 193

Figure 7.84- Normalised mean tangential velocity; SB, RB2 and beads P3; Re=20,000 194

Figure 7.85- Tangential velocity turbulence; SB, RB2 and beads P3; Re=20,000 194

Figure 7.86- Shear stress; SB, RB2 and beads P3; Re=20,000 194

Figure 7.87- Tangential velocity turbulence; SB, RB2 and beads P1, P2, P3 and P4; Re=20,000 195

Figure 7.88- Tangential velocity field; wavy lids; Re=20,000..... 197

Figure 7.89- Tangential velocity field; L2 197

Figure 7.90- Axial velocity field; wavy lids; Re=20,000..... 198

Figure 7.91- Axial velocity field; L2..... 199

Figure 7.92- Turbulence intensity; Re=20,000..... 199

Figure 7.93- Turbulence intensity; L2..... 200

Figure 7.94- Normalised mean tangential velocity; wavy lids effects; Re=10,000 201

Figure 7.95- Shear stress; wavy lids effects; Re=10,000 202

Figure 7.96- Tangential velocity turbulence; wavy lids effects; Re=10,000 202

Figure 7.97- Normalised mean tangential velocity; wavy lids effects; Re=20,000 203

Figure 7.98- Tangential velocity turbulence; wavy lids effects; Re=20,000 203

Figure 7.99- Shear stress; wavy lids effects; Re=20,000 204

Figure 7.100- Normalised mean tangential velocity; wavy lids effects; Re=40,000 205

Figure 7.101- Tangential velocity turbulence; wavy lids effects; Re=40,000 205

Figure 7.102- Shear stress; wavy lids effects; Re=40,000 205

Figure 7.103- Tangential velocity field; combined effect RB1-L1; Re=20,000 206

Figure 7.104- Axial velocity field; combined effect RB1-L1; Re=20,000 206

Figure 7.105- Tangential velocity turbulence; combined effect RB1-L1; Re=20,000.....207

Figure 7.106- Normalised mean tangential velocity; wavy lid effect on a rough bed; Re=10,000 207

Figure 7.107- Shear stress; wavy lid effect on a rough bed; Re=10,000.....208

Figure 7.108- Tangential velocity turbulence; wavy lid effect on a rough bed; Re=10,000.....208

Figure 7.109- Normalised mean tangential velocity; wavy lid effect on a rough bed; Re=20,000 209

Figure 7.110- Tangential velocity turbulence; wavy lid effect on a rough bed; Re=20,000.....209

Figure 7.111- Shear stress; wavy lid effect on a rough bed; Re=20,000.....210

Figure 7.112- Normalised mean tangential velocity; wavy lid effect on a rough bed; Re=40,000 210

Figure 7.113- Tangential velocity turbulence; wavy lid effect on a rough bed; Re=40,000.....210

Figure 7.114- Shear stress; wavy lid effect on a rough bed; Re=40,000.....211

Figure 7.115- Axial velocity filed truncating the scale; L1; Re=20,000.....212

Figure 7.116- Recirculation pattern in a flume; wavy lid 212

Figure 7.117- Tangential velocity turbulence; wavy lid effect on a deformable bed; Re=20,000 213

Figure 7.118- Tangential velocity turbulence; wavy lid effect on a deformable bed; Re=40,000 213

Figure 7.119- Tangential velocity turbulence; wavy lid effect on a smooth, a rough and a deformable bed; Re=20,000 215

Figure 7.120- Tangential velocity turbulence; wavy lid effect on a smooth, a rough and a deformable bed; Re=40,000 215

Figure 7.121- Mean tangential velocity; two-fluid bed; Re=2,500 216

Figure 7.122- Velocity profile modification at a deformable interface 216

Figure 7.123- Mean tangential velocity; two-fluid (TFB), rigid (SB) and deformable (P1) beds 217

Figure 7.124- Tangential velocity turbulence: two-fluid bed; Re=2,500 217

Figure 8.1- Mean tangential velocity: seasonal effects; samples close to the water 220

Figure 8.2- Tangential velocity turbulence: seasonal effects; samples close to the water 220

Figure 8.3- Wall shear stress: seasonal effects; samples close to the water 221

Figure 8.4- Wall shear stress: seasonal effects; samples far from the water line 224

Figure 8.5- Mean tangential velocity: sampling site effects 226

Figure 8.6- Tangential velocity turbulence: sampling site effects 226

Figure 8.7- Wall shear stress: sampling site effects 227

Figure 8.8- Wall shear stress: estuaries comparison 229

Figure 8.9- Mean tangential velocity: estuaries comparison 230

Figure 8.10- Mean axial velocity; sample C19 230

Figure 8.11- Mean axial velocity; sample W 231

Figure 8.12- Mean tangential velocity: surface roughness; Re=20,000 232

Figure 8.13- Tangential velocity turbulence: surface roughness; Re=20,000 233

Figure 8.14- Mean tangential velocity: surface roughness; Re=10,000 234

Figure 8.15- Mean velocity profile: sandy surface roughness; Re=10,000 234

Figure 8.16- Tangential velocity turbulence: deformable bed; Re=20,000 235

Figure 8.17- Mean tangential velocity: sediments without surface waves; Re=20,000 236

Figure 8.18- Tangential velocity turbulence: sediments without surface waves; Re=20,000 236

Figure 8.19- Mean tangential velocity: sediments with surface waves; Re=20,000 237

Figure 8.20- Wall shear stress: sediments with wavy lids 237

Figure 8.21- Tangential velocity turbulence: sediments with and without surface waves; Re=20,000 238

Figure 8.22- Mean tangential velocity: sediments with and without surface waves; Re=20,000 239

Figure 8.23- Mean tangential velocity: combined effects; Re=20,000 239

Figure 8.24- Tangential velocity turbulence: combined effects; Re=20,000 240

Figure 8.25- Tangential velocity turbulence: absence of surface waves; Re=20,000 240

LIST OF SYMBOLS

A	Constant in the law of wake equation	(-)
B	Total bias error	(-)
B , E	Constant in the log-law equation	(-)
B_i	Bias error component	(-)
B_O	Beams orthogonality bias	(-)
B_{proc}	Processor bias	(-)
B_S	Parameter in the general form of the log-law equation	(-)
B_{Sfs}	Fringe spacing bias	(-)
$B_{\bar{u}}$, $B_{\tilde{u}}$	Bias in the mean and the RMS velocity	(-)
$B_{mvg}^{\bar{u}}$, $B_{mvg}^{\tilde{u}}$	Mean and RMS velocity gradient bias	(-)
$B_{\overline{u'v'}}$	Bias in the cross moments	(-)
C	Constant in the velocity profile (Equation 6.13)	(-)
c	Suspended matter concentration	(kg/m^3)
c_f	Local skin friction coefficient	(-)
c_μ , $c_{\varepsilon 1}$, $c_{\varepsilon 2}$	Constants	(-)
d_h	Hydraulic diameter	(m)
$d_{\max}$, $d_{\min}$	Maximum and minimum diameter of the particles	(m)
d_{mn}	Mean particle size	(m)
d_{mv}	Measurement volume diameter	(m)
d_p , d	Particle diameter	(m)
$E_{0.95}$	Total uncertainty for a 95 % confidence interval	(-)
$\bar{e}_i$	Unit vector in the direction of the incident light	(-)
E_μ	Error related to the viscosity	(-)
$\bar{e}_s$	Unit vector in the direction of the scattered light	(-)

$E^{\tau}_{0.95}$	Total uncertainty in the shear stress	(-)
E_T	Traverse error	(-)
$E^{\bar{u}}_{0.95}$	Total uncertainty in the mean velocity	(-)
$\boldsymbol{F}$	Flatness factor	(-)
f	Focal length	(m)
f_D	Doppler frequency	(Hz)
f_i	Frequency of the incident light	(Hz)
f_μ, f_ε	Wall-damping functions	(-)
$f_N(d)$	Probability density function (frequency)	(-)
f_s	Frequency of the scattered light	(Hz)
f_s'	Frequency shift	(Hz)
$F_V(d)$	Cumulative distribution function (volume)	(-)
$f_V(d)$	Probability density function (volume)	(-)
g	Gravitational acceleration	(m/s^2)
h_{mv}	Probe volume height	(m)
$\hat{i}, \hat{j}, \hat{k}$	Cartesian coordinate directions	(-)
κ	von Kárman constant	(-)
$\bar{k}$	Mean roughness height	(m)
k	Turbulent kinetic energy	(m^2/s^2)
k_l	Roughness length scale	(m)
k_l^+, k_S^+	Roughness Reynolds number	(-)
k_S	Nikuradse's equivalent sand roughness	(m)
l	Mixing length	(m)
l_e	Characteristic size of large eddies	(m)
l_{mv}	Probe volume length	(m)
l_t	Dissipation length scale	(m)
M	Erosion rate coefficient	(kg/m^2s)
N	Sample size (number of measurements)	(-)

n_1	Refractive index of the medium in which the incident ray travels	(-)
n_2	Refractive index of the medium in which the refracted ray travels	(-)
N_{fs}	Number of fringes	(-)
n	Width parameter of Rosin-Rammler distribution	(-)
$\overline{p}$	Mean pressure	(Pa)
P , P_k	Production rate of turbulent kinetic energy	(m^2/s^3)
r	Radial distance measured from the centre of the tube	(m)
R	Tube radius	(m)
RC , RS	Range centre and range span of the velocity	(m/s)
Re	Reynolds number	(-)
Re_t	Turbulent Reynolds number	(-)
Re_ψ	Reynolds number based on momentum thickness	(-)
Ri	Richardson number	(-)
$\boldsymbol{S}$	Skewness factor	(-)
S	Total precision error	(-)
S_b	Beams spacing	(m)
S_{fs}	Fringe spacing	(m)
S_i	Precision error component	(-)
$S_{\bar{u}}$, $S_{\tilde{u}}$	Precision error in mean and RMS velocity	(-)
t_{95}	Student value for a 95 % confidence level	(-)
t	Time	(s)
T	Temperature	(^oC)
Ta	Taylor number	(-)
t_g	Gap thickness inside the flume	(m)
$\boldsymbol{u}$	Velocity vector	(m/s)
u^*	Shear velocity	(m/s)
u^+	Dimensionless velocity	(-)
u_∞	Free stream velocity	(m/s)

$u_{f's}$	Velocity correspondent to frequency shift	(m/s)
u_i, u_j	Spatial velocity vector (tensor notation)	(m/s)
$\overline{u}_{(k)}$	Central moment k of the velocity component u	(-)
$U_{\max}$	Maximum velocity of the fluid	(m/s)
$u_{\max}, u_{\min}$	Maximum and minimum expected velocity	(m/s)
$u_{\perp}$	Component of $\boldsymbol{u}$ perpendicular to the fringes in the laser probe	(m/s)
$u'_{\perp}$	Corrected component of $\boldsymbol{u}$ perpendicular to the fringes in the laser probe	(m/s)
U_{ref}	Reference velocity	(m/s)
u, v	Instantaneous velocity components in a Cartesian system	(m/s)
u', v'	Fluctuating velocity components	(m/s)
$\overline{u}, \overline{v}$	Mean values of the velocity components	(m/s)
$\widetilde{u}, \widetilde{v}$	RMS values of the velocity fluctuations	(m/s)
$\overline{u'v'}$	Reynolds shear stress	(m^2/s^2)
u_{θ}, u_z	Tangential and axial component of the velocity	(m/s)
V_t	Turbulent velocity	(m/s)
$\overline{X}$	Peak parameter of the Rosin-Rammler distribution	(m)
x_i, x_j	Spatial coordinate (tensor notation)	(m)
x, y, z	Space coordinates	(m)
y^+	Dimensionless distance from the wall	(-)
y, z	Distance from the wall	(m)
Zc	Confidence coefficient for a normal distribution	(-)

Greek symbols

α_c	Critical angle of incidence	(-)
α_i	Angle between the incident ray and the normal	(-)
α_r	Angle between the refracted ray and the normal	(-)

α_{rl}	Angle between the reflected ray and the normal	(-)
β_{cr}	Shields parameter	(-)
δ	Boundary layer thickness	(m)
δ^*	Displacement thickness	(m)
δ_{ij}	Kronecker-Delta tensor	(-)
$\Delta\theta$	Tolerance of the half intersection angle of the beams	(-)
Δt , Δt_i	Residence or transit time of the particle	(s)
Δu	Velocity absolute error	(m/s)
Δu^+	Shift in the velocity profile	(-)
$\Delta^{\bar{u}}_{mvg}$, $\Delta^{\tilde{u}}_{mvg}$	Mean and RMS absolute error related to mean velocity gradient	(m/s)
δ_v	Viscous sub-layer thickness	(m)
ε	Dissipation rate of turbulent kinetic energy	(m^2/s^3)
ε_r	Erosion rate	(kg/m^2s)
ε_{rf}	Floc erosion rate	(kg/m^2s)
Γ	Gamma function	(-)
γ	Empirical coefficient	$(mN^{-0.5})$
$\dot{\gamma}$	Shear rate	(s^{-1})
η	Amplitude ratio	(-)
φ	Beams inclination angle	(-)
λ	Light wavelength	(m)
μ_f , μ	Fluid viscosity	(kg/ms)
μ_t	Eddy or turbulent viscosity	(kg/ms)
ν	Kinematic viscosity	(m^2/s)
θ	Half crossing angle of the laser beams	(-)
θ'	Corrected half crossing angle of the laser beams	(-)
ρ_f , ρ	Fluid density	(kg/m^3)
ρ_p	Particle density	(kg/m^3)
ρ_s	Sediment density	(kg/m^3)
σ_k , σ_ε	Prandtl numbers	(-)

τ	Shear stress	(Pa)
τ_0	Parameter in Bingham model	(Pa)
τ_b	Bed shear stress	(Pa)
τ_{cr}	Critical shear stress	(Pa)
$\bar{\tau}_{ij}$	Mean viscous stress tensor	(Pa)
τ_{lam}, τ_{turb}	Laminar and turbulent shear stress	(Pa)
τ_s	Bed shear strength	(Pa)
τ_w	Wall shear stress	(Pa)
ω	Fluid eddy frequency	(s^{-1})
Ψ	Momentum thickness	(m)

CHAPTER 1

INTRODUCTION

The present chapter stresses the relevance in studying sediment erosion. It also summarises the objectives of the present work, which is subsequently followed by the structure of this thesis.

1.1 THE IMPORTANCE OF EROSION STUDIES

Coastal regions are of great importance to both human communities and natural ecosystems. Therefore, understanding the dynamics of these regions is of strategic relevance. The erosion of coastal sediment and the transport of suspended material are critical factors in predicting the changes to coastal environmental systems.

Erosion, the detachment of particles of soil sediments and rocks, occurs by hydrologic processes of sheet erosion, rilling through mass wasting and the action of wind (Soulsby, 1997). Where land uses causes soil disturbance, erosion may greatly increase above natural rates.

Sediments erosion is an important social and economic problem and a prime factor in assessing ecosystem health and function. Erosion studies are essential in issues of land and water management, including sediment transport and storage in reservoirs and estuaries. It is a fundamental and complex process that is strongly modified (generally increased) by human activities as well as natural forces.

Because mud particles can absorve a large quantity of contaminants, their erosion has been extensively studied during the last decades (Besley and Delo, 1990; Torfs, 1995). Furthermore, understanding the behaviour of natural sediments in rivers, estuaries and coastal zones is important for the maintenance of minimal navigable depths, the disposal of the dredged sediments, the extension and maintenance of harbours, and the flood defence (integrity of beaches and offshore banks is crucial to dissipate wave attack), as example (Besley and Delo, 1990). Therefore, this subject has been investigated in a variety of European projects such as CLIMEROD ("The Influence of Climate Change on Coastal Sediment Erosion", MAST III contract MAS3-CT98-0166). Most of the research described in this thesis was carried out in the framework of this project.

Mudflats are important in coastal protection as rich environments that suport wild life of high ecological value and of a high potential for fisheries. However, they are too vulnerable to sea level. Thus, a better understanding of the processes involved is important in order to take appropriate conservation measures. However, the erosion process involves a complicated feedback mechanism between fluid and sediment dynamics: once the sediment starts moving, the mobile grains extract energy from the flow, thus reducing the ability of the flow to move sediment. Furthermore, the bed topography greatly affects all aspects of the sediment transport, such as fluid motion, initiation of sediment motion, suspension and bottom roughness.

In estuaries, both cohesive or cohesive-like sediments that are usually a mixture of coarse and fine material are found. Depending on the mixture composition a different erosional behaviour can be encountered; thus their erosion and transport mechanisms require further research.

1.2 RESEARCH OBJECTIVES

At present, the factors controlling sediment stability are not fully understood, thus making the prediction of erosion and sediment transport a difficult task.

The main goal of this research is to understand some of the key physical mechanisms leading to estuary sediments erosion. To reach this goal, several experiments were carried out, in laboratory, using the laser Doppler velocimetry technique by measuring the velocity profiles in both natural and simulated beds.

The shear stress induced by the flow in cohesive sediments results in their break up and subsequent erosion. The mechanisms leading to this phenomenon are of great importance to the stability of intertidal sediment systems; however they are still insufficiently investigated.

Amongst the various factors that may affect the erosion process, one may include the sediment surface because irregularities resulting from solid bodies or from small cavities associated with the presence of living organisms. In turn, they will change the local turbulence patterns (Soulsby, 1997), which may be responsible for the onset of erosion. These local regions of turbulent flow may lead to sediment erosion and, once this process is initiated, solid particles are entrained into the water flow, which may enhance turbulence and transport the erosion process downstream.

This phenomenon deals with another interesting factor: the presence of suspended particles. Suspended particles affect the erosion and sediment transport mechanisms (Hagiwara *et al.*, 2001). Because the turbulent structure is modified by the presence of suspended particles, it is suggested that the local turbulent structure near the sediment plays an important role in the breakdown of the sediment. In addition, the flow patterns close to the bottom will change the transport properties of the suspended particles, their dispersion and eventual deposition downstream.

Other factors may contribute to the turbulence patterns in the flow field. It is known (Thais and Magnaudet, 1996) that surface waves (either mechanical or wind generated) may

modify substantially both the turbulent energy and dissipation rates relatively to the solid wall. There is strong evidence that the turbulence levels may be enhanced, leading to a continuous break up of the sediment.

Such a knowledge is of great importance to fully understand the erosion mechanisms. In this context and considering the individual contribution of each factor affecting the flow turbulence near the sediment layer and, consequently, the erosion process, the main goal of this work can be broken up into specific objectives:

1. To study the effects of surface roughness;
2. To investigate the influence of entrained particles;
3. To examine the effect of surface waves;
4. To evaluate the behaviour of a two-fluid bed.

These will be pursued using simulated beds, appropriated to each case. This work also aims to obtain velocity profiles in natural sediments and, with such profiles, to determine their critical erosion shear stress. These results will be compared with the previous ones, in order to discuss a simulated bed appropriate to duplicate, in laboratory, the conditions relevant to sediments erosion.

The search of an appropriate surface structure duplicating the behaviour of a natural sediment has enormous advantages in the process of investigating the flow structure and its interaction with the erosion mechanisms. In this way, the hurdles usually found in obtaining the velocity profiles and shear stresses directly in sediment samples (de Jonge and van den Bergs, 1987; Besley and Delo, 1990) would be overcome. Experiments could be carried out in a controlled manner and either flow visualization or direct velocity measurements would be readily available and easily reproduced. Furthermore, the use of fixed bedforms allows the acquisition of detailed and reproducible measurements of flow and turbulence.

The present work aims to evaluate a variety of bed structures, which may be used to simulate natural sediments. The assessment is based in comparisons of velocity field and surface shear stress measurements between natural sediments and those from the artificial ones.

1.3 THESIS OUTLINE

Based on the proposed research objectives, work was carried out in a sequential manner. The thesis reports this sequence, which includes the experimental apparatus, the simulated beds and finally the main results on natural sediments.

The relevant literature to the understanding of the erosion mechanisms (in particular, the factors affecting erosion and surface shear stress) is summarised in Chapter 2. Chapters 3 and 4 present the experimental techniques used throughout the experimental work. The main tool was the Laser Doppler Anemometer (LDA), a technique described in detail in Chapter 3. In Chapter 4 different techniques are presented, for a comprehensive sample analysis. The sample is collected in an annular mini flume at the estuary, being

subsequently transported and eroded in laboratory at various velocities (erosion tests). The onset of erosion and the physical mechanisms involved in the process are recorded on a VHS film, using a high speed video camera. The fluid obtained from the erosion tests was used for rheology tests. An undisturbed part of the sediment is used with a laser diffraction technique for particle size measurements. A small sediment sample collected in the vicinity of the previous one is used for chemical composition determination, water content and salinity.

Chapter 5 includes basically three types of information: firstly, describes the experimental apparatus, shows the manufacturing details of the test beds and presents some technical aspects of the LDA, as well as its accuracy and levels of uncertainty; subsequently, some results are shown detailing the physical and chemical characterisation of the estuary samples, which are subsequently used in defining the simulated beds; finally, the test conditions in both simulated and natural beds are outlined.

For a better understanding of the results, a flow characterisation in the mini flume is made in Chapter 6 by means of the velocity field; in this way, experimental and numerical results obtained using a CFD code (CFX) are compared and discussed. A description of CFD numerical models used and simulation conditions are also presented. The isolated contribution of each factor affecting the turbulence is discussed in Chapter 7. Chapter 8 presents the results obtained with natural sediments as well as comparisons with the simulated beds. The main conclusions obtained in this research and suggestions for further study are drawn in Chapter 9.

CHAPTER 2

LITERATURE REVIEW

Because of its relevance, physical complexity and scope of interest, studies in sediments erosion are regarded with great interest by numerous researchers. It must be stated at this early stage that this field of interest is a research domain with ramifications into a wide variety of sciences.

This chapter describes previous work carried out by other authors in sediments erosion, which is categorised into the following topics: sediments characterisation, factors affecting its erosion, flow characteristics and interface shear stress measurements in natural and simulated beds.

2.1 SEDIMENTS CHARACTERISATION

In the evaluation of sediment transport, sediment deposits can be labelled into two categories (according their mineralogy): cohesive and non cohesive. Cohesive sediments are muddy sediments, composed of clay and silt (grain size inferior at 63 μm). In these, in addition to electro-chemical forces, organic content, biological processes and bed consolidation are parameters that affect sediment erosion (Mitchener and Torfs, 1996). Cohesive sediment particles tend to stick together forming large aggregates (mud flocs) that have a much higher settling velocity than that of individual particles. This, in turn, requires higher bed shear stress for erosion (Houwing and van Rijn, 1998). Non cohesive sediments are coarser, do not tend to adhere to each other (inter-particle forces are not present), and are primarily composed of sand and gravel (grain size greater than 63 μm). Thus, their erosion is dependent on factors such as grain size distribution, the density and shape of individual grains (Mitchener and Torfs, 1996). In sediment transport there are difficulties in understanding the erosion behaviour of mixed cohesive and non cohesive sediments (Torfs, 1995; Mitchener and Torfs, 1996; van Ledden *et al.*, 2004). Furthermore, the cohesionless particles can exhibit apparent cohesivity effects if the particle size is small enough or if there is a small amount of cohesive material present (Torfs, 1995). Other differences between both types of sediments are related to the critical shear stress. For cohesive sediments, the erosion stress was found to be larger than that for deposition (Krishnappan and Marsalek, 2002). In cohesionless sediment, the two critical stresses are

equal. The same authors also underline that cohesive sediments do not deposit while being eroded at a constant shear stress. On the other hand, with non cohesive sediments, simultaneous erosion and deposition of the same sediment at a constant shear stress takes place.

The deposition of sediments depends on their size and bed shear stress. In cohesive sediments, in which flocculation takes place, the flocs formation and preservation depends on the turbulence: if bed shear stress is low, the turbulence is low and hence the particle interactions are not enough intense to cause flocculation; but if turbulence is too high, particle collisions are increased and the flocs break up (Mikkelsen, 2002). However, the floc density (Van der Lee, 2000) and strength (critical force need to break up the floc) (Kranenburg, 1999) have also to be taken into account.

Cohesive sediments will resist erosion up to a point, but when they do fail, it is commonly in a catastrophic way, changing the bed roughness, resulting in more erosion (Kelly and Gularte, 1981). Erosion in clay beds tends to occur in the upper layers of the clay surface (sediment-water interface). However, it depends on various factors, as previously referred.

Sediment grains are classified according to their diameter, d_p (Soulsby, 1997): clays ($d_p < 4$ μm); silts ($4 < d_p < 63$ μm); sands ($63 < d_p < 2000$ μm); granules ($2 < d_p < 4$ mm); pebble ($4 < d_p < 65$ mm); cobble ($65 < d_p < 250$ mm); boulder ($d_p > 250$ mm). Clays and silts are collectively called mud, and granules, pebbles and cobbles are called gravel.

Based on the percentage of mud content, Flemming (2000) distinguishes six classes of sediment on the basis of sand/mud mixtures: sand (< 5 % mud); slightly muddy sand (5-25 % mud); muddy sand (25-50 % mud); sandy mud (50-75 % mud); slightly sandy mud (75-95 % mud); mud (> 95 % mud). In this way, intertidal flats are defined in three groups: sand flats (> 95 % sand), mixed mud flats (10-50 % mud) and mud flats (> 50 % mud) (Lumborg and Windelin, 2003). Mud consists of organic and inorganic components and water. The organic material includes living and dead material as bacteria, benthic algae, faecal pellets. The inorganic part contains quartz, clay minerals, calcite, hydroxides, silicates, amongst others (Dankers, 2002). Because organic material and water decreases due to drying and consolidation of sediment layers, surface mud is completely different from older mud, presenting a higher biological activity.

The finest particles (the clay minerals) are mainly responsible for the cohesion, although the organic matter can contribute to cohesion and adhesion as well. Important properties of clay minerals include their particle size and shape, chemical composition, surface area, particle charge, pH and cation exchange capacity (Caywood, 1999). These properties control the behaviour and degree of interaction of clay particles with other particles in the sediments.

Estuarine sediments are generally a mixture of mud, sand and organic material. Depending on the mixture composition and the bed structure, the sand fraction can change the erosion and deposition characteristics of the mud significantly (Torfs *et al.*, 2003).

In experiments using quartz particles ranging from 5 to 1,350 μm and bulk densities of 1.65 to 1.95 g/cm^3, it was found that larger particles behaved in a non cohesive manner, consolidating rapidly and being eroded particle by particle, while smaller particles behaved in a cohesive manner, consolidating slowly and being eroded "in chunks" (Roberts *et al.*, 1998).

If enough mud is added to sand, the sediment may behave as mud (Mitchener and Torfs, 1996). These authors found that the transition from cohesionless to cohesive behaviour occurs by adding, to sand, mud contents in the range between 3 to 15 % of mud by weight. Moreover, they observed that adding mud to sand significantly increases the critical erosion shear stress, being maximum at a mud content between 30 to 50 % by weight.

Nevertheless, until now the erosion of sand/mud beds is not fully understood (Dankers, 2002; van Ledden *et al.*, 2004).

2.2 FACTORS AFFECTING THE SEDIMENTS EROSION

Sediment erosion processes in marine systems involve complex interactions between hydrodynamics, sediment dynamics in cohesive and non cohesive bed and sediment loading. Sediment erosion rates are essentially controlled by bottom shear stress, which is the shearing force due to friction, on the sediment bed. In estuaries, the hydrodynamic processes that generate bottom shear stress are a combination of wind waves and currents (Soulsby, 1997).

Although turbulent flows lead to sediment erosion, it has been observed that in laminar flows, erosion may also occur. Some erosion occurs at stresses below the critical value, that may be due to the stochastic nature of turbulence, in which even relatively low velocity flows may have some high energy eddies (Ravens and Gschwend, 1999).

While the erosion of cohesive sediments is dependent upon many physical-chemical parameters, the critical shear stress (τ_{cr}) to initiate the erosion of cohesionless sediments is dependent only upon particle size and bulk density of the bed (Roberts *et al.*, 1998). The initiation of motion of these sediments is determined by the ratio between driving hydrodynamic and stabilizing forces, frictional forces due to gravity, which is known as the Shields parameter, β_{cr} (Lelieveld *et al.*, 2003):

$$\beta_{cr} = \frac{\tau_{cr}}{(\rho_s - \rho_f) g d_p} \tag{2.1}$$

being ρ_s and ρ_f the sediment and fluid density, respectively, g the acceleration due to gravity and d_p the sediment grain size. Below a critical value of Shields parameter no sediment particles will be transported. That value is always $\leq$ 0.3, being 0.055 for large grain sizes ($d_p > 10\,mm$) (Soulsby, 1997). Grant *et al.* (1982) questioned the use of the Shields criterion to predict initial motion, as in the natural environment it may occur biological modifications as well as changes in the processing of the sediment particles at the interface.

For cohesive sediments, erosion is much more complex because it is necessary to include a balance between cohesive, shear and gravitational forces (Mehta and Lee, 1994). When using a mixture of cohesive and non cohesive material, all parameters must be taken into account, including the amount of each sediment present to determine which behaviour is dominant. Mitchener and Torfs (1996) found that the presence of sand causes an increase

in the surface erosion shear stress as well as a decrease in the depth of sediment eroded by a given shear stress. In addition to the sand fraction, dependence upon the mineralogy and grain size of the mud is found.

Once the particle is eroded from the bed, it can be transported either as bedload or suspended load, depending upon the flow conditions. When the bed shear stress is low, the particle movement is in close contact with the bed and in intermittent suspension (rolling, jumping), being this mode of transport called bedload. At higher values of fluid shear, when the upward velocity of the particle exceeds the settling velocity, there is no more contact with the bed, the grain will stay in suspension (transportation of finer material), which is called a suspended load. If there is a decrease in the lift force, the grain will fall back onto the bed (Kostaschuk and Ilersich, 1995).

The mode of erosion varies with the magnitude of the bed shear stress (Mehta, 1981). Mehta (1991) presents various modes of cohesive sediment erosion: surface erosion of bed aggregates (occurs floc-by-floc due to the breaking of inter-particle, electromechanical bonds); mass erosion (the sediment bed fails along a plane below the bed surface, which allows all of the material above this plane become suspended in the flow); entrainment of fluid mud (the sediment bed is fluidised, which destabilizes the sediment-water interface and then the fluid mud is entrained from the bed). Mass erosion occurs at shear stress considerably higher than those for surface erosion, and a sediment bed may become fluidised as a result of wave action over the surface (Mehta, 1991).

Erodibility is an index for the ease at which a sediment is worn away. The erosion of a sediment is characterised by two parameters: the erosion threshold (corresponds to the fluid velocity at which erosion begins) and the erosion rate (the amount of sediment that erodes in a given time). The factors influencing the erosion threshold and erosion rate are very complex and dependent upon physical, biological and chemical components of the sediment, as well as the overlying water. The main factors which affect the erosion of cohesive sediments were presented by Young and Southard (1978), Mehta (1981), Nichols (1986) and Amos *et al.*, (1992a). Some of them are briefly summarised in this section, according to previous investigations that examined these factors: effects of bed structure; salinity; water temperature; rainfall; biological activity; pH; depositional history; sediment composition; sediment water content; erosive force of the fluid (bed shear stress, waves and currents); bed characteristics; suspended particles. Various processes controlling erodibility of mud were also referred by Dyer (1998).

- Bed structure

The bed structure can be classified in beds with relatively uniform properties over depth and stratified beds in which sediment properties vary with depth. Uniform sediment beds (i.e. critical shear stress is constant over depth) will erode at a constant rate if the shear stress remains constant (Mehta, 1991). Stratified beds are formed by deposition of suspended sediment under low flow velocity, or under quiescent conditions, having higher water contents. In addition, these beds have a very low mechanical strength (Parchure and Mehta, 1985). Erosion studies performed by these authors on uniform beds indicate that a constant rate of erosion is characterised by a linear increase of suspended sediment concentration. Considering the estuarine conditions, the stratified (deposited) bed represents the upper part of the sediment, while the lower part has uniform properties (Parchure and Mehta, 1985).

Placed and settled beds have been used in laboratory. For the first type, the natural sediments taken from the estuary are reconstituted, by stirring, and then inserted in the flume; the settled beds allow the simulation of the natural conditions by settling directly into the flume (Black and Paterson, 1997).

When a sediment suspension is deposited on the bed surface, it will begin to consolidate. Deposited muds may be classified according to their degree of consolidation. It depends on the sediment particle size and the mineralogical composition. As consolidation progresses, cohesion, bed density and resistance to erosion will increase (Parchure and Mehta, 1985). A comprehensive discussion on the influence of bed structure on the erosion of cohesive sediments was made by Krone (1999).

- Sediment salinity

Salinity modifies the inter-particle bound strength by increasing the flocculation of particles, changing the critical shear stress (Kelly and Gularte, 1981). Parchure and Mehta (1985) investigated the influence of salinity in different beds, including sediments, and found that increasing the salinity, the bed shear strength also increased. In addition, salinity up to approximately 2 *ppt* was found to double the critical shear stress of muds and, as a result, the rate of erosion should decrease with increasing salinity up to that value. However, in estuarine applications involving salinities greater than approximately 10 *ppt*, the influence of salinity on erosion can be considered negligible (Parchure and Mehta, 1985).

- Water temperature

The effects of water temperature on the erosion of consolidated sediments were evaluated by Ariathurai and Arulanandan (1978). They found that as water temperature increased, the critical shear stress required to initiate erosion decreased. Also, Nichols (1986) reported that lowering the water temperature over a range of 20 *ºC*, its viscosity can change by a factor of 1.4. This fact reduces the settling rate of particles, remaining in suspension (mainly in Winter), which means that consolidation is reduced, decreasing the bed shear strength. On the other hand, microbiological activity is also decreased with lower temperatures (Caywood, 1999).

In their review on erosion of cohesive soils, Kelly and Gularte (1981) report results and conclusions obtained by other researchers. Thus, Raudkivi and Hutchison concluded that only at low salinities, temperature is important on erosion rates, increasing when temperature increases. In the same way, Abon-Seida and Arafa found that an increase in water temperature reduced bed resistance. The water temperature also affects the bedload sediment transport rate (Grass and Ayoub, 1982).

- Rainfall

Rainfall is believed to be an important physical mechanism increasing particle delivery to the estuary and subsequent attenuation in light. Studies in sediment stability were carried out by Paterson *et al.* (2000) and they concluded that rain reduces sediment stability.

However sediment recovery is fast. Rainfall studies were also made by Römkens *et al.* (2001), and they concluded that periods of high rainfall intensity affect soil loss.

- Biological activity

In addition to hydrodynamic mechanisms, biological forces are also very important in sediment erosion and transport (Paterson, 1994). Several reviews have considered the nature of biological influences on the physical response of sediment to erosive stresses. The major mechanisms of sediment stabilisation recognised in the literature include physical binding by biological elements (filaments), the increase of inter-particle cohesion by coating with organic material and the formation of a cohesive matrix including the sediment particles (Paterson, 1989; Paterson *et al.,* 1998; de Brouwer, 2002; Black *et al.*, 2002). These mechanisms are the result of the secretion of extracelular polymeric substances (EPS) by benthic organisms (organisms that live in sediments). These effects may dominate grain-grain interactions and must be considered in conjuction with any physical parameterisation of cohesive sediment properties and behaviour (Friend, 2001; Black *et al*., 2002; Lelieveld *et al.*, 2003).

An important part of the biological component of cohesive coastal sediments are the benthic diatom communities (microscopic algae) (Kornman and de Deckere, 1998; de Brouwer *et al.*, 2000). Due to their photosynthetic activity, they continuously produce organic matter in the sediment. However, EPS may also be produced by bacteria (Black *et al.*, 2002). The diatoms become embedded in a matrix of EPS that is attached to the sediment, and by forming biofilms they are protected from the fast changing conditions in intertidal mudflats. These biofilms bind the sediments and increase the stability of the sediment surface (enhance erosion resistance) by increasing the erosion threshold (Kornman and de Deckere, 1998; Sutherland *et al.*, 1998; Paterson *et al.*, 2000). Diatoms migrate through the sediment in response to tidal conditions, light and physical-chemical factors such as nutrients availability (Paterson, 1989). Because diatoms require light, they are restricted to the sediment-air and sediment-water interface of estuary sediments. Thus, their influence is mainly upon the critical erosion stress rather than erosion rate (Black *et al.*, 2002).

Another important factor controlling natural sediment stability is the activity of other larger organisms (macrofauna), such as snails, crustaceans, bivalves (Black *et al.*, 2002). They may increase bed roughness and so, enhance erosion, by burrowing, grazing, faecal pellet production, particle sorting or tracking of the sediment surface (bioturbation activities).

While benthic diatoms and bacteria are considered biological stabilisers (contribute to sediment stability by enhancing cohesion and promoting flocculation and deposition), the larger organisms are destabilisers. Both types of organisms do not exist in high quantities in estuary simultaneously because macrofauna feeds from diatoms (Widdows *et al.*, 2000; Black *et al.*, 2002). Bioturbation studies were carried out by Grant and Daborn (1994). They observed the effect of amphipod species on sediment transport and found that they have two opposite effects: destabilizing (inhibiting diatoms films) and stabilizing (inhibiting initiation of grain motion). The authors emphasized the necessity in measuring both erosion rate and erosion threshold for assessing the effects of benthic biota on sediment transport.

Other studies with mud snails have been made and it is widely assumed that they increase significantly the erosion rate and decrease the erosion threshold. The effect of snails density was also evaluated by Andersen *et al.* (2002). Also, Dabron *et al.* (1993) found that migratory shorebirds affect erosion. In fact, when birds arrive, macrofauna decreases, resulting in an increase of sediment cohesion and strength.

Because biological processes are inherently linked to temperature, muddy systems can exhibit a strong seasonal variations (Black *et al.*, 2002). In the Dollard estuary, Kornman and de Deckere (1998) observed an increase in erosion resistance in April, that was correlated with a diatom bloom, and an increase in sediment erodibility at the beginning of June (coincident with the disappearance of diatoms in May). In addition, Widdows *et al.* (2000) observed, in the Humber estuary, a high erosion threshold in sediments between March and June, which was related with the presence of benthic organisms and low quantity of bioturbating bivalves. In the same way, de Brouwer *et al.* (2000) observed an increase in sediment stability in Spring, due to the presence of diatoms. The presence of diatom biofilms increased the sediment water content by water retention. In late Autumn, the biologically induced adhesion reaches a maximum, which is subsequently destroyed by Winter storms and ice (Grant *et al.*, 1982). The destruction of the macrofauna results in a bloom of diatoms in Spring. By late Spring macrofauna began to recover and diatom biofilms began to degrade by grazing, nutrient limitation, dessication, and resuspension (Black *et al.*, 2002).

The Winter ice cover of the intertidal flats was investigated by Staats *et al.* (2001). The authors found that ice in late Winter strongly affects water turbidity and algal blooms. Thus, ice cover increases the consolidation of bed material and the reduction of wave energy, resulting in an increase of microalgae and EPS levels. Consequently, bed strength is greater, leading to a lower concentration of suspended particulate mater.

The relative advantages of experiments carried out in laboratory or *in situ* (field) depends upon the researcher point of view. Thus, Black and Paterson (1997) refer the problems concerning laboratory tests as the requirement for a sediment sample from the field, that produce some structural damage on the sample. In addition, sampling inevitably affects the biological component, changing the sediment structure and strength. Thus, the authors strongly suggest measurements directly in the field over undisturbed sediments.

The limitations of laboratory based measurements were also emphasized by Young and Southard (1978) and Dabron *et al.* (1993). On the other hand, in tests using macrofauna, Andersen *et al.* (2002) highlight the importance of field studies as a supplement to laboratory studies, being both kind of studies needed to fully understand the system. Also, Grant and Daborn (1994) argue the case for laboratory tests, allowing an assessment of various biotic and abiotic factors that affect sediment transport. Furthermore, laboratory flumes permit small-scale and specific measurement at sediment surface, as well as a detailed visual assessment during erosion, which is less feasible *in situ*.

- Sediment pH

In general, the erodibility of abiotic cohesive sediments increases with increasing pH (Ravisangar *et al.*, 2001). The sediment pH affects the strength of the inter-particle forces: low pH values increase the attractive forces between particles, leading to a stronger cohesive bond and increasing resistance to erosion (Rand and Melton, 1977).

The pH in estuarine sediments typically ranges from 6 to 8. Nevertheless, the algae density may cause fluctuations in pH during the day due to photosynthesis. As a result, the pH may increase to near 10, receding to 5.5 during night. These strong variations affect the sediment stability (Montague, 1986). Variations in sediment pH may cause changes in sediment water content, changes in rheological properties, as well as modification from a stratified to a uniform sediment bed (Ravisangar *et al.*, 2001).

- Depositional history

The influence of the previous flow conditions, i.e. the depositional history of sediments on their stability has also been investigated (Lau and Droppo, 2000; Droppo *et al.*, 2001; Kleinhans, 2001). In experiments on the Hamilton harbour, it was found that the flow conditions prior to bed formation strongly affect its erodibility. Thus, deposited beds which are formed under quiescent conditions present a critical shear stress up to eight times lower than that for beds formed under flowing conditions. These are deposited under shear flows and are much more resistant to erosion than the others (Lau and Droppo, 2000). In addition, critical shear stress on both types of bed formation and on a biostabilised bed was measured by Droppo *et al.* (2001). These authors observed that biostabilised beds and those formed under shear conditions are much stronger than the others.

The depositional history of a bed must be taken into account in modelling sediment transport, particularly in fluvial environments, where sediments are typically stratified (Lau *et al.*, 2001).

- Exposure

Increases in sediment stability, during the Summer, were observed when tidal flat exposure occurred at noon, due desiccation by the sun (Mitchener and O'Brien, 2003). On the lower flats, with durations of exposure of 0-2.5 *h*, the sediment surface will be heated and dried out by sunlight and wind. As a consequence, an increase in the threshold erosion takes place, reducing erosion during next inundation (Dyer, 1998). If exposed to rainfall, the opposite effect is expected.

- Waves and currents

Mudflats within an estuary are less exposed to the action of hydrodynamic forces than those on open coasts. Their shape is influenced by a complex interaction with the morphology and the hydrodynamics of the sand, which may be transported by currents surrounding estuary, waves, or by both acting together (Soulsby, 1997). Although waves in estuaries are usually smaller than those found on the open coast, they can have an important influence on sediment transport and the onset of erosion, because most of them are locally generated (Dyer, 1998; Roberts *et al.*, 2000; French *et al.*, 2000). Currents may be caused by tidal motions, wave-induced forces, wind-stress, amongst others. Waves may be generated by local winds (are locally-generated) or may result from distant storms (Soulsby, 1997). Their size depends on fetch length (distance exposed to the wind action), wind speed and length of time for which it blows. A detailed classification of the wave growth mechanisms was presented by Belcher and Hunt (1993). Both hydrodynamic forces move sediments on mudflats and are present on any particular mudflat. However, long-

shore currents will generally dominate over the other types of hydrodynamic forcing (cross-shore currents and waves) in deep water, but are much smaller in shallow water.

For both deep and very shallow water, the influence of waves at the bed is weak. In the lower part of the mudflats during high tide, the depth is large enough to reduce the influence of waves. In the upper mudflats that depth is lower and the influence of waves is observed over a longer proportion of the immersion period (Roberts *et al.*, 2000). Waves can erode the muddy bed by two main mechanisms: surface erosion and fluidisation, depending on the properties of the waves and the bed.

Roberts *et al.* (2000) investigated the effect of tidal currents and waves on mudflats, using mathematical models, and they concluded that the action of waves makes the mudflat steeper and more concave. Moreover, wind generated waves cause the resuspension of benthic diatoms (de Brouwer, 2002).

Experiments involving both wind and mechanically generated surface waves were performed by Thais and Magnaudet (1996), in order to study wave-turbulence interactions. In their work, the authors tried to extract the turbulent component from the total fluctuating motion. These researchers found that turbulence levels below surface waves can be substantially higher than that on solid wall flows, for the same stress. In addition, they observed the enhancement of both the turbulent kinetic energy and its dissipation rate, being the energy transfer greatly affected by wave-turbulence interactions. These interactions are related to mechanisms responsible for vorticity generation near the crest of the dominant wave. However, the application of periodic stress due to water waves over mud has various consequences such as bed weakening, turbidity generation (high suspended sediments concentrations) and surface wave attenuation (Maa and Mehta, 1987).

Laboratory wave flumes have been used in measurements of wave-induced flows, to study the bed response (sediment entrainment mechanisms) to changing hydrodynamic forcing near bed (Williams *et al.*, 2002).

Thais and Magnaudet (1996) emphasize the problems existent in field studies. Although there is not a limited fetch, it is difficult to make accurate and non-perturbing measurements. In addition, sudden changes in wind intensity and direction, makes it more difficult to identify the real turbulent velocity in the field. Nevertheless, because the complexity of erosion in the field, involving factors such as waves and currents, laboratory results may not be directly comparable to the real conditions (Wang, 2003).

- Bed characteristics

The characteristics of the bed (or bedform) depend on the strength and type of flow, which can be induced by steady or tidal current, waves or their combination (Soulsby, 1997). An initially flat bed, under a given shear stress, may deform into various configurations, ranging from small ripples up to sandbanks, including dunes and sandwaves. These patterns may be only a few centimetres or several meters high (Raudkivi, 1997). Steady currents in rivers form small ripples and large dunes. Tidal currents form similar features in estuaries and sandwaves (due the oscillatory nature of the tides) (Soulsby, 1997). The bedforms may be predominantly oriented parallel to the cross shore or oriented in the shore direction (Whitehouse *et al.*, 2000).

The bed shape has a large influence on the total bed roughness and hence on the frictional characteristics and turbulence production in flows, which affects erosion and the transport of sediments (Whitehouse *et al.*, 2000). Ripples are small scale patterns (associated with fine to medium sand, and low flow velocities), whose wavelength and height are small compared to the water depth. They are washed out at very high flow speeds (Soulsby, 1997) and are independent of flow depth (Raudkivi, 1997). Once formed, ripples are usually no longer than 0.6 *m* and no higher than 0.03 *m*, and are formed from cohesionless sediment grains smaller than 0.6 *mm* in diameter (Bennett and Best, 1996). Dunes and sandwaves are generally larger bed patterns and their heights and wavelengths are dependent on the water depth as well as the bed shear stress, because they develop at higher stresses (Soulsby, 1997). The formation of antidunes may occur in high energy environments, where free surface waves exist. The mechanisms of formation of those structures is unknown at the moment, but may be related to the existence of secondary flows (Dyer, 1998).

Ripples and dunes play a significant role in the definition of the hydraulic roughness. Ripples act as roughness elements, with wakes between them, changing the boundary layer. Thus, they affect both the velocity distribution and bed shear stress (Raudkivi, 1997). Ripples were found to migrate at a constant rate, which depends on wave and sediment characteristics (Blondeaux *et al.*, 2000). In bedform migration, the mobile grains roll over the bedform, up the upstream (stoss) and down the downstream (lee) faces, resting in the throat. The flow field will change as the bed roughness is modified by bedforms and as suspended sediment is added to the flow. In the presence of bedforms, the bed shear stress will have two components: the skin friction, which is responsible for bedload transport and entrainment of sand; and the form-drag component, inducing the diffusion of the suspended sediment into the flow (Bennett and Best, 1995; Soulsby, 1997).

Fluid flow over dunes can be classified into five zones: accelerated flow occurring over the dune crest; flow separation and recirculation on the crest lee side; decelerated wake zone, extending downstream; outer, near-surface region and downstream growth of a new boundary layer at reattachment (Bennett and Best, 1995). As far as dunes morphology is concerned, they can be symmetric or asymmetric. The first have stoss and lee sides of similar length and topographically regular rounded crests and smoothed lee side slope angles; asymmetric dunes have small superimposed dunes on stoss side, steeper lee sides and sharp crests (Villard and Kostaschuk, 1998). However, the physical mechanisms of dune formation are still not well understood, because it is nearly impossible to simulate dunes at real scale in laboratory (Herrmann, 2002). Villard and Kostaschuk (1998) examined the effect of dune geometry on the relationship between shear velocity and suspended sediment concentration and they concluded that shear velocity is much higher for asymmetric dunes. Also, for symmetric dunes sediment suspension is controlled by total stress, while for the others it is related with skin friction as well as roughness because the superimposed dunes.

In macroturbulence studies generated by dunes in an estuary, Kostaschuk and Church (1993) observed large turbulent structures generated on the lower stoss sides, appearing at the surface as strong boils. These boils, which correspond to slowly rotating upward vortices whose origin is near the bed, are very important for sediment suspension from the bed (Bennett and Best, 1995; Venditti and Bennett, 2000).

Bennett and Best (1995) investigated the flow structure in the vicinity of fixed dunes in a laboratory recirculating flume, using LDA. This flume was used to avoid bedform

migration and remotion from the experimental setup. These researchers used artificial bedforms moulded in dunes generated in sand, and the surface with appropriate grain roughness was reproduced using glass spheres. Thus, it enabled the acquisition of detailed and reproducible measurements. They found that dune-related macroturbulence is mainly due Kelvin-Helmholtz instabilities (which are greater for dunes than ripples), that control both the local flow and the sediment entrainment and transport. A comprehensive review on the experimental work carried out on a flow over fixed bedforms was also made by the authors.

Bennett and Best (1996) carried out measurements over fixed ripples made of a rubber surface moulded over a bed of glass spheres (220 μm in diameter). Contour maps showed that velocity is affected by bed morphology through acceleration/deceleration near bed. The ripple-dune transition was also investigated. They found that, as flow velocity, bed shear stress and sediment transport rate increase over ripples, their height and length also increases, forming larger bedforms. These cause higher turbulent fluctuations in velocity, generating higher Reynolds stresses near reattachment, which increases bed erosion. However, the authors refer that the flow over these artificial bedforms cannot replicate mobile bed conditions exactly due to the absence of a sediment load and a reduction in bed porosity. By far, the most frequent option for constructing an artificial sediment is that referred as a rigid surface.

Field and laboratory modelling studies were made and compared, to quantify flow over natural sand dunes, and in both cases it was observed a flow acceleration over the dune crest and deceleration in the lee side, without permanent flow separation (Best *et al.*, 2000).

As flow magnitude increases, the loss of dune mass to suspended load may flatten its shape (Prent and Hickin, 2001). Because the shear exerted on a dune is maximum at the dune crest, that region is eroded as flow energy increases, and the dune length continues increasing, decreasing its steepness. Prent and Hickin (2001) concluded that roughness and flow resistance increased rapidly with dune size, until a threshold height or length is obtained. In fact, the bed roughness is one of the various important factors affecting the erosion process. Smoother surfaces show less soil loss than rough surfaces. In addition, surface topography strongly influences the development of drainage networks (Römkens *et al.*, 2001). The sediment bed is usually not smooth, exhibiting perturbations that contribute to the bed roughness and affecting the drift velocity (Ridler and Sleath, 2000).

- Suspended particles

It is known that the contribution of entrained particles in suspension to turbulence is very important in the erosion process. In the presence of a flow beyond the motion threshold, sediments and sand are entrained from the bed and into suspension. They remain in suspension and are carried by the flow if their settling velocity is smaller than the upward turbulent velocity component (Soulsby, 1997).

Because of their small particle size distribution, fine-grained cohesive sediments are more likely to be entrained into the flow and be transported as suspended load. Dredging in estuaries may increase turbidity (reducing light penetration) by higher suspended matter concentrations, and enhance sediment deposition, affecting the growth and survival of benthic organisms (Dankers, 2002). Sediments disturbed by dredging usually loose their

cohesive strength and concentration of suspended sediment may increase 10^3 to 10^5 times the normal (Nichols, 1986). Within hours or a day, concentrations typically return to normal.

Particle entrainment depends on many of the factors previously mentioned, such as: turbulent stress at the sediment-water interface; sediments composition (mineralogy, particle size, organic content); water content; depositional history and biological activity (Lick, 1982).

Experiments carried out by Lick (1982) in natural sediments, using an annular flume, showed that when sediment is entrained, its concentration in the overlying water increased rapidly in the early stages and then more slowly, until a steady state is achieved. Interaction between particles affect turbulence production by processes such as low-speed streaks, streamwise vortices, ejection or sweep associated with the structure (Hagiwara *et al.*, 2001). In addition, larger particles cause an increase in the number of ejections, turbulence intensity and Reynolds shear stress (Rashidi *et al.*, 1990), which may be due the formation of turbulent wakes behind such particles (Graham, 2000).

Hagiwara *et al.* (2001) investigated the effect of settling clusters of particles on the turbulence. They found that particle clusters, which modify near-wall turbulence structure, cause an increase in the streamwise and downward mean velocities and a decrease in the streamwise turbulence intensity. If the concentration of the dispersed phase is high enough, the presence of particles may affect the turbulence characteristics of particle-laden flows. However, due to its complexity, this effect is still not completely understood (Graham, 2000; Dyer *et al.*, 2004). Turbulence studies in particle-laden turbulent homogeneous shear flows have been made by Graham (2000), developing prediction models, and it was concluded that the presence of small particles has an effect in attenuating the turbulence, by energy extraction from the primary flow turbulence. Also, a decrease in turbulence with increasing mass loading was predicted.

As shown, the behaviour and properties of sediments in estuaries are dependent on a large number of factors. Therefore, it is not entirely unexpected that the prediction of sediment behaviour in a coastal environment is difficult.

2.3 FLOW CHARACTERISATION

The flow pattern inside a section depends on the configuration of the test rig. It is fundamental to understand the hydrodynamics of a given device prior to its fabrication, in order to find the ideal dimensions (based on the requirements of a reasonable uniform shear stress and a stable flow field) (Maa, 1990). The secondary flows, which have a negligible contribution to the total bed shear stress, will strongly affect erosion of cohesive sediments, because they circulate the sediments particles and flocs (Maa, 1990; Besley and Delo, 1990).

Several devices have been developed to investigate sediment erodibility; some of them have been designed for *in situ* studies of intertidal muds and others are suitable for laboratory study. Almost all of the devices operate on the principles of uni-directional fluid shear stress acting on the sediment/water interface in such a way as to replicate the fluid

shear stress generated by hydrodynamic conditions in the field. These devices differ in configuration, size, flow geometry, mechanism of flow generation and measurement methodology, and are usually used to determine erosion rates and shear stresses for sediments. Their shape varies between linear, oval or annular patterns (Amos *et al.*, 1992a). The purpose of a flume is not only to simulate the field conditions near the sediment surface, but also to simplify the flow patterns, enabling later replication (Nowell and Jumars, 1987). As a result, it is important to select an appropriate flume design. Because there is not a general purpose flume to simulate accurately the field environment, it is important to define previously the problem under research, in the laboratory.

Black and Paterson (1997) presented a review of erosion devices currently used to measure sediment stability. These devices are generally used *in situ*, on cohesive sediments and use a variety of methods to induce stress and measure erosion. The authors classify the instruments into benthic flumes and miscellaneous devices. For each device the operational mode (subaerial or submerged) is given as well as the criterion of erosion (primarily based in the suspended sediment concentration). The benthic flumes were sub-divided into recirculating and flow-through flumes. Recirculating flumes were defined as infinitely long channels (they are closed systems), and included, among others, the benthic annular Sea-bed flume or VIMS Sea carousel (Maa, 1990); the recirculating benthic flume-Sea carousel (Amos *et al.*, 1992a); the vertical recirculating flume or ISEF - In Situ Erosion Flume (Houwing and van Rijn, 1995), which has a race-way geometry to reduce the magnitude of the secondary flows. On the other hand, flow-through flumes (consisting of a long straight channel) include e.g. the Seaflume used by Young and Southard (1978). However, the recirculating flumes seem to reproduce better the erosion process as it occurs in natural environments, although they are associated to secondary flow patterns (Black and Paterson, 1997). Because of the centrifugal forces, the secondary flow, in annular flumes, is inwards near the sediment/water interface, upwards at the inner wall of the flume, outwards near the lid/water interface, and down at the outer wall (Sheng, 1989). As examples of miscellaneous devices, one may consider the Cohesive strength Meter – CSM (Paterson, 1989); the Instrument for Shear Stress In Situ – ISIS (Williamson and Ockenden, 1996); the Microcosm (see Tolhurst *et al.*, 2000a), among others (Black and Paterson, 1997). As referred by the authors, these devices, which push a core into the mud before the erosion test, will modify the sediment structure. A detailed description of all devices and specific details is available in the literature.

The choice of the appropriate flume depends on many factors, such as flume size, area of sediment tested, deployment method, weather dependence, construction cost, instrument portability, the required precision, reproducibility of the fluid flow (Black and Paterson, 1997).

Some of the most common devices used to study the erosion of cohesive sediments were also reviewed by Caywood (1999). Furthermore, Mitchener and Torfs (1996) presented different types of flumes used in laboratory experiments, applying a variety of sediment beds, including the wave flume and settling tank. A large wave flume recently used is the Deltaflume (Williams *et al.*, 2002), which is 230 *m* long and is considered to replicate sediment resuspension at approximately field-scale, although it is for lab use.

The appropriate flume to model flows in laboratory is selected by taking into account some dimensionless groups, such as: Strouhal number; Froude number; Reynolds number (Nowell and Jumars, 1987). Strouhal number is used as a measure of the unsteadiness of the flow, being steady or unsteady when this parameter is zero or 1, respectively. Froude

number is relevant when free-surface effects need to be considered, like in the presence of surface waves or when the boundary layer extends through the entire flow depth. This parameter is used to classify the flow as subcritical (if less than unity), where the flow is deep and slow, or supercritical, if greater than unity. Reynolds number corresponds to the ratio of inertial to viscous forces. When Reynolds number increases, so does the Froude number, which requires a compromise (Nowell and Jumars, 1987).

When modelling studies are made over a deformable bed (movement of the sediment as bedload or as suspended load), other dimensionless groups must be considered: roughness Reynolds number (it is a measure of bed interaction with flow); Rouse number (of which small values indicates rapid diffusion of the particles across the boundary layer); the Shields parameter (Nowell and Jumars, 1987). Depending on the specific conditions of the study, some of these dimensionless groups can be neglected.

A channel with constant geometry and infinite flow length enables a fully developed boundary layer, which is an important requisite in the application of flume erosion studies in natural systems (Amos *et al.*, 1992a). Depending on the technique used for the determination of the strength of a sediment bed, flumes can be either smaller or bigger. Thus, the technique in which the shear stress is induced by a horizontal flow (a circulating or straight water flow exerts a shear force on the surface) is generally used in flumes such as the benthic annular flume, mobile recirculating seawater flume (MORF), annular Sea-bed flume, or straight flumes (Houwing and van Rijn, 1998). This technique requires large size flumes (in the order of 2 *m* and test section ranging 0.1-1 m^2) to allow a logarithmic velocity distribution.

Smaller flumes usually use other techniques: generating a water jet impacting on the sediment bed surface (e.g. the CSM); inducing a turbulent motion near the bed surface, using a propeller (EROMES; Schünemann and Kühl, 1991); generating a turbulent motion of the fluid above the sediment by oscillation of a horizontal grid (e.g. Shaker; Tsai and Lick, 1986); generating a stream of water between an inverted bell-shaped funnel, located near the sediment surface (ISIS). Although they are easier to handle, due to their small test section (approximately 0.01 m^2), results are affected by the irregularities on the bed surface (Houwing and van Rijn, 1998).

The effects of the shape and the scale of laboratory flume cross-section on the bed shear stress were evaluated by Torfs *et al.* (1994) and Torfs (1995). In narrow flumes, the side walls effects on velocity distributions are stronger as well as on shear stress distributions in the cross-section. Torfs (1995) investigated the flow behaviour over a rectangular and semi-circular flume cross-section and found a much higher erosion in the semi-circular flume, at the same shear stress. In this flume the side wall influence is more significant, leading to secondary flows and irregular shear stress distributions, that results in the development of irregular bedforms and local deep holes during the erosion. In a rectangular cross section these characteristics are uniform and the maximum bed shear stress is obtained in the centre, while in the other flume there are several local maxima. The average bed shear stress is higher on the semi-circular flume, inducing higher erosion rates because of the secondary flows. In the same way, Torfs *et al.* (1994) observed the formation of very irregular ripples and dunes in a circular cross-section, because the side walls affect the shear stress distribution, while in a rectangular flume they were regular, with no significant side walls influence. In addition, they found no significant differences in critical shear stresses for similar sediment mixtures, measured in the circular and rectangular cross-sections. However, when mixtures were made of more than 30 % of fine

particles, they behaved as cohesive in rectangular cross-section and as non cohesive in circular cross-section, with higher erosion rates. In this manner, the influence of the cross-section shape is most important when the sediment transport and bedforms are evaluated, once the erosion has started (Torfs *et al.*, 1994).

Although secondary flows are typical of annular flumes, they reach an approximately uniform shear stress environment, in opposition to the straight flumes, in which non uniform flow occur where the boundary layer is developing (Ravens and Gschwend, 1999). In addition, the channel length of straight flumes is usually not long enough to guarantee a fully developed boundary layer. Thus, they are not appropriate to be used in field tests due to the long lengths required. This problem is overcome using annular flumes due their infinite flow length (Williamson and Ockenden, 1996; Black and Paterson, 1997).

The advantages of annular flumes were also highlighted by Maa (1990), who used an *in situ* Sea-bed flume, arguing that it does not need a pump and, therefore, does not break the sediment flocs. In addition, the secondary flows will distribute the suspended sediment, avoiding stratification. This flume was used on the floor of shallow waters, has no bottom and the flow is induced by an annular ring rotating at the top. The sediment beds are nearly undisturbed with this flume. Some of these advantages were also referred by James *et al.* (1996).

In experiments carried out in a closed annular flume with a rectangular cross-section and using particles with 3 *mm*, it was also observed a Couette type flow, although of much more complicated pattern (Engelund, 1975). Thus, it became helical due the curved channel, and the bed was unstable, non planar, forming a number of sandwaves, depending on the interaction of the flow and sediment motion. These patterns induced instabilities in the flow. The secondary flows observed in these flumes have been minimised, by rotating the top lid and the bottom in opposite directions. However, a comprehensive experimental and modelling study is necessary to analyse the flow field within the rotating annulus (Sheng, 1989). Therefore, this researcher has modified the one-dimensional boundary layer equation, introducing the effect of a radial pressure gradient.

Sheng (1989) presents some types of rotating annuli used for sediment erosion/deposition studies, having different aspect ratio (ratio between depth and annulus size). When that ratio is small, secondary flow becomes more evident. However, other secondary flows may also occur in straight flumes due the formation of Taylor vortex instability (Sheng, 1989).

2.4 INTERFACE SHEAR STRESS

In short, erosion is a result of a non-equilibrium between the force on the sediment-water interface and the forces within the bed material, which resist to erosion (Soulsby, 1997). Shear stress is dynamic, varies from point to point, and is not a fluid property. The bed shear stress is the most important parameter controlling the erosion and deposition of cohesive sediments (Maa, 1990). Critical shear stress of a sediment depends on many factors such as sediment water content, pH, salinity, particle size, organic content, degree of compaction or consolidation before erosion, i.e. the factors affecting sediments erosion.

Its value can be significantly affected by the experimental procedure as well as the test device used.

The erosion flux is based on whether the local fluid shear stress (τ_b) at the bed is greater than the critical shear stress (τ_{cr}) of the bed material. Below this, virtually no erosion occurs, and above that significant erosion takes place (Parchure and Mehta, 1985; Tolhurst *et al.*, 1999). The critical shear stress is the characteristic parameter that defines erosion and characterises different types of sediment beds in terms of erosion resistance (Houwing and van Rijn, 1995). The most important variables for studying sediments cohesiveness are the critical erosion shear stress (which defines the maximum shear strength of the top layer of the bed) and the erosion rate (Tolhurst *et al.*, 2000b).

The erosion rate (ε_r) is commonly expressed by (Parchure and Mehta, 1985):

$$\varepsilon_r = M\left(\frac{\tau_b - \tau_{cr}}{\tau_{cr}}\right) \tag{2.2}$$

where M is the erosion rate coefficient, which is equal to the rate of erosion (ε_r) when $\tau_b = 2\tau_{cr}$. This expression is based on the excess shear stress ($\tau_b - \tau_{cr}$). Erosion studies using uniform beds correspond to a constant erosion rate under a constant τ_b, since τ_{cr} does not vary with depth. The value of M is dependent on physical-chemical parameters, which determine the inter-particle forces characteristic of cohesive sediments (Parchure and Mehta, 1985; Mehta, 1991). De Vries (1992) rearranged this equation, substituting the time derivative of the total suspended load, and obtained a relationship between the bed shear stress and the measured erosion rate. Using this method, the parameters τ_{cr} and M were easily determined.

However, when there is a non-uniform bed shear strength (τ_s) it is recommended to use the following expression (Parchure and Mehta, 1985):

$$\varepsilon_r = \varepsilon_{rf} \exp\left[\gamma\left(\tau_b - \tau_s\right)^{1/2}\right] \tag{2.3}$$

being ε_{rf} defined as the floc erosion rate and γ an empirical coefficient. The floc erosion rate is dependent on the type of sediment and the extent of the bed shear stress.

The problem of defining critical flow conditions associated with the initial instability and entrainment of bed sediment particles is of fundamental importance in the study of sediment erosion mechanics. The importance of defining a reliable method to determine the shear stress under laboratory and field conditions has been emphasized by de Jonge and van den Bergs (1987). The strength of intertidal mudflats is strongly related to physical, chemical and biological parameters. Because of its complexity, bed shear strength must be found experimentally from laboratory tests using either artificial or natural muds, or through *in situ* field tests.

Depending on the physical system, different methods have been used in the shear stress measurements and in determining erosion threshold. Besley and Delo (1990) present four different methods for measuring the shear stress exerted by the fluid on the bed, within the carousel flume: involving direct measurement of the energy input to the roof (predicts the average bed shear stress); measuring the velocity profiles close to the bed, using LDA; using flush mounted shear stress probes (through hot wire anemometry technique, to

measure shear stress along the base and side walls of the flume) and inferring the shear stress (qualitative data) across the flume from eroded profiles of muds (assuming that the mud bed shear strengths increase with depth). In this method, the concentration of suspended solids is continuously measured, increasing rapidly at the beginning (strong erosion) and slowly decreasing until a constant value is achieved, when no erosion occurs. These results were directly correlated with the erosion depth, which was found to be proportional to the bed shear stress. Despite some disadvantages in using the hot-film stress probes, such as the calibration in a flow where the wall shear stress is known, satisfactory results were obtained (Graham *et al.*, 1992). The authors also refer that the maximum shear stress in this flume is 1 *Pa*.

In determining the critical shear stress corresponding to the erosion of the bed top layer, the maximum shear strength of that layer is obtained. Houwing and van Rijn (1995) determined, *in situ*, the critical bed shear stress in cohesive sediments using the ISEF flume. The bed shear stress was calculated by measuring the velocity profile in a vertical direction at a height of 25 *mm* above the bed, assuming a logarithmic distribution. Subsequently (1998), these authors used the same flume and the same technique to determine the bed shear stress and erosion of a kaolinite bed, in laboratory. They stated that this device measures the minimum shear stress at the onset of bed erosion, leading to the maximum bed shear strength. It is important to mention that sediment bed preparation procedures (like consolidation time) cause significant variations in the critical shear stresses obtained (Parchure and Mehta, 1985). Velocity distribution was found to be dependent on flow depth and bed roughness (Alvarez-Hernandez, 1990; Peterson, 1999).

The erosion shear stress obtained using the previous flume is compared with that found by other three *in situ* devices: Microcosm, SedErode (ISIS) and CSM (Tolhurst *et al.*, 2000a). All of them use different strategies to induce and measure erosion and the definition of erosion threshold is different between users, therefore it is not easy to compare the data. As stated by the authors, there is not a standard methodology, universally accepted, to measure the critical erosion shear stress. The suspended particulate matter is generally measured and, to allow a comparison between devices having different test sections, it is normalised by the area. For the Microcosm, the suspended particulate matter is used to calculate the erosion rate and the critical erosion shear stress (determined usually from a time series graph of suspended particulate matter). The critical shear stress on SedErode is determined from the turbidity in the water column (resulting from bed erosion). The CSM uses a vertical jet of water to erode the sediment surface, and erosion shear stress is calculated from a relationship involving the eroding pressure. These investigations found similar values for the critical erosion threshold from ISEF and Microcosm (0.19 and 0.26 *Pa*, respectively), as well as with the SedErode device. However, those obtained with CSM were larger (from 0.32 to 1.25 *Pa*). It was also observed that the critical erosion threshold increases as the device test section area decreases, due to topographic variation and bed irregularities in the field. Similar observations were made when comparing CSM (field) with laboratory EROMES flume results, using field sediments (Tolhurst *et al.*, 2000b). In the field it is possible to select the place where the quantity of diatom biofilms is higher and because CSM has a smaller test section, it can measure entirely within those regions, resulting in higher erosion thresholds.

The CSM can generate a wide range of erosion shear stresses (0.2-9 *Pa*), allowing its deployment in diversified intertidal areas. In this device, the critical erosion threshold is defined as the pressure step at which light transmission drops below 90 *%*. When it stays above approximately 95 *%* no erosion is assumed to occur (Tolhurst *et al.*, 1999).

Erodibility has been evaluated as an increase in sediment concentration in the flume with the shear stress (Staats *et al.*, 2001). The suspended particulate matter was determined by sampling and filtering through glass fibres filters (1 μm) and was monitored using a turbidity sensor. These techniques were also applied by other researchers, e.g. Tolhurst *et al.* (2000a).

In situ studies on the erodibility of cohesive sediments were made using a benthic annular flume Sea carousel (Amos *et al.*, 1992a). Erodibility was detected from the rate of change in suspended sediment concentration within the annulus. Critical shear stress at the surface is determined assuming that the bed shear stress is equivalent to the shear strength at the depth in the sediment at which erosion is concluded, and is derived by extrapolation of the least squares best-fit line to the surface. Recently, Amos *et al.* (2003) presented three different methods to estimate the surface erosion threshold in the Sea carousel: the first one adjusts the bed strength to eroded depth and analyses the threshold; the second correlates the erosion rate with the applied bed shear stress and the third extrapolates the value of sediment concentration and applied shear stress at ambient concentrations. On that flume, the authors found that the mean erosion thresholds were 0.5, 0.27 and 0.34 *Pa* for the three methods, respectively, concluding that the third method is recommended for the evaluation of the erosion threshold, giving reproducible and objective results.

Even using the same device and the same method for predicting erosion, the shear stress at each site in the field will be dependent on many factors such as chemical and biological influences and the history of the bed, as previously referred (Mitchener and Torfs, 1996).

Other *in situ* devices have been used to measure surface erosion shear stress on the mud. Williamson and Ockenden (1996) developed the instrument ISIS, in which critical shear stress is given by an increase in turbidity due to a significant removal of material from the bed surface. The average surface erosion shear stress may be calculated through the flow and gap measurements at the point of erosion. Laboratory tests were also made with ISIS and results compared with those obtained using the HR carousel, in similar mud beds. Their surface erosion shear stress was similar (in the range 0.11-0.25 *Pa*) and it was observed in both an increase in erosion shear stress with depth of erosion. When compared with results obtained using CSM, the shear stress was approximately 10 times greater with this device, which may be due the difference between pulsed and continuous shear stresses applied by the CSM and ISIS, respectively. In fact, while ISIS measures erosion shear stress, CSM measures erosion shear strength. Typical values of critical shear stress for estuarine tidal mudflats range between 0.02 and 2 *Pa* (Black *et al.*, 2002).

In experiments using a straight flume *in situ* it was found that critical shear stress increases with depth, doubling for each 1 *mm* in the sediment (Ravens and Gschwend, 1999). Critical shear stress has also been calculated as a function of the particle diameter, using different expressions depending on the range of that diameter (Roberts *et al.*, 1998).

Many experiments have been carried out using laboratory flumes. The critical bed shear stress for erosion, using an annular flume, has been determined by observing bed movement and by monitoring the suspended solid concentration through an optical backscatter probe (OBS) (Droppo *et al.*, 2001). These researchers made tests using kaolinite clay and natural sediments and they obtained stronger critical shear stress values (0.325 *Pa*) when a biofilm was present on sediment surface (known as biostabilization), than when it was absent (0.024 *Pa*). The OBS sensors have also been used to measure the suspended sediment concentrations directly in the field (Tattersall *et al.*, 2003). On the other hand, Wiberg and Smith (1987) obtained an expression for the critical shear stress of

non cohesive sediment, based upon a balance of forces on individual particles at the bed surface: near-bed drag force, lift to drag force ratio, gravity and resisting force. At the surface, the sediment particle starts moving when the downstream and upward forces acting on the particle overcome those binding it to the bed. The authors found the results close to those determined using Shield's diagram, for uniformly sized sediment. They also stated that critical shear stress for a particle on a poorly sorted bed can be much different from that for a well sorted bed. A similar balance of forces was also taken by Mehta and Lee (1994) to estimate the threshold condition for the grain transport. These authors emphasize that, for purposes of sediment transport, in the transition between cohesionless and cohesive behaviour, the settling velocity is more important than the grain size. In the same way, Dade *et al.* (1992) predict the critical bed shear stress required for the entrainment of a cohesive grain, by analysing the forces on the grain, taking into account the inter-particle adhesion or cohesive force. They stressed the importance of cohesive yield stress and particle size, shape, density and packing geometry for the evaluation of erosion resistance.

Depending on the surface threshold stress in erosion, Amos *et al.* (1992b) classify two patterns of erosion in fine-grained sediments: type I (asymptotically decreasing with time) and type II (constant with time). The critical bed shear stress is in the range of 0.2-2.5 *Pa* and greater than 4.1 *Pa* for type I and type II, respectively.

Furthermore, the average bed shear stress has been determined as a function of the ring rotation speed (*rpm*), which was obtained specifically for the VIMS Sea carousel (Maa *et al.*, 1995). Because it is easy to measure the ring speed, the sediment behaviour can be related with bed shear stress. Peterson (1999) presents a relationship to estimate benthic shear stress in shallow waters, based on the surface velocity and water depth. This researcher classified the sediments into six distinct zones, according to benthic shear stress: dead zone, where benthic shear stress is below at 0.001 *Pa* and sediment scouring is insignificant; cell zone, where single cells and small algal particles move at shear stresses in the range 0.001-0.003 *Pa*; feed zone, corresponding to the motion of larger algal flocs and feed pellets (0.003-0.01 *Pa*); clay zone, where movement of non cohesive clay sized particles takes place at stress of 0.01-0.03 *Pa*; silt zone, corresponds to erosion of non cohesive silts sized particles (0.03-0.1 *Pa*); sand zone, corresponding to sand movement at a shear stress of 0.1 *Pa*. Finally, for very small particles, critical shear stress is determined by density rather than size.

The calculation of bed shear stress may also be based on the slope of the energy line (Petit, 1990; Torfs *et al.*, 1994; Torfs, 1995), using a side wall elimination technique, in which the influence of the walls is eliminated (see Torfs, 1995). Threshold erosion conditions were also determined by visual observation using high-resolution photography, allowing the determination of the critical shear velocity (Young and Southard, 1978). Recently, erosion studies in non cohesive sediments have been made using an in-line digital video holography technique, which records three-dimensional information on particle positions and sizes, overcoming the limitations of photography (Sun *et al.*, 2002). This technique was found to be very useful, particularly in the observation of incipient erosion of sediments.

Because of the complexity of erosion process, Amos *et al.* (1992a) stressed that realistic results are obtained when measurements are taken within the natural environment, such as using field flumes. Also, Mitchener and Torfs (1996) consider differences in the erosion behaviour between undisturbed (core samples or *in situ* measurements) and artificial

sediments, arguing that in artificial beds (mechanically mixed or deposited from suspension) there is not enough time to develop biological growth and chemical reactions, which effect erosion. On the other hand, Houwing and van Rijn (1995, 1998) argue that measurements of the erosive resistance in cohesive sediments should be taken *in situ*, because handling and storing of the samples under laboratory conditions will change sediment properties, resulting in higher strength of the samples than under natural conditions. In some cases, laboratory flumes may overestimate the critical shear stress by a factor of 2 (Ravens and Gschwend, 1999). However, results obtained in laboratory and *in situ* can be approximated if sediment in laboratory is colonized by organisms, as in the field, although it is not easy to maintain a healthy and representative benthic community. Thus, parallel *in situ* and laboratory tests for the same mud are suggested, using the same device (Black and Paterson, 1997).

Both in field and in laboratory tests made on remoulded sediment using a benthic flume showed an erosion rate up to seven times lower (for both tests) when compared with tests on natural undisturbed *in situ* sediments, although critical erosion stress was approximated. These differences were caused by the greater boundary roughness of undisturbed muds, increasing the turbulence and interface bed stress. It was also found that remoulding a cohesive sediment and using it in a laboratory flume, the sediment becomes stronger than without remoulding (Black and Paterson, 1997). Also, Young and Southard (1978) concluded that there may exist significant differences between laboratory and field measurements of erosion threshold, due biological and mechanical factors, changing the sediment characteristics.

The effects of transportation on sediment stability have been investigated (Tolhurst *et al.*, 2000b). It was observed that erosion thresholds of transported cores was considerably higher than that measured *in situ*. This was related with water loss, increasing sediment stability, and disturbances due vibration, and causing sediment compactation. In addition, modifications in organisms behaviour, during transportation, may occur. Therefore, the authors state that it is important to take precautions to minimise disturbance during transport, and to make measurements within a few hours of collection. The same authors also emphasize that it is not possible to compare directly erosion thresholds obtained by different devices when they use different criteria to define the threshold condition. Furthermore, this factor and differences caused by spatial heterogeneity (when sample is collected on the field) caused a much higher effect on erosion threshold than disturbance due transportation.

The shear stress distribution along the bed of the flume (annular carousel) have also been predicted using Harwell-Flow 3D model (Besley and Delo, 1990; Graham *et al.*, 1992). Researchers found a good correlation between laboratory and numerical results, although they had observed some differences in the bed shear stress behaviour close to the outer wall. These differences are linked to the hydrodynamics of the flume, particularly the occurrence of secondary flows within the channel. In addition, experimental tests showed higher erosion rates in that region, where the shear stress is larger. Good predictions were also obtained for slow flows and shear thinning fluids, in a miniature annular flume, using Harwell-Flow 3D code (James *et al.*, 1996).

Cohesive sediment dynamics has been modelled in estuaries, although being a complicated task due the complex properties of these sediments (Lumborg and Windelin, 2003).

2.5 CONCLUSIONS

Although the existent literature on erosion studies in estuary sediments is quite comprehensive, it has been made clear by some researchers that additional investigation is needed, either in artificial or natural sediment beds. Because there are various physical phenomena that affect the flow turbulence characteristics, such as roughness and irregularities of the sediment, the presence of suspended matter and the existence of surface waves, it is important to isolate each contribution and to evaluate each one of them per si. This investigation is possible in specific simulated beds in laboratory, which have not been considered in the literature. These aspects are integrated into the main objectives of this work. Also, tests on natural mud samples prove to be very interesting on three counts: to integrate all the individual contributions to the erosion process; to validate the accuracy on the simulated beds and to enable the determination of the "real" shear stress on a sample. LDA technique has been recommended by some researchers to obtain the velocity profiles and shear stresses measurements near the interface. However, the existing literature shows the difficulty associated in using this technique for such tests.

CHAPTER 3

THE LDA TECHNIQUE FOR FLOW MEASUREMENTS

In this chapter, a brief discussion on the methods available for velocity and turbulence measurements is presented. The LDA technique is amongst the most versatile tools to investigate the fluid patterns of a wide variety of complex flows because it is accurate, non-intrusive and high data collection rates may be achieved.

3.1 MEASUREMENT OF FLUID VELOCITY

The experimental fluid mechanics has, for many years, made use of mechanical probes to obtain information on fluid velocity. Therefore, pressure probes have provided the main method of measuring mean velocity, and hot-wire or hot-film anemometers the measurement of instantaneous velocity and, therefore, mean and turbulent velocities.

The Pitot tube is a flow velocity meter, which is capable of measuring fluid velocities (averaged) at a localized point. It relates the fluid velocity to the difference between the total and the static pressures. Nevertheless, despite its simple construction and low cost, its accuracy and spatial resolution may fall short for some applications, particularly for highly turbulent flows.

The hot-wire anemometer relates the changes in heat transfer from a small electrically heated sensor to the surrounding fluid, in response to the fluid velocity changes. Although it has been used for some time for quantitative research of the structure of turbulent flows (Keirsbulck *et al.*, 2002), its application has been substantially limited to constant property flows of low temperature, low speed and low turbulence intensity, outside regions of recirculation (Fingerson and Freymuth, in Goldstein, 1983). In addition, this instrument needs calibration and, as Pitot tube, is an intrusive technique, although at a much lower scale. On the other hand, in mud erosion experiments the flush mounted hot wire anemometry probes are not appropriate because, when exposed to mud, they are very susceptible to damage (Besley and Delo, 1990).

The laser Doppler anemometry (LDA) is one of the most widely used techniques for the detailed measurement of local turbulence properties and, particularly, velocity fluctuations

(McLelland *et al.*, 1999). This technique measures the velocity at a point in a flow by relating the frequency of the scattered light, from a light source, by small tracer particles to the fluid velocity. Its non-intrusive principle and directional sensitivity makes it very suitable for applications such as in reversing flows, where physical sensors are difficult or impossible to use. In addition, this technique has a linear relationship between velocity and the signal output, is insensitive to temperature and pressure variations, does not require calibration, can be used in flows of unknown direction, gives accurate measurements in unsteady and turbulent flows and has very high frequency response. The only necessary conditions for the LDA use are a transparent window to reach a transparent medium with a suitable concentration of tracer seeding particles moving with the fluid.

It has been largely used in a very wide range of experiments: over fixed dunes (Bennett and Best, 1995); in roughness studies (Ridler and Sleath, 2000); in experiments related with biological processes studies (de Jonge and van den Bergs, 1987); in flow field characterisation (Besley and Delo, 1990; Petersen and Krishnappan, 1994).

Although the LDA has been extensively used on the velocity measurements applicable to erosion studies, other techniques have been applied: an electromagnetic flow meter (Houwing and van Rijn, 1998), a phase Doppler anemometer (Bennett *et al*., 1998), an acoustic Doppler velocimeter (Venditti and Bennett, 2000), an ultrasonic Doppler velocimeter (Best *et al*., 2000), a particle image velocimeter (Doron *et al*., 2001), among others.

The electromagnetic flow meter is suitable mainly in river stream and sewer flow. It is based on Faraday's law that a conductor (water or other fluid) moving in a magnetic field produces a voltage (measured by a pair of electrodes) proportional to the flow rate. However, it is very sensitive to turbulent flows, indicated by apparently noisy real-time readings.

The phase Doppler anemometer (PDA) is an extension of the LDA principle. With this technique, the simultaneous measurement of size and velocity of a particle at a point can be derived from the phase difference between specially separated detectors.

In particle image velocimetry (PIV) seeding particles (buoyant and efficiently scatter light), which follow the flow, are introduced into the flow and their motion is used to estimate the kinematics of the local fluid. The motion of the particles is recorded consecutively; thus, the velocity of the particles can be obtained by knowing the time between successive frames, the particle position and the camera magnification.

Considering the conditions and the objectives of the present work, the LDA technique is the most adequate. The main advantages of this optical flow measurement technique over others such as PIV are the high spatial and temporal resolution, which ensures the ability to capture the high frequency fluctuations of turbulent flows.

LDA technique has been recommended by some researchers (Houwing and van Rijn, 1998) to measure the velocity fluctuations and bed shear stress in the near-bed region, in laboratory, arguing that it may lead to a more precise description of the shear stress at the interface.

3.2 BASIC PRINCIPLES

As previously mentioned, the LDA technique is based in measuring the fluid velocity by detecting the Doppler frequency shift of laser light that is scattered by small particles moving with the fluid.

Laser Doppler theory is well documented by Durst *et al.* (1981), Adrian (in Goldstein, 1983), amongst many others. Therefore, the basic ideas and formulae are only briefly presented, including the differential Doppler technique that is used in the present LDA configuration.

The laser light has the unique properties of spatial and temporal coherence, which makes it possible to obtain the velocity only as a function of the frequency of scattered light, or Doppler frequency, and the wavelength of the laser light.

Doppler shift

The Doppler shift is produced by the movement of a particle that scatters light from the source to the receiver. The frequency of the scattered light (f_s) in a certain direction has suffered a relatively small shift relatively to the frequency of the incident light (f_i), which is called the Doppler shift (f_D). The value of this Doppler shift is proportional to the velocity of the particle and the angle between the direction of the incident light and that of the scattered light. Because the velocities commonly found are very small when compared with that of the light, the frequency shift is of much lower magnitude than that of the incident beam. Therefore, a direct measurement of the Doppler shift is impossible to perform.

Figure 3.1 shows the dual beam mode of LDA, where $\bar{e}_i$ and $\bar{e}_s$ are unit vectors in the direction of the incident light and the scattered light, respectively.

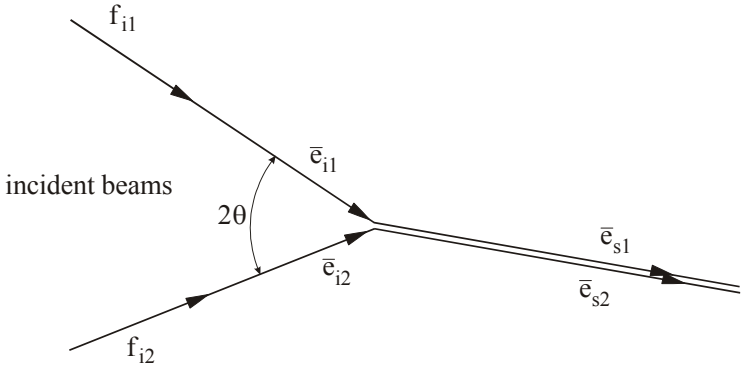

Figure 3.1- Dual beam mode of LDA

The Doppler shift is given by:

$$f_D = \frac{\boldsymbol{u}(\bar{e}_s - \bar{e}_i)}{\lambda} \tag{3.1}$$

where ***u*** is the velocity vector of the particle and λ the wavelength of the light.

The only technique suitable for measuring very small Doppler shifts use the principle of heterodyning of two frequencies. In this, laser light beams are heterodyned by presenting them simultaneously to a light detector. The scattered light observed by the photodetector is the combination of the two Doppler signals, $\sin(f_{i1}t)+\sin(f_{i2}t)$. Because the photodetector is a square-law device, its output has the form $[\sin(f_{i1}t)+\sin(f_{i2}t)]^2$, which includes the cross product $\sin(f_{i1}t)\sin(f_{i2}t)$. Manipulating the expression, one arrives at the identity (Adrian, in Goldstein, 1983):

$$2\sin(f_{i1}t)\sin(f_{i2}t)=\cos(f_{i1}+f_{i2})t+\cos(f_{i1}-f_{i2})t \tag{3.2}$$

Because the sum $(f_{i1}+f_{i2})$ is of a much higher frequency than the frequency response of any detector, only the term $(f_{i1}-f_{i2})$ is actually present in the signal.

Differential Doppler technique

The most commonly used technique, and the one that is employed in the LDA equipment of the present study, is the dual beam or differential Doppler technique. In this method, the intense and highly collimated light beam is split into two parallel beams of equal power, which are focused and crossed at the point under investigation. The differential Doppler method is based on the direct measurement of the difference between the frequency of the scattered light in a certain direction from one incident beam and the frequency of the scattered light in the same direction from a second incident beam (Figure 3.1).

The frequency of the scattered light from the first beam (f_{s1}) is:

$$f_{s1}=f_{i1}-f_{D1}=f_{i1}-\frac{1}{\lambda}\boldsymbol{u}(\bar{e}_s-\bar{e}_{i1}) \tag{3.3}$$

and, similarly, from the second beam:

$$f_{s2}=f_{i2}-f_{D2}=f_{i2}-\frac{1}{\lambda}\boldsymbol{u}(\bar{e}_s-\bar{e}_{i2}) \tag{3.4}$$

Thus, the output from the detector is:

$$f_D=f_{s1}-f_{s2}=\frac{1}{\lambda}\boldsymbol{u}(\bar{e}_{i1}-\bar{e}_{i2}) \tag{3.5}$$

Being $\bar{e}=(\bar{e}_s-\bar{e}_i)$, $u_\perp$ the component of ***u*** perpendicular to the bisection of the two laser beams and 2θ their crossing angle, Equation 3.5 becomes:

$$f_D=\frac{u_\perp 2\sin\theta}{\lambda} \tag{3.6}$$

Fringe model

The fringe model of the dual beam is an alternative explanation for the measured frequency, and is based on the fact that the light waves from both beams interfere with each other to form a set of alternate light (interfering light waves are in phase) and dark (light waves are out of phase) fringes in the intersection region (probe volume). With this

model, which is shown in Figure 3.2, it is usually much easier to understand the operation of the differential Doppler technique (Durst *et al.*, 1981).

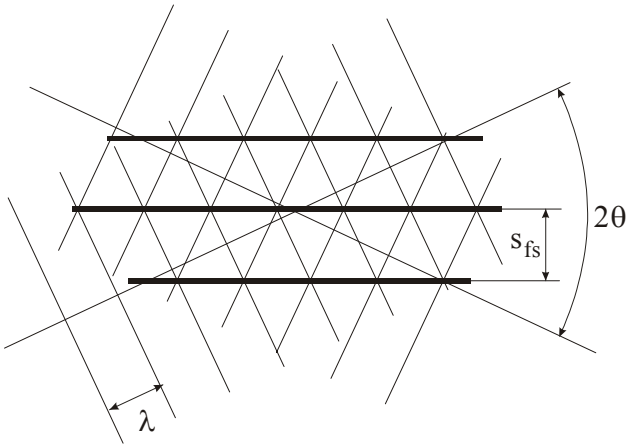

Figure 3.2- Fringe model for laser-Doppler signals

The spacing of the interference fringes (S_{fs}) is a function of geometry and laser wavelength, and is given by:

$$S_{fs} = \frac{\lambda}{2\sin\theta} \tag{3.7}$$

If a very small particle crosses this fringe pattern, with a velocity $u_{\perp}$ perpendicular to the fringes, it will scatter light only when it crosses the light fringes. The frequency of that signal will be:

$$f_D = \frac{u_{\perp}}{S_{fs}} \tag{3.8}$$

giving exactly the same result as Equation 3.6, when combined with Equation 3.7.

However, particles with the same velocity but crossing different parts of the probe volume may produce different Doppler signals. In this way, a particle tracing a path through the centre of the fringe pattern gives the ideal signal (Figure 3.3a), the Doppler burst is more intense. Here, it has the maximum depth of the modulation possible corresponding to the high fringe contrast in the central region, due to the gaussian profile of the light intensity in the beam. The fluctuations are not centred around zero because it is not possible to have a negative light intensity. As a consequence, the signal can be splited into two parts: a low frequency part (pedestal) and a high frequency part that contains the Doppler signal. As the particle travels through the edge of the probe volume, where fringes are weakly illuminated, the signal fluctuations are also weak.

Figure 3.3b shows an imperfectly modulated signal resulting from the intersecting beams with different intensity, or from a large particle when compared with the fringe spacing. A particle whose trajectory is displaced from the centre of the fringe region would produce the intensity variation such as shown in Figure 3.3c.

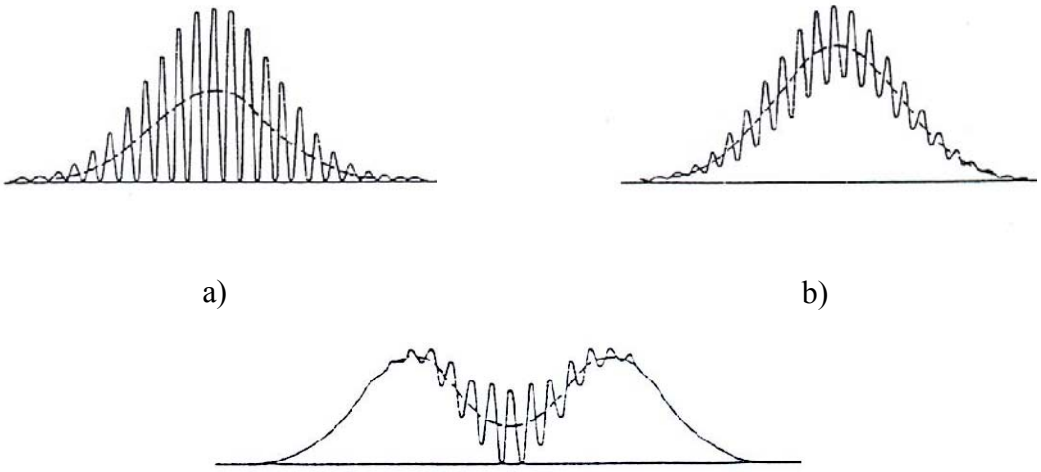

Figure 3.3- Types of signal from particles crossing a region of intersection of laser light beams

The probe volume dimensions become very important in measurements where the positioning and the distance to a wall are of interest, since they determine the maximum resolution that can be achieved. It has an ellipsoidal shape and depends on the beam waist size and the beam intersection angle. With the ratio between the measurement volume diameter (d_{mv}) and the fringe spacing, it is possible to define the number of fringes (N_{fs}) (when a seeding particle moves straight through the centre):

$$N_{fs} = \frac{d_{mv}}{S_{fs}} \tag{3.9}$$

In order to obtain good results from the LDA equipment, it is important to ensure a sufficiently high number of fringes in the measuring volume. Typical LDA setups produce between 10 and 100 fringes, but in some cases it is possible to get reasonable results with less.

It is important that, in differential Doppler arrangement, the beams are focused in the interference region. If not, the fringe pattern is not constant through the probe volume and erroneous results may be obtained. Well focused beams will give a higher fringe intensity and consequently better scattered light signals from each particle.

3.3 OPERATION TECHNIQUE

3.3.1 DIRECTIONAL DISCRIMINATION AND FREQUENCY SHIFT

A problem associated with the LDA technique is the ambiguity in the flow direction. Thus, and according to the Equation 3.8, negative velocities will produce negatives frequencies, but the receiver cannot distinguish between positive and negative frequencies and, in this way, there will be a directional ambiguity in the measured velocities. In addition, a stationary particle will produce no signal. This is a fundamental problem, mainly in highly turbulent conditions where reverse flows can occur, and in any situation where the fluid velocity may approach zero. This problem is solved by shifting the frequency of one of the laser beams (usually using a Bragg cell), which, for the differential Doppler system, yields a frequency difference (f_s') between the two intersecting beams. Therefore, the frequency of the signal collected by the photodetector (f_D) is:

$$f_D = f_s' + \frac{u_\perp 2\sin\theta}{\lambda} \tag{3.10}$$

Because the particle velocity does not introduce a negative frequency shift numerically larger than f_s', the Bragg cell will always ensure a positive Doppler frequency. The Bragg cell contains a transparent medium through which the laser beams passes; the medium is excited by ultrasonic waves, which diffract the laser beam.

The use of the fringe model allows a better understanding of the frequency shift. Introducing a fixed frequency shift (usually $f_s' = 40\ MHz$) in one of the beams, will cause the movement of the fringe pattern with a constant velocity $(S_{fs} f_s')$. It means that even a stationary particle exposed to these moving fringes, will produce signals at constant frequency (this frequency turns out to be the same as frequency shift). A seeding particle that moves towards the fringes will produce a Doppler burst of higher frequency, while when moving in the same direction as the fringes will produce a lower frequency. Thus, the directional ambiguity is removed.

Also, it is important to mention the number of fringes crossed by the seeding particle while it is in the probe volume. It may be determined in the following way:

$$N_{fs} = f_D \Delta t \tag{3.11}$$

being f_D the measurable Doppler frequency according to Equation 3.10 and Δt the particle's residence time within the measuring volume. This value will usually differ from the fringe number calculated from Equation 3.9 (without frequency shift).

The use of the frequency shift technique has a number of advantages: it requires only one reception channel and no major modifications to the optical and signal processing unit; it enables velocity fluctuations to be followed smoothly through zero, which is not possible with other techniques; it is not affected by depolarisation on scattering.

3.3.2 SIGNAL

In a general way, the frequency of a LDA signal that is measured by the photodetector may be different of the Doppler frequency, mostly due to the noise existent in that signal. That difference in the frequencies represents a mean error that increases with decreasing signal-to-noise ratio (SNR). The frequency information is the main result of a laser anemometer measurement, which is related with the velocity. Various factors may contribute to that noise, such as the photodetector shot noise (which is typical from the detection process) with the DC currents, and shot noise from the undesired light reaching the photodetector. Other noise sources are related with the signal processing unit.

The laser anemometer is advantageously operated under the conditions that the shot noise in the signal is the predominant noise source. Its performance is obtained by selecting adequately the laser power, seeding particle size and optical parameters. In addition, noise may be partially eliminated from the real signal using appropriate bandpass filters (according the desired velocity range). They will remove low frequency components and frequencies not containing Doppler information before any frequency detection. In addition, the noise introduced by the processing unit can be partially removed by filtering the acquired data before computing any flow statistics.

The signal quality is directly related with fringe visibility (ratio of the amplitude of the Doppler signal to the amplitude of the pedestal) and depends on the size of scattering particles. Experiments showed that the increase in particle size does not necessarily yield an increase in SNR as one might predict by only considering the increase in light intensity with the square of particle diameter (Albrecht *et al.*, 2003).

The Lorenz-Mie light scattering theory, applicable when particle sizes are comparable to the wavelength of light, describe the dependency on particle size, assuming spherical particles. However, in practice also the shape and orientation of seeding particles are important factors to take into account in the scattering of light.

The Doppler signal was explained by the fringe model as the rate at which scattering particles cross a set of fringes inside the crossing region of the two beams. However, as pointed out by Adrian (in Goldstein, 1983), the use of the fringe model to describe the intensity characteristics of the Doppler burst when the particle is not small compared to fringe spacing is limited. Instead of the signal being proportional to the total light flux striking the particle, the peak visibility of the Doppler signal depends on the ratio of particle diameter to the fringe spacing (d_p / S_{fs}).

The number of seeding particles simultaneously present in the probe volume is a very important detail for the signal quality and the efficiency of the signal processor. If one particle is present in the volume, there is a burst type Doppler signal (see figure 3.3a). Figure 3.4 presents the filtered signal with the Doppler pedestal removed, which is actually the input to the signal processor (Durst *et al.*, 1981).

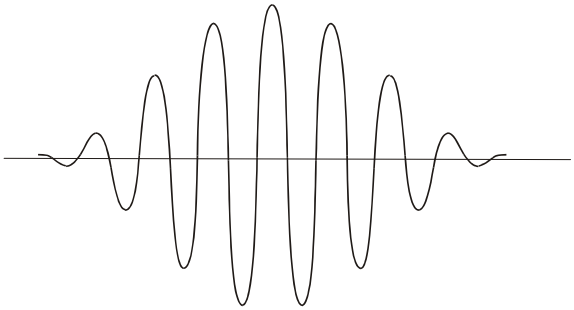

Figure 3.4- Filtered signal with the DC-component removed

Otherwise, if more particles are simultaneously present in the probe volume, there is a multi-particle signal. The detector current will be the sum of the current bursts from each individual particle within the probe volume. Because particles are located randomly in space, each individual current contribution is added with random phases, and the resulting Doppler signal envelope and phase will fluctuate (this adds a phase noise to the detected Doppler frequencies, which is difficult to remove). The Doppler signal processor must either be able to handle this situation correctly or reject estimations based on such measurements as invalid.

In summary, there are some factors that influence the magnitude of the signal (Adrian, in Goldstein, 1983):

- Focussing of the laser beams: because they are coherent and monochromatic, the laser beams focus into a very small diameter, thus, the light intensity in the probe volume can be very large.
- The scattering particles: the strongest signal is obtained when there is no more than one particle in the probe volume at any time. If multiple particles are present, the signals they produce may cancel out.
- The direction in which the light scattered is collected: the percentage of light scattered by the particles strongly depends on the direction relative to the incident beams. If the LDA system is arranged in forward scatter mode, it means the receiving lens and photodetector are on the opposite side of the laser. With this arrangement, improvements in scattered light intensity can be achieved, once most of the light is scattered in the direction of the beams. However, unfortunately it is often necessary to have all the equipment on the same side of the flow, operating in a backscatter mode. In this case, it is the light that scatters backwards is collected, which is much weaker. Nevertheless, it has the advantage that the receiving optics move simultaneously with the transmitting optics, and thus they are always aligned.
- Use of a pinhole: a pinhole is a mask located at the front of the photodetector that enables light only through a small hole located at the point where scattered light from the measurement volume is focussed. Light scattered from other parts of the beams or apparatus is rejected, preventing noise production, which easily drowns the signal.

The signal processors are electronic components designed to analyse each burst and extract the frequency (thus, the velocity) at any instant. The most common types of signal

processors are: burst spectrum analysers (BSA's), frequency trackers, burst counters and photon correlators, being the first used in the present study. The choice of a signal processor for a particular application will depend on various factors: particle density; signal quality; intensity of velocity (frequency) fluctuations; required accuracy; stationary/transient flow; time averaged quantities or time resolved and cost. The BSA is the preferred LDA signal processor for the most demanding applications. It includes: frequency shifting, photomultiplier high-voltage supply, preamplifier, a micro-processor which controls the front panel, an output buffer, signal gain, filters and an IEEE-488 interface (a standard GPIB- General Purpose Interface Bus) (BSA/FVA Flow Software, 2000).

BSA operating principles

The principle of the BSA is to perform a spectral analysis of the Doppler signals in order to extract the Doppler frequencies by the Fourier Transform technique. This converts a time signal, the Doppler signal, directly to a frequency signal. A method named Fast Fourier Transform (FFT) is used to implement the Fourier Transform direct in hardware, and makes a full use of the information contained in the Doppler signal.

In the BSA, the Doppler signal is fed in to a mixer unit, where it is mixed with a frequency preset (the centre frequency) and then it is low-pass filtered and A/D converted. The digital signals are then transferred to a buffer but it is the burst detector which determines if the signals are stored in the buffer. Subsequently, they are treated through the FFT processor and then the post processor estimates the Doppler frequency from the measured spectrum. Finally, the measured parameters are then transferred via the IEEE-488 interface to a computer, for further analysis.

BSA uses a maximum of 64 complex samples (record length) of the input signal to calculate the spectrum. The position of the global maximum of the spectrum is interpreted as the Doppler frequency. The BSA determines the Doppler frequency with the specified resolution, for signals with good SNR. To validate a spectrum, the absolute level of the global maximum must be greater than 4 times the next maximum in the spectrum (User's Guide BSA enhanced, Dantec, 1991). With such technique the BSA works correctly with poor SNR signals, down to 13 *dB*, that is: signals that are fully embedded in the noise.

3.3.3 SELECTION OF A SUITABLE TRACER

In LDA it is not the actually flow velocity that is directly measured, but the velocity of particles suspended in the flow. Thus, in most applications, artificial tracer particles must be added to the flow. The need to employ tracer particles for the measurement of the flow velocity requires a careful checking for each particular experiment whether the particles will faithfully and passively follow the motion of the fluid. These particles must have some characteristics: be small enough to follow the flow accurately; be large enough to scatter sufficient light for the photodetector (to detect the Doppler frequency); have approximately the same density as the fluid itself; be cheap, non-toxic, non-corrosive, non-volatile and chemically inactive (Durst *et al.*, 1981; BSA/FVA Flow Software, 2000). The scattering particles are the basic source of the Doppler signal and they can have more influence on the quality of the signal than any other component (Adrian, in Goldstein, 1983). Depending on the nature of the flow, seeding particles used for LDA measurements usually have particle diameters ranging from 0.1 to 50 μm (Durst *et al.*, 1981). In general, the maximum

allowable particle size decreases with increasing flow velocity, turbulence and velocity gradients.

Since larger particles should be preferred as scatters (providing better light scattering efficiency), this is in contradiction to the demand of having as small particles as possible in order that they follow the flow accurately. Thus, a compromise has to be found in most applications. Also, careful matching of particle size and fringe spacing is desirable to obtain a optimum SNR. Durst *et al.* (1981) have shown that the ratio of the mean particle size to the fringe spacing should be of the order of $1/4$. However, the absolute magnitude of the ratio is not critical, having these authors obtained SNR's of 40 *dB* with ratios of the order of 0.5 to 2 and 25 *dB* with a ratio of 20, after band pass filtering. With BSA's processing this is not problematic.

Generally, the motion of particles suspended in a fluid is affected by: particle shape, particle size, relative density of particle and fluid, concentration of particles in the fluid and body forces (in creeping flows). The natural concentration of very small particles is usually much greater than that of particles in the useful range, thus, when measuring in liquids, this causes an undesirable shot noise level because the incoherent signals from the many small particles. The concentration of particles influences particle motion through the interaction between different particles. An adequate concentration to maintain at least one particle in the scattering volume for most of the time is ideal. Agglomeration of more particles in the tiny control volume lead to light attenuation and signal interference and, therefore, a degraded photomultiplier signal and turbulence damping (Durst *et al.*, 1981).

However, turbulence in the flowing fluid may cause variation in the concentration of the discrete particles, and consequently variations in the local scattering and absorption of light.

The motion of a small particle in a turbulent flow has been investigated by Hinze (1987) and Durst *et al.* (1981). The authors, based upon the transient transport equation of a particle by a carrier fluid, have determined the particle response to flow turbulence by an amplitude ratio (η), defined by:

$$\eta = \left[1 + f_1(\omega)\right]^2 + f_2{}^2(\omega) \tag{3.12}$$

where,

$$f_1(\omega) = \frac{\omega(\omega + a_3\sqrt{\pi\omega/2})(a_2 - 1)}{(a_1 + a_3\sqrt{\pi\omega/2})^2 + (\omega + a_3\sqrt{\pi\omega/2})^2}$$

and

$$f_2(\omega) = \frac{\omega(a_1 + a_3\sqrt{\pi\omega/2})(a_2 - 1)}{(a_1 + a_3\sqrt{\pi\omega/2})^2 + (\omega + a_3\sqrt{\pi\omega/2})^2}$$

In these equations,

$$a_1 = \frac{36\mu_f}{(2\rho_p + \rho_f)d_p{}^2};\quad a_2 = \frac{3\rho_f}{2\rho_p + \rho_f};\quad a_3 = \frac{18}{(2\rho_p + \rho_f)d_p}\sqrt{\frac{\mu_f\rho_f}{\pi}}$$

μ_f and d_p are the fluid viscosity and the particle diameter, respectively, and ρ_f and ρ_p are their densities; ω is the fluid eddy frequency. Lee and Durst (1979) stated that, if $\eta = 1$ the particle motion is completely controlled by the diffusional motion of the turbulent eddies and, on the opposite way, if $\eta = 0$ the particle is not affected by the fluid turbulence. In this way, a suitable particle as a fluid tracer requires $\eta \approx 1$. As shown above, the amplitude ratio, for a given frequency of the eddy motion, is controlled by the particle diameter and density, the fluid density and viscosity. If the density ratio $\rho_p / \rho_f = 1$, particles will follow the flow exactly regardless of size, assuming that: there is homogenous turbulence; particles are smaller than turbulence microscale; Stokes drag law is valid; particle is always surrounded by same fluid molecules and there is no interaction between particles. The density ratio and the particle diameter are the most important factors in η.

3.4 DATA PROCESSING

In most flows, turbulent motions contribute significantly to the transport of momentum and mass and, therefore, have an important influence on the velocity distribution within the flow field.

In the LDA measurements, the particle velocity is calculated for each detected Doppler-burst. That velocity is sent to a computer for subsequent analysis, together with other information such as particle arrival and transit time. The LDA velocity data coming from the processor consists of *N* validated bursts. For a two-component system, for each burst the arrival time and the transit time of the seeding particle is recorded. Assuming a gaussian probability function for the two velocity components, the mean values (or first moment) of u_i and v_i (i = 1, 2, … N) are obtained:

$$\overline{u} = \frac{1}{N}\sum_{i=1}^{N} u_i \; ; \quad \overline{v} = \frac{1}{N}\sum_{i=1}^{N} v_i \tag{3.13}$$

Also, and for each one of the velocity components, the central moments are defined as:

$$\overline{u}_{(k)} = \frac{\sum_{i=1}^{N} (u_i - \overline{u})^k}{N} \tag{3.14}$$

The variance (or second moment) is obtained for $k = 2$. The instantaneous velocity (u_i) value can be expressed as:

$$u_i = \overline{u} + u' \tag{3.15}$$

being u' the fluctuating component of the velocity. Thus, the RMS value of the velocity distribution ($\widetilde{u}$) becomes:

$$\widetilde{u} = \sqrt{\frac{\sum_{i=1}^{N}(u_i - \overline{u})^2}{N}} = \sqrt{\frac{\sum_{i=1}^{N} u_i'^2}{N}} \tag{3.16}$$

These RMS values characterise the flow turbulence, whose intensity (TI) is given by:

$$TI = \frac{\widetilde{u}}{U_{\max}} \times 100\% \tag{3.17}$$

in which $U_{\max}$ refers to the maximum velocity in the flow field.

The other central moments $\overline{u}_{(3)}$ and $\overline{u}_{(4)}$ are also of interest, usually referred as the skewness (third moment) $(\boldsymbol{S})$ and the flatness (fourth moment) $(\boldsymbol{F})$:

$$\boldsymbol{S} = \frac{\overline{u}_{(3)}}{(\overline{u}_{(2)})^{3/2}} = \frac{\overline{u}_{(3)}}{\widetilde{u}^3} \tag{3.18}$$

$$\boldsymbol{F} = \frac{\overline{u}_{(4)}}{(\overline{u}_{(2)})^{2}} = \frac{\overline{u}_{(4)}}{\widetilde{u}^4} \tag{3.19}$$

The second moment gives an indication of the width of the distribution; the third moment indicates symmetry about the mean; and the fourth one indicates the relative amounts of data near the mean and away from that.

From the velocity information in two orthogonal components, the cross-moments can be derived from:

$$-\overline{u'v'} = -\frac{1}{N}\sum_{i=1}^{N}(u_i - \overline{u})(v_i - \overline{v}) \tag{3.20}$$

It must be referred that when particles arrive individually in the scattering volume, the LDA provides velocity information averaged according to the occurrence of particles.

Properly applied, the LDA system can provide accurate measurements of mean velocities and turbulence even when the turbulence levels are very high. There exists, however, considerable discussion over whether corrections to the measurements must be made for a bias toward higher velocities (Durst *et al.*, 1981).

During the periods of higher velocity (mainly in highly turbulent flows), a larger volume of fluid flows through the measuring volume, and a greater number of discrete data points are recorded. The result is a non uniform sampling of the distribution of velocity about a mean value. In this way, using an arithmetic averaging (as Equation 3.13) to evaluate the statistics of the flow field may bias the results towards higher velocities, because of the more frequent arrival of faster particles. This bias is commonly referred as "sampling bias", and it occurs because the particle arrival time rate is dependent on the local instantaneous speed of the fluid at the laser intersection volume.

The integral time-scale of the velocity fluctuations, which represents the typical turbulent activity duration of the large energy-containing eddies, is important in determining the appropriate sampling rate when taking velocity measurements. Samples separated by greater than two integral time-scales contribute to the evaluated quantities as statistically

independent samples, avoiding the velocity bias and, in this case, the arithmetic average can be used. This can be obtained using a dead-time feature, consisting in the above specified period of time after each detected Doppler burst, during which further bursts will be ignored (BSA/FVA Flow Software, 2000). Sampling much more slowly will extend the measuring time without any significant increase in accuracy, and a faster sampling rate will increase the uncertainty because the samples will no longer be statistically independent.

Other alternative in performing statistical averages, bias-free, is weighting the biased data by introducing the transit time weighting (Durst *et al.*, 1981):

$$\overline{u} = \frac{\sum_{i=1}^{N} u_i \times \Delta t_i}{\sum_{i=1}^{N} \Delta t_i} \tag{3.21}$$

where Δt_i is the transit time of the particle crossing the measuring volume (from the instant it enters the volume to the instant it exits).

To have average quantities, such as mean and RMS velocity, the data rate is not critical, but it is important to acquire sufficient samples for reliable statistics. This usually means 1,000-2,000 samples per position, but depends on the flow characteristics and on required confidence level (BSA/FVA Flow Software, 2000).

3.5 TURBULENCE ANALYSIS

If the flow is laminar and steady, the velocity will not fluctuate around the mean (i.e. at any point the instantaneous values of u will be equal to $\overline{u}$ since $u' = 0$).

The instantaneous velocity measurements made at any point in a turbulent flow will depend on the relative contributions of the fluctuating velocity component (White, 1986), which is defined as the deviation of u_i from its average value (see Figure 3.5).

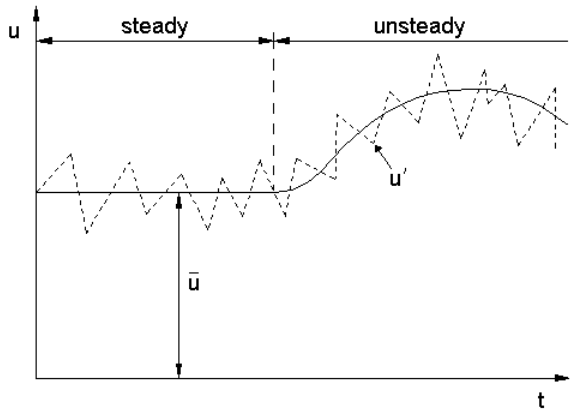

Figure 3.5- Steady and unsteady turbulent flow

A turbulent flow field is characterised by rapid fluctuations and is far too complicated to be known in complete detail. At the moment, literature is mostly restricted to the study of isotropic turbulence in incompressible flow. In isotropic turbulence the mean velocity fluctuations in the three coordinate directions are equal to each other, $\overline{u'^2} = \overline{v'^2} = \overline{w'^2}$ and $\overline{u'v'} = \overline{v'w'} = \overline{w'u'} = 0$, i.e. the turbulence is homogeneous (the same at every point) and statistically independent of orientation and location of axis (Goldstein, 1983; Tritton, 1988). In practice, it means that $\frac{\widetilde{u}}{\widetilde{v}} = 1$. In a flat plate boundary layer, the structure is anisotropic near the wall (once there is only a production of $\overline{u'^2}$) becoming more isotropic far away from the wall (Bird *et al.*, 1976).

Shear stresses

For a better studying of the fluid behaviour near the bed, some assumptions are made: the flow is steady (it does not change with time); the flow is uniform (it is the same in all cross-sections; the fluid is incompressible and Newtonian, being characterised by it density (ρ_f) and dynamic viscosity (μ); no-slip condition (the velocity of fluid in direct contact with a boundary has the same velocity as the boundary itself). The viscosity relates the local stresses in a moving fluid to the strain rate of the fluid element (White, 1986). In a laminar flow, the shear stress (τ_{lam}) is given by the Newton's law of viscosity:

$$\tau_{lam} = \mu \frac{\partial u}{\partial y} \tag{3.22}$$

In this situation, fluid momentum caused by gravity induces the fluid to be transported towards the boundary by molecular diffusion. Close to the boundary the momentum is consumed increasingly by the high shear resistance force, in order to maintain the no-slip condition.

In the case of turbulent flows, an additional shear stress (τ_{turb}) is defined as:

$$\tau_{turb} = -\rho \overline{u'v'} \tag{3.23}$$

being known as the Reynolds stresses.

Even in flows where the mean velocities vary in only one or two dimensions, turbulence fluctuations have a three-dimensional character. Turbulent flows reveal rotational flow structures (turbulent eddies) with a wide range of length scales, that can be described as pockets of fluid displaying a sense of intensity and rotation (Schlichting, 1979). The largest turbulent eddies interact with, extracting energy from the mean flow though the process called vortex stretching. This process provides the energy which maintains the turbulence. The smallest scale of motion that can occur in a turbulent flow is dictated by viscosity, being viscous effects very important. The action of viscous stresses is partially obstructed by the work done by eddies, thus the energy associated with the eddy motions is dissipated and converted into thermal energy. In this way, at high Reynolds number the smallest eddies in a turbulent flow are isotropic (non-directional), while the structure of the largest eddies is highly anisotropic (directional) and flow dependent.

The total shear stress includes both the laminar and turbulent contributions (van Driest, 1956):

$$\tau_{total} = \mu \frac{\partial u}{\partial y} - \rho \overline{u'v'} \tag{3.24}$$

Similarly to Equation 3.22, the turbulent shear stress resulting from the diffusion of eddy momentum can also be written as:

$$\tau_{turb} = \mu_t \frac{\partial \overline{u}}{\partial y} \tag{3.25}$$

where μ_t is an artificial quantity known as the eddy or turbulent viscosity. This viscosity is not a property of the fluid like μ, but actually of the flow itself, depending on the mean velocity $\overline{u}$ (Schlichting, 1979) .

Except close to the wall, where viscous shear stress predominate due to shearing on a molecular scale, the turbulent shear stress accounts for the majority of the total shear stress in Equation 3.24.

Maa (1990), using the annular sea-bed flume, determined the total bed shear stress including both the tangential and radial (induced by the secondary flow inside the flume) components. He found that radial component is not significant when compared with the tangential bed shear stress.

Once the results are obtained, it is possible to achieve a more detailed analysis of the turbulence, such as determining the turbulent kinetic energy and its production and dissipation rates. Turbulent kinetic energy (k) is defined as (Launder and Spalding, 1974):

$$k = \frac{1}{2}\overline{u_i' u_i'} = \frac{1}{2}\overline{u_i'^2} \tag{3.26}$$

Assuming that the flow inside the flume is axisymmetric and two-dimensional, it is admitted symmetry in which $u_2 = u_3$ (Besley and Delo, 1990, found experimentally in an annular flume that maximum radial and vertical velocities were approximately equal), the equation becomes:

$$k = \frac{1}{2}\left(\overline{u_1'^2} + 2\overline{u_2'^2}\right) \tag{3.27}$$

being u_1 the velocity in the dominant direction of the flow (u_θ).

The production rate of turbulent kinetic energy (P) is given by:

$$P = -\overline{u'v'}\frac{\partial \overline{u}}{\partial y} \tag{3.28}$$

The dissipation rate of turbulent kinetic energy (ε), that corresponds to the rate at which the energy produced at the largest scales is dissipated into heat at the smallest scales (molecular diffusion), is defined by (Ferziger and Perić, 1999):

$$\varepsilon = \nu \frac{\overline{\partial u_i' \partial u_i'}}{\partial x_j \partial x_j} \tag{3.29}$$

or, in a simpler way (Krogstad and Antonia, 1999):

$$\varepsilon = \frac{15\nu}{\overline{u^2}}\overline{\left(\frac{\partial u'}{\partial t}\right)^2} \tag{3.30}$$

being ν the kinematic viscosity.

In a dimensionless way (with normalisation by the friction or shear velocity, u^*), the turbulent kinetic energy is given by Equation 3.31 (Antonia and Krogstad, 2001), and the production and dissipation rates are given by Equations 3.32 and 3.33, respectively (Krogstad and Antonia, 1999):

$$k^+ = \frac{1}{2}\left(\overline{u'^{+2}} + 2\overline{v'^{+2}}\right) \tag{3.31}$$

$$P^+ = -\overline{u'v'^+}\frac{\partial \overline{u^+}}{\partial\left(\frac{y}{\delta}\right)} \tag{3.32}$$

$$\varepsilon^+ = \frac{\varepsilon\delta}{u^{*3}} \tag{3.33}$$

where y and δ are the distances from the wall and the boundary layer thickness, respectively. The Reynolds normal stresses ($\overline{u'^{+2}}$ and $\overline{v'^{+2}}$) and the Reynolds shear stresses ($-\overline{u'v'^+}$) are defined as:

$$\overline{u'^{+2}} = \frac{\widetilde{u}^2}{u^{*2}} \;;\; \overline{v'^{+2}} = \frac{\widetilde{v}^2}{u^{*2}} \;;\; -\overline{u'v'^+} = -\frac{\overline{u'v'}}{u^{*2}} \tag{3.34}$$

The superscript + refers to a normalisation. The friction or shear velocity (u^*) can be estimated from the relationship (Bradshaw, 1971):

$$u^* = \sqrt{\frac{\tau_w}{\rho_f}} \tag{3.35}$$

where τ_w is the wall shear stress.

3.6 LDA CONFIGURATION

The LDA basic configuration consists of: a continuous wave laser; transmitting optics, including a beam splitter and a focusing lens; receiving unit, including a focusing lens and a photodetector; a signal conditioner and a signal processor. Modern LDA optics employs optical fibres to guide the laser light from the often bulky laser to compact probes and to guide the scattered light to the photodetectors. The technique employed to establish 2D measurements is that of a dual colour system (four beams). Two of the dominant

wavelengths, corresponding to blue (λ= 488 *nm*) and green light (λ= 514.5 *nm*), inherent in the Argon-ion laser are filtered and both beams are treated as in a single colour system.

Figures 3.6a and 3.6b show the schematic layout of the LDA and the transmitting/receiving optics, respectively, used in the present study.

In this configuration, a water cooled, 6 *W* laser beam is splitted (by the beam splitter) into the two colours mentioned and the resulting beams are steered into the transmitting/receiving optics (Dantec 55x modular LDA optics–based 85 *mm* FiberFlow system) through a fiber optic cable, 5 *m* long. In this Fiber Flow optical probe (reference 60x81), the receiving fiber, which has an active diameter of 80 μm, plays the role of a pinhole, i.e., works as a filter to stop the light coming from elsewhere than the measuring volume. There is a lens (receiving lens), 160 *mm* in focal length, which is located inside the optical probe, giving an image of the measuring volume on the input plane of the receiving fiber. Using an external lens of 310 *mm* in focal length (transmitting lens), the photomultipliers "see" a section of 150 μm. The transmitting lens changes the direction of the beams causing them to cross at the point where they are focussed and produce a tiny measurement volume. Flow direction sensitivity is provided through 40 *MHz* Bragg cell shifting the frequency of one of the beams. The scattered light is collected in the backscatter mode through the same 310 *mm* lens and steered through the fiber optical cable into two photomultipliers. These devices are fixed at the end of the receiving fiber. The photomultipliers have very good dynamic response and are highly sensitive. However, they require high-voltage supplies to produce the electric field, typically above 1,000 *V* (FiberFlow, Dantec, 1995). The optical unit has also a shutter control that blocks the laser beams, as a safety measure, whenever they are not needed.

The transmitting/receiving optics are mounted on a 3D programmable traversing table (Lightweight traverse table). The traversing mechanisms are high-precision components used to move the optical part of the LDA system, allowing the measurement of complete flow fields. In this way, it is possible to control the measurement position from the computer, using a standard IEEE-488 interface (NI-488.2 1.60 from National Instruments, for GPIB-PCII/IIA board) to connect the control of the mechanical system with the computer. The Doppler signals are processed through a couple of spectrum analysers (Dantec BSA's 57N20/57N35 models). The burst detection criteria, processing parameters of the processor and traverse movement coordinates are set from the computer, which is also used to store and analyse the results. The oscilloscope (Fluke PM 3370B 60 *MHz* Combiscope) allows monitoring the filtered and amplified signal. It provides the necessary visual information such as the Doppler burst shape and the presence of noise in the BSA's output signals, helping the optimisation of the processing parameters. BSA's operation was in Burst processing mode. The Doppler frequency is calculated with a resolution resulting from the 14 bit binary frequency information.

All the hardware control, setup, configuration, data acquisition and statistical processing of data are controlled by an integrated software package, Dantec BSA Flow v. 1.4.1. In combination with BSA processors and FiberFlow optical system, it provides an integrated, flexible and easy-to-use system for the LDA experiments. With BSA Flow Software, data from both BSA's is acquired, analysed and presented graphically (User's Guide BSA enhanced, Dantec, 1991). Results can be presented in lists, histograms, plots and vector plots.

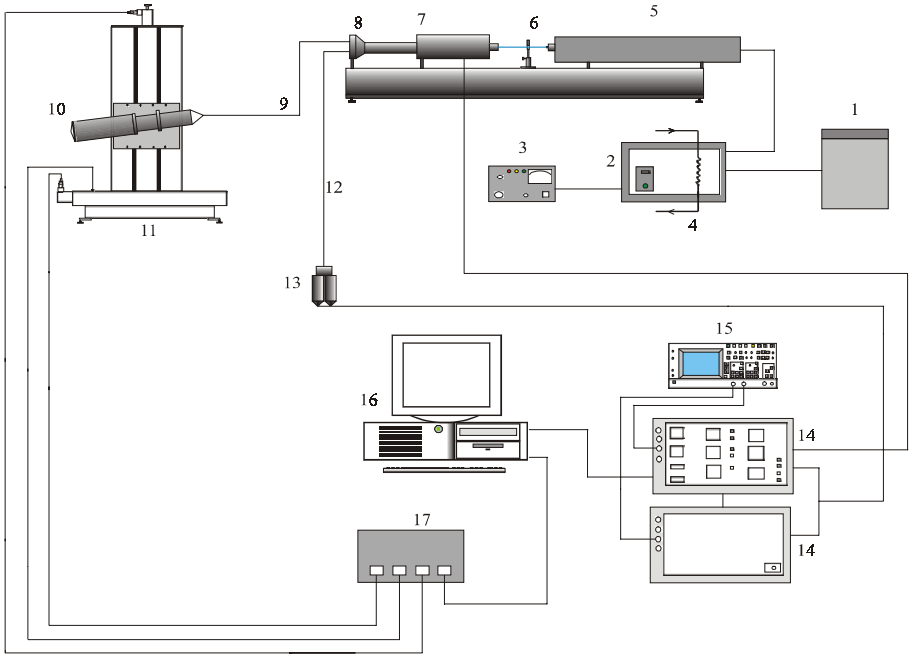

1- Transformer
2- Power supply
3- Controller
4- Water flow
5- Laser head
6- Shutter
7- Beam splitter and Bragg cell
8- Fiber manipulators
9- Fiber optic
10- Transmitting/receiving optics
11- 3D traverse table
12- Scattered signal
13- Photomultipliers
14- Burst Spectrum Analyser
15- Oscilloscope
16- Computer
17- Traverse controller

a)

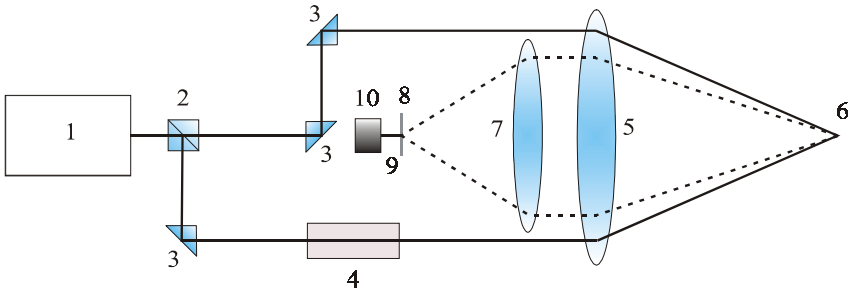

1- Ar-Ion laser
2- Beam splitter
3- Prism
4- Bragg cell
5- Transmitting lens
6- Measurement volume
7- Receiving lens
8- Filter
9- Receiving fiber
10- Photomultipliers

b)

Figure 3.6- a) Schematic layout of the LDA instrumentation; b) Transmitting/receiving optics

A key element in BSA flow software is its integrated user-interface, enabling the user to control the setup of all instrumentation in the LDA system, making experiments straightforward and flexible.

Other advantage using BSA flow software is that before starting a measurement procedure, it is possible to define a sequence of data acquisition, analysis and display options leading to the required end-result. This end-result is updated through the measurement, providing immediate feedback on measurement quality. The data is stored in a database and can be further analysed by adding or deleting objects from an existing data analysis sequence (BSA/FVA Flow Software, 2000).

CHAPTER 4

EXPERIMENTAL TECHNIQUES

Although the LDA technique is the main equipment deployed in the current project, other techniques used are also discussed in this section: the laser diffraction technique (for particle sizing); the use of a high speed video camera (to visualize the erosion in natural sediments); the sample collection technique; the physical-chemical characterization of the sediments and the rheological characterisation of the fluids.

4.1 LASER DIFFRACTION TECHNIQUE

There are various laser light based optical techniques for measuring the size of particles within a flow, such as the intensity based technique, visibility technique, the diffraction technique and the phase difference technique (PDA) (Tayali and Bates, 1990).

Diffraction technique for particle sizing is based on near forward scatter angles where, for particles larger than the light wavelength, the diffracted light is much stronger than the reflected or refracted light. In this way, the scattered light intensity as a function of angle can be predicted for various particle sizes from Fraunhofer diffraction theory (assumes the particle scatter light like a disc of the same diameter), which does not require knowledge of the refractive index. According to this theory, when a parallel beam of monochromatic light interacts with a particle, a diffraction pattern is formed whereby some of the light is deflected by an amount depending on the size of the particle (Pedrotti and Pedrotti, 1993).

Swithenbank *et al.* (1976) developed a system based on the light energy captured by a set of concentric semicircular photosensitive rings, whose radius increases towards the periphery. The particle size distribution can be related to the light energy distribution on those rings and each one is related to a particular size interval, corresponding the dimension of the smallest and largest rings to the largest and smallest measurable particles, respectively.

There are many advantages using the laser light scattering principle: it is non intrusive; it is fast, requiring normally around 3 minutes to complete a measurement; it is accurate, giving high resolution size discrimination; large dynamic range; the instrument has a number of ranges to cover the range size in the sample; no calibration is required; it is simple and

highly versatile, providing highly repeatable measurements (Malvern Instruments, User Manual, 1991).

4.1.1 THE MALVERN 2600

The Malvern 2600 particle sizer, marketed by Malvern Instruments, has been widely used and tested by various authors, and has been used in this project.

This instrument has been used for some time both in spray analysis (Swithenbank *et al.*, 1976; Chigier, 1983) and annular flow (Azzopardi *et al.*, 1978; Teixeira, 1988) and is based on the principle of laser light scattering previously described. Its layout is shown in Figure 4.1. The light from a low power 2 *mW* He-Ne laser (633 *nm*) is used to form a collimated beam of light, typically 9 *mm* in diameter (18 *mm* for long bed option). This beam is known as the analyser beam and the particles within its path will scatter the light.

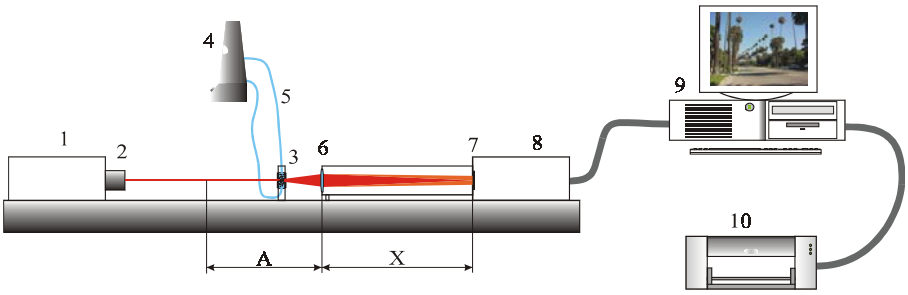

1- He-Ne laser
2- Beam expander lens
3- Sample cell
4- Particle sampler
5- Water lines
6- Receiver lens
7- Detector (rings)
8- A/D converter
9- Computer
10- Printer
A- *Lens cut- off distance*
X- *Distance to the detector*

Figure 4.1- Layout of the Malvern 2600

A Fourier transform lens collects the diffracted and undiffracted light onto a detector, which consists of 31 concentric annular rings. The analogue signal is amplified and digitised for subsequent reading and processing by the computer. That signal is proportional to the light energy measured by the rings. On the other hand, the unscattered light is focussed into a central detector and is not evaluated by the optical system. In this way, it is possible to determine the sample volume concentration, based on the laser power passing out of the system. Large particles scatter at low angles and small particles scatter at higher angles (Malvern Instruments, User Manual, 1991).

Figure 4.2 shows an overall view of the Malvern 2600, including the detector in the foreground and the particle sampler.

Figure 4.2- Malvern during a measurement

The instrument used in the present experiments has six different receiver lenses, which, for the available combination of detectors and light wavelength, give different particle size ranges (Malvern Instruments, User Manual, 1991), as summarised in Table 4.1.

Table 4.1- Particle size ranges and correspondent lens

Focal lengths (mm)	Particle size ranges (μm)
63	1.2 - 118
100	1.9 - 188
300	5.8 - 564
600	11.6 - 1,128
800	15.5 - 1,503
1,000	19.4 - 1,880

The adequate lens is selected by the resulting data fitting. The lens is such that the particle size distribution should be within the dynamic range expected for that lens.

Usually, many particles are simultaneously present in the analyser beam, being the scattered light focused on the detector the sum of all individual patterns overlaid on the central axis. In this way, the system integrates the scattered light from all particles. It is very important to ensure that the particle concentration is in the range of acceptability for an accurate measurement (below 50 % of light being diffracted).

There is a time averaged observation of the scattering as the dispersed material is continuously fed through the analyser beam.

When the particle field to be measured is located too far from the collection lens, the light scattered at large angles by the small particles is lost due to the limited lens aperture or window, causing the measured size distribution to be biased towards large particles. This is called the *vignetting* or lens cut-off effect (Malvern Instruments, User Manual, 1991). Therefore, it is important that, for any measurement, all particles are illuminated by the beam within the lens cut-off distance (distance A in Figure 4.1), which depends on the lens used, being smaller for the smaller size ranges. According to the focal plane position of each lens, the detector is moved along the distance X (see Figure 4.1), in order to be located at the lens focal plane.

The sample handler unit consists of a tank ("small volume sample presentation unit") used for sample preparation and stirring, to keep the solid particles suspended, and water lines to circulate the sample through the measurement cell. The cell is placed at any distance from the range lens, providing it is within the *vignetting* distance of the lens being used. Also, before starting the measurement, it is fundamental to zero the instrument by measuring the background light. Thus, the instrument will remove the background light from that scattered by the sample, yielding more accurate results.

Concerning the data analysis and results presentation, the computer assumes a known distribution. Subsequently, an iterative optimisation procedure adjusts the function parameters in order to obtain the best fit to the experimental data. It is a volume distribution characterised over the size limits of the optical configuration applied. That distribution can be presented as a table or graph, showing the distribution in both frequency and cumulative forms.

4.1.2 PARTICLE SIZE DISTRIBUTION

There are different distribution functions commonly used in the analysis of dispersed particle populations: Nukyama-Tanasawa; Rosin-Rammler; Log Normal and Upper Limit Log Normal (Mugele and Evans, 1951).

Among the available alternatives in the system software, the Rosin-Rammler distribution was chosen by its simplicity and accuracy. It was put forward by Rosin and Rammler (1933) and is generally presented by cumulative volume of particles:

$$F_V(d) = 1 - e^{\left(-d/\overline{X}\right)^n} \tag{4.1}$$

where d is the particle diameter and, $\overline{X}$ and n the distribution parameters.

Mugele and Evans (1951) assessed this distribution by comparing with others and concluded that it represents a good compromise in terms of efficiency and in ease of use.

Equation 4.1 may be put in the form:

$$\ln\left(\ln\frac{1}{1-F_V(d)}\right) = n\ln d - n\ln\overline{X} \tag{4.2}$$

which is a straight line and enables the determination of the Rosin-Rammler parameters.

Knowing the distribution parameters, all the statistical properties of the distribution can be evaluated. In many flow processes, it is desirable to work only with a characteristic mean of the population instead of the complete particle size distribution.

Based on the particles frequency, Mugele and Evans (1951) had established the following equation, for the mean diameter, based on a continuous probability function $(f_N(d))$:

$$d_{mn} = \left[\frac{\int_{d_{min}}^{d_{max}} d^m f_N(d) dd}{\int_{d_{min}}^{d_{max}} d^n f_N(d) dd} \right]^{\frac{1}{m-n}} \tag{4.3}$$

being d_{max} and d_{min} the maximum and the minimum diameter of the particles, respectively.

If the probability function is based on a volumetric (mass) probability $(f_V(d))$ the equation for the mean diameter becomes:

$$d_{mn} = \left[\frac{\int_{d_{min}}^{d_{max}} d^{m-3} f_V(d) dd}{\int_{d_{min}}^{d_{max}} d^{n-3} f_V(d) dd} \right]^{\frac{1}{m-n}} \tag{4.4}$$

When the functions $f_N(d)$ and $f_V(d)$ are not continuous, the integral in the Equations 4.3 and 4.4 is replaced by a sum. Other diameters may be obtained through:

$$(d_{mn})^{m-n} = \frac{d_{m0}{}^m}{d_{n0}{}^n} \tag{4.5}$$

The parameters *m* and *n* are usually integers and some of the possible combinations are shown in Table 4.2. Each one of these mean diameters correspond to a different field of application (Mugele and Evans, 1951).

Table 4.2- Mean diameters

d_{mn}	Name of mean diameter	Field of application
d_{10}	Linear	Comparison and evaporation studies
d_{20}	Surface	Absorption
d_{30}	Volume	Hydrology
d_{32}	Sauter	Efficiency studies and mass transfer

The Sauter mean diameter (m=3 and n=2) represents the volume/area ratio of the whole sample and is widely used as a representation of the mean particle size:

$$d_{32} = \frac{d_{30}^{\ 3}}{d_{20}^{\ 2}} \tag{4.6}$$

From Equation 4.4, d_{32} can also be obtained through:

$$d_{32} = \frac{\overline{X}}{\Gamma\left(1 - \frac{1}{n}\right)} \tag{4.7}$$

However, the Gamma function (Γ) may cause problems in determining mean diameters from the Rosin-Rammler parameters, because it assumes a probability function whose maximum diameter is infinity.

4.1.3 MEASURING PROCEDURE

The sampler measuring cell and the water lines should be thoroughly cleaned before starting the measurement. Then, the system should be aligned and zeroed. For this purpose, the measuring cell must already be in the beam path and a suitable collection lens in place (for starting, the 300 *mm* lens should be a good approximation). Changing the lens will require a new alignment. The water is subsequently introduced into the sampler and the mixing rotor (at the controller) is turned on; then, particles are introduced in very small amounts into the solution. Their concentration must be checked and should be somewhere between 20 % and 40 %. Special care must be taken in order to avoid *vignetting*.

4.1.4 ACCURACY AND LIMITATIONS

The accuracy of the instrument was extensively tested and discussed by Teixeira (1988), among others. It was concluded that it is efficient, giving results that could differ by 3 *%*, for a standard sample. The results also proved to be reproducible.

Despite the many advantages of the laser diffraction technique, it is limited to ensemble measurements of average size of spherical particles. No velocity information is provided. In addition, the theory is invalid for very small particles (below approximately 1 μm), where there are very large diffraction angles and the diffraction pattern depends also on its optical properties. In that case, it can be fully described by the Mie scattering theory. However, in this study, this is not a problem due to the very small amount of particles with such small dimensions. Furthermore, the accuracy of this method is questionable for large particles because reflections can be significant, causing larger angles of diffraction (Bayvel and Jones, 1981).

Teixeira (1988) has also shown that multiple diffraction limits the applicability of the Malvern instrument, once the system may assume a distribution with a lower mean diameter than the real value.

4.2 HIGH SPEED VIDEO CAMERA

The samples taken from the estuary were moved into the laboratory and eroded in the Perspex mini flume. Throughout the course of the erosion tests, high speed videos (HSV) were made, using a high speed video camera (at 500 frames per second, *fps*), for flow visualization of the natural sediments. Because particles were entrained into the flow, the footage proved to be a valuable tool in order to get an insight into the physical process.

Figure 4.3- High speed video system

This CCD camera (NAC HSV-1000) records at 500 or 1,000 *fps*, with a variable shutter that helps capture sharper pictures than similar systems, enabling to understand what is occurring during a high speed event. It consists of a video tape recorder (VCR) and video monitor mounted on an integral cart and the HSV-1000 colour camera. An easy-to-use hand held keypad controls all record and playback functions. In addition, for added versatility, the camera is easily switched to monochrome operation to use when a black and white image is more adequate. The recording format is S-VHS or VHS, the pixel count is 649 x 491 and it is possible to visualize frame by frame. The resolution is 350+ and 750+ horizontal lines of the video tape recorder and of the monitor, respectively, and 400+ lines for the video camera. Besides, the gain can be 0, +6 or +12 *dB*, switchable (www.hadlandphoto.com.au/NAC.htm). The lens provided (Fujinon TV lens, C6 x 17. 5 B, 1:1,8) is 17,5-105 *mm* in focal length. The amplification lenses available are: +1, +2 and +4.

With this high speed video system it was intended to assess both the Reynolds number at which the onset of erosion occurs and the size and shape of the flocs eroded.

In the current investigation, the following conditions were considered: records were made on S-VHS tapes for a better image quality; it was applied the lenses +1 and +4 and the gain was 0 *dB*. Before start recording, two light sources were positioned towards the mini

flume, choosing the best angles to optimise the illumination with low reflections. Also, the camera was placed perpendicular to the flume and a rule was used in order to have a vertical and horizontal scale. Experiments were carried out at an increasing Reynolds number, starting at 3,300 and going up to 60,000. The movies were subsequently digitised and analysed.

The resolution of the camera was 0.385 *mm*. This low resolution is related with the video recording conditions: the flume used in the erosion tests is made of Perspex, which causes high reflections and, in this way, it is very difficult to obtain a good image on the monitor. This fact is made worse due to the high curvature of the flume, yielding image distortions. Considering the conditions previously referred, the incident light on the flume was not uniform, giving different contrast levels and making the image less valuable.

It was attempted to modify the illuminating system, using a different layout for the light sources. Nevertheless, any improvement was obtained. Because of all limitations of the system (low resolution, non-uniform light, light reflections), it was not possible to analyse the images correctly and to determine the size of the sediment flocs eroded.

Various researchers have used video techniques to study the initiation of sediment movement and bedload transport, measuring the velocity and acceleration of the particles as well as fluid velocity, at 30 *fps* only (Roarty, 2000), however it was using a simpler geometry.

4.3 SAMPLE COLLECTION

The site of collection was chosen to be representative of the average sediment of the estuary. It has to be under the daily tidal effects and a special care has to be taken not to be close to pollution sources. All the samples were collected at low tide.

Most of sediment samples used during the present project where collected at Cávado estuary, at the town of Esposende (Portugal); two of them where taken on Gironde estuary (France) and other two on Westerschelde estuary (the Netherlands). The Cávado estuary (Figure 4.4) is located in the west coast of Portugal (41º 31’ N, 8º 46’ W); the Gironde is the largest estuary in Europe (channel with 130 *km* in length), is located along the southern France’s Atlantic sea coast and the sampling site was near the Pointe de Richard’s lighthouse (45º 26’ 41’’ N, 0º 55’ 69’’ W); the Westerschelde estuary is situated in the south-western part of the Netherlands (known as the Delta) and the sampling place was the Biezelingse Ham (51º 26,474’ N, 3º 55,506’ E).

Figure 4.4- The Cávado estuary

The sampling procedure was the same for any estuary. It consisted in placing and gently pushing the mini flume through the mud (Figure 4.5) using a metal sheet and then removing the flume with the mud and putting it on the owner basis. Great care must be taken during the collection as well as during the transportation to the laboratory, to minimize changes on the layers of the sediments inside the flume (Grant and Daborn, 1994), in order to simulate the real conditions. In laboratory, the flume is filled with estuary water.

At the Cávado estuary, the samples were taken in two regions of the river bed: one close to the water and another further away from the water.

Figure 4.5- Sampling natural sediments at the estuary

4.4 SEDIMENT ANALYSIS

The full characterisation of the sediment requires the application of a wide range of techniques. These are detailed over the following sections.

4.4.1 CHEMICAL COMPOSITION

The chemical composition analysis is made using an X ray fluorescence spectrometry instrument (Philips X'Unique II). A sediment sample (50 *g*) is dried on the oven for around two days at 110 *ºC*. Once pressed on an aluminium mould, the analysis is carried out in the instrument.

4.4.2 WATER CONTENT

The sediment water content (*WC*) is measured at approximately 2 and 4 *mm* in depth from the top layer of mud surface. The sediment sample is placed in a previously weighed weigh-boat (b); the total weight is recorded (b_w) as soon as possible. The wet sediment in the weigh-boat is then dried at 110 *ºC* for about 2 days (until a constant weight is obtained), and is subsequently weighed (b_d). The sediment water content is expressed as a percentage of the water relative to the sediment wet weight through:

$$WC(\%) = \frac{(b_w - b) - (b_d - b)}{b_w - b} \times 100 \tag{4.8}$$

4.4.3 SALINITY

The salinity is determined by filtering the sediment liquid, on the field. The liquid drained is re-filtered to remove any suspended sediment and placed in a previously weighed weigh-boat. Subsequently, the procedure is similar to sediment water content determination and the water content on the solution is also determined by Equation 4.8.

The salinity is then calculated by Equation 4.9:

$$Salinity(\%) = 100 - WC(\%) \tag{4.9}$$

4.5 RHEOLOGY

This technique consists on the measurement of the rheological properties of the fluids, using a rheometer. It studies a relationship between the shear stress and the shear rate of fluids, classifying them according specific parameters (White, 1986).

The rheometer is a key unit throughout the experimental programme because it is used to measure the rheological properties of the fluids as well as to drive the fluid inside the flume on a speed or torque controlled mode. The rheometer system Physica Rheolab MC 1 was used.

To the fluid rheological properties measurements, the system has a set of cylinders, whose selection depends upon the fluid viscosity range. The most appropriate was the double-gap cylinder system, usually known as Z1 DIN. The fluid sample is positioned in the measuring gap between the stationary measuring *cup* and the rotating measuring *bob*. The measuring geometry of Z1 DIN as well as its characteristics and some rheometer technical data are presented in Annex A. In this way, it is possible to simulate a Couette flow, i.e. a laminar flow between two parallel surfaces in which one moves parallel to the other (Schlichting, 1979).

This rheometer enables rotational tests where the desired speed is pre-set (shear rate controlled) and the torque acting on the measuring *bob* from the flow resistance of the sample is measured (shear stress).

Experiments were carried out on the fluids resulting from the erosion tests and to the various types of fluids employed on the experimental tests. Each test had a duration of 60 *s* approximately.

The rheometer accuracy is ± 1 *%*. Pinho (1999) analysed the uncertainty of viscosity measurements and concluded that the double-gap systems provide a higher accuracy than single-gap systems, because the errors in each of the two gaps are nearly symmetric and cancel out.

CHAPTER 5

EXPERIMENTAL DETAILS

This chapter details the experimental setup and techniques. It includes the description of the experimental apparatus, the refractive index compensation of the LDA and its optical configuration. Attention is also dedicated to the seeding and to the main experimental procedures. The LDA accuracy is evaluated and an uncertainty analysis of the experimental results is carried out.

The field surveys carried out along this work are referred in addition to the physical and chemical characterisation of the sediment samples. Based on these results, the simulated beds were specified. Finally, the test conditions for each measurement are described in detail.

5.1 EXPERIMENTAL APPARATUS

A schematic layout of the experimental facility is shown in Figure 5.1. The main components of the test rig are: the LDA, a driving motor and the toroidal mini flume.

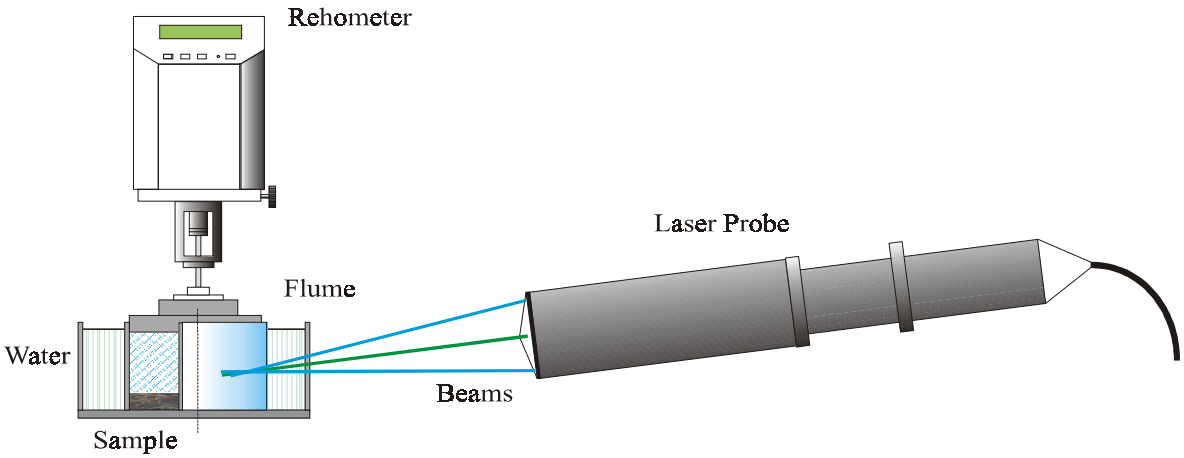

Figure 5.1- Basic experimental rig

The entire flume was enclosed inside a squared section glass box (194 × 194 *mm* and 3 *mm* thick) to minimise the optical distortions of the laser beams resulting from the combined effect of a mismatch in the refractive index and a curved surface (see Figure 5.2). It was attempted to minimise the deformation of the interference pattern of the measuring control volume in order to obtain a strong signal for backscattering operation. Early tests, without the glass box, have clearly identified the effect of a difference in the refractive index (air to quartz/fluid) and that of a curved wall. The resulting misalignment of the control volume lead to a sharp reduction in the signal acquisition data rate, a parameter that is of the greatest importance for turbulence analysis.

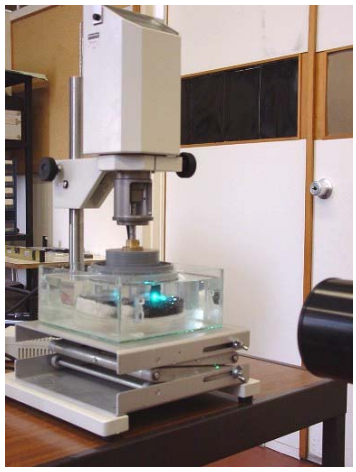

Figure 5.2- Test rig

The space between the box and the flume was also filled with water, to provide a better optical access, increasing the signal acquisition data rate. A circular flat lid (with an internal and external diameters of 62 and 124.6 *mm*, respectively) is connected to the shaft of a rheometer on top of the toroidal channel to drive the fluid on a tangential flow at controllable speeds.

The laser beams paths cross different media between the transmitting optics and the annular section of the flume, where fluid velocity measurements take place. Their positioning inside the flume is easily obtained through the 3D traverse table (where the transmitting/receiving optics are mounted), which is computer controlled, within very small increments: a resolution of 0.0125 *mm* on the x (radial) and y (horizontal) coordinates and 0.0063 *mm* on the z (vertical) direction, with an estimated error (E_T) of 1.25 % (Figure 5.3). Figure 5.4 shows a view of the laser source.

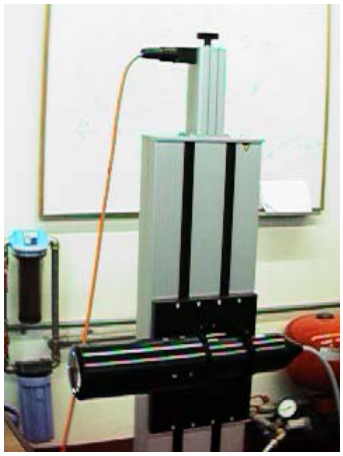

Figure 5.3- Traverse mechanism with the transmitting/receiving optics

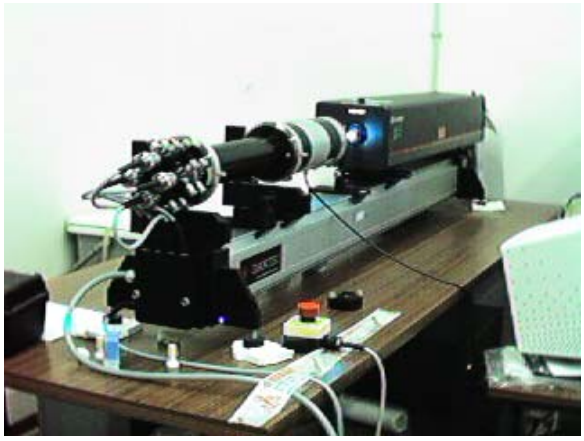

Figure 5.4- The laser source

5.1.1 THE MINI FLUME

Experiments where carried using a miniature annular flume (mini flume) as shown in Figure 5.5. This flume has been extensively used in critical shear stress measurements in sediment beds to determine the erosion properties, yielding a fairly accurate reproduction of the main flow pattern near the sediment, as observed in natural beds (James and Jones, 1992; James *et al.*, 1996), although large-scale circular flumes have also been used (Graham *et al.*, 1992). Previous work has shown that a circular mini flume mounted on a controlled stress rheometer can be used to accurately predict critical stress levels if the flow of the fluid above the bed can be characterised. Field work studies have shown that this mini flume provides a more accurate erosion stress values than other much larger scale flumes (Ruddy *et al.*, 1996).

In the present arrangement, the mini flume is made of two concentric tubes, 70 *mm* high and the inner tube, which is made in Perspex, is 60 *mm* in outer diameter and 3 *mm* thick. Depending on the type of experimental test, the outer tube has different characteristics: for the simulated beds it is built in quartz, 2.5 *mm* thick, and its internal diameter is 131 *mm*; for the natural sediment tests it is built in Perspex, 6.5 *mm* in thickness and with an inner

diameter of 126.8 *mm*. The outer wall made of quartz is preferable for a better optical access into the flow and has a smaller thickness. However, if used in natural sediments it is easily damaged by the sediment itself. A solid Perspex wall is used at the bottom (subsequently referred as "smooth bed"), holding both walls. In addition, the basis and the inner wall of the flume were painted with black paint in order to reduce beams reflections. In Figure 5.5 it is sketched the orientation of the measurement volume relatively to the flow. Measurements included both the tangential (u_θ) and axial (u_z) components of the velocity.

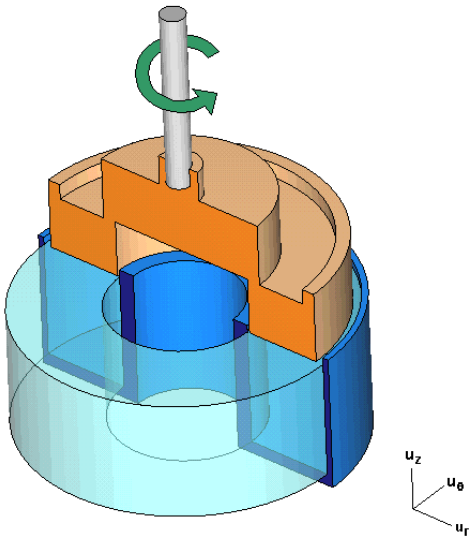

Figure 5.5- The mini flume

Pourahmadi and Humphrey (1983) consider a channel having a strong curvature if it obeys to the relationship: $R_c / D \leq 20$. R_c is the channel mean radius of curvature and D is the channel width. For this mini flume that ratio is 1.35, being therefore considered a channel with very strong curvature.

5.1.2 REFRACTIVE INDEX COMPENSATION

As previously shown, during the LDA measurement, the beams paths interfere with various walls and media before converging on each other. These media have different refractive index, which is a fundamental property of transparent materials, and is defined as the ratio of the velocity of light in a vacuum (or air) to its velocity in that medium (Hecht, 1991).

Using geometrical optics principles for the law of reflection and refraction, the resulting interference on the probe volume may be calculated and taken into proper account.

When light passes from a transparent medium to an other, changes in its speed and direction are observed as a function of the refractive index of adjacent media and the angle (angle of incidence, α_i) between the luminous beam and the normal to the interface

(Figure 5.6). On the other hand, the angle between the normal direction and the refracted beam is known as the refraction angle (α_r). As observed in Figure 5.6, light rays that cross a surface into another medium with a different index of refraction (n_1 to n_2) will bend. Light will travel slower in denser materials (higher refractive index) and this slowdown as the light crosses the boundary is the cause of the light bending.

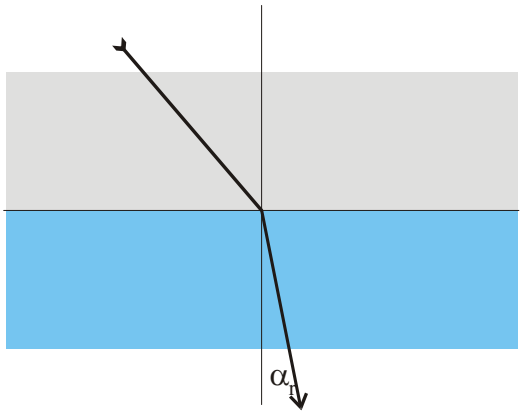

Figure 5.6- Light ray through an interface

In 1621, Willebrord Snell put forward the relation between angle of incidence, the angle of refraction and the media refractive indices, which has the form:

$$n_1 \sin(\alpha_i) = n_2 \sin(\alpha_r) \tag{5.1}$$

known as the Snell´s Law (Pedrotti and Pedrotti, 1993). Using this law, one can calculate the beams path through various media with different refractive indexes. When $n_2 < n_1$, the refracted ray bends away from the normal; on the other hand, if $n_2 > n_1$, it bends toward the normal. However, if the incident ray is normal to the surface $(\alpha_i = 0)$, it will be refracted with no change of direction $(\alpha_r = 0)$, regardless of the ratio of refractive indices.

Figure 5.7 shows that, at increasing angles of incidence with the interface, by Snell's law corresponds to a refraction of larger angles.

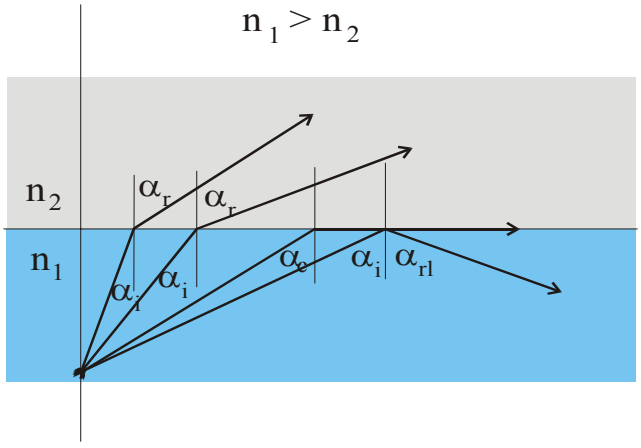

Figure 5.7- Effect of the incidence angle on the refraction angle

In a special case, when light moves from a dense medium to another of lower density, a critical angle of incidence, α_c, is reached when the angle of refraction is 90 ^{o}. In this case, the light diffracts along the interface (Figure 5.7). Thus, using Snell's law, the critical angle is easily determined:

$$\alpha_c = \sin^{-1}\left(\frac{n_1}{n_2}\right) \tag{5.2}$$

Further increasing the angle of incidence, the incident beam will be totally reflected within the denser medium with an angle (α_{rl}) equal to that of incidence. Some materials have the ability to double the luminous beam; a mineral able to split light is called birefractive (will introduce more refractive indices), otherwise it is monorefractive (a single refractive index).

In this experimental work, due to the test rig configuration, the laser beams had to cross different media prior to the measuring volume. This fact causes a displacement of the measuring volume away from the focussing lens. Therefore, the cross angle of the beams must be corrected.

The refractive index is dependent upon the light wavelength. For the current computations the same value was assumed for both light wavelengths, which are summarised in Table 5.1.

Table 5.1- Refractive index of the different media

Medium	Refractive index	Source
Air	1	Weast (2000)
Glass	1.525	Measured
Water	1.333	Weast (2000)
Quartz	1.495	Measured
Solution of glycerine	1.373	www.dow.com/glycerine/
Perspex (PMMA)	1.491	Progelhof and Throne (1993)
Ethyl alcohol	1.359	Weast (2000)
Oil	1.477	Measured

The refractive index of glass and quartz were determined using the "Becke's line" technique, applying the immersion method, which uses clear field microscopy with solutions of calibrated indexes of refraction. The refractive index of oil was measured using a refractometer: type Abbe, Eloptron, Schmidt and Haensch GmbH & Co. However, measuring the index of refraction of the solution with natural sediments proved to be not possible due to the presence of suspended solids. In this way, for the determination of the correction angle, it was assumed the same refractive index as that of water.

The refraction value for the solution of glycerine was obtained considering a glycerine percentage of 32 % in weight.

Preliminary experiments were carried with the transmitting/receiving optics with a horizontal orientation on the traverse. Subsequently, an update was installed which enabled the unit to be tilted by as much as the half crossing angle, allowing one of the vertical beams to enter parallel to the bottom surface. In this way, the velocity measurements could be made in the close vicinity of the bed.

Tilting the beams will require an application of the object Transform (in BSA Flow software), which will perform a coordinate transformation for the measured velocity components based on a transformation matrix. Mouazé and Bélorgey (2001) refer the problem of an excessive tilting, causing a loss of coincidence conditions in the measuring control volume. However, that is not a problem in the current study since the transmitting beams were only tilted (φ) by approximately 7.2 ^{o}.

The actual crossing angles of the vertical and horizontal beams were corrected considering both the influence of the various media with different refractive indexes in the light paths and the inclination of the transmitting/receiving optics (φ).

The detailed determination of such corrections is presented in Annex B. It involves a variety of trigonometric expressions, that had to be treated with more detail and care in the case of the horizontal beams, for which the flume surface curvature is a further complicating parameter. In such conditions, the Snell's law is applied at each position on the surface, but the incidence angle will depend upon the local curvature. This results that incident rays at different positions are bent by different amounts. In the case of the vertical beams, the flume walls behave as a plane surface.

Table 5.2 shows the corrections for the crossing angle at the probe volume for the vertical beams, for each of the experiments carried out.

Table 5.2- Corrections of the vertical beams (blue) full crossing angle

Type of experiment	2θ (without correction)	$2\theta'$ (with correction)
Using solution of glycerine	14.342 ± 0.09	10.394
Using ethyl alcohol	14.342 ± 0.09	10.502
Using oil	14.342 ± 0.09	9.655
In natural sediment beds	14.342 ± 0.09	10.709

For the horizontal beams (green), neglecting the corrections due to the refractive index and for all tests, the crossing angle is 19.874^{o} ± 0.09 (see Annex B). The correspondent corrections, for the solution of glycerine, are presented in Figure 5.8. These vary with the traverse displacement, as the probe volume is moved further into the measuring section.

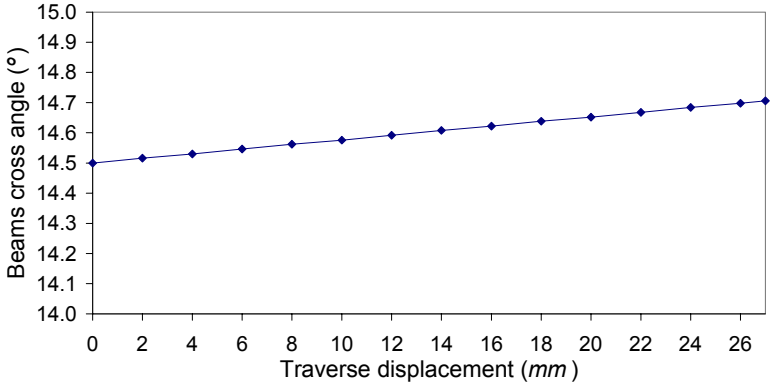

Figure 5.8- Corrected horizontal cross angles to the glycerine solution

For the remaining fluids, the experiments were carried out at a radial position around 7.5 *mm* from the flume outer wall. The corrected cross angles ($2\theta'$) were: 14.678^o, 13.648^o and 15.780^o to the ethyl alcohol, oil and natural sediment beds, respectively.

Using Equation 3.6 and taking into account the beams crossing angle, it is possible to determine the correct velocity value:

$$u'_{\perp} = f_D \frac{\lambda}{2\sin\theta'} \tag{5.3}$$

Because the actual angle ($2\theta'$) is lower on both vertical and horizontal velocity components, this yields an increase in the fluid velocity ($u'_{\perp}$). As an example, and using the tests with the solution of glycerine, an increase of 39.39 % and 36.85 % for the vertical and horizontal velocity components was found, respectively.

Annex B also shows the difference between the traverse table displacement and the real distance travelled by the beams inside the flume (radial distance), due the modifications in the beam trajectory. For the quartz flume with a solution of glycerine, the maximum travelled distance by the beams was 35.5 *mm* (real distance), that corresponded to a distance of approximately 27 *mm* in the traverse. Both distances were also different when the Perspex flume was used.

5.1.3 OPTICAL CONFIGURATION OF THE LDA

The LDA configuration used in the present work has already been described in Chapter 3 (section 3.6). Taking into consideration that the green and blue are the horizontal and vertical beams, respectively, the optical characteristics inherent to both laser beams are presented in Table 5.3.

Once the corrected crossing angles were known, an equivalent beam separation was determined, as presented in Table 5.4, for each type of experiment. As referred in Annex B (Table B.1), without any corrections the beam spacing was 75 and 78 *mm* for the green and blue beams, respectively.

Table 5.3- Optical properties of the system

Optical property	Green	Blue
Wavelength (*nm*)	514.5	488.0
Focal length (*mm*)	310	310
Beam diameter[1] (*mm*)	1.3	1.3
Expansion factor	1.95	1.95

[1] Before expansion

Table 5.4- Equivalent beam spacing at the transmitting optics for the various experiments

Beam spacing (*mm*)	Green	Blue
Using solution of glycerine	79.46	56.39
Using ethyl alcohol	79.85	56.98
Using oil	74.20	52.37
In natural sediment beds	85.93	58.12

The output properties obtained for both components are presented in Tables 5.5 through Table 5.8.

Because the horizontal (green) beams crossing angle changes with the traverse motion, for the measurements carried out along a radial direction of the flume, the beam spacing was taken as an average between the two limiting conditions.

Table 5.5- Output properties referent to the solution of glycerine

Output property	Green	Blue
Number of fringes	39	28
Fringe spacing (μm)	2.024	2.694
Beam half angle (^{o})	7.304	5.197
Probe volume (*mm*)		
Height	0.081	0.076
Width	0.080	0.076
Length	0.630	0.839

Table 5.6- Output properties referent to ethyl alcohol

Output property	Green	Blue
Number of fringes	40	28
Fringe spacing (μm)	2.014	2.666
Beam half angle (^{o})	7.339	5.251
Probe volume (mm)		
Height	0.081	0.076
Width	0.080	0.076
Length	0.627	0.830

Table 5.7- Output properties referent to oil

Output property	Green	Blue
Number of fringes	37	26
Fringe spacing (μm)	2.165	2.899
Beam half angle (^{o})	6.824	4.828
Probe volume (mm)		
Height	0.081	0.076
Width	0.080	0.076
Length	0.674	0.903

Table 5.8- Output properties referent to natural sediment beds

Output property	Green	Blue
Number of fringes	43	29
Fringe spacing (μm)	1.874	2.614
Beam half-angle (^{o})	7.890	5.355
Probe volume (mm)		
Height	0.081	0.076
Width	0.080	0.076
Length	0.584	0.814

5.2 FLOW SEEDING

As referred in section 3.3.3, the selection of the seeding particles for LDA measurements depends upon the ratio *particle density/fluid density*, particle size and the turbulence level expected in the flow. In general, seeding particles should be chosen as large as possible in order to increase the intensity of the scattered light. However, the particle size is limited to the fact that, if particles are too large, they will not follow properly the flow. The correct selection can be justified in terms of the frequency response of a particle under the effect of turbulence. In conclusion, despite the wide range of available alternatives (Durst *et al.*, 1981) none is universal and the final choice must be tailored to each particular application.

In the present work, a first approximation was based on the use of polystyrene particles made by Coulter Electronics (1-2 μm and density of 1,050 kg/m^3). It was observed that, although they are expected to follow the flow very well, the fluid and the walls would reduce the amplitude of the scattered signal and, consequently, the data rate. They are also very expensive, so other alternatives were considered.

After consulting DANTEC, polyamide particles were selected and used in all tests. They are produced by a polymerisation process and, therefore, have a round but not exactly spherical shape; their mean linear diameter is approximately 20 μm and have a density close to that of water (1,030 kg/m^3). These particles are micro porous and strongly recommended in water flow applications. By switching to these particles, the data acquisition rate was greatly improved.

A particle is suitable as a fluid tracer if the amplitude ratio (η) is approximately 1 throughout the frequency spectra, as mentioned in section 3.3.3. Figure 5.9 shows the influence of the fluid eddy frequency (estimated) on the amplitude ratio to both polystyrene and polyamide particles, in a water flow (ρ_f = 1,000 kg/m^3 and $\mu_f = 1\times10^{-3}$ $Pa.s$). η was calculated by Equation 3.12.

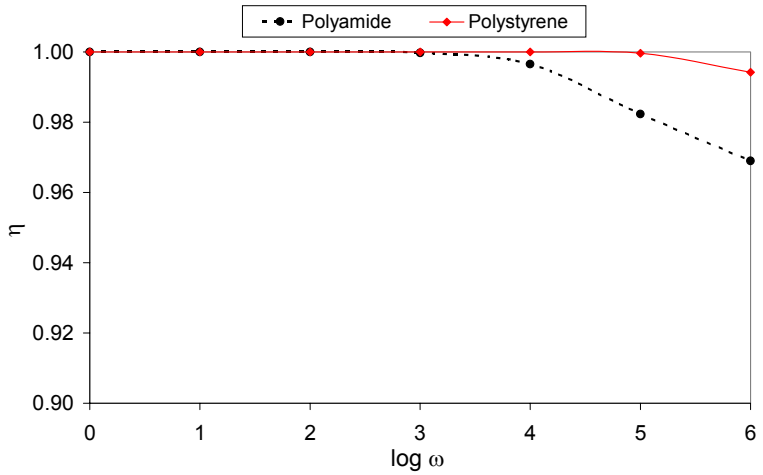

Figure 5.9- Influence of the fluid eddy frequency on the amplitude ratio for two seeding media

These results confirm the option made in choosing the polyamide particles. Compared with polystyrene particles, those one are much cheaper and able to follow the flow properly (except for very high eddy frequencies).

The seeding was made by introducing a small quantity of such particles inside the mini flume, immediately before a measurement session.

Throughout the experimental programme, various fluids were used, depending on the required investigation. Because the polyamide particles were always used as the seeding medium, their ability to follow the various fluids was investigated. Figure 5.10 shows the results obtained for a variety of media: a solution of glycerine; ethyl alcohol; oil and water over natural sediment beds.

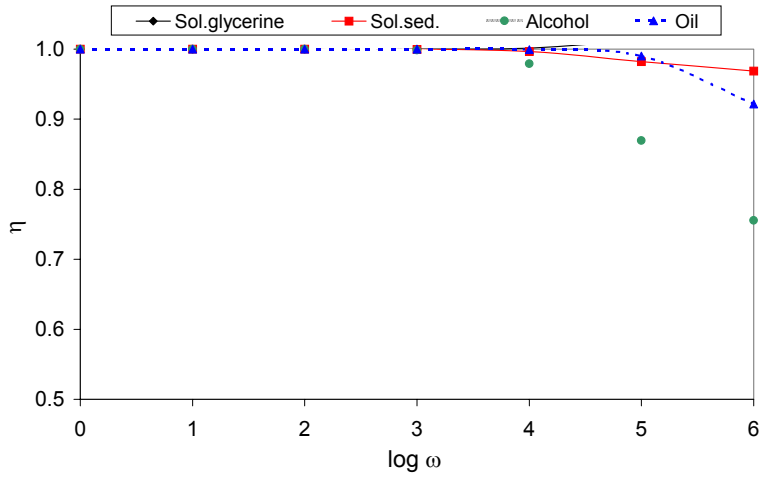

Figure 5.10- Influence of the fluid eddy frequency on the amplitude ratio for the various fluids

As observed in Figure 5.10, the response of the particles at high frequencies is worse because of their higher density ratio. Nonetheless, they are acceptable as a seeding medium.

Figure 5.10 was obtained considering the fluid properties listed in Table 5.9.

Table 5.9- Physical properties of the fluids

Fluid	$\rho_f\ (kg/m^3)$	$\mu_f\ (Pa.s)$
Solution of glycerine	1,076	3×10^{-3}
Ethyl alcohol	790	1.3×10^{-3}
Oil	844	20.5×10^{-3}
Natural sediment beds (except Gironde)	1,000	1×10^{-3}

The *particle/fluid* density ratio is presented in Table 5.10.

Table 5.10- *Particle/fluid* density ratio

	Sol. of glycerine	Sol. nat. sed.	Ethyl alcohol	Oil
Density ratio	0.957	1.030	1.304	1.220

Crucial in this analysis is the estimation of the fluid eddy frequency for each case. As a starting point one may use the turbulence characteristics of pipe flow, which has been comprehensively studied in the past. Hutchinson and Hewitt (1971) argued that only energy containing eddies influence the particle motion. The authors show some results for the turbulent characteristics of the flow, based on data provided by Laufer (1954). They stated that the ratio *large eddies size/tube radius* (l_e / R) is independent of the Reynolds number and it decreases when r / R approaches the wall. The group $\frac{\omega R}{2\pi u^*}$, which is also independent of the Reynolds number, is equal to R / l_e. r is the radial distance measured from the centre of the tube.

In the present study, it was considered that $l_e / R = 0.25$ (close to the wall) and R is half of the hydraulic diameter (d_h). Thus, for each fluid, the value of ω can be determined and the resulting data is shown in Table 5.11, for the most unfavourable situations.

Table 5.11- Fluid eddy frequency using different conditions estimated from Hutchinson and Hewitt (1971)

	Sol. of glycerine	Sol. nat. sed.	Ethyl alcohol
ω (*rad/s*)	61.52	73.23	18.89
$\log\omega$	1.79	1.87	1.28

The data also shows that the frequency of the most energetic eddies is well below the cut-off frequency ($\geq 1000\, s^{-1}$), above which the particle's ability to follow the flow is questionable.

Another question of concern is the mixing of seeding particles and entrained sediment particles, which covers a wide range of sizes. In this way, velocity data could be resulting from unsuitable tracers. This question will be discussed at the end of this chapter.

The effect of the seeding particles diameter upon the amplitude ratio is observed in Figure 5.11, for the various fluids tested.

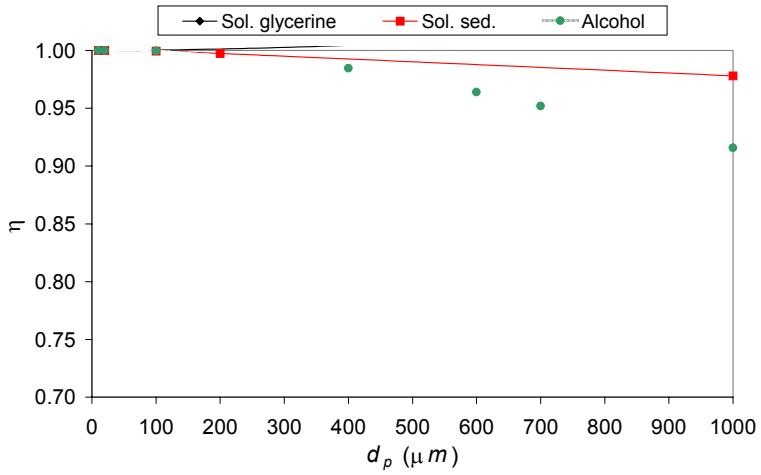

Figure 5.11- Effect of the seeding diameter upon the amplitude ratio

It shows that to the test conditions using either the solution of glycerine or natural sediments, the particles are good tracers even at very large diameters (700 μm). In the least favourable tests (with alcohol), only those above ≅ 400 μm may not follow the flow properly.

Seeding errors

The bias errors introduced by seeding particles may be due to flow distortion bias caused by their injection and an error caused by the inability of some particles to follow the flow.

As previously referred, in the present work the seeding was introduced inside the flume prior to any measurement. In addition, Figure 5.10 shows that the seeding follows the fluids properly to the eddy frequencies estimated as the most severe conditions. Thus, the seeding bias errors are negligible. On the other hand, due to particle dispersion by the flow, the problem in obtaining a uniformly seeded flow is non-existent. This is not true in situations where there is not an internal or enclosed flow arrangements such as in jets (external flow), in which the seeding is problematic (Baker, 1974).

5.3 EXPERIMENTAL PROCEDURES

- Prior to any experiments, a standard test was carried out in a simple flow, and the performance parameters, such as data rate, were compared with those previously obtained under optimal configuration.
- As previously referred, accurate LDA data requires a careful alignment of the optical systems. The laser alignment was verified periodically. In order to infer if the system was in need of alignment, before commencing any series of

measurements, the spray produced by a small nebulizer was used for comparison tests.

- The BSA's processing parameters were selected in order to obtain an optimised signal, with a high data rate and validation, and using an appropriate gain/voltages combination in order to "fill" most of the voltage range. Thus, the high voltage and signal gain were chosen, optimising the data rate and the data validation. The high voltage was selected within the 1,000/1,200 *V* range and the signal gain at 30/35 *dB*. Extremely high values of the high voltage setting generate noise, reducing the validation. Low gains yield high data validation but low data rate because bursts from the smallest particles will not be detected. Before starting any measurements, a section of the flume was divided in different regions and the data acquisition settings were optimised. For measurements close to the walls the high voltage setting was reduced because the photomultipliers were likely to saturate due to light reflections.
- Before any measurements, a two dimensional measuring grid was built. As it will be shown in section 5.8, the grid arrangement varied with the type of experiment.
- Laser power was set at a high value in order to improve the signal to noise ratio (SNR).
- A reference point on the flume was chosen at the beginning and was always used in each measurement. The measuring volume was positioned in the flow by visual observation of the beams and signal disappearance when it hits the wall.
- All tests were carried out with the two components in "coincidence mode". This would enable the calculation of the Reynolds stresses.

5.4 ACCURACY AND UNCERTAINTY ANALYSIS IN LDA

The accuracy and uncertainty of LDA measurements is discussed in this section. The accuracy also includes a repeatability test. The uncertainty was computed by considering bias errors on the mean and RMS velocities and for the cross moments, and precision errors. The velocity bias effects were also referred. Finally, the uncertainty of the shear stresses was evaluated.

5.4.1 ACCURACY

The accuracy measurement is a combination of a variety of factors ranging from the physical measuring process itself to the methods of evaluation of the data collected.

Assuming that the optical parameters are accurately known and the signal is properly sampled and correctly processed, the LDA is an accurate technique and does not require calibration. However, the accuracy of the present apparatus was assessed. In this way, a metal filament was fixed into a rotating disc and driven at 2,230 *rpm* by a small DC motor (power source of 5 *V* and 0.12 *A*). The measuring volume was positioned at 1 *cm* from the

centre of the rotating disc, in different positions, in order the filament would cross the measuring volume with different components of the horizontal and vertical velocities. For the various configurations, a good agreement between both values (error below 2 %) was obtained.

Repeatability test

To ensure the validity of the results obtained with the LDA measurements, a test was repeated in exactly the same conditions. It was observed that both set of results have a maximum difference of 3 %. Therefore, the characteristics of the flow field are repeatable.

5.4.2 UNCERTAINTY ANALYSIS OF THE VELOCITIES

Although laser Doppler anemometers are among the most accurate flow measurement devices, small errors are involved and, as with any other measurement technique, it is important to know the sources of error when taking measurements. Due the large variety of relevant parameters (optical and electronic), an estimation of the measurement uncertainty for a complex device such as the LDA is not an easy task.

Usually an error, defined as the difference between the true value and the measured value, is a fixed number and cannot be a statistical variable. The uncertainty is regarded as the maximum error which may appear in a parameter being measured; it can be calculated using statistical procedures (Taylor, 1997). In this section, the major type of errors that lead to experimental uncertainty will be referred and quantified.

Uncertainty analysis has been a topic of much research and thought by many investigators for many years. The multiple measurement uncertainty analysis is divided into three categories (Martin *et al.*, 2000): calibration uncertainty (study of sources of uncertainty in the optics alignment); data acquisition uncertainty (study of sources of uncertainty in the frequency measurements); data reduction uncertainty (study of the propagation of the both previous sources of uncertainty to the final result).

The total error or the experimental uncertainty is usually expressed in terms of two combined components: a fixed or bias error (B) and a random or precision error (S), such that (Abernethy *et al.*, 1985; Steele *et al.*, 1994; Martin *et al.*, 2000) :

$$E_{0.95} = \pm\sqrt{B^2 + (t_{95}S)^2} \tag{5.4}$$

according to the Standard model, where the Student t value is a function of the degrees of freedom used in calculating S (for this case, 95 % confidence interval). For large samples (N>30), $t_{95} = 2$ (Abernethy *et al.*, 1985).

In order to provide a maximum uncertainty level for the present research, those values are determined for the most unfavourable condition throughout the experiments. In this way, it was considered: the measurement tests with a solution of glycerine; smooth bed at Re = 10,000; for the position at 7.5 *mm* from the outer wall and at 1 *mm* from the bottom surface. This analysis was also made at 10 *mm* from the bottom, in order to assess the influence of the measuring position.

• **Bias errors**

As described by Kline (1985) and Abernethy *et al.* (1985), a bias error is the systematic error which is considered to remain constant during a given test, also called a fixed error. Thus, in repeated measurements of a given set, each measurement has the same bias. These uncertainties cannot be sampled (via replication) with available procedures and, therefore, must be estimated.

Since the systematic errors are unknown, estimates must be made of the systematic uncertainties (bias limits) from each error source, B_i, in each variable at a 95 % confidence level. The overall bias limit of a certain measurement is defined as the root sum square combination of all the fixed error components (Abernethy *et al.*, 1985; Steele *et al.*, 1994):

$$B = \sqrt{\sum_{i=1}^{N} B_i^{\,2}} \tag{5.5}$$

- Errors related to the mean velocity:

These errors may have different sources: fringe spacing uncertainty; processor errors; mean velocity gradient broadening and negative bias velocity.

The fringe spacing uncertainty is caused by uncertainty in beam intersection angle and is given by (Patrick, 1985):

$$B_{Sfs} = \pm \frac{|\Delta\theta|}{\sin\theta'} \tag{5.6}$$

where θ' has the meaning and values presented in section 5.1.3 (see Table 5.5) and $\Delta\theta$ is the tolerance of the half angle measurement as shown in Table 5.2 ($\Delta\theta = \pm 0.045^{o}$).

Substituting the beams intersection angle and $\Delta\theta$ (in radians) into Equation 5.6, yields $\pm 6.2\times10^{-3} \le B_{Sfs} \le 8.7\times10^{-3}$.

Concerning the processor errors, processing takes place in the BSA's, by performing a digital spectrum analysis. As mentioned before, the BSA's determine the Doppler frequency with a 14 bit resolution.

Being the minimum and the maximum expected velocity given in function of the range centre (*RC*) and range span (*RS*), $u_{\min} = RC - \frac{RS}{2}$ and $u_{\max} = RC + \frac{RS}{2}$, and for BSA_1 $RC = 0\,m/s$ and $RS = 2.14\,m/s$, it is possible to calculate the velocity error in each measurement, through Equation 5.7:

$$\Delta u = \frac{u_{\max} - u_{\min}}{2^{14}} \tag{5.7}$$

The processor error is subsequently determined:

$$B_{proc} = \frac{\Delta u}{\overline{u} + u_{f's}} \tag{5.8}$$

in which $u_{f's}$ is the velocity correspondent to the frequency shift (calibration factor = 2.024 *m/s*/*MHz*). Thus, the processor error is 1.61×10^{-4} *%*.

Mean velocity gradient broadening occurs if a scattering volume of finite size covers a region of the flow where there is a mean velocity gradient. It is usually influenced by the measurement volume's dimension and the existence of significant velocity gradients within it. This leads to a broadening of the probability density function and to a mean velocity bias which, for a one-dimensional flow, can be estimated by (Melling, 1975):

$$\Delta^{\bar{u}}_{mvg} = \frac{1}{2}\left(\frac{d_{mv}}{4}\right)^2 \times \frac{\partial^2 u}{\partial z^2} + \cdots \tag{5.9}$$

for the vertical direction, where the higher order terms are neglected. For the radial direction, it is given in the same way:

$$\Delta^{\bar{u}}_{mvg} = \frac{1}{2}\left(\frac{l_{mv}}{4}\right)^2 \times \frac{\partial^2 u}{\partial r^2} + \cdots \tag{5.10}$$

being l_{mv} the measurement volume length. The bias is easily calculated for both cases using the expression:

$$B^{\bar{u}}_{mvg} = \frac{\Delta^{\bar{u}}_{mvg}}{\bar{u}} \tag{5.11}$$

The small control volume used in the measurements (Table 5.5) avoided high velocity gradients within its limits, leading, therefore, to a negligible bias related to the mean velocity. The results obtained for both positions at 1 and 10 *mm* from the wall, for vertical and radial directions are presented in Table 5.12.

Table 5.12- Mean velocity gradient broadening bias related to the mean velocity

	1 *mm*	10 *mm*
Vertical (*%*)	-0.015	4.79×10^{-5}
Radial (*%*)	-0.070	-0.041

Negative velocity bias occurs in recirculating and highly turbulent flows if frequency shifting is not used. In the present investigation the frequency shift (40 *MHz*) was introduced in one of the beams. In this manner, the directional ambiguity was removed and, therefore, the negative velocity bias is negligible.

The total bias error in each measurement (*B*), that is given using Equation 5.5, is 0.870 *%* (for both 1 and 10 *mm*). The uncertainty to the mean velocity ($B_{\bar{u}}$) is obtained by the expression:

$$B_{\bar{u}} = \frac{\sqrt{N}}{N} \times B \tag{5.12}$$

this error is 0.024 % and 0.028 % at 1 and 10 *mm* from the bottom wall, respectively. *N* is the number of samples.

- Errors related to the RMS velocity:

These type of errors include both the errors referred for the mean velocity measurement and for the mean velocity gradient broadening.

For the first one, and taking the Equation 3.16, the RMS bias error ($B_{\tilde{u}}$) is achieved:

$$B_{\tilde{u}} = \sqrt{\frac{N+1}{N}} \times B_{\bar{u}} \tag{5.13}$$

which gives an error of 0.024 *%* (at 1 *mm*). As observed, it depends on the mean velocity bias.

The errors on RMS values related to the mean velocity gradient broadening are given for the vertical (Equation 5.14) and radial (Equation 5.15) directions (Melling, 1975), through:

$$\Delta^{\tilde{u}}_{mvg} = \sqrt{\left(\frac{d_{mv}}{4}\right)^2 \times \left(\frac{\partial u}{\partial z}\right)^2 + \cdots} \tag{5.14}$$

$$\Delta^{\tilde{u}}_{mvg} = \sqrt{\left(\frac{l_{mv}}{4}\right)^2 \times \left(\frac{\partial u}{\partial r}\right)^2 + \cdots} \tag{5.15}$$

and the bias is determined as usual:

$$B^{\tilde{u}}_{mvg} = \frac{\Delta^{\tilde{u}}_{mvg}}{\tilde{u}} \tag{5.16}$$

The results for each case are presented in Table 5.13

Table 5.13- Mean velocity gradient broadening bias related to the RMS velocity

	1 *mm*	10 *mm*
Vertical (*%*)	13.70	0.111
Radial (*%*)	3.360	5.048

The total bias associated with the RMS velocity, for the vertical direction, is 13.70 *%* and 0.114 *%* at the distances of 1 and 10 *mm*, respectively.

- Errors related to the cross moments ($\overline{u'v'}$):

These errors include those related with the mean velocity measurement and those resulting from the beam orthogonality bias.

The first error is calculated knowing the relationship with the mean velocity bias, that is given by:

$$B_{\overline{u'v'}} = \sqrt{\frac{2(N+1)}{N}} \times B_{\overline{u}} \tag{5.17}$$

Substituting the appropriate values, this bias is 0.034 *%* at 1 *mm* from the wall.

The beam orthogonality bias (B_O) corresponds to the errors generated by the intersection of two laser components at an angle other than 90^o. Only the Reynolds shear stress is affected and the error is calculated as follows (Patrick, 1985):

$$B_O = \left(\frac{\overline{u}^2}{U_{ref}^2} - \frac{\overline{v}^2}{U_{ref}^2} \right) \times \sin\left|\Delta\theta\right| \tag{5.18}$$

in which U_{ref} is a reference velocity (U_{ref} = 1.07 *m/s*) and $\Delta\theta = \pm 0.045^o$.

Taking into account the velocity range ($\overline{u} \in [0;0.262]$ and $\overline{v} \in [-0.033;0.064]$), the beam orthogonality bias is 4.43×10^{-5}, which is considered negligible.

The total bias associated with the cross moments is 0.034 *%* and 0.040 *%* at 1 and 10 *mm*, respectively.

- **Precision errors**

The precision errors are also known as random or statistical errors or repeatability (Kline, 1985). *S* is more often called the precision index of a measurement (Abernethy *et al.*, 1985), and it represents a measure of the measurement random error. This variable can be estimated from the measured data only and is equal to its standard deviation.

In a more complex situation, in addition to the standard deviation, variations in the measured value appear among repeated measurements. In this way, the precision index is calculated as (Abernethy *et al.*, 1985; Steele *et al.*, 1993; Martin *et al.*, 2000):

$$S = \sqrt{\sum_{i=1}^{N} S_i^{\,2}} \tag{5.19}$$

These errors are introduced on both mean and RMS velocities due to the finite sampling size and can be estimated if a gaussian velocity probability function is assumed. The relative precision error in mean velocity ($S_{\overline{u}}$) can be determined using the following relationship (Yanta and Smith, 1973; Bates and Hughes, 1977):

$$S_{\overline{u}} = \frac{Zc}{\sqrt{N}} \times \frac{\widetilde{u}}{\overline{u}} \tag{5.20}$$

being *Zc* the confidence coefficient for a normal distribution (its value is based on the desired confidence level for the relative error). For 95 *%* confidence interval, *Zc* = 1.96 (Yanta and Smith, 1973).

Referring the RMS velocity, the relative precision error is given applying:

$$S_{\tilde{u}} = \frac{Zc}{\sqrt{2N}} \tag{5.21}$$

This equation shows that the result is independent of RMS magnitude and depends on the number of instantaneous samples considered only.

For the example considered at 1 *mm* from the wall, the error in the mean and RMS velocities is 0.642 *%* and 3.86 *%*, respectively. The correspondent turbulence intensity is 3.45 *%*.

- Velocity bias effects:

The source of this bias is the dependency of the rate of seed particles travelling through the measurement volume on the flow velocity. In this work, it was applied the Burst mode on BSA's and the transit time weighting was considered on the software. Therefore, there are no velocity bias effects.

Finally, the total experimental uncertainty for a 95 % confidence interval, at 1 *mm* from the wall, is presented in Table 5.14.

Table 5.14- Total uncertainty to the mean and RMS velocities and to the cross moments

Error	Error in mean velocity	Error in RMS velocity	Error in cross moments
B (%)	0.024	13.70	0.034
S (%)	0.642	3.86	------
$E_{0.95}$ (%)	± 1.284	± 15.725	± 0.034

This table shows that the total error in the RMS velocity is the largest. Also, considering the error in the mean velocity, the precision error has higher weight when compared with the bias error. The opposite is observed for the RMS velocity, where the larger bias error was due the contribution of the mean velocity gradient broadening.

Table 5.15 presents these uncertainties at the distance of 10 *mm* from the bottom surface. The turbulence intensity for this position is 1.87 *%*.

Table 5.15- Total uncertainty to the position at 10 *mm* from the wall

Error	Error in mean velocity	Error in RMS velocity	Error in cross moments
B (%)	0.028	0.114	0.040
S (%)	0.346	4.50	------
$E_{0.95}$ (%)	± 0.693	± 9.001	± 0.040

Comparing this table with the previous one, it is observed that in regions far way from the bottom wall the total errors decreased. Special attention is given to the bias error associated with the RMS velocity, which was significantly lower than that at 1 *mm*.

5.4.3 UNCERTAINTY ANALYSIS OF THE SHEAR STRESSES

Being the shear stress given by:

$$\tau = \mu \frac{du}{dz} \tag{5.22}$$

the uncertainty associated to this variable depends on uncertainties of viscosity (E_μ), mean velocity ($E_{0.95}^{\bar{u}}$) and on the traverse errors (E_T). Thus, the total uncertainty for a 95 *%* confidence interval ($E_{0.95}^{\tau}$) is given by:

$$E_{0.95}^{\tau} = \sqrt{E_\mu^2 + 2(E_{0.95}^{\bar{u}})^2 + 2E_T^2} \tag{5.23}$$

Table 5.16 presents the total uncertainty to the shear stress, referent to both positions.

Table 5.16- Uncertainty to the shear stress to both study cases

	1 *mm*	10 *mm*
$E_{0.95}^{\tau}$ (*%*)	± 2.724	± 2.255

5.5 CONSTRUCTION OF TEST BEDS

In order to obtain the simulated beds, the miniature annular flume described in 5.1.1 (Figure 5.5) is slightly modified to include a sediment model to reproduce the interface roughness, at the bottom, and a wavy lid to be used instead of the flat one.

5.5.1 SEDIMENT INTERFACE REPRODUCTION

Because in this work the effect of sediment shape and roughness upon the flow patterns in the vicinity of the interface is investigated, the sediment interface was reproduced by moulding gypsum over a sample of natural sediment, here referred as “rough bed”. Thus, the roughness and shape of the sediment bed were entirely reproduced.

Even in modelling the natural marine environment, non uniform roughness must be into account since it is not common, in the field, to have a flat bed or a bed with uniform roughness (Nowell and Jumars, 1987).

Figure 5.12 shows a view of the sediment model. Two moulds were built, from two different natural samples.

Figure 5.12- Sediment model (rough surface)

The region where measurements took place was painted in matt black, reducing the laser reflections at the surface.

5.5.2 SURFACE WAVES GENERATOR

In order to investigate the effect of wavy surfaces upon the flow field and to study their contribution to the turbulence (and erosion), the test rig was modified. Thus, four circular lids with various combinations of amplitude/wavelength were designed and built. They were made of cast aluminium and the shape for each one of the wavy surfaces was defined as a sine function. The shape was designed on a *solid-design* software linked to a rapid prototyping machine, which enabled the accurate reproduction of a complex surface.

Figure 5.13 presents some of the steps necessary to make the wavy lid.

Figure 5.14 shows a view of one type of the wavy lid (adjusted to the flat lid), connected to the drive shaft.

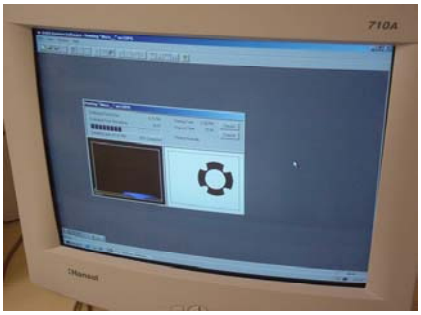

a)

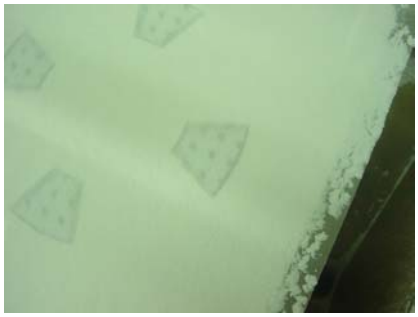

b)

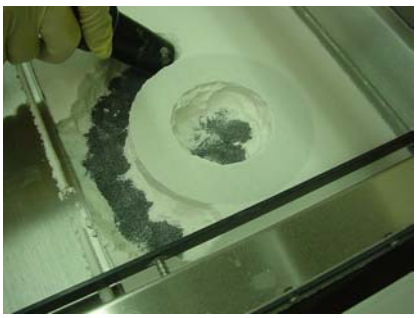

c)

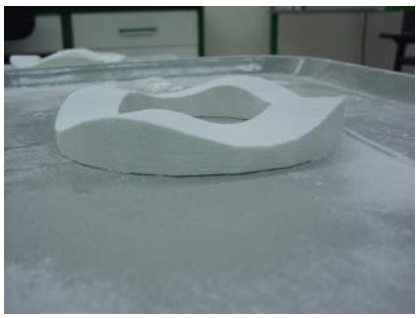

d)

Figure 5.13- The making the prototype for a wavy lid

Figure 5.14- View of a wavy lid

5.6 FIELD SURVEYS

This section will present the information relevant for each sample collected in the three estuaries. The samples are identified by the location, and in those from the Cávado estuary that identification also includes the collection date. The physical appearance of each sample when collected from the estuary is described, as well as the weather conditions at that time. The type of tests made at each one of the samples is also summarised.

5.6.1 GIRONDE ESTUARY

Two samples (G1 and G2) were collected in the mini flumes at Gironde estuary in September 1999, during a field campaign. The sediment thickness at the estuary was very high; it looked very cohesive and apparently made up of very small particles. The weather was dry. The sampling took place at top shore site (around 100 *m* from the shoreline) and was located in an area that appears to be flat and morphologically regular, without any discontinuities in the mud surface. The gap between the sediment bed and the rotating lid was 16 and 13 *mm*, in samples G1 and G2, respectively.

The analysis on the samples consisted of: erosion tests, fluids characterisation and suspended matter concentration (for the sediment laden fluid resulting from erosion tests); chemical composition of the sediments and particle sizing. It was also determined the estuary water salinity. The erosion tests were carried out in the field, immediately after collection. Because they were made at different levels of bed erosion for both samples, the suspended matter concentration is different in both cases with implications on their physical properties.

The sediment particle size was measured on the samples G1 and G2 and also on two small samples collected further away: at mid shore (around 500 *m* from the shoreline) and at low shore site (close to the low tide water mark). The macroscopic mud configuration of the mid shore site is characterised by surface irregularities (ridges and troughs) of around 10-20 *cm*; in the troughs the water is trapped for most of the low tide cycle and the sediments remain soft, not drying out to the same extent as on the ridges.

5.6.2 WESTERSCHELDE ESTUARY

The Westerschelde survey was carried out in April 2001. During this field campaign, various sediment samples were collected at top shore site: two samples on the mini flumes (W1 and W2); one sample to determine the water content at various depths (at 2 and 4 *mm*); five small samples, at different depths (2, 4, 6, 8 and 10 *mm* from the top layer) to determine the particle sizing. The weather was dry and cold. The sediment thickness at the estuary was lower than that in the Gironde.

Sample W1 was subsequently used for LDA measurements and sample W2 was used for erosion tests. Similarly to the Gironde estuary, a full characterisation of the fluid resulting from erosion tests was carried out. A chemical analysis on the sediments was also made as well as the estuary water salinity. All measurements were carried out in laboratory and, due

to transport requirements, a time gap of two days was necessary. Apparently, both samples were muddy and very cohesive.

5.6.3 CÁVADO ESTUARY

The Cávado survey took place for a period of three and half years, between November 1999 and June 2003. During this period, 11 field trips were carried out, at least, and for each one, two samples were collected in the mini flumes.

In a general way, in each field trip the estuary water salinity was determined. Erosion tests were carried out only on the early surveys, in order to assess their properties. The last four field trips were made at different seasons, to investigate the influence of the season on the sediment properties. For that, a more detailed analysis was made on the sediment. In each one of these trips, one sample was collected close to the water and another further away, approximately in the same place as the previous season. In this manner, the tests may be comparable.

A time gap of 3 hours occurred between the sample collection and the laboratory analysis.

Table 5.17 summarises the different tests made to the Cávado estuary samples.

Table 5.17- Samples identification and respective tests carried out

Sample	November 1999		May 2000		August 2000		December 2000	September 2001		October 2002	
Test	C1	C2	C3	C4[1]	C5	C6[2]	C7	C8	C9	C10	C11
Erosion tests	✓	✓	✓		✓		✓	✓			
Concentration and fluid characterisation	✓	✓			✓		✓	✓			
Chemical sed. analysis	✓							✓			
Particle sizing		✓							✓		✓
Sediment water content									✓	✓	✓
LDA tests									✓		✓

1 Sample used as a mould to rough bed number 1 (RB1)

2 Sample used as a mould to rough bed number 2 (RB2)

Samples C2 and C11 were collected at some distance from the river water, while all the others were collected close of it. In addition, during the erosion tests on samples C1, C2 and C3, flow visualization was carried out using the high speed video camera.

Sample C7 was collected on a very rainy day and, because of that, the water level was high at "low tide". The collection site was at a long distance from the usual river bed and the sample appeared very sandy. A similar weather pattern is associated to samples C8 and C9 that had to be also collected away from the water and, for that, presented a large content of sand. It was observed a low quantity of mud at the estuary surface, of small depth, if existent.

It must be stressed that other attempts to sample the Cávado estuary between December 2000 and September 2001 proved to be unsuccessful because of the extreme wet weather during the Winter of 2001 (it rained exceptionally all the period from November 2000 through April 2001). Frequent storms and floods depleted completely the top sediment surface rendering useless any samples collected on that period.

When samples C10 and C11 were collected, the quantity of mud on estuary was much higher than before, with sample C11 (away from the water) without any granules of sand. In this case, the mud was not very consistent, was deep, hydrated. Sample C10 was collected closer to the water, where the mud was somewhat consistent, only a few centimetres thick.

The samples collected after October 2002 are presented in Table 5.18. They were sampled at different seasons, except those at 6th December 2002.

Table 5.18- Samples identification at different seasons

Date	3rd December 2002		6th December 2002		February 2003		April 2003		June 2003	
Sample	C12	C13	C14	C15	C16	C17	C18	C19	C20	C21

Both samples C14 and C15 were collected close to the water and used for LDA measurements, for studying the influence of surface waves. All the other samples were used for: sediment water content; sediment salinity; particle sizing; chemical analysis to the sediment (to samples C13, C17, C19 and C21, only) and LDA tests. It was measured the temperature of the sediment, water and air, as well as the sediment pH.

Samples C12, C14, C15, C16, C18 and C20 were collected close to the water while the others were sampled further away.

Samples C12 and C13 have shown similar characteristics as samples C10 and C11. The quantity of sand in the estuary increased again for samples C16 and C17 (collected in dry days). The sample closer to the water (C16) was collected a little further away because of the sand. There was only around 1.5 *cm* of mud and it was very consistent. Further away, the sediment was much wet and soft, so it was impossible to sample exactly in the usual place. Therefore, sample C17 had to be collected at its vicinity, where sand was present (whose size was larger than usual in that region).

As far as samples C18 and C19 are concerned, it must be referred that it rained heavily in the days before collection. The estuary presented again much sand (close to the river water) and a non plane surface. As opposite, when sampling C20 and C21 the weather was hot and dry. Large quantities of sand were, once again, present even far from the water,

and a non uniform surface observed. Sample C21 (far from the river) was collected at the vicinity, where other sediments presented a lower percentage of sand. It was also observed the presence of grass on the sand and in the river water.

The physical aspect for each sample is summarised in Table 5.19.

Table 5.19- Physical aspect of each sample

Sample	Physical aspect
C12	Slightly cohesive and muddy
C13	Muddy and cohesive
C14	Slightly cohesive and muddy
C15	Slightly cohesive and muddy
C16	Slightly muddy at the surface layer and sandy below
C17	Muddy, with some sand at surface and very sandy below
C18	Very sandy and non cohesive
C19	Slightly cohesive and muddy
C20	Sandy and non cohesive
C21	Muddy, with some sand

Samples close to the river water were always collected first, although the water drainage was higher because sampling took place generally in a slope. Those collected further away were able to retain the water (as this may be observed in Figure 4.4) for longer periods.

5.7 PHYSICAL AND CHEMICAL CHARACTERISATION

In order to accurately study the erosion mechanism and due to its complexity (because of the simultaneous contribution of various factors), it is of crucial importance the evaluation at controlled conditions.

A comprehensive characterisation of the real physical process in the vicinity of an estuary sediment was undertaken. Based on the flow visualization in natural mud (erosion tests) and on the physical and chemical characterisation of the fluid and the sediments, then it was possible to duplicate the real conditions in laboratory.

5.7.1 WATER SALINITY IN ESTUARIES

The water salinity of the three estuaries was measured for every one the samples collected. This parameter was determined using the same procedure as the sediment salinity determination, by previously filtering the water.

It is important to refer that the average ocean salinity is 35 *ppt* (3.5 *%*). This value does vary, usually between 32 and 37 *ppt*, depending on rainfall, evaporation, river runoff, and ice formation. Freshwater salinity is usually less than 0.5 *ppt*, while drinking water has to have a salinity below 0.2 *ppt*. Estuaries, where fresh river water meets salty ocean water, exhibit a water salinity typically between 0.5 and 17 *ppt* (www.cwr.uwa.edu.au/).

Figure 5.15 presents the comparison of water salinity to the three estuaries.

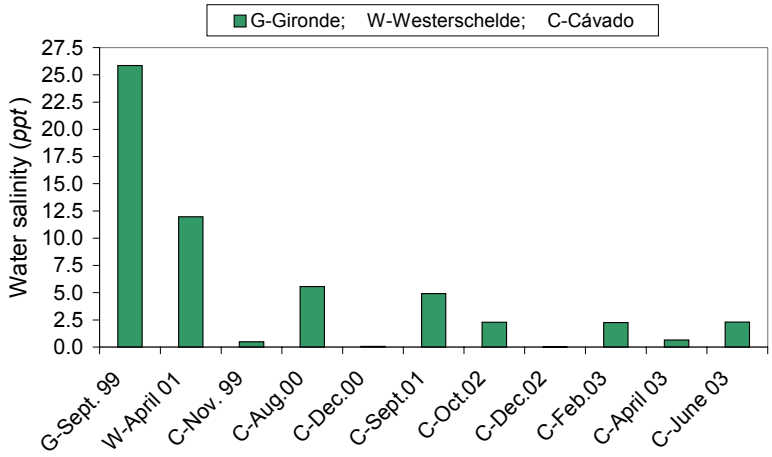

Figure 5.15- Water salinity results

It is observed that the water salinity is much lower in the Cávado estuary. This fact could be related with the location of the sampling site further inland. On the other hand, this estuary shows higher water salinity in Summer, possibly due to lower rainfall in that period. Furthermore, the water samples collected in December present a very low percentage of salt because of continuous rain. The same may hold for samples collected in April.

5.7.2 EROSION TESTS

This section presents the results on the sediment erosion on a sample from the Gironde estuary (G2). These results were used to define the erosion Reynolds number, which were subsequently used in the simulated bed experiments. The results concerning sample G1 and those from Cávado and Westerschelde estuaries are presented in Annex C.

The sediment samples were eroded, using the rheometer, at increasing velocities, in the circular mini flume. From these tests, it was possible to infer the speed at which erosion would occur, in addition to an estimation of the stress levels in the bed.

By recording the erosion process with the help of a high speed movie, it was possible to observe the details concerning the transport of sediment matter into the moving liquid. This enables the assessment of the onset of erosion and the visual identification of the local mechanisms relevant for sediment break up.

During this process, it was observed that, in general, erosion initiates in locals where strong recirculation patterns are visible, and, once the process is initiated, the growth of the eroded cavities coupled with the presence of suspended matter drives further the erosion of the sediment. Close to the outer wall of the flume, erosion seems to occur faster. It appears that local turbulent structures are a key physical factor. The sediments are entrained into the moving fluid, increasing its concentration with time. In this way, the amount of sediment eroded may affect the rheological properties of the fluid.

It was possible to observe that the onset of erosion would occur at a Reynolds number of approximately 20,000 and at Reynolds number close to 40,000 the bed was completely eroded. In addition, the onset of erosion appears to be affected by the local sediment shape and roughness, and it occurs systematically near the outer edge of the cross section. For this particular flow configuration, the reasons for such pattern will become evident in the subsequent chapters.

The flume torque was measured, assuming the geometry Z1 DIN in the rheometer. Figure 5.16 shows the torque measured in the flume, to the above referred sample.

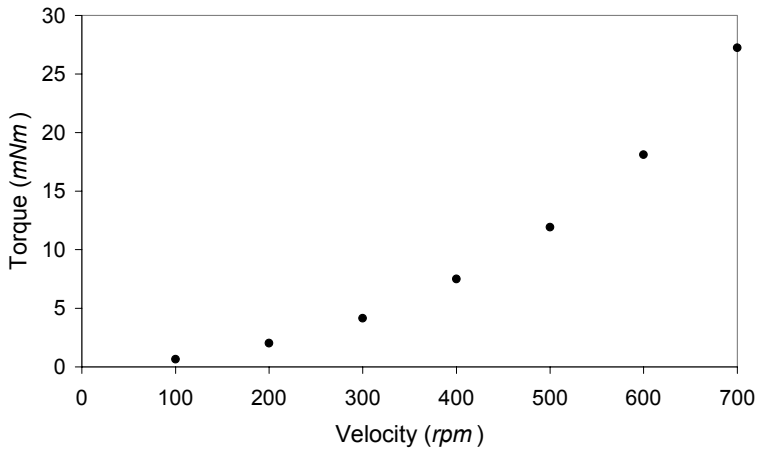

Figure 5.16- Torque *versus* velocity

The onset of erosion is linked to a shift in the slope of the torque/velocity curve, since a linear torque variation would indicate no entrainment of the sediment particles. This is in line with the visual evidence recorded by the camera.

5.7.3 FLUIDS CHARACTERISATION

In this section the fluid viscosity was measured, to be used in the simulated beds.

Considering, from Figure 5.16, that the critical velocity is approximately 250 *rpm* and knowing that the gap thickness between the mud and the lid (t_g) is 13 *mm*, a rough estimative of the critical shear stress (τ_{cr}) can be made. This variable is given by Equation 5.24, that depends on the type of sediment and the gap.

The sediment laden fluid, resulting from a complete destruction of the sediment (sample referred in section 5.7.2), was measured using the rheometer, coupled with the measuring Z1 DIN geometry.

For this sample, the suspended matter concentration (*c*) is 191.8 kg/m^3 and the fluid density (ρ_f) is 1,076 kg/m^3.

Regarding the rheology of that fluid, the viscosity (μ_f) is approximately 3×10^{-3} *Pa.s*, as shown in Figure 5.17. That shows the results concerning the apparent viscosity at increasing shear rates ($\dot{\gamma}$).

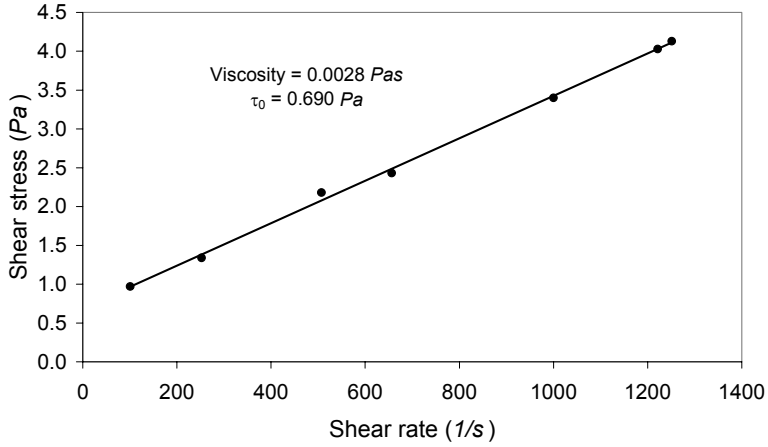

Figure 5.17- Viscosity of the fluid

The viscosity is given by the slope of the curve.

Assuming a linear velocity profile, the critical shear stress would be:

$$\tau_{cr} \propto \mu_f \frac{U_{\max} - 0}{t_g} \tag{5.24}$$

where $U_{\max}$ is the maximum velocity of the fluid (as referred in Equation 3.17), which was considered to occur at the top of the flume and at half distance between both rings, yielding a value of $\tau_{cr} \approx 0.283$ *Pa*. This value is of the right order of magnitude for cohesive sediments (Graham *et al*., 1992; Williamson and Ockenden, 1996; Tolhurst *et al*., 1999).

From Figure 5.17, it may also be concluded that the sediment laden fluid appears to be a Bingham type fluid:

$$\tau = \mu_f \dot{\gamma} + \tau_0 \tag{5.25}$$

being τ_0 the Bingham parameter.

It must be stressed that, although this fluid exhibits a Bingham type behaviour (this is the case of very fine suspended matter), for the samples taken from other two estuaries the sediment laden fluid has a Newtonian behaviour (see Annex C). Le Hir *et al.* (2003) also found that, based on data from the Gironde estuary, highly concentrated suspensions with fine sediments become non-Newtonian, exhibiting a viscoplastic behaviour, very close to a Bingham type.

As referred by Torfs (1995), mud is a thixotropic material (with rheological properties varying with time) and the rheological behaviour of cohesive sediments is strongly dependent on the sediment concentration.

These rheology tests were also carried out at University of Porto (FEUP), using the rheometer Physica Rheolab MC 100. This rheometer enables the measurements over a wider shear rate range.

Because the suspended sediment fluids resulting from erosion tests have a high concentration, it is possible that they settle inside the measuring *cup*, becoming this rheometer not entirely adequate for such type of fluids. A capilar rheometer would probably be more accurate.

Care must be taken because of the instabilities that occur in the annulus of the two concentric cylinders of the rheometer, leading to a more complex pattern. These instabilities are vortices of alternate opposite directions that circulate in that space, always in the outer side of the rotating *bob*, because of the centrifugal forces. Each vortex extends toroidally around the annulus, being the overall flow axisymmetric. These vortices are known as Taylor vortices or Taylor cells (White, 1986; Tritton, 1988).

This effect causes an increase in the apparent viscosity value measured by the rheometer, above a critical velocity, that is easily calculated for each fluid, from the determination of the Taylor number, Ta (Schlichting, 1979):

$$\mathrm{Ta} = \frac{u_i w_g}{\nu} \sqrt{\frac{w_g}{R_i}} \tag{5.26}$$

in which u_i, w_g, R_i and ν are the peripheral velocity of the inner cylinder, the width of annular gap, the radius of the inner cylinder and the kinematic viscosity, respectively. The flow becomes unstable if Ta ≥ 41.3 (with Taylor vortices), and is considered a laminar Couette flow if Ta < 41.3.

In this work, and taking distilled water at room temperature, the critical velocity was 230 *rpm*, corresponding at a Reynolds number of 283. This means that all viscosity values measured at higher shear rates must be discarded (see Annex D). However, if Ta > 400, the flow is considered turbulent. For the same fluid, these conditions take place at velocities above 2,227 *rpm*, which corresponds to a Reynolds number of 2,740.

5.7.4 CHARACTERISATION OF THE MUD SAMPLES

The chemical composition, the particle size, the water content and the salinity of the sediment are shown in this section. As an example, a comparison of the results obtained in

the Cávado estuary will be presented for each analysis, at different seasons (samples in Table 5.18, except those collected by 6th December 2002). The results are compared throughout the year in order to evaluate the seasonal effects. The full set of results as well as those concerned to the other two estuaries are detailed in Annex C.

Table 5.20 presents the sediment temperature ($T_{sed.}$) and pH for each one of the samples. The temperature of estuary water (T_{water}) and air (T_{air}) is presented for all seasons in Table 5.21.

Table 5.20- Sediment temperature and pH

Sample	C12	C13	C16	C17	C18	C19	C20	C21
$T_{sed.}$ (ºC)	12.5	12.5	9	11	14	15	17	19
pH	5	6	6	6	7	7	7	8

Table 5.21- Temperature of water and air in each season

Season	Autumn (December 2002)	Winter (February 2003)	Spring (April 2003)	Summer (June 2003)
T_{water} (ºC)	13	10	14	18
T_{air} (ºC)	12	8	17	17

Chemical composition

Figure 5.18 shows the chemical composition for all the sediments collected in the Cávado estuary.

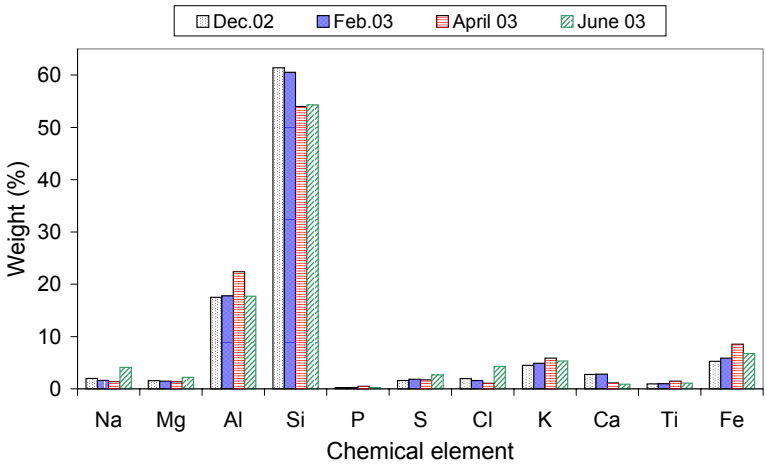

Figure 5.18- Chemical composition of the sediments for different seasons

Particle sizing

The determination of the particle size is an important parameter in sediment characterisation. This data was set as a basis for the specification of the glass/polymer spheres used to replicate in the laboratory the size distribution of such particles.

The particle size distribution in the sediments (top 2 *mm* layer) is presented in Figures 5.19 and 5.20, for samples collected close to the river water and for those collected further away, respectively.

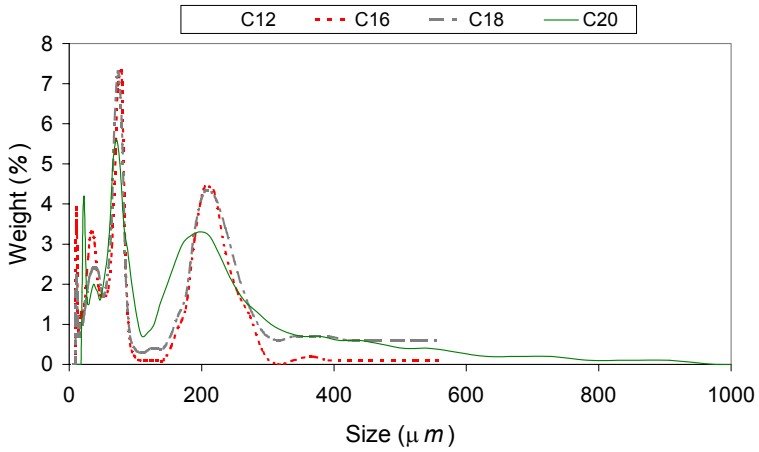

Figure 5.19- Particle size of the sediments (close to the water)

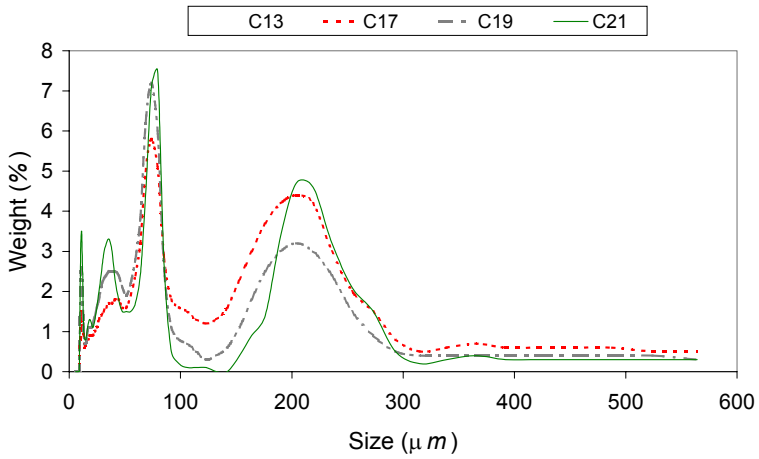

Figure 5.20- Particle size of the sediments (away from the water)

The results from each one of the samples were obtained using appropriate focussing lens being of 300 *mm* in focal length, except for sample C20, where a 600 *mm* lens was used, in order to adjust the dynamic range of the instrument.

From this data, the average diameter (d_{32} - Sauter mean diameter) is shown in Tables 5.22 and 5.23, respectively.

Table 5.22- Sauter mean diameter: samples close the water

Sample	C12	C16	C18	C20
d_{32} (μm)	40.13	32.20	40.86	55.16

Table 5.23- Sauter mean diameter: samples away from the water

Sample	C13	C17	C19	C21
d_{32} (μm)	35.34	48.95	37.47	34.29

Soulsby (1997) presents a classification of the sediments as a function of their grain size. According to the author, mud includes clays and silts, having an average grain size less than 63 μm. The range size for sand is between 63 μm and 2 *mm*, and above that value it is considered gravel. The cohesiveness of the sediments depends on their composition: they are cohesive or non cohesive if they are composed by mud or sand, respectively (Mitchener and Torfs, 1996). Table 5.24 shows the percentage of mud for each Cávado sample (on the top 2 *mm* layer).

Table 5.24- Mud percentage to Cávado samples

Sample	Mud (%)
C12	47
C13	54
C16	53
C17	34
C18	43
C19	47
C20	38
C21	50

It must be stated that the mud composition was silts, without clay (the minimum particle size was above 4 μm). Also, according with Soulsby (1997) classification and taking into account the maximum particle size, the largest particle found in all samples was coarse sand (the remaining of the sediments composition in percentage was: very fine, fine, medium and coarse sand). Results obtained in other estuaries are shown in Annex C

(Tables C.4 and C.5). For the Westerschelde estuary, the percentage of mud was found to be above 90 % and the maximum particle size was a very fine sand. For the Gironde, that percentage was around 90 % at top and mid shores and only 3 % to low shore (being found, in this case, very coarse sand).

Taking into account the conclusions found by Mitchener and Torfs (1996) in mud/sand mixtures experiments, where a cohesive behaviour of sediment is obtained when more than 15 % mud by weight is presented, it was supposed that all samples collected in the three estuaries (except at low shore in Gironde) present a cohesive-type behaviour. However, this may not be appropriate to the present research, because in the Cávado samples sediment grain size is not uniform in depth, and these mud percentages are referred to the top 2 *mm*, only.

One conclusion that may be taken from this data is that the grain size on natural sediments varies over a wide range: from micron size particles up to the millimetre. This observation is also in agreement with the other samples.

Comparing Figures 5.19 and 5.20, the size distribution is similar presenting both a maximum for particles around 80 μm, a minimum around 123 μm and then other maximum at approximately 200 μm. However, for the samples collected closer to the water, the particles are bigger than to the others one. This is also shown in Tables 5.22 and 5.23 by the average Sauter mean diameter. Surprisingly, the opposite takes place for samples collected in February. This is due the presence of sand, as explained before.

Regarding the seasonal effects, the results show the presence of large quantities of sand which result from the occurrence of rain prior to sampling. As referred, sample C13 had no granules of sand, which justifies the lower percentage of big particles. On the other hand, sample C20 has the highest percentage of those particles because of the sand.

Water content

The water content in the sediment is mostly dependent on the time elapsed between the sampling moment and the receding tide. The comparison between the various samples at different seasons could be affected by this factor. In addition, the sediment water content depends on the ease of the water drainage, which is different for both places where sampling was made. The sediment cohesion and consistence is related to the water content.

The water content on the sediment was measured for the two top layers of 2 *mm* thick in all samples. The results are presented in Figure 5.21.

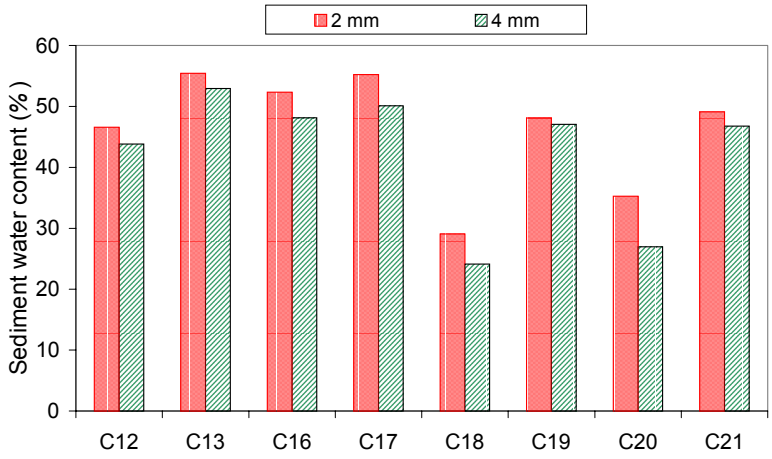

Figure 5.21- Sediment water content

Figure 5.21 shows, as expected, a higher percentage of water at the sediment surface. Furthermore, samples C13 and C17 show a higher value because, apparently, the sediments were very hydrated, presenting low consistence. Because both samples were collected in different weather conditions (rain), this means that this analysis is not related with the rain before sampling. On the other hand, C18 and C19 were sampled in the same day and show a very different percentage of water.

Furthermore, those samples collected far from the river water present always a greater water content. This is probably due to the local shape of the sediment flat, which may yield a delayed water runoff during the tide receding (see Figure 4.4).

A salt correction was not applied once the error for sediments having low void ratios is negligible, being important for fine-grain marine soils, only (Noorany, 1984), and Cávado samples are usually sandy.

Salinity

The sediment salinity is shown in Figure 5.22.

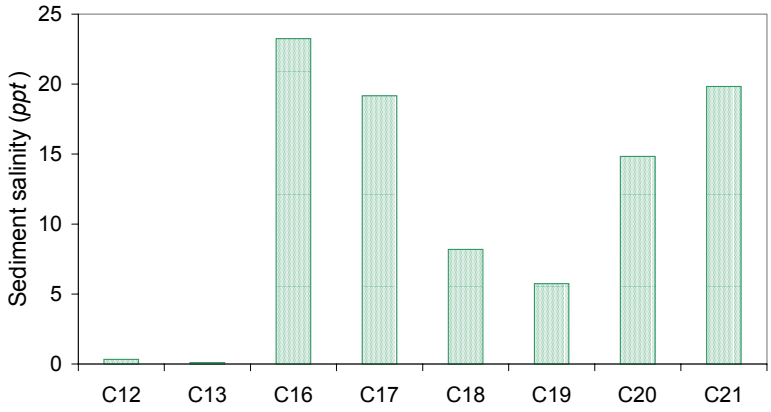

Figure 5.22- Sediment salinity

Figure 5.22 shows that the sediment salinity is very low for samples C12 and C13 (collected in December 2002), which is in agreement with the nearly non existent water salinity observed in Figure 5.15 for this month (the three samples were collected in the same day). In a similar manner, the sediment salinity is affected by the occurrence of rain before sampling. Therefore, samples C18 and C19, that were sampled in April 2003 after a long spell of rainy days, present low salinity. Again, this is in agreement with the water salinity for this month.

Also, as a general rule, the sediments collected away from the river bed show a lower percentage of salt (C13, C17 and C19).

5.8 TESTS CONDITIONS

Firstly, the LDA was tested in water flow, in order to define correctly the optical and processing setup and to get used with the data acquisition and processing facilities. Furthermore, it provided a reference data basis for the more complex measurements.

This section reports the most relevant conditions for all of the testing programme.

5.8.1 TESTS IN SIMULATED BEDS

The simulated beds include aspects such as the surface roughness, the presence of entrained particles, and a deformable two-fluid bed. The influence of surface waves effects are also investigated. All tests were carried out under controlled laboratory conditions.

The natural fluid, as it was characterised, is basically a muddy suspension of water, which is not very easy to use for laser velocimetry measurements. Therefore, some effort was invested into finding a substitute fluid that would be physically similar to the natural

system and, at the same time, be optically suitable for LDA measurements. Based on the sediment analysis and on the physical characterisation of the sediment laden fluid, a low viscosity fluid was used. In order to fulfil these requirements, an aqueous solution of glycerine was used as test fluid (concentration of 366.2 kg/m^3), which properties are presented in Table 5.9.

Tests were carried out at three Reynolds numbers, covering different stages of the erosion process: starting with stable bed, at Re = 10,000, going through the erosion initiation, at Re = 20,000, up to a completed eroded bed, at Re = 40,000. The Reynolds number is defined as:

$$\mathrm{Re} = \frac{d_h U_{\max} \rho}{\mu} \tag{5.27}$$

where d_h is the hydraulic diameter, ρ and μ are the density and the viscosity of the fluid.

Surface roughness effects

The relevance of bed roughness in the sediment erosion became evident from the tests with a high speed video camera. These experiments have shown that the bed topology affects the local flow patterns and, therefore, the erosion process. The existence of cavities and saliencies lead to the occurrence of recirculation pockets in its vicinity with high local shear stresses, which strongly contribute to the onset of erosion. Furthermore, once erosion is initiated, the bed cohesiveness is reduced, surface irregularities are enhanced leading to a larger recirculation vortices (and shear rates). In brief, the whole process becomes self-sustainable.

To simulate the bed roughness, two models were constructed (RB1 and RB2) as described in section 5.5.1. They have a mean roughness height of 0.571 and 0.512 *mm*, respectively. Figures 5.23 and 5.24 depict the mapping of the surface, for both models, obtained using data taken from a high precision coordinate measuring system (Mitutoyo, BHN 706). It is important to mention that although the roughness (as an average value) does not differ in great amount between the two surfaces, the local details and the shape of the surface are different.

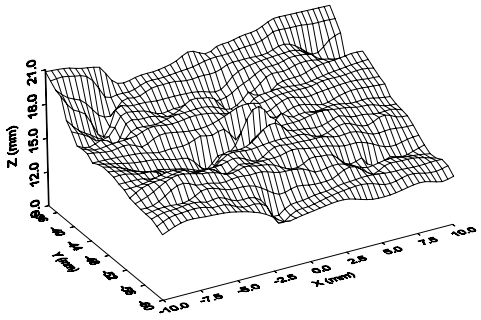

Figure 5.23- Surface map (RB1)

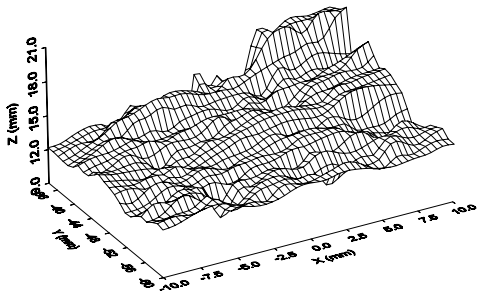

Figure 5.24- Surface map (RB2)

Experiments were carried out on a smooth bed (SB), consisting of a smooth PVC plate, and the two rough surfaces, at the different Reynolds number. The gap inside the flume was 49 and 34 *mm* for beds SB and RB, respectively.

The grid used in these experiments was built defining four regions with different increments, according to the interest of the measurements. Thus, the grid on both regions close to the bottom and external walls was more refined, which correspond to the regions of higher gradients. The grid is represented in Figure 5.25 (distances are shown in *mm*).

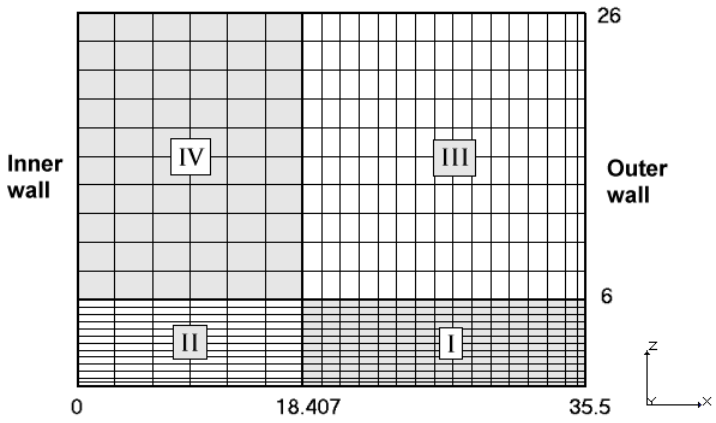

Figure 5.25- Grid used for measurements

The increments (x; z) for regions I, II, III and IV are, respectively: (1; 0.5), (2; 0.5), (1; 2) and (2; 2).

Concerning the data collection, the number of validated samples was set 3,000 and the measurement interval limited to 50 *s*. The data rates obtained were in the range of 200 *Hz* and the data validation was above 95 *%*.

A test was conducted at Re = 2,000, on a smooth bed and with a solution of glycerine, in order to compare with the numerical solution at low Re.

Effects of particle dispersion and entrainment

For a better understanding of the physical mechanisms leading to bed erosion, the investigation of the influence of entrained particles upon the flow configuration is of great importance, not only on the initial stages but also in the latter stages when a significant amount of matter has already been entrained into the carrier fluid.

The basic rational for this study is that it is known in other flow configurations that the turbulent structure is modified by the presence of suspended particles as well as surface irregularities. For this purpose, a range of mono-dispersed polymeric (for lower sizes) and glass beads of various sizes and densities were tested over the smooth surface of the flume. Depending on particle size and concentration, the flow field may be modified by the energy exchanges between the continuous and dispersed phases resulting from particle transport.

The size choice was based on various factors: results of particle sizing range on mud samples, as reported in section 5.7.4; commercial availability and feasibility. Thus, very small particles are most likely to follow fluid turbulence and their contribution will be difficult to assess. Furthermore, they will be easily entrained into the fluid and a homogeneous solution will be formed; light penetration will be reduced and measurements made difficult.

Combining these factors, tests were carried out using different size ranges and densities, as summarised in Table 5.25.

Table 5.25- Ranges of particle size and density

Particles	Range (μm)	Density (kg/m^3)
Polymer micro spheres (P1)	250-750	1,050
Glass beads (P2)	850 - 1,400	2,600
Glass beads (P3)	1,400 - 1,700	2,600
Glass beads (P4)	1,700 - 2,850	2,500

Due to the density difference between the liquid and the particles, when the liquid is stationary, a layer of particles is formed at the bottom. By setting the fluid in motion, the flow drag deforms the bed and moving “dunes” are formed on the bed. This configuration acts both as a moving (deformable) non cohesive bed and as a suspension because bed deformation occurs by the movement of the top layer of particles, entrained into the moving liquid and deposited further downstream.

Such mechanism for bed deformation is depicted in Figure 5.26. Because LDA is a point measurement technique, for this particular flow configuration, velocity statistics have to be related to the relative position to the moving bed. Thus, measurements were carried out, at each point, over a period of time long enough to span at least the entire rotation period of the deforming bed. At each point above the surface, the experiments were initiated at the same relative position to the bed, in order to synchronize all the measurements with the deforming bed.

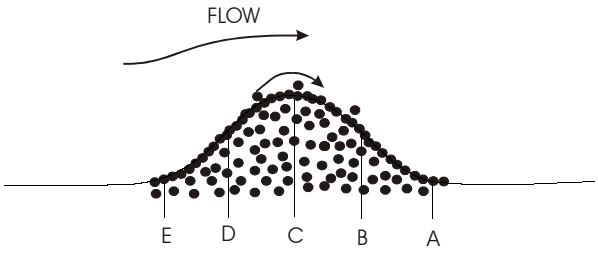

Figure 5.26- Measuring positions along the dune length

In order to keep the particle/fluid density ratio close to that observed with the other particles, experiments with the smaller beads (P1) were carried out using ethyl alcohol as fluid as opposed to the aqueous solution of glycerine. Reynolds numbers were also matched at 20,000.

Experiments were carried out at Reynolds numbers of 20,000 and 40,000. Data were collected at x = 28 *mm* (Figure 5.25), measuring a profile along a vertical line, from the basis of the dune up to around 10 *mm* above the crest. This position was selected because, from experimental evidence, it is the flume location where higher shear stresses are measured (by LDA) and is visually observed by erosion initiation. In all the experiments, the particle concentration was set at 326 kg/m^3. It was assumed that the density and viscosity of the fluid is not affected by the presence of the beads.

In order to compare with results obtained with the rough beds mentioned, the larger beads (P4) were also tested at low Reynolds number (Re = 10,000), ensuring the total absence of movement of these beads, producing an entirely non deformable surface. In this way, a third alternative for a rough bed (made by the beads) was considered (RB3). This configuration is a traditional alternative for surface roughness research (sand roughness) and differs from the previous two rough beds on two counts: a) it is a regular roughness; b) the internal porosity of the surface is maintained.

Table 5.26 presents the density ratio of the beads to the carrier fluid.

Table 5.26- Density ratio of the beads and the fluids

	P1	P2 and P3	P4
Density ratio	1.329	2.416	2.323

The amplitude ratio is given in Figure 5.27 in function of the fluid eddy frequency, to the various types of beads employed (referred to their minimum on the range size).

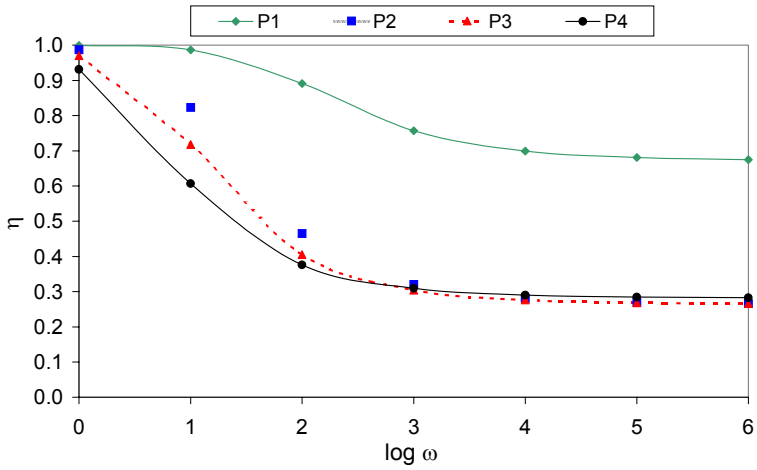

Figure 5.27- Amplitude ratio for the different beads

As referred in section 5.2, the corresponding value for $\log\omega$ was 1.79 and 1.28 on tests using a solution of glycerine and ethyl alcohol, respectively. Therefore, in such conditions only the beads P1 are easily dragged by the flow.

Figure 5.28 shows the maximum diameter of particles P1 to follow the flow properly, at $\omega = 18.89$ *rad/s*.

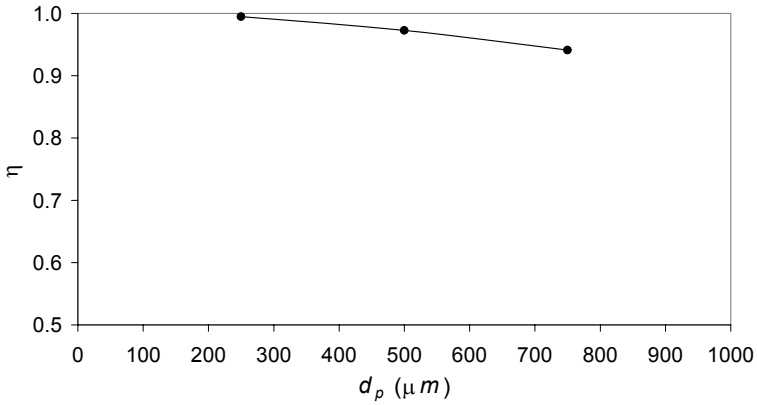

Figure 5.28- Effects of the beads P1 size on the amplitude ratio

As observed in Figure 5.28, particles P1 with a diameter below 700 μ*m* are good fluid followers.

Surface waves effects

In free surface flows, waves are generated by wind shear. The interaction of this motion with the main flux may modify the flow structure in the vicinity of the sediment and, therefore, the local shear stresses.

In order to evaluate the influence of various waves parameters, four lids with various combinations of amplitude/wavelength were built and attached to the flat lid at the top of the flume in order to artificially induce a wavy motion to the fluid upper surface.

Table 5.27 presents the main characteristics of the four lids.

Table 5.27- Geometric characteristics of the lids

Lid reference	Number of waves (*p/cycle*)	Amplitude (*mm*)	Wavelength (*mm*)
L1	4	10	75
L2	2	10	150
L3	4	5	75
L4	2	5	150

Tests were carried out over both a smooth and a rough bed, and also adding suspended particles into the flow. As in previous tests, an aqueous solution of glycerine was used and the flow field was characterised at Reynolds numbers of 10,000, 20,000 and 40,000 (for lids L3 and L4 Re was set at 20,000). The hydraulic diameter was determined calculating the average gap from the wavy lid to the bottom. The data grid was the same as in the roughness tests.

Multiple factors

The experimental analysis was extended by combining the effect of surface waves with other parameters previously investigated, such as the sediment surface and the presence of suspended matter.

Roughness and surface waves: In order to evaluate the effects of surface waves over a rough surface on the velocity field, and consequently on the turbulence, tests were carried out by combining bed RB1 with lid L1 and at Reynolds number of 10,000, 20,000 and 40,000.

The data grid was the same as previously described (in the roughness tests).

Particles and surface waves: Another relevant component for this study is the evaluation of the influence of the transport and deposition of suspended particles by surface waves, upon the flow field. Thus, beads P3 and lid L1 were combined at Reynolds numbers of 20,000 and 40,000. Data was taken at the usual position $x = 28$ *mm*.

Deformable two-fluid bed effects

Another possible implementation in laboratory of an artificial bed is by the simultaneous use of two non miscible fluids: a non-Newtonian at the bottom and a Newtonian on top of it. It was assumed by other investigators (Jones and Hughes, 2001) that the cohesive sediment bed is a non-Newtonian fluid, which has been simulated using a solution of benecel, and the flowing overlying layer is a Newtonian fluid.

The non-Newtonian fluid was an aqueous solution of benecel (at 3 *%* p/v) and was 2.3 *cm* in height, while the Newtonian fluid was a layer of oil, of approximately 3 *cm* in height. The oil is transparent, lightly yellow, which physical properties have been presented above, as well as its refractive index compensation. The solution of benecel has a density around 1,000 kg/m^3 and a very high viscosity. This is a purified product of methylcellulose, among others, being used in food and pharmaceutical products. Its functional properties include, for example, water retention, binding, emulsifying; for a solution concentration of 2 *%* at 20 ^oC the viscosity range is 3.8-5.7 *Pa.s* (Hercules Inc., Product Data- Aqualon, 1995).

Measurements were carried out in a vertical line located, again, at approximately 7.5 *mm* from the outer wall of the flume (x = 28 *mm*), at Re = 2,500 and from the fluids interface, up to 10 *mm* above.

Summary

A summary of all experiments performed in simulated beds is presented in Table 5.28.

Table 5.28- Experimental plan with simulated beds

Re / Simulated bed	2,000	2,500	10,000	20,000	40,000
SB	✓		✓	✓	✓
RB1			✓	✓	✓
RB2				✓	
RB3			✓		
SB-P1				✓	
SB-P2				✓	✓
SB-P3				✓	✓
SB-P4			✓	✓	✓
SB-L1			✓	✓	✓
RB1-L1			✓	✓	✓
SB-L1-P3				✓	✓
SB-L2			✓	✓	✓
SB-L3				✓	
SB-L4				✓	
Two-fluid bed		✓			

5.8.2 TESTS IN NATURAL SEDIMENTS

LDA experiments in natural sediments were based on samples taken from both Westerschelde and Cávado estuaries. These samples were tested in laboratory and it was possible to measure the velocity profiles above the natural sediment bed.

Measurements were carried out at various Reynolds numbers, starting at low velocities up to the point that mud erosion is strong enough to generate high turbidity inside the sample. Because of the high light power of the laser source, experiments could be carried out with a substantial quantity of suspended matter. As with other experiments, measurements were taken along a vertical line located at $x = 28$ *mm*. The grid has different increments and was defined as shown in Figure 5.29. The increments were lower close to the bottom (0.25 *mm*), increasing when distance to wall increases (0.5 between 3 and 6 *mm* and 1 above that distance).

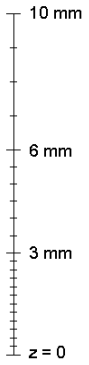

Figure 5.29- Grid points for measurements in natural samples

In the BSA software, 3,000 bursts and a measurement interval of 70 *s* were selected. At higher velocities, the data rates were higher than those obtained using simulated beds and the validation rate was close to 100 *%*.

Prior to any measurement, it is fundamental to measure the correct gap between the sediment surface and the lid, for each sample, in order to calculate the hydraulic diameter. With this parameter the velocity can be adjusted in order to maintain the flow Reynolds number. These procedures were also made in all the tests with simulated beds.

All the measurements in natural beds were carried out on the Perspex flume, with no glass box. This detail was taken into account in the refractive index compensation. After each measurement at a selected velocity, around 50 *ml* of fluid were immediately removed with a syringe, at approximately the same location inside the flume, for subsequent determination of viscosity, density and concentration as a function of the flow shear rate. It was always obtained a viscosity and density close to that of water. As expected, the fluid concentration increased with time.

Sample from Westerschelde estuary

This sample (W1) was analysed around 48 hours after the field trip, due to transportation requirements. The Reynolds number was set at: 3,300; 6,600; 13,200; 20,000; 26,400 and 33,200. The last one was the maximum possible, even though the measurements were limited to the first three positions on the grid. In this sample, the gap between the sediment inside the flume and the lid was 17 *mm*.

Samples from Cávado estuary

The measurements were carried out approximately 3 hours after the field trips. Depending on the type of sample, its physical properties, cohesion, water content and the sampling collection, tests were carried out at different Reynolds number.

Table 5.29 shows the Reynolds numbers tested for each sample.

Table 5.29- Reynolds numbers referent to each sediment sample

Sediment sample	C9	C11	C12	C13	C16	C17	C18	C19	C20	C21
Re = 3,300	✓	✓	✓	✓	✓	✓	✓	✓	✓	✓
Re = 6,600	✓	✓	✓	✓	✓	✓	✓	✓	✓	✓
Re = 10,000	✓	✓	✓	✓	✓	✓	✓	✓	✓	✓
Re = 13,200	✓	✓	✓	✓	✓	✓	✓	✓	✓	✓
Re = 20,000	✓		✓	✓	✓	✓	✓	✓	✓	✓
Re = 26,400	✓		✓		✓	✓	✓	✓	✓	✓
Re = 33,200	✓				✓	✓	✓	✓	✓	✓
Re = 40,000	✓				✓		✓	✓	✓	
Re = 46,500					✓		✓		✓	
Re = 53,000					✓					

The gap size between the sediment bed and the rotating lid is presented in Table 5.30 for the samples from Cávado estuary.

Table 5.30- Gap size for the Cávado samples

Sample	C9	C11	C12	C13	C16	C17	C18	C19	C20	C21
Gap (*mm*)	17	16	15	17.6	23.7	19	19	22	21.5	17

Two mud samples (C14 and C15) were deformed by the action of surface waves, using lid L1 on sample C14 and lid L2 on sample C15. These tests were carried out to evaluate the waves effects on the onset of erosion and subsequent transport of the sediments. The data grid was set as previous and the Reynolds number for both samples were: 3,300; 6,600; 10,000; 13,200; 20,000 and 26,400.

In experiments using sediment samples, a problem of concern is the possibility of entrained particles triggering the LDA. Because such particles are of unknown size, the data may not be representative of the flow field.

In order to assess such ambiguity, it was determined the diameter below which the sediment particles follow the fluid properly. In this way, and considering a eddy frequency of 73.23 *rad/s* (see Table 5.11, for a solution of natural sediments), the influence of the particle diameter on the amplitude ratio is presented in Figure 5.30.

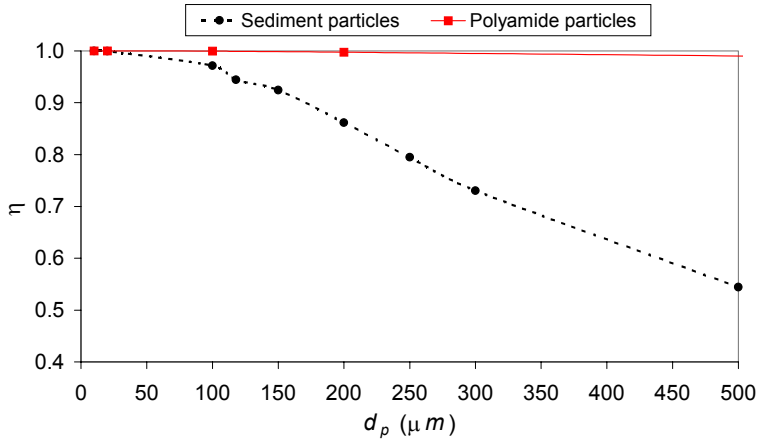

Figure 5.30- Effects of particle diameter on the amplitude ratio

For comparison, the curve to the polyamide particles at these conditions is also shown. From Figure 5.30 it is possible to state that the sediment particles with size lower than around 120 μ*m* follow the fluid adequately. Such particles are 6 times larger than the polyamide tracers. Considering that the largest particles in the Westerschelde estuary are 118 μ*m* in diameter, it was concluded that all of them are good flow tracers.

In LDA measurements, the particle size is limited on the lower side by the minimum intensity detection level (scattered light) and on the upper side by signal saturation in the photodetectors. Knowing that for particles above 2 μ*m* the signal intensity is directly proportional to the particle diameter square (Albrecht *et al.*, 2003), those at 120 μ*m* scatter light 6^2 times than the tracers. In this way, and since all the conditions on BSA's where optimised for the polyamide particles, giving a good signal, all the other particles with the size above will saturate the signal, being automatically excluded. On the other hand, the very small sediment particles will not be detected by the LDA. However, those which size is close to that of the polyamide particles behave as natural seeding. There are around 2.2 % of sediment particles which size is exactly the same as the polyamide, and their smallest size is 6.48 μ*m* (2 %). In this range there are around 54 % of particles.

CHAPTER 6

FLOW CHARACTERISATION IN A SMALL DIAMETER FLUME

In this chapter, a detailed description of the fluid behaviour in toroidal mini flumes is carried out. Following a brief theoretical discussion, the experimental data of the flow over a smooth surface is detailed.

In addition, numerical results from CFX software are included. Various turbulence models are assessed and the results compared with the experimental data.

6.1 VELOCITY PROFILES IN TURBULENT FLOWS

6.1.1 VELOCITY PROFILES NEAR A SMOOTH WALL

The velocity near the wall is determined by the conditions at the wall (wall shear stress), the fluid properties (ρ and μ) and the distance from the wall (y).

Using "wall" boundary conditions (with normalisation by wall variables), a dimensionless representation of the velocity may be given by:

$$u^+ = \frac{\overline{u}}{u^*} \tag{6.1}$$

in which u^* is the friction or shear velocity, as defined by Equation 3.35.

The dimensionless distance from the wall (y^+) has the form of a Reynolds number:

$$y^+ = \frac{\rho u^* y}{\mu} \tag{6.2}$$

or

$$y^+ = \frac{u^* y}{\nu} \tag{6.3}$$

being ν the kinematic viscosity ($= \mu/\rho$).

The relationship between u^+ and y^+ represents the law of the wall (Sabersky *et al.*, 1989):

$$u^+ = f(y^+) \tag{6.4}$$

and describes the velocity profile inside the boundary layer as shown in Figure 6.1 for a smooth wall (Clauser, 1956; White, 1986; Sabersky *et al.*, 1989; Versteeg and Malalasekera, 1998). The boundary layer is usually split into three regions.

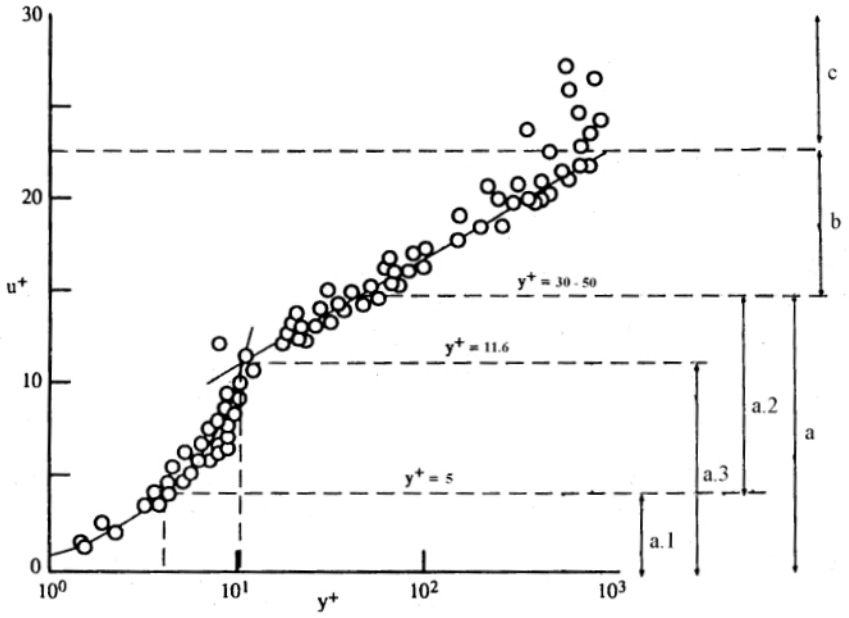

a- *Inner layer* b- *Overlap layer* c- *Outer layer*
a.1- *linear sub-layer*
a.2- *buffer layer*
a.3- *viscous sub-layer*

Figure 6.1- Velocity distribution near a solid wall in a turbulent boundary layer (Clauser, 1956)

- Inner layer

As shown in Figure 6.1, the inner layer includes three sub regions. The region nearest to the surface ("linear sub-layer") follows a linear distribution in which the flow is laminar, and is valid for $y^+ \leq 5$. The data is well approximated by the linear relationship (White, 1986; Versteeg and Malalasekera, 1998):

$$u^+ = y^+ \tag{6.5}$$

In this region, viscous stresses dominate the flow adjacent to the surface. Although the flow is predominantly laminar, it experiences some fluctuations that are generally parallel to the flow. Near the rigid boundary, vertical motions are negligible approaching zero at the wall.

The region between $y^+ \approx 5$ and $y^+ \approx 30-50$ is called the "buffer layer" or transition region. This region provides a smooth transition from the linear sub-layer to the outer region ("overlap layer"). In this region the profile is no longer linear; there are high velocity gradients and the flow is predominantly turbulent, although the viscous forces are too important to be neglected. This layer is also known as the turbulence generation layer in which energy is removed from the mean flow, resulting in the generation of turbulent eddies, and the subsequent dissipation and removal of energy from them. The "buffer layer" includes a level (δ_v) where the viscous and turbulent stresses are equally dominant (at $y^+ = 11.6$). The region below this level is known as the "viscous sub-layer", where the flow is dominated by viscous forces and is laminar (Versteeg and Malalasekera, 1998).

- Overlap layer

This layer is considered in the interval of $30-50 \le y^+ \le 500$, for smooth walls (Versteeg and Malalasekera, 1998), being the value 30 or 50 according to the author (Clauser, 1954). This region is also called the "logarithmic overlap layer" (or log-law) because it follows a logarithmic distribution (Ferziger and Perić, 1999):

$$u^+ = \frac{1}{\kappa}\ln(y^+) + B \tag{6.6}$$

κ is the von Kárman constant ($\kappa = 0.41$ for pipe flow) and B an empirical constant related to the thickness of viscous sub-layer ($B \approx 5.2$ for a flat plate boundary layer). Turbulent Reynolds stress dominate in this region. Because the shear stress varies very slow with the distance from the wall in the region close to the bed, this is also considered a constant stress layer.

The large scale eddies, generated as the Reynolds stress absorb energy from the flow, travel from their point of generation transferring gradually their momentum by a diffusion process. As the eddies travel they loose energy, which is used to generate small scale eddies and subsequently converted into heat. The distance that any eddy travels from its point of generation before it loses its integrity and assumes the mean velocity of its surroundings, is referred as the "mixing length", l (Bird *et al.*, 1976). In a turbulent stream over a smooth wall, in the vicinity of the surface there is proportionality between mixing length and wall distance, y (Schlichting, 1979):

$$l = \kappa y \tag{6.7}$$

Equation 6.6 may also be presented in the following form:

$$u^+ = \frac{1}{\kappa}\ln(Ey^+) \tag{6.8}$$

where E, the log-layer constant, depends on the wall roughness and assumes a value of 9.8 for smooth walls (Versteeg and Malalasekera, 1998).

The depth of this layer is considered to vary between 10 and 20% of the turbulent boundary layer thickness (δ), which is defined as the distance from the surface to the position where $\overline{u} = 0.995u_\infty$, being u_∞ the free stream velocity (Bradshaw, 1971).

- Outer layer

This region is far from the wall, thus inertia forces dominate in the flow, being the log-law not applicable. The velocity ($\overline{u}$) is independent of molecular viscosity, but its deviation from the stream velocity (u_∞) depends on the boundary layer thickness through (Hama, 1954; Krogstad *et al.*, 1992):

$$\frac{u_\infty - \overline{u}}{u^*} = -\left[\frac{1}{\kappa}\ln\left(\frac{y}{\delta}\right) + A\right] \tag{6.9}$$

where A is a constant. This formula is called the velocity-defect law or the law of the wake. Thus, this region is also known as law of the wake layer (Coles, 1956; Versteeg and Malalasekera, 1998, amongst others).

From Equations 6.6 and 6.9, it is possible to obtain the turbulent skin friction law (relating the free stream velocity, boundary layer thickness and viscosity) eliminating $\overline{u}$ and y by subtraction (Clauser, 1956):

$$\frac{u_\infty}{u^*} = \frac{1}{\kappa}\ln\left(\frac{\delta u^*}{\nu}\right) + B - A \tag{6.10}$$

The skin friction is related with the flow resistance and can be given, for a zero pressure gradient turbulent boundary layer over a smooth wall, by (Clauser, 1956):

$$c_f = 2\left(\frac{u^*}{u_\infty}\right)^2 \tag{6.11}$$

where c_f is the local skin friction coefficient.

In addition, the boundary layer may be characterised by both the momentum thickness, ψ (a measure of the drag of the solid body on which the boundary layer has developed), and the displacement thickness, δ^* (the displaced distance by external streamlines normal to the surface), according to Bradshaw (1971). The Reynolds number of the boundary layer can be related to the momentum thickness and the free stream velocity by:

$$\mathrm{Re}_\psi = \frac{u_\infty \psi}{\nu} \tag{6.12}$$

For laminar layers, the following ratios are assumed: $\delta/\psi = 9$ and $\delta^*/\psi = 2.6$. However, for turbulent layers these ratios depend upon the value of the skin friction coefficient (Clauser, 1956).

Experimental investigations in turbulent boundary layers over rough walls show that the turbulence depends on the surface roughness and is different from that on smooth walls (Acharya *et al.*, 1986; Krogstad and Antonia, 1999; Antonia and Krogstad, 2001).

6.1.2 VELOCITY PROFILES NEAR ROUGH WALLS

The effects of surface roughness on a turbulent boundary layer are also important and directly applicable in sediments investigation. In fact, the sediment is made up of particles of different sizes, from rocks to silt, as well as bedforms ranging from dunes to ripples. All these conditions contribute to define the bed roughness, which may affect the velocity profile in the turbulent boundary layer.

In the immediate vicinity of the surface, the mean velocity is determined by the distance y form the wall relatively to the characteristic length scale of the roughness (k_l). Therefore, very close to the surface, the universal law for the turbulent region near the wall becomes (Clauser, 1954):

$$u^+ = \frac{1}{\kappa}\ln\left(\frac{y}{k_l}\right) + C \tag{6.13}$$

C is a constant that integrates the wall boundary condition and, therefore, depends on the roughness geometry.

The major effect of roughness is to change the structure of the boundary layer near the wall, increasing the surface skin friction.

Clauser (1954, 1956) showed that, for a rough wall, the logarithmic region (Equation 6.6) is shifted downwards parallel to itself by an amount Δu^+:

$$u^+ = \frac{1}{\kappa}\ln(y^+) + B - \Delta u^+ \tag{6.14}$$

where $\Delta u^+ (= \Delta u / u^*)$ is the so called roughness function or shift in mean velocity due to the change in wall condition ($\Delta u^+ = 0$ for smooth-wall flows); B and κ are the constants referred in Equation 6.6, for smooth surfaces. Equation 6.14 represents the mean flow at a sufficiently large distance from the roughness elements.

As explained by Krogstad and Antonia (1999), the outer layer wake function in zero pressure gradients should not depend on the surface roughness, because in that region the flow characteristics are assumed to be independent of the surface geometry. Combining Equations 6.13 and 6.14, the downward shift can be expressed as:

$$\Delta u^+ = \frac{1}{\kappa}\ln(k_l^+) + B - C \tag{6.15}$$

in which $k_l^+ = \frac{k_l u^*}{\nu}$, is often referred as the roughness Reynolds number.

Roughness can be classified in various ways. To determine its effect on the boundary layer, parameters such as the mean roughness height ($\bar{k}$), shape, density and manner of distribution (Dvorak, 1969) must be considered. The roughness elements may be discrete or distributed and their geometry may be regular (deterministic) or random (stochastic).

Back in 1950, Nikuradse made a detailed study of the turbulent flow through rough pipes and ever since it is common practice to standardize the effects of a particular roughness in terms of an “equivalent sand grain roughness”. The Nikuradse’s equivalent sand roughness

(k_S) takes into account both the roughness due to the shape and size of the grains, and the roughness related with the size distribution of the sediment and bedforms. Therefore, it is usual to use the term k_S to describe the roughness of a bed, whether it is a mixed or mono-sized sediment and whether it is flat or rippled (Gallagher, 1998). According to Acharya *et al.* (1986), k_S is related with the mean roughness height through:

$$k_S = 1.6\bar{k} \tag{6.16}$$

However, there is a degree of uncertainty in determining this value for a general roughness geometry. The extent to which roughness affects the viscous sub-layer is classified in three regimes, defined by the dimensionless parameter k_S^+ (Schlichting, 1979):

$$k_S^+ = \frac{u^* k_S}{\nu} \tag{6.17}$$

k_S^+ is also known as roughness or grain Reynolds number. If k_S is small when compared to the viscous sub-layer thickness (δ_v), the bed shear stress is controlled by viscous forces and Equation 6.13 becomes valid between δ_v and the upper layer limit of the overlap layer (upper limit of region b in Figure 6.1). In this case, the flow is considered "hydraulically smooth" and the velocity profile above the viscous sub-layer is independent of the bed roughness k_S (the size, shape and pattern of the roughness elements have a negligible effect on the flow structure). Therefore, the velocity profile for smooth walls will apply and is valid for $k_S^+ < 5$.

On the other side, if $k_S > \delta_v$, the Reynolds numbers of local flow around the roughness elements are large enough to generate pressure forces, that are greater than the viscous forces. The viscous sub-layer is therefore completely destroyed and the protruding particles create a turbulent wake and vortices. In this case, the roughness affects the velocity profile and the flow is called "hydraulically rough". This regime occurs when $k_S^+ > 55-70$. Equation 6.13 is valid from an origin at a depth k_S up to the upper limit of the overlap layer and this flow is independent of Reynolds number.

The "transitional rough" regime does not refer to an interface between laminar and turbulent flow across the boundary layer, but to the state of the viscous sub-layer within a turbulent boundary layer over the rough surface. This region corresponds to the range $5 < k_S^+ < 55-70$, whereby the velocity profile is a function of both δ_v and k_S (the roughness elements are slightly larger than the thickness of the viscous sub-layer). The transition to fully rough conditions is not clearly defined, thus it occurs in the range 55-70 for various types of roughness.

Equation 6.13 can be rewritten in a different way, considering the lower and upper boundaries of the overlap layer. The lower limit is referred to a depth equal to either δ_v or k_S (whichever is larger) and the upper limit is the upper limit of the overlap layer. Therefore, it becomes (Schlichting, 1979; Ligrani and Moffat, 1986):

$$u^+ = \frac{1}{\kappa}\ln\left(\frac{y}{k_S}\right) + B_S \tag{6.18}$$

being B_S a dimensionless constant to maintain dimensional equilibrium, which depends on the roughness Reynolds number (k_S^+) and on roughness-geometry characteristics.

The relationship between B_S and k_S, investigated by Nikuradse (1933) in flow through pipes covered uniformly with a single layer of mono-sized sand grains, is shown in Figure 6.2 (Schlichting, 1979).

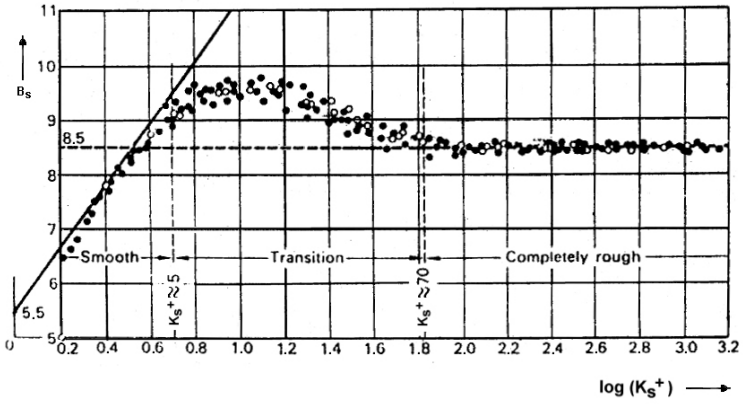

Figure 6.2- Variation of parameter B_S with roughness Reynolds number (Schlichting, 1979)

In the case of a hydraulically smooth flow ($k_S << \delta_v$ and $k_S^+ < 5$) (Schlichting, 1979; Ligrani and Moffat, 1986):

$$B_S = \frac{1}{\kappa}\ln(k_S^+) + C_{smooth} \tag{6.19}$$

where $C_{smooth} = 5.5$. Substituting Equation 6.19 into Equation 6.18 it is observed that the flow regime is independent of k_S.

For hydraulically rough flow ($k_S >> \delta_v$ and $k_S^+ > 55-70$):

$$B_S = 8.5 \tag{6.20}$$

Finally, for the transitional region ($k_S \approx \delta_v$ and $5 < k_S^+ < 55-70$) B_S is estimated using Figure 6.2 for a given k_S^+, and can be then substituted into Equation 6.18.

From these considerations, in Equation 6.13 C takes the value of 8.5 for sand grain roughness and Equation 6.15 becomes:

$$\Delta u^+ = \frac{1}{\kappa}\ln(k_l^+) - 3.3 \tag{6.21}$$

The effect of surface roughness on a turbulent boundary layer results in an increase in surface skin friction. Combining Equations 6.9 and 6.14, it is obtained the following skin friction law for rough surfaces (Clauser, 1956):

$$\frac{u_\infty}{u^*} = \frac{1}{\kappa}\ln\left(\frac{\delta u^*}{\nu}\right) + B - A - \Delta u^+ \tag{6.22}$$

It is well known that the pressure gradient effects are most important in the outer region of the turbulent boundary layer, being small near the wall (Clauser, 1954). Experiments by Perry and Joubert (1963) on rough wall boundary layers in adverse pressure gradients, have also shown that the roughness function is independent of the pressure gradients imposed on the flow.

The above equations are known to hold for smooth, moderately rough, and extremely rough walls without pressure gradients and for smooth walls with pressure gradients.

6.2 EXPERIMENTAL RESULTS IN SMOOTH BEDS

In an attempt to characterise the flow inside the mini flume, various experimental tests were carried out. These will serve as a test basis for subsequent comparisons, in more complex flows. As mentioned in section 5.1.1, this flume has a very strong curvature, that greatly affects the flow.

Results obtained using a smooth simulated bed are presented in this section, for Reynolds number of 10,000; 20,000 and 40,000.

Figure 6.3 shows a schematic representation of the mini flume with a velocity profile and the coordinate axis referred throughout this work.

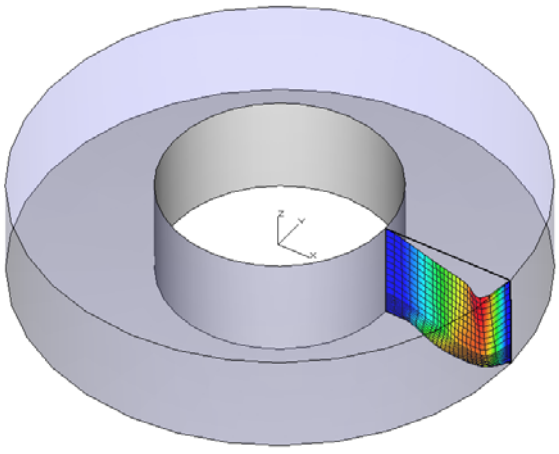

Figure 6.3- Flume and velocity profile representation

The streamwise or tangential velocity field is presented for each Reynolds number in Figure 6.4.

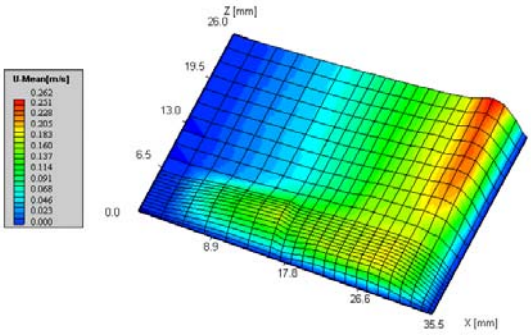

a) Re = 10,000

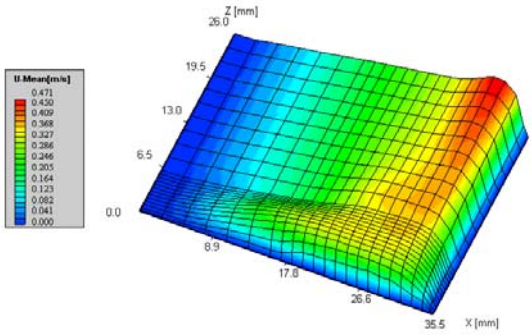

b) Re = 20,000

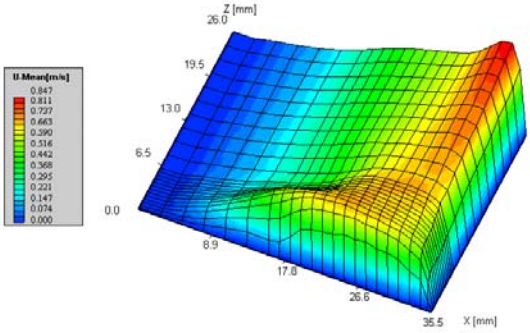

c) Re = 40,000

Figure 6.4- Tangential velocity field; smooth bed

By observing these figures, it can be concluded that the flow is skewed to the outer wall, i.e. developed towards the outer wall of the flume, which is due to the centrifugal forces. As a result, close to this region, there are strong velocity gradients (and, therefore, shear stresses) near the outer ring. Because the flow is driven from the top layer, this pattern is more evident in those regions. By increasing the flow velocity (Re), this pattern becomes more evident (Figure 6.4c).

This means that the shear stresses increase with the Reynolds number and its maximum occurs near the outer ring, particularly at higher velocities. This finding is in close agreement with visual observations which show that in this flow configuration, erosion is stronger in the vicinity of the outer ring of the flume.

Of great relevance to this study, is the vertical velocity profile above the bottom wall. In this, close to the wall, the velocity profile shows a sharp gradient, reaching a maximum in the vicinity of the solid surface. The velocity reported in Figure 6.4 is a small fraction of the upper lid velocity. Although measurements were not carried out beyond 26 *mm* of the

surface, the velocity profile remains flat for most of the flow cross section and approaches that of the upper solid wall near the top region of the section.

It is also of interest to show the crosswise or axial velocity field, at the same flow conditions as reported above (Figure 6.5).

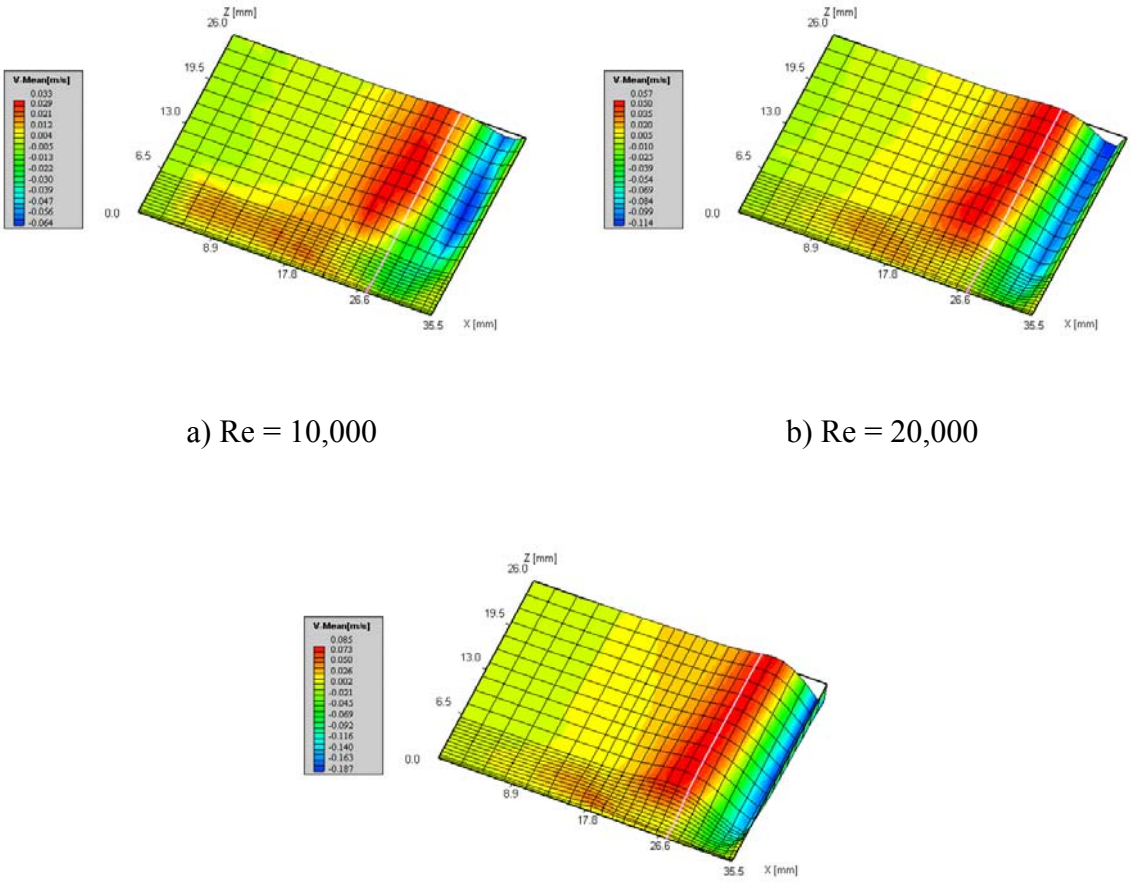

a) Re = 10,000

b) Re = 20,000

c) Re = 40,000

Figure 6.5- Axial velocity field; smooth bed

The data shows the existence of a recirculation zone near the outer wall and this secondary flow is induced by the centrifugal force produced by the rotating upper lid. Centrifugal forces drive the fluid outwards near the upper lid and is subsequently pushed downwards near the outer wall (negative velocity). After leaving the outer wall most of the flow is driven towards the inner side. Mass conservation requires an upward flux (positive velocity), leading to the occurrence of a recirculation bubble near the outer wall, as depicted in Figure 6.6. As the flow momentum increases, this pattern becomes confined to a smaller area, though with increasing flow vorticity. Also, the recirculation zone is pushed outwards and is stronger.

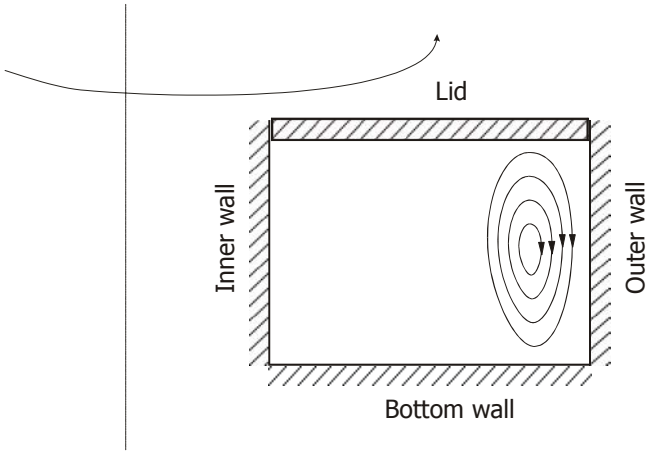

Figure 6.6- Recirculation pattern in a flume

By reducing the liquid viscosity, the movement of the recirculation bubble towards the outer wall is also observed. This suggests that the flow pattern is controlled by the balance between the inertia and viscous forces of the flow.

As a result of the occurrence of a secondary flow (the vertical velocity may be up to 25 *%* of the main component of the velocity, u_θ), shear stresses near the bed are enhanced and eventually leading to higher erosion rates.

Figure 6.5 also shows a vertical line located at 7.5 *mm* (position of x = 28 *mm*) from the outer wall and will be a reference for later discussions. Visual evidence (from the high speed video movies taken over various samples) indicates that the onset of erosion occurs systematically at the outer edge of the cross section. This observation is consistent with the fact that the overall shear will be greater in that region as a result of the secondary flow pattern previously discussed.

Secondary flows were also observed by Jones (2000) in a bigger annular flume (2 *m* in diameter and the annulus is 15 *cm* wide) and by Besley and Delo (1990) using a much bigger annular flume (carousel flume: outer diameter of 6 *m*). In the same way, Sheng (1989) provides a quantitative analysis of the secondary flow within a rotating annulus.

Some attempts have been made to minimise the effects of the secondary flows: by rotating the circular channel in the opposite direction to the lid (Kuijper *et al.*, 1989; Petersen and Krishnappan, 1994; Inamuro *et al.*, 1997), or by using flumes with a different geometry, such as race-way shaped flumes (Black and Paterson, 1997). Petersen and Krishnappan (1994) found even an optimal ratio between the lid and the flume speeds. Tests at different ratios were also carried by Inamuro *et al.* (1997). They observed a flow independent of the vertical direction in the flume, except close the bottom and the top. Using an annular Sea-bed flume, Maa (1990) concluded that, due to the secondary flow, this flume cannot be used to study the dispersion and settling of sediment, being restricted to erosion and deposition processes at the water-mud interface, only.

Although the present mini flume has a very strong curvature, there is not strong swirling flow, in which the tangential component of the velocity is of the same order of magnitude as the other velocity components and will produce a large adverse pressure gradient in the flow direction (Sloan *et al.*, 1986). As observed in Figures 6.4 and 6.5, such patterns were

not verified, even at Re = 40,000 where the mean axial velocity is up to 22 % of the mean tangential velocity. On the other hand, no reverse flows were observed (mean tangential velocities were always positive).

Figure 6.7 shows the tangential velocity turbulence profiles (RMS) for the same flow conditions reported above.

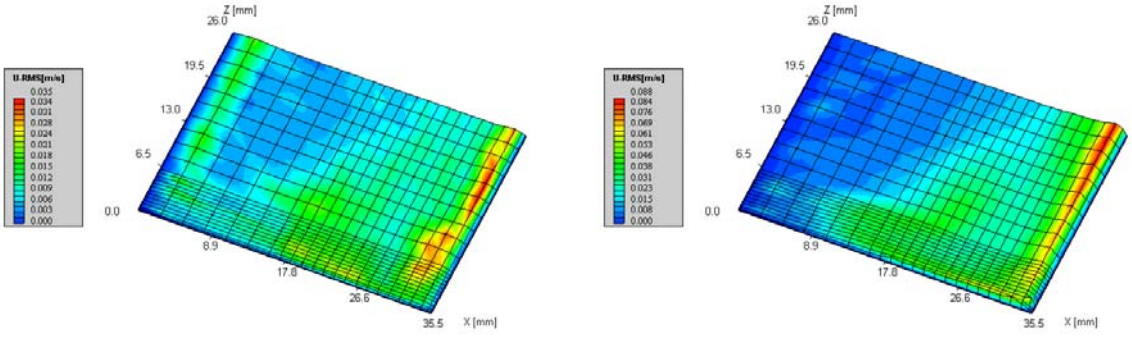

a) Re = 10,000 b) Re = 20,000

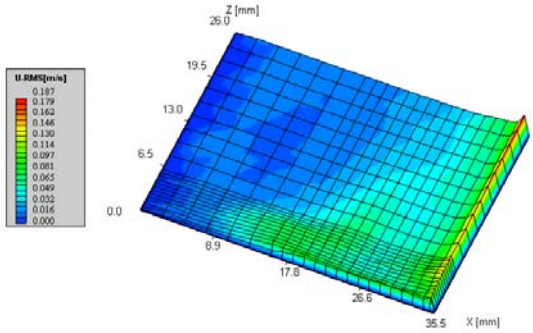

c) Re = 40,000

Figure 6.7- Tangential velocity turbulence field; smooth bed

It is possible to observe that the RMS of the tangential or streamwise velocity component increases with the Reynolds number. It is also observed high turbulence near the inner cylinder, at low velocities, being then transferred to the outer wall at higher velocities. This may be due to instabilities in the flow (due to the centrifugal forces) which are know to occur in Couette type flows between concentric cylinders, when the flow is not driven by the outer cylinder.

Identical behaviour is observed for the RMS of the axial velocity component (Figure 6.8), though the maximum value is lower.

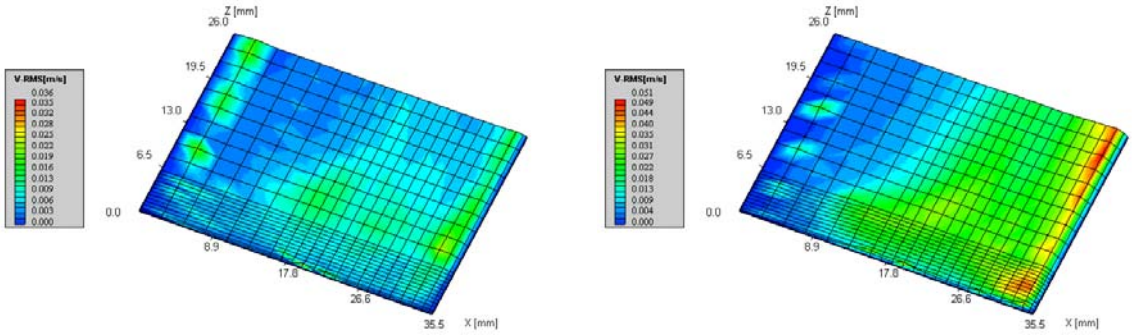

a) Re = 10,000

b) Re = 20,000

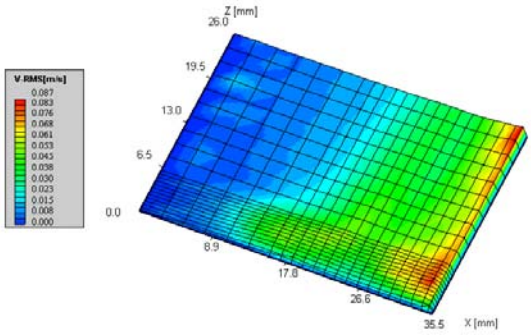

c) Re = 40,000

Figure 6.8- Axial velocity turbulence field; smooth bed

The fluctuations in the direction of the flow are larger than those in the crosswise direction of the flow. However, this difference becomes negligible near the outer wall (specially at higher velocities) which shows that the flow becomes nearly isotropic, as shown in Figure 6.9. As referred in section 3.5, there is isotropy when the isotropic ratio is approximately 1, thus grey regions are considered non isotropic.

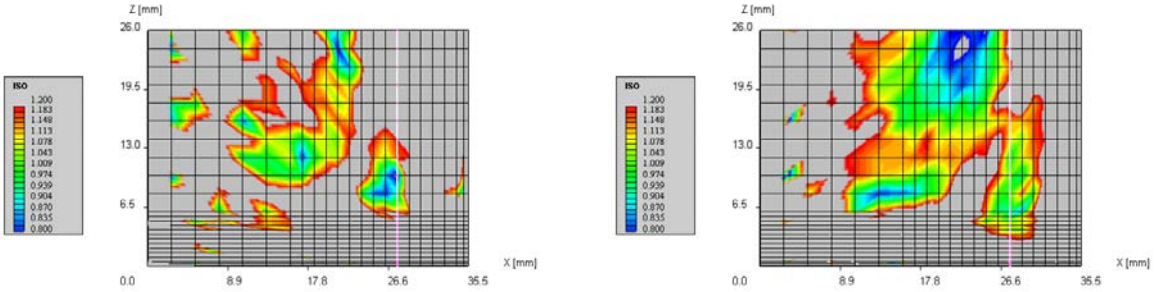

a) Re = 10,000 b) Re = 20,000

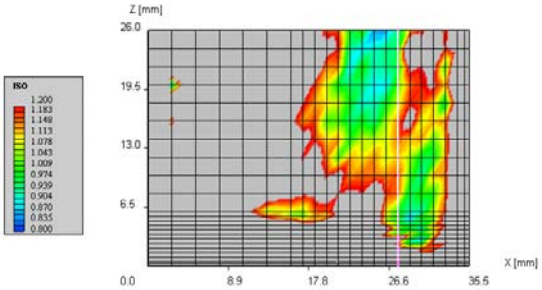

c) Re = 40,000

Figure 6.9- Isotropic ratio; smooth bed

As the Reynolds number increases, the regions of isotropic flow are displaced towards the outer wall, following a pattern similar to that of the recirculation bubble.

The cross-moments ($-\overline{u'v'}$), that are associated with the turbulent energy production, are shown in Figure 6.10.

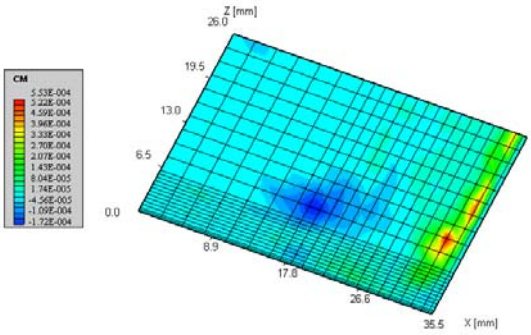

a) Re = 10,000

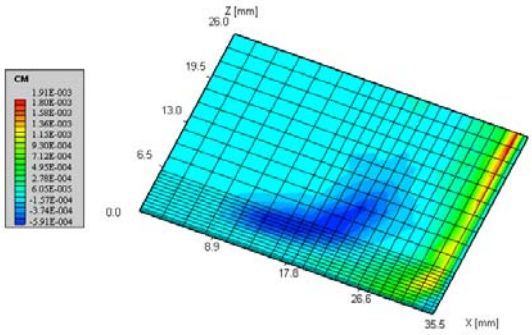

b) Re = 20,000

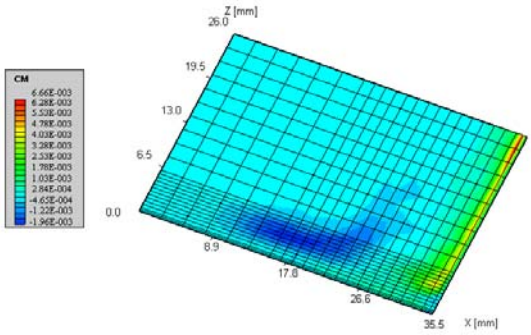

c) Re = 40,000

Figure 6.10- Cross-moments field; smooth bed

In the same way, Figure 6.10 shows that the turbulent energy production appears to be higher close to the outer ring and in the zone where recirculation take place. That zone appears to be located further away from the outer ring at lower Reynolds number and then pushed towards this ring by increasing the Reynolds number.

In order to characterise the flow inside the mini flume for each one of the Reynolds numbers, the turbulence intensity (*TI*) was determined at each position of the flume section (Equation 3.17). The results are shown in Figure 6.11.

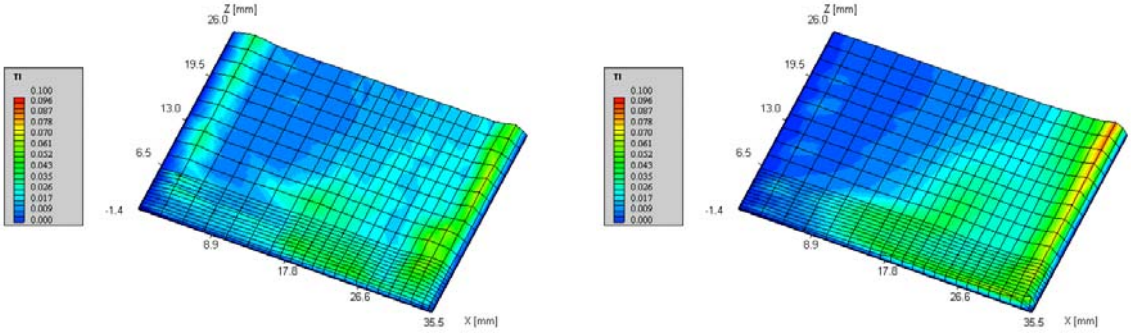

a) Re = 10,000 b) Re = 20,000

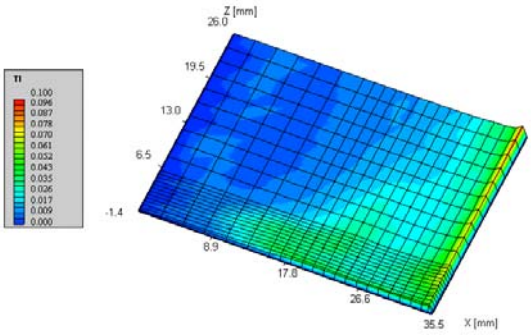

c) Re = 40,000

Figure 6.11- Turbulence intensity field; smooth bed

For all the Reynolds number tested, the flow is clearly turbulent. It is also observed that at Re = 10,000 the turbulence intensity is high close to the inner ring and, as Re increases, that effect is not evident. This occurrence could be related with the location of the recirculating flow zone, which is pushed outwards.

In addition, a more detailed analysis of the outer region (at the radial distance between 22 and 30 *mm*) and close to the bottom wall (at 1 *mm*) shows that at high Re (40,000) the turbulence intensity is lower and approximately constant, at around 3.2 %. This may be related with the fact that, at this location, the flows at the lower Re are downwards at higher velocity than this flow is going upwards. Further away from the bottom wall (at 4 *mm*), the local velocity for this Re increases with the turbulence intensity, although oscillating between 2.5 and 4 %.

Finally, the total shear stresses in this type of bed are depicted in Figure 6.12. These stresses include both the laminar and turbulent contributions, as defined in Equation 3.24.

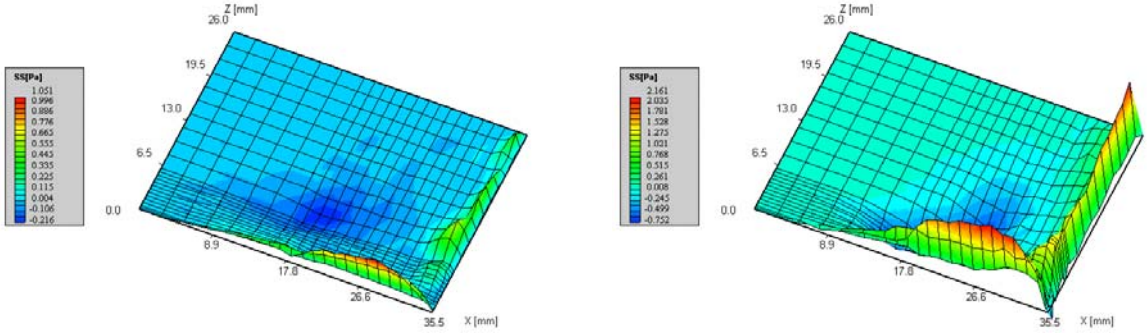

a) Re = 10,000 b) Re = 20,000

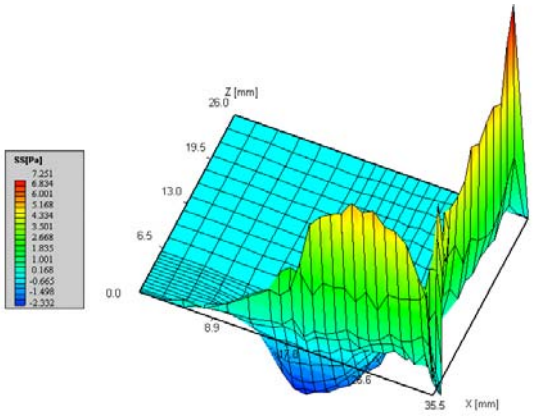

c) Re = 40,000

Figure 6.12- Shear stress field; smooth bed

Higher shear stresses are observed at the bottom wall close to the outer ring and along this ring. Increasing Re, these effects are emphasized and at Re = 40,000 the shear stresses are much higher throughout the outer wall. The data also shows the existence of negative shear stresses in the same position of the flume. These shear stresses values are mainly due the cross-moments contributions which, as observed in Figure 6.10, have also large negative values in this region.

From this set of experiments, it may be summarised that the properties of measured velocity fields are in close agreement with visual observations using the high speed video camera. In this, it was observed that erosion would initiate in a region near the outer wall. The LDA measurements show that the highest shear stress (induced by both the main and the secondary flows) occurs in the same region. In addition, the RMS velocity (which may be up to 22 % of the mean flow velocity) is also higher near the solid surface. Therefore, it may be concluded that local shear stresses (either due to the mean flow, to turbulence or to the combined effect of both) are closely linked to the erosion process. The data also shows that the flow Reynolds number is related to the stress levels in the vicinity of the surface, as the flow turbulence increases with the flow velocity. Again, the same behaviour is

observed if the flow Reynolds number is increased by reducing the liquid viscosity, keeping the velocity constant.

6.3 NUMERICAL SIMULATION

Computational fluid dynamics (CFD) can be described as the ability to replace the governing partial differential equations of fluid flow with algebraic equations, which can be more easily solved, obtaining a numerical description of the flow field (Ferziger and Perić, 1999). Most flows include turbulent structures, which cannot be solved numerically on currently available computers. To overcome these limitations, CFD methods solve the Reynolds-Averaged Navier-Stokes (RANS) equations using turbulence models to compute the averaged turbulent stresses.

An important issue is the formulation and the numerical treatment of the equations in regions close to solid walls. The near-wall formulation determines the accuracy of the wall shear stress and the wall heat transfer predictions, having an important influence on the development of boundary layers, including the onset of separation (CFX Manual, 1997).

This section describes the computation of the flow field in the mini flume used in the present work (with smooth bed). Thus, it was investigated the curvature and centrifugal forces effects with possible recirculation as well as swirl zones, on numerical models. For that, some of the available turbulence models were tested to investigate the confidence on numerical simulations in channels with the configuration of the current flume. For this purpose, the theory behind the numerical fluid flow calculation package (CFX) used to model the present flow is discussed.

CFX is a general purpose computer program for prediction of laminar and turbulent flow, and heat transfer, together with additional models such as combustion, multiphase flows and particle transport (CFX Manual, 1997).

As in any CFD code, CFX includes three stages: pre-processing, solver and post-processing. The pre-processing includes the definition of the geometry; grid or mesh generation; definition of fluid properties; selection of the physical phenomena to be modelled and specification of appropriate boundary conditions. The solver solves the conservation equations for mass, momentum and energy using, in this case, the finite volume method (FVM). At this stage, there is an approximation of the unknown flow variables; discretisation using the approximations and mathematical manipulations and solution of the algebraic equations. Finally, post-processing is used to display the results, including good graphical facilities to present the final converged solution (Versteeg and Malalasekera, 1998).

The governing equations of fluid flow are presented, following by the turbulence models used in the present simulations and the test conditions. In the last part of the chapter, the simulated results are discussed and compared with the experimental one.

6.3.1 GOVERNING EQUATIONS OF FLUID FLOW

The three-dimensional motion of a Newtonian fluid is described by a system of partial differential equations: the equation of continuity (mass conservation) and the momentum equations (Navier-Stokes) (Bird *et al.*, 1976). However, it is impossible to obtain a direct analytical solution for this system.

In the finite volume method, the computational domain is discretized into a grid, which is used to define storage locations for each variable of the system. Then, finite control volumes are created around each of these locations, being the governing equations integrated over each control volume. The algebraic equations obtained are solved by an iterative method (Versteeg and Malalasekera, 1998).

Conservation equations contains terms as Reynolds stresses, that have to be written in terms of time-averaged quantities. The averaged continuity and momentum equations written in tensor notation in cartesian coordinates, for a Newtonian, incompressible and isothermal flow become (Ferziger and Perić, 1999):

continuity:

$$\frac{\partial\left(\rho\overline{u}_i\right)}{\partial x_i} = 0 \tag{6.23}$$

momentum:

$$\frac{\partial\left(\rho\overline{u}_i\right)}{\partial t} + \frac{\partial}{\partial x_j}\left(\rho\overline{u}_i\overline{u}_j + \rho\overline{u_i'u_j'}\right) = -\frac{\partial\overline{p}}{\partial x_i} + \frac{\partial\overline{\tau}_{ij}}{\partial x_j} \tag{6.24}$$

being $\overline{\tau}_{ij}$ the mean viscous stress tensor:

$$\overline{\tau}_{ij} = \mu\left(\frac{\partial\overline{u}_i}{\partial x_j} + \frac{\partial\overline{u}_j}{\partial x_i}\right) \tag{6.25}$$

and μ the dynamic viscosity. The term $-\rho\overline{u_i'u_j'}$ is the Reynolds stresses term (turbulent stresses) and cannot be expressed as a function of the mean flow variables. Furthermore, the three velocity components ($\overline{u}_i$) and the pressure ($\overline{p}$), the Reynolds stresses introduce another six unknowns to the above system of equations, since $\overline{u_2'u_1'} = \overline{u_1'u_2'}$, $\overline{u_3'u_1'} = \overline{u_1'u_3'}$ and $\overline{u_3'u_2'} = \overline{u_2'u_3'}$. This leads to a turbulence closure problem. Thus, these terms must be related to known quantities through a turbulence model, in order to have a closed solution of the above equation (Nallasamy, 1987; Ferziger and Perić, 1999).

6.3.2 TURBULENCE MODELS

A turbulence model is a computational procedure that enables the closure of the system of mean flow equations.

The turbulence models can be classified in different ways, ranging from classical models based on Reynolds stresses decompositions up to large eddy simulation based on space filtered equations (Versteeg and Malalasekera, 1998). Among the classical models,

including mixing length theory, the *k*-ε model is by far the most widely used and validated. These two models are based on the Boussinesq eddy-viscosity concept which assumes that the turbulent stresses act in a way analogous to the viscous stresses in laminar flows, being equal to the product of an eddy viscosity and the mean velocity gradient. However, when the turbulent transport or non-equilibrium effects are important, this assumption is no longer valid being, in this case, the Reynolds stress models the most accurate because they represent the highest level of closure (Nallasamy, 1987). Nevertheless, computing costs and numerical stability problems with these models often prevent their use in complex flows.

The initial eddy-viscosity concept (Boussinesq's relationship) is expressed as (Versteeg and Malalasekera, 1998):

$$-\rho\overline{u_i'u_j'} = \mu_t\left(\frac{\partial\overline{u}_i}{\partial x_j}+\frac{\partial\overline{u}_j}{\partial x_i}\right) \tag{6.26}$$

being μ_t the turbulent or eddy viscosity. Equation 6.26 is analogous to Equation 6.25, for the mean viscous stress tensor.

The mixing length and *k*-ε models assume that the turbulent viscosity is isotropic, thus the ratio between the Reynolds stresses and mean strain rate is the same in all directions (Versteeg and Malalasekera, 1998).

A number of turbulence models are available on the CFX code: standard *k*-ε; low Reynolds number *k*-ε; RNG *k*-ε; low Reynolds number *k*-*w*; algebraic Reynolds stress model; differential Reynolds stress and differential Reynolds flux (CFX Manual, 1997). In this work, the standard *k*-ε model and the low Reynolds number *k*-ε are used. A short description of these models is subsequently presented.

- **The standard *k*-ε model**

The *k*-ε model of turbulence has been considered a powerful tool for the prediction of various complex flows. This model is based on two additional partial differential equations: one for the transport of turbulent kinetic energy (*k*) and another for the rate of dissipation of turbulent kinetic energy (ε). It is therefore a two-equation model, in which the two additional variables *k* and ε are introduced to model the Reynolds stresses (Mohammadi and Pironneau, 1994).

This model uses an extended Boussinesq`s relationship to relate the Reynolds stresses to the mean velocity gradients and the turbulent viscosity (Ferziger and Perić, 1999):

$$-\rho\overline{u_i'u_j'} = \mu_t\left(\frac{\partial\overline{u}_i}{\partial x_j}+\frac{\partial\overline{u}_j}{\partial x_i}\right)-\frac{2}{3}\rho k\delta_{ij} \tag{6.27}$$

where *k* (turbulent kinetic energy) is defined in Equation 3.27 and δ_{ij} is the Kronecker-Delta tensor. The turbulent viscosity (μ_t) is modelled as the product of a turbulent velocity ($V_t = k^{1/2}$) and a dissipation length scale (l_t), that is related with *k* and ε ($l_t = \frac{k^{3/2}}{\varepsilon}$) (Versteeg and Malalasekera, 1998):

$$\mu_t = \rho c_\mu V_t l_t = \rho c_\mu \frac{k^2}{\varepsilon} \tag{6.28}$$

c_μ is a dimensionless constant.

Equations for k and ε result from several manipulations of the momentum equations. The equation for the turbulent kinetic energy (k) takes the form (Ferziger and Perić, 1999):

$$\frac{\partial(\rho k)}{\partial t} + \frac{\partial(\rho \overline{u}_j k)}{\partial x_j} = \frac{\partial}{\partial x_j}\left(\mu \frac{\partial k}{\partial x_j}\right) - \frac{\partial}{\partial x_j}\left(\frac{\rho}{2}\overline{u'_j u'_i u'_i} + \overline{p' u'_j}\right) + P_k - \rho\varepsilon \tag{6.29}$$

where ε (dissipation of k) is defined in Equation 3.29 and P_k (production of k) is given by:

$$P_k = -\rho \overline{u'_i u'_j} \frac{\partial \overline{u}_i}{\partial x_j} \tag{6.30}$$

The term $\frac{\rho}{2}\overline{u'_j u'_i u'_i} + \overline{p' u'_j}$ represents turbulent diffusion of kinetic energy (pressure-velocity fluctuation term) and, using a gradient diffusion assumption, becomes:

$$-\left(\frac{\rho}{2}\overline{u'_j u'_i u'_i} + \overline{p' u'_j}\right) \approx \frac{\mu_t}{\sigma_k}\frac{\partial k}{\partial x_j} \tag{6.31}$$

In turn, the equation for the turbulence kinetic energy dissipation (ε) is given by:

$$\frac{\partial(\rho\varepsilon)}{\partial t} + \frac{\partial(\rho \overline{u}_j \varepsilon)}{\partial x_j} = \frac{\partial}{\partial x_j}\left[\left(\mu + \frac{\mu_t}{\sigma_\varepsilon}\right)\frac{\partial \varepsilon}{\partial x_j}\right] + c_{\varepsilon 1}\frac{\varepsilon}{k}P_k - c_{\varepsilon 2}\rho\frac{\varepsilon^2}{k} \tag{6.32}$$

The above equations contain five empirical parameters: c_μ, $c_{\varepsilon 1}, c_{\varepsilon 2}$ and Prandtl numbers σ_k and σ_ε. These parameters often assume the values (Launder and Spalding, 1974; Rodi, 1984; CFX Manual, 1997): $c_\mu = 0.09$; $c_{\varepsilon 1} = 1.44$; $c_{\varepsilon 2} = 1.92$; $\sigma_k = 1.00$ and $\sigma_\varepsilon = 1.30$.

Although these values are based on extensive examination of free turbulent flows, they can also be used for wall flows. However, these constants may require modifications to include effects such as curvature, low Reynolds number, near walls (Nallasamy, 1987).

It must be stated that the production and dissipation of turbulent kinetic energy are always linked, being the dissipation rate (ε) large where production of k is large.

• Boundary conditions

The k-ε turbulence model is not valid in the vicinity of solid walls, because it is valid only for high Reynolds numbers (turbulent flows). Near the wall there are small velocities, corresponding to low local Reynolds number (measured with y^+); this is due to the no-slip condition at the wall, being the flow in this region laminar (Mohammadi and Pironneau, 1994). In addition, close to solid walls the turbulent variations and fluctuations normal to the wall are damped, thus violating the assumption of isotropic turbulence underlying the k-ε model. Hence, the model cannot be applied to the viscous sub-layer very near walls.

At high Reynolds number, because of the very large gradients in the dependent variables near walls (a thin boundary layer develops), a large number of grid nodes would be required to fully solve the flow in those regions. In this situation, the standard *k*-ε model avoids direct integration near the wall by using the universal behaviour of near wall flows, as discussed in section 6.1. Thus, boundary conditions are specified using wall functions, which are formulated based on the concept of a universal law of the wall. As referred before, this concept assumes that the near wall region is a region of constant shear stress and the length scale of a typical turbulent "eddy" in this region is proportional to the distance from the wall, resulting in a logarithmic velocity profile (Equation 6.6). Based on these considerations and if local equilibrium is assumed (i.e. the production of turbulence equals the rate of dissipation), the following wall functions are developed (Versteeg and Malalasekera, 1998):

$$k = \frac{u^{*2}}{\sqrt{c_\mu}} \text{ and } \varepsilon = \frac{u^{*3}}{\kappa y} \tag{6.33}$$

Due to failures of the *k* and ε equations in the viscous sub-layer region, it is recommended that the near wall nodes be used in the log-law region (Ferziger and Perić, 1999).

One of the major disadvantages of the standard wall-function approach is that the predictions depend on the location of the nearest point to the wall, being influenced by the near-wall meshing (CFX Manual, 1997).

- **Flows with strong curvature**

The simplicity of the *k*-ε model to calculate the Reynolds stresses combined with better numerical convergence properties are its principal attractions. However, the deficiencies of this turbulence model are related with the prediction of highly swirling flows with recirculation. The weakness of the model are attributed to the assumption of an isotropic turbulent viscosity (c_μ is constant) and the failure to take into account the effect of streamline curvature on the Reynolds stresses (Sloan *et al*., 1986; Versteeg and Malalasekera, 1998). In fact, the isotropic eddy viscosity concept is not valid in complex or turbulent flows that are influenced by forces acting in a preferred direction such as rotation and streamline curvature.

Therefore, the *k*-ε model has been extensively modified in order to enhance its performance with respect to streamline curvature. In highly curved boundary layers the wall-function approach becomes critical once the production of turbulent kinetic energy is reduced by the curvature very close to the wall. Thus, the local equilibrium is no longer observed (Rodi and Scheuerer, 1983).

Various extensions of the *k*-ε turbulence model have been proposed for shear-layer flows with streamline curvature (Launder *et al.*, 1977; Rodi and Scheuerer, 1983; Sloan *et al.*, 1986; Hirsch and Leuckel, 1996, to name a few). Curvature exerts a large influence on the turbulence structure of a shear flow, affecting mainly the turbulent Reynolds stresses by producing "extra rates of strain", for which turbulence models are not optimised. Thus, recirculating flows may be the responsible for the disagreement between the computational results and the physical reality (Sloan *et al.*, 1986).

Curvature corrections for the *k*-ε model may take at least two forms (Hirsch and Leuckel, 1996): source-term modifications in the dissipation equation or corrections to the eddy viscosity (c_μ is a function of curvature). Dissipation source-term modifications are usually of Richardson number type corrections (Sloan *et al.*, 1986).

The Richardson number (Ri), which corresponds to an adjustment of the local ratio of the turbulent kinetic energy to the dissipation rate, is a dimensionless group defined as (Launder *et al.*, 1977):

$$\mathrm{Ri} = \frac{\frac{2U}{r}\frac{\partial}{\partial y}(U \cdot r)}{\left(\frac{\partial U}{\partial y}\right)^2 + \left(r\frac{\partial U/r}{\partial y}\right)^2} \tag{6.34}$$

being r the curvature radius of the streamline, y the distance normal to the surface and U the velocity component in the circumferential direction. These authors introduced the turbulent Richardson number in the dissipation equation. However, the Richardson number type corrections (including gradient, flux and stress Richardson number) have the inconvenience of being empirical (Sloan *et al.*, 1986).

Rodi and Scheuerer (1982) have tested three extensions of the *k*-ε turbulence to account for the curvature effects. The first one consisted of an algebraic stress model (ASM), which simulate the curvature effects not involving any additional curvature-specific empirical input (c_μ is obtained as a function of the curvature); the other two use a modified form of the ε equation, introducing an extra production term in one case and making the destruction term a function of a curvature parameter, in the other. As opposed to the first extension, the last two are based on purely empirical arguments. The authors refer also that Reynolds stress models (RSM) are usually adequate to simulate flows of curved shear layers, however they have very large computing costs. They concluded that, in a general way, the algebraic stress model gives better results.

As reported by Pourahmadi and Humphrey (1983), a general expression was derived for c_μ, accounting simultaneously for the curvature and pressure strain effects, using algebraic approximations for the Reynolds stress equations. It must be stressed that, for strongly swirling flows, other considerations have to be accounted (Sloan *et al.*, 1986).

Hirsch and Leuckel (1996) analysed a RSM and identified the terms responsible for its improved results in flows with strong streamline curvature. Thereby, they developed a correction for the Boussinesq stress closure, obtaining much better results in swirling flows than with uncorrected *k*-ε predictions. In this manner, the numerical complexity of an RSM computation is avoided.

- **The low Reynolds number *k*-ε model**

This model is an extension to the standard *k*-ε model, allowing the calculation of turbulent flows at low Reynolds numbers. In these conditions, the log-law velocity distribution is not valid and, therefore, the above boundary conditions cannot be used.

Wall damping has to be applied to ensure the transport of turbulent Reynolds stresses to viscous stresses in the viscous sub-layer adjacent to solid walls. Thus, for the case of low Reynolds number *k*-ε model, the equations become:

$$\mu_t = \rho c_\mu f_\mu \frac{k^2}{\varepsilon} \tag{6.35}$$

$$\frac{\partial(\rho k)}{\partial t} + \frac{\partial(\rho \overline{u}_j k)}{\partial x_j} = \frac{\partial}{\partial x_j}\left(\mu \frac{\partial k}{\partial x_j}\right) - \frac{\partial}{\partial x_j}\left(\frac{\rho}{2}\overline{u'_j u'_i u'_i} + \overline{p' u'_j}\right) + P_k - \rho\varepsilon - 2\mu\left(\frac{\partial k^{1/2}}{\partial x_j}\right)^2 \tag{6.36}$$

$$\frac{\partial(\rho \varepsilon)}{\partial t} + \frac{\partial(\rho \overline{u}_j \varepsilon)}{\partial x_j} = \frac{\partial}{\partial x_j}\left[\left(\mu + \frac{\mu_t}{\sigma_\varepsilon}\right)\frac{\partial \varepsilon}{\partial x_j}\right] + c_{\varepsilon 1}\frac{\varepsilon}{k}P_k - c_{\varepsilon 2} f_\varepsilon \rho \frac{\varepsilon^2}{k} + 2\nu\mu_t\left(\frac{\partial^2 \overline{u}_i}{\partial x_j \partial x_k}\right)^2 \tag{6.37}$$

When compared with Equations 6.28, 6.29 and 6.32, the main modifications are concerned to the multiplication of constants c_μ and $c_{\varepsilon 2}$ by wall-damping functions f_μ and f_ε, respectively. These functions are dependent on the local turbulent Reynolds number $\mathrm{Re}_t = \frac{\rho k^2}{\mu\varepsilon}$ through (Launder *et al.*, 1977; CFX Manual, 1997):

$$f_\mu = \exp\left(\frac{-3.4}{\left(1 + \frac{\mathrm{Re}_t}{50}\right)^2}\right) \tag{6.38}$$

$$f_\varepsilon = 1 - 0.3\exp\left(-\mathrm{Re}_t^2\right) \tag{6.39}$$

Furthermore, new source terms in both *k* and ε equations (last term of each equation) are added, including a viscous contribution. Thus, in Equation 6.36 that extra term is introduced for computational reasons, while in Equation 6.37 it corresponds to a destruction term (Launder and Spalding, 1974; Launder *et al.*, 1977; CFX Manual, 1997).

6.3.3 SIMULATION CONDITIONS

The mini flume described in section 5.1, that has a rectangular cross-section, has been modelled as a three-dimensional block. The block dimensions were 49, 35.5 and 6.28 *mm* in axial ($\hat{i}$), radial ($\hat{j}$) and tangential ($\hat{k}$) directions, respectively (see Figure 6.13). The flow was assumed axisymmetric in $\hat{k}$ direction (Petersen and Krishnappan, 1994), with three nonzero components of velocity. It was considered statistically stationary, isothermal, incompressible and with constant fluid properties. The fluid properties were those used on the experimental tests.

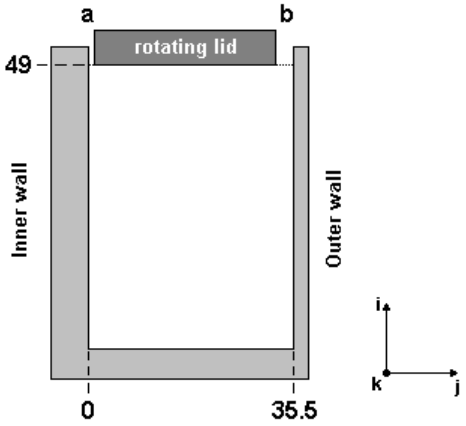

Figure 6.13- Sketch of the flume

In this configuration, *a* and *b* are the gaps (located at the edges of the lid), being $a = 1$ and $b = 3.2\ mm$.

Laminar model and standard *k*-ε and low Reynolds number *k*-ε turbulence models were tested at different Reynolds number: 2,000, 10,000 and 40,000. Continuity and momentum equations were formulated in cylindrical coordinates.

The no-slip condition ($u = v = 0$) was the boundary condition for all the side walls. Moreover, the solid boundaries in this computation are assumed smooth. The top boundary condition was a known uniform tangential angular velocity (in $\hat{k}$ direction).

For velocity computations near the wall, various near-wall profiles were imposed: quadratic, linear and logarithmic for the laminar, low Reynolds *k*-ε and standard *k*-ε models, respectively.

The discretised equations are solved sequentially and the SIMPLE algorithm for pressure-velocity coupling has always been used, with a SIMPLEC correction.

The grid generation involves filling the spatial domain with non-overlapping cells. It is defined by the vertices of the control volumes and the number of mesh vertices (nodes) depends on the purpose of study, required accuracy and computational power. A rectangular grid was considered.

Preliminary tests proved that the use of 5 grid blocks for discretisation of the entire domain (including the gaps) has not shown visible advantages over the solution in which those gaps are neglected (one single block).

Block Stone (BLST) solver method was applied for *u*, *v* and *w* velocities and Incomplete Conjugated Gradient (ICCG) solver was considered for pressure. Concerning the differencing scheme, it was used the Hybrid Differencing Scheme (HDS) for the three velocity components and Central Differencing Scheme (CDS) for the pressure. It is recommended by CFX to use the Algebraic Multi Grid (AMG) linear solver when there are convergence difficulties. Because *k* and ε must always remain positive, it was used a HDS and the solver method was Linear Relaxation (LRLX).

An iterative solution procedure is employed until the specified convergence criteria are achieved. The new calculated values of a given variable obtained in each iteration are then updated with the previous values of the variable using an under-relaxation technique. The best relaxation factors (URF) must be chosen for each variable in order to optimise the convergence. A small URF usually yields a more accurate solution of the transport equations; however, if it is chosen too small, the convergence is very slow. By default, CFX considers 0.65. During the simulating tests, the URF was in the range 0.3-0.65 for the velocity components.

In all the tests, the number of iterations was, at least, 1,000. An initial guessed value was required to start the simulation. Often the converged results previously obtained were used.

The complex character of the present flow made it difficult to obtain a converged solution. The convergence analysis, for each of the models studied, consisted in the analysis of the evolution of the residuals (mainly the mass source residuals), and changing the URF and/or the grid fineness. The number of cells in the grid could be a very important factor in the accuracy of a CFD solution. Generally, a coarse grid was tested first and then, depending on the convergence, grid refinements were made. If with such modifications the results did not converge or fit the experimental data, a different model was used. Also, tests were made using a non-uniform grid spacing and refined grids near the walls (where higher velocity gradients occur).

Finally, it was attempted to correct the curvature and swirl effects on the mini flume. Therefore, and according to section 6.3.2, modifications were made in Fortran source code introducing the Richardson number and modifying the $c_{\varepsilon 1}$ constant (taking a null value instead 1.44) in the ε equation.

A summary of the numerical tests is presented in Table 6.1. The grid used ($\hat{i}$, $\hat{j}$, $\hat{k}$) is also presented.

Except for the test at Re = 10,000 using the laminar model, all simulations have converged. The last two tests at Re = 40,000 were run at the same conditions, in order to evaluate the influence of the code modifications on the results.

Table 6.1- Simulation tests using CFX

	Model
Re = 2,000	Laminar (50, 50, 1) Standard *k*-ε (20, 20, 1) Low Reynolds *k*-ε (100, 100, 1)
Re = 10,000	Laminar (50, 50, 1) Low Reynolds *k*-ε (115, 126, 1)[1] Standard *k*-ε (50, 50, 1) Standard *k*-ε (20, 20, 1)
Re = 40,000	Standard *k*-ε (20, 20, 1) Standard *k*-ε (50, 50, 1) Standard *k*-ε (50, 50, 1)[2]

1 – the grid spacing was non-uniform and refined near the walls.

2 – with Fortran modifications.

6.3.4 RESULTS AND DISCUSSION

The results obtained using CFX provide an analysis of the applicability of some models available in the code, when used in geometries such as the mini flume and over a wide range of velocity conditions.

In order to have an overall view of the flow field inside the entire cross section of the flume, Figure 6.14 presents an example of those profiles for the three Reynolds numbers, along a vertical line located at 7.5 *mm* from the outer wall.

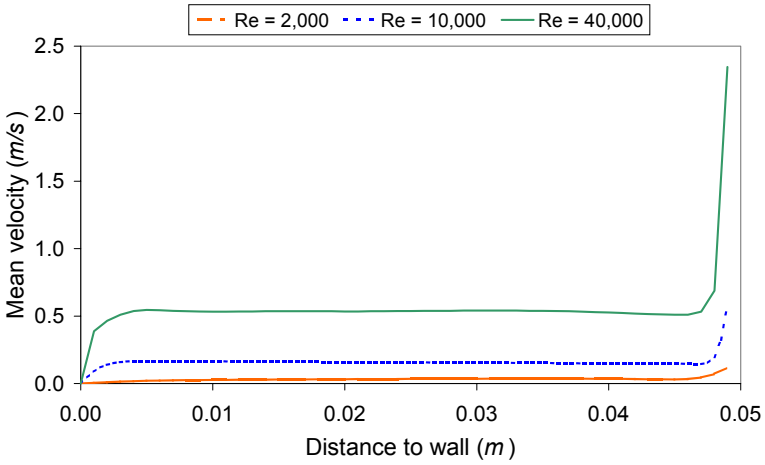

Figure 6.14- Numerical velocity profiles at different Re

It is shown that most of the flow field is of uniform velocity and, of interest to this study, the velocity gradients are confined to a very narrow region near the lower surface. The effect of the rotating lid is also evident over a small layer near its surface.

Also, Figure 6.15 shows the radial/vertical vector plot and the tangential, axial and radial mean velocities in the entire flume section. This data refers to Re = 40,000.

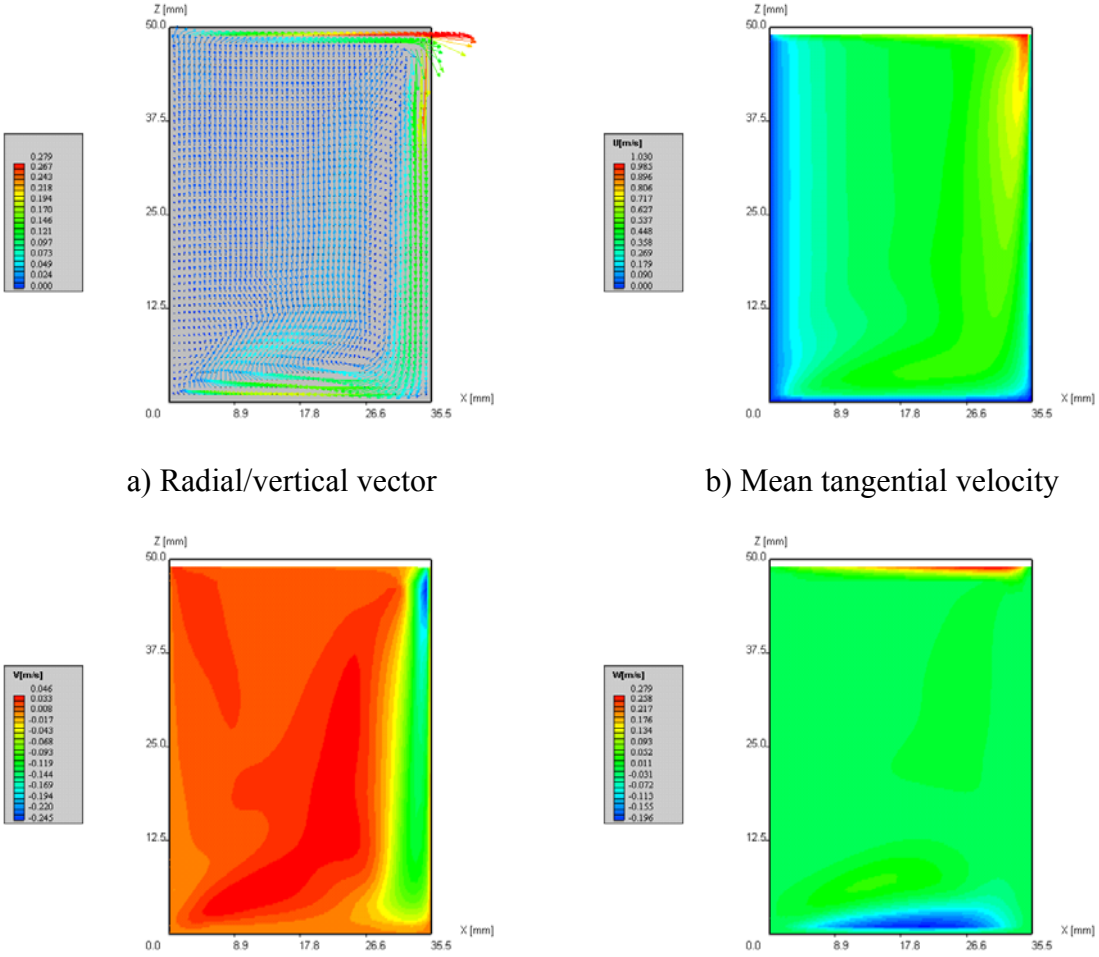

a) Radial/vertical vector

b) Mean tangential velocity

c) Mean axial velocity

d) Mean radial velocity

Figure 6.15- Numerical profiles in the entire flume section

As expected, at the walls the mean velocity is zero (Figure 6.15b), being maximum at the top of the outer wall because the lid motion. It is also evident from Figure 6.15c that the fluid moves downwards close to the outer wall (negative velocity), being upwards for most of the flume section. The radial velocity (Figure 6.15d) is predominant on top and bottom of the section, being the fluid displaced to the outer wall direction at the top and to the inner wall direction at the bottom. All these results are in complete agreement with Figure 6.15a, which clearly shows the existence of a strong recirculation zone inside the cross section of the flume.

➢ **Experimental validation**

The main results are presented for the various models tested: laminar (Lam.), standard *k*-ε with grid 20, 20, 1 or 50, 50, 1 or with code modifications (KE-20 or KE-50 or KE-Rich., respectively) and low Reynolds number *k*-ε with grid 100, 100, 1 (LRKE-100) or low Reynolds number with local refinements (LRKE-ref.) models. A comparison with the experimental data (LDA) is made.

- Re = 2,000

Figure 6.16 compares the experimental and numerical results for Re = 2,000, for a vertical profile at 7.5 *mm* from the outer wall.

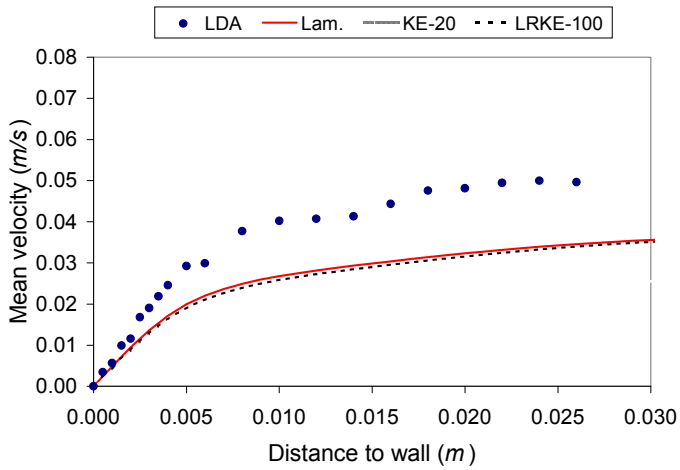

Figure 6.16- Experimental and numerical data; Re=2,000

Figure 6.16 shows that the numerical models give a better fit to the experimental data in the region close to the wall. This is more evident for both the laminar and the low Reynolds *k*-ε models. Using the standard *k*-ε model, the results are in disagreement, what means that this model is inaccurate at very low velocities.

As observed, both laminar and low Reynolds *k*-ε profiles nearly overlap. This is an indication that the flow is of very low turbulence. For this turbulence model the location of the nearest cell to the wall was at $y^+ = 2$, which means that the flow is dominated by viscous effects. For this reason, standard *k*-ε does not work correctly (y^+ cannot be so small for this model).

The results obtained using the laminar model are presented for the flume section in Figure 6.17, which depicts the radial/vertical vector plot and the mean tangential and axial velocities.

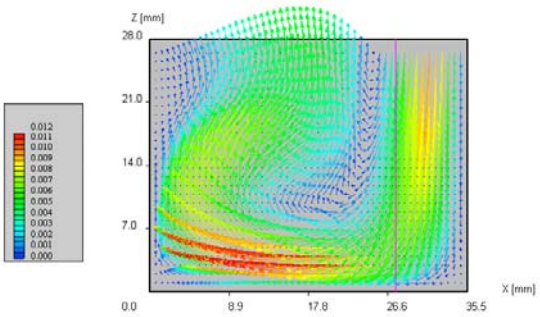

a) Radial/vertical vector

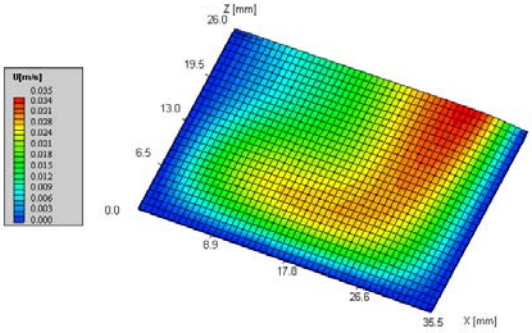

b) Mean tangential velocity

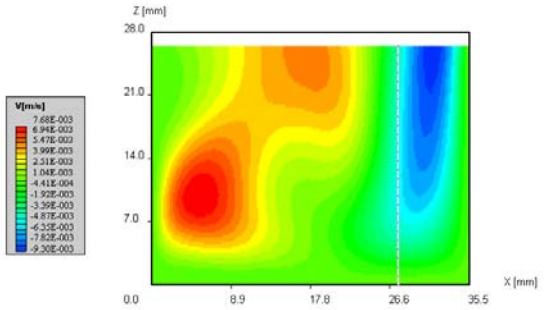

c) Mean axial velocity

Figure 6.17- Numerical results; Re=2,000

The vertical line shown corresponds to the position discussed in Figure 6.16. As observed in Figure 6.17a, this line is located at the downward section of the fluid, which is in perfect agreement with Figure 6.17c. It can be also observed, in Figure 6.17a, a large recirculation zone occupying most of the test section. Because the reference line is inside the recirculation zone, the numerical models tested exhibit difficulties to work correctly. This fact justifies the discrepancy between experimental and numerical results observed in Figure 6.16.

Figure 6.18 shows the experimental data obtained in a smooth bed, at Re = 2,000. Comparing both Figures 6.17b and 6.18a, it can be observed strong similarities between the CFX and the experimental results at this Reynolds number, although the absolute maximum of the experimental velocity is higher. Also, results obtained for the axial velocity are in good agreement with the experimental data (Figures 6.17c and 6.18b).

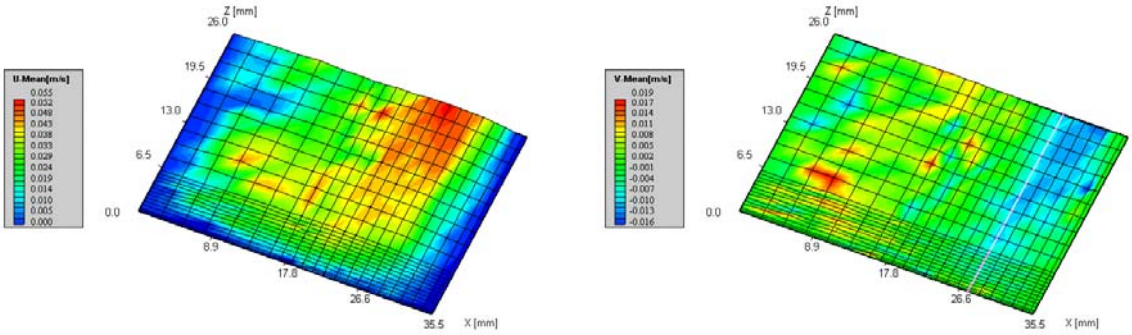

a) Tangential velocity field b) Axial velocity field

Figure 6.18- Experimental data; smooth bed; Re=2,000

- Re = 10,000

The experimental velocity profiles are compared with those obtained by the numerical models in Figure 6.19.

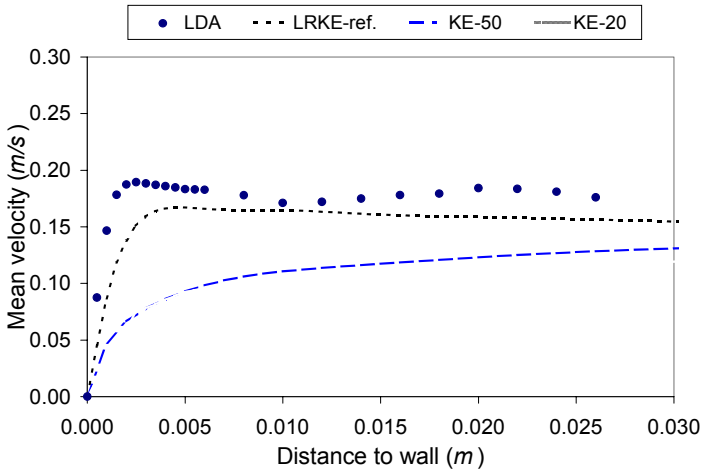

Figure 6.19- Experimental and numerical data; Re=10,000

As previously reported, the laminar model did not converge, thus it was not considered in Figure 6.19. From this figure, it may be concluded that the low Reynolds number *k*-ε model gives much better results when compared with standard *k*-ε.

It has been mentioned that the *k*-ε model assumes isotropic turbulence. A detailed analysis of Figure 6.9a, and considering the reference vertical line, shows a low level of isotropy along this line, being non isotropic in the lower 6 *mm*. This is the reason for which the turbulent models do not work well. Although the standard *k*-ε model converges, the

position of the nearest cell to the wall was at low values for y^+, even when the grid was coarsen (closest point to the wall at $y^+ \approx 16$). This is not the most favourable condition.

For the low Reynolds number *k*-ε model, the convergence was difficult to obtain, because the values of y^+ are a little high for this kind of model ($y^+ = 1.8$). It works correctly if y^+ is small (< 1). Results obtained with this model were improved after the refinement to the grid was made in the regions near the walls. In this way, it was possible to obtain lower y^+ values. The opposite is required for the standard *k*-ε model (uses wall functions) that needs coarse grids in order to have high y^+ values (> 30 – 50), to allow the application of the log-law as a wall function.

Because of the referred above, the grid size choice was always dependent upon the turbulence model and on the y^+ values obtained for the nearest point to the wall.

It may be concluded that, amongst the models tested for this Reynolds number, the low Reynolds number *k*-ε with refinements is preferable and the fitting of the experimental LDA data is acceptable. The differences obtained may also be related with simplifications in boundary conditions, which was also mentioned by Besley and Delo (1990).

The flow pattern inside the flume section is sketched in Figure 6.20 for the low Reynolds number *k*-ε model.

Figure 6.20a, which presents the velocity vectors, shows a recirculation zone of smaller dimensions than that obtained at Re = 2,000 (Figure 6.17a), which is in agreement with the experimental evidence (see Figure 6.5a). In this case, the vertical line is located in the recirculation zone where the flow has two directions: downwards on the lower 7 *mm* and upwards above that position. This configuration yields strong shear velocities in the flow. Such observations can also be made in Figure 6.20b, where the mean axial velocity is presented.

Concerning the mean tangential velocity, and although the model slightly underpredicts the data (Figure 6.20c) the profile is similar to that measured (see Figure 6.4a).

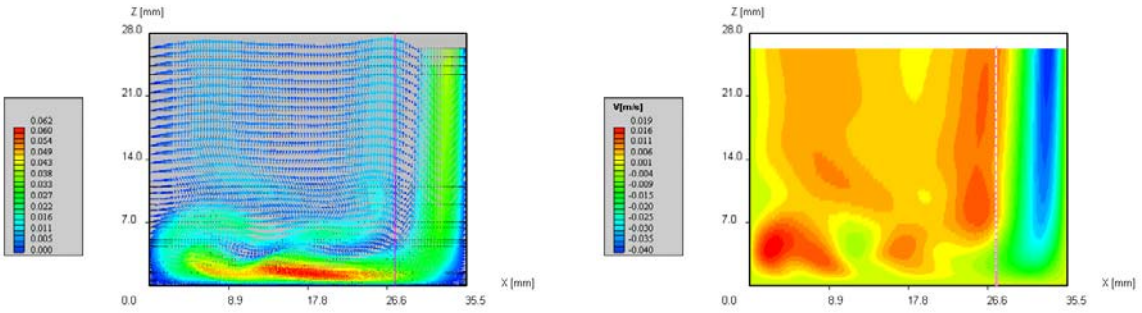

a) Radial/vertical vector b) Mean axial velocity

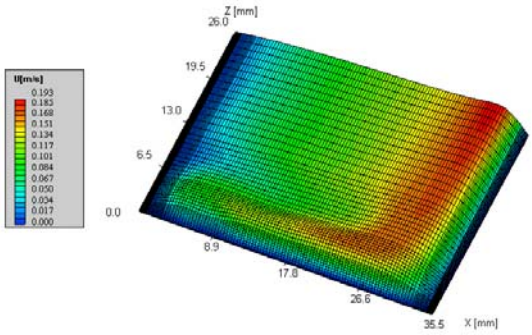

c) Mean tangential velocity

Figure 6.20- Numerical results; Re=10,000

- Re = 40,000

At this Reynolds number the standard *k*-ε model works better. Experimental and numerical results are compared in Figure 6.21 for the same vertical position on the flume section.

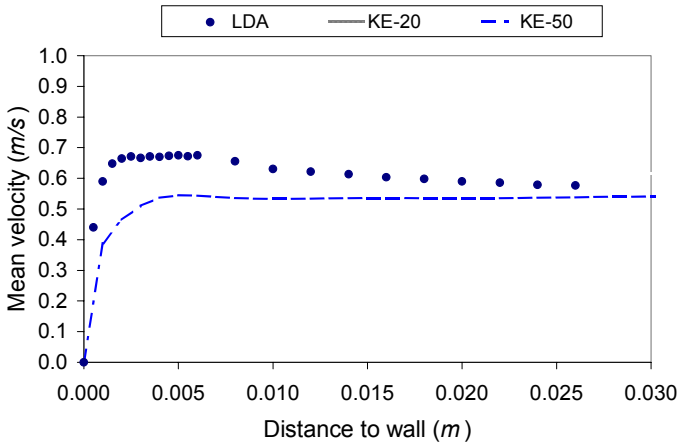

Figure 6.21- Experimental and numerical data; Re=40,000

Two different grids were tested for the turbulence model and it is observed a variation on the slope in function of the grid size. The y^+ values for the closest grid point to the wall were 42 and 19 for the coarser and finer grids, respectively, which shows that, for this model, coarse grids are needed in order to have high y^+ values. This means that for the coarse grid the minimum value of y^+ to get within the fully turbulent region ($y^+ > 30 - 50$) is practically achieved.

This turbulence model gives much better results at this Reynolds number because, as observed in Figure 6.9c, the vertical line is located in a region of isotropic flow, except for a small region near the lower surface. This fact may justify the not so good agreement observed near the wall (Figure 6.21). On the other hand, it may be also an indication that the law of the wall used may not be entirely appropriate.

These conclusions were obtained taking the results without considering the flume curvature and swirl (the employed models do not consider secondary flows, recirculating flows, curved walls and swirl). As previously mentioned, modifications in the standard k-ε model were introduced in order to account for the flume curvature and swirl. The grid was set at 50×50×1 cells.

Figure 6.22 depicts the velocity vector, the mean axial velocity and the mean tangential velocity.

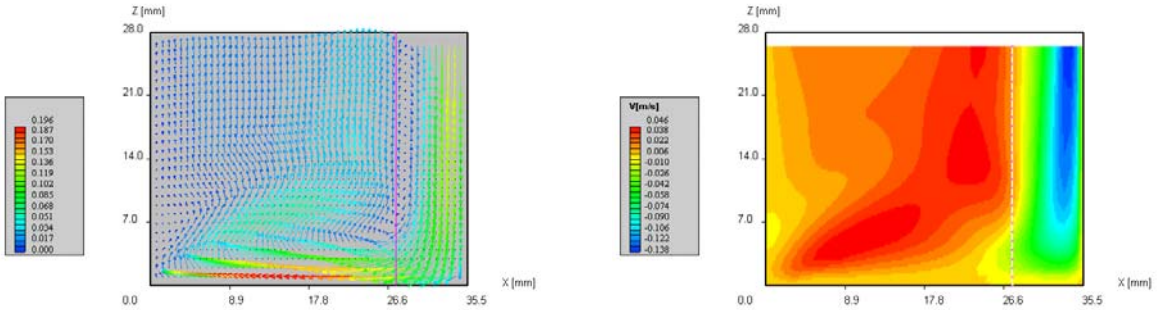

a) Radial/vertical vector b) Mean axial velocity

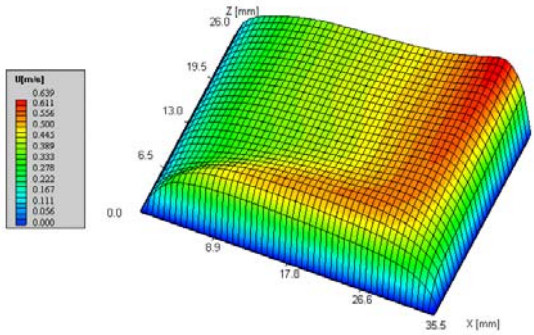

c) Mean tangential velocity

Figure 6.22- Numerical results; Re=40,000

Figure 6.22a shows that the recirculation zone is small when compared with flows at lower Reynolds number and its location is shifted towards to the outer ring, which is in agreement with the experimental evidence. The vertical line is fully located in the

recirculation zone, as it was at Re = 10,000, where the flow is downwards in the lower 7 *mm* and upwards above that position. Figure 6.22b confirms these results.

By comparison with the experimental data, Figure 6.5c shows a clear localisation of the downward flow very close to the outer wall, being the line located a little far away from the recirculation zone and thus, the flow is completely upwards along the profile length. In the same way, Figure 6.22c shows a much smoother evolution of the mean velocity towards to the outer wall, when compared with the experimental data (Figure 6.4c). This may suggest that the curvature, centrifugal force and swirl were not considered in detail by the model.

Because at this Re the regions of isotropic flow are located mainly close to the outer wall, the *k*-ε model does not work correctly throughout the entire flume section. At Re = 10,000, 3D velocity profiles fit better experimental results because isotropy was evenly distributed throughout the flume section.

Selecting a second vertical line, now at the radial distance of x = 13.14 *mm*, where for Re = 40,000 the flow is highly anisotropic (see Figure 6.9c), the velocity profiles are shown in Figure 6.23.

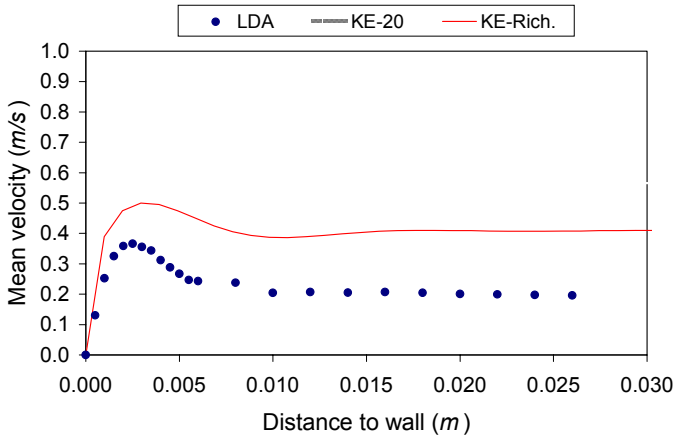

Figure 6.23- Experimental and numerical data (at radial distance x=13.14 *mm*)

Comparing these results with Figure 6.21, it is observed a clear deviation of the numerical results from experimental data. This confirms the importance of isotropy when applying such turbulence models.

Without the referred corrections to the flume, it was observed some differences comparing with figures above. In this case, the recirculation zone is more distant from the outer wall and, in this way, the vertical line is completely located in the descending zone of the flow. Also, the mean velocity profile is much smoother. In any case, by neglecting the model modifications the results show a stronger deviation than those reported above. Clearly, better models are required for a satisfactory simulation. Therefore, it may be concluded that, when applying some corrections to the model it is possible to get improvements on the results, although there are still differences comparing simulated with experimental profiles.

- **Main conclusions**

The application of CFD models to compute the flow inside a mini flume has shown that a good qualitative agreement with the experimental data was found. The models tested presented some difficulties in predicting flows in channels with strong curvature and where the centrifugal forces are very important. Some difficulties were found in estimating correctly the recirculation zone, particularly at high Reynolds number. Furthermore, they do not work perfectly in these regions. Although at lower Reynolds number (Re = 2,000 and Re = 10,000) some similarity in numerical and experimental 3D profiles was found, it is not enough to validate the models tested.

It will be interesting to test a more sophisticated turbulence model, such as the Reynolds Stress models (RSM), which is non isotropic. In fact, it has been suggested by some researchers (Sloan *et al.*, 1986; Nallasamy, 1987) to use Algebraic Stress models (ASM) or RSM models to account curvature effects and secondary flows.

James and Jones (1992) have made some numerical simulations of the flow field for an identical flume using the Harwell-Flow 3D software, but using a fluid with high viscosity and at much lower lid speeds. They obtained a good agreement with the experimental data in laminar flow. However, they have modified previously the software and made treatment of the boundary conditions and grid near the edges of the rotating lid. A detailed numerical investigation, taking into account the effect of the gaps, was also presented for a flume with similar configuration by James *et al.* (1996).

Numerical studies were also made in larger flumes (Graham *et al.*, 1992), with outer diameter of 6 *m* (HR annular carousel), using the CFD code Harwell-Flow 3D. Both the standard k-ε and a modified mixing-length turbulence models were tested and good agreement was found with experimental data, although the flume curvature is not so strong as in the present work. In the same way, Petersen and Krishnappan (1994) found a reproduction of the main characteristics of the flow in a rotating circular flume (5 *m* in mean diameter), using the Phoenics code with the standard k-ε model.

CHAPTER 7

FACTORS AFFECTING THE TURBULENCE - EXPERIMENTAL RESULTS

From physical evidence, it is known that for a certain sediment structure, fluid turbulence is a major parameter controlling the onset of erosion.

This chapter aims to investigate the various factors that might affect the turbulent interaction between the fluid and the sediment. Because of the high physical complexity, a careful set of experiments was designed to assess each factor in separate: surface roughness; entrained particles (presence of suspended matter in form of aggregated sediments); surface waves including some combined effects, and a deformable two-fluid bed. In each experiment a simulated bed was used as a test medium.

In order to have a clear understanding of the various factors contributing to the erosion process, Figure 7.1 shows an example of a sediment bed being eroded, at different stages. It depicts some frames from a high speed video camera, during the erosion tests carried out on sample C3. It is evident an increase of the suspended particles concentration as the velocity increases. At the highest Re (60,000) the fluid is completely turbid. Also, it is observed the roughness of the sandy bed. Obviously, these factors will affect the flow turbulence.

7.1 INFLUENCE OF SURFACE ROUGHNESS

Three different rough beds were used to evaluate the influence of the surface roughness upon the velocity field in general and turbulence in particular: two gypsum models of a marine sediment (RB1 and RB2) and an artificial rough bed formed by loose glass beads (RB3). Experiments on RB3 were carried out at a lower Reynolds number (10,000) in order to avoid the entrainment of the bed into the fluid.

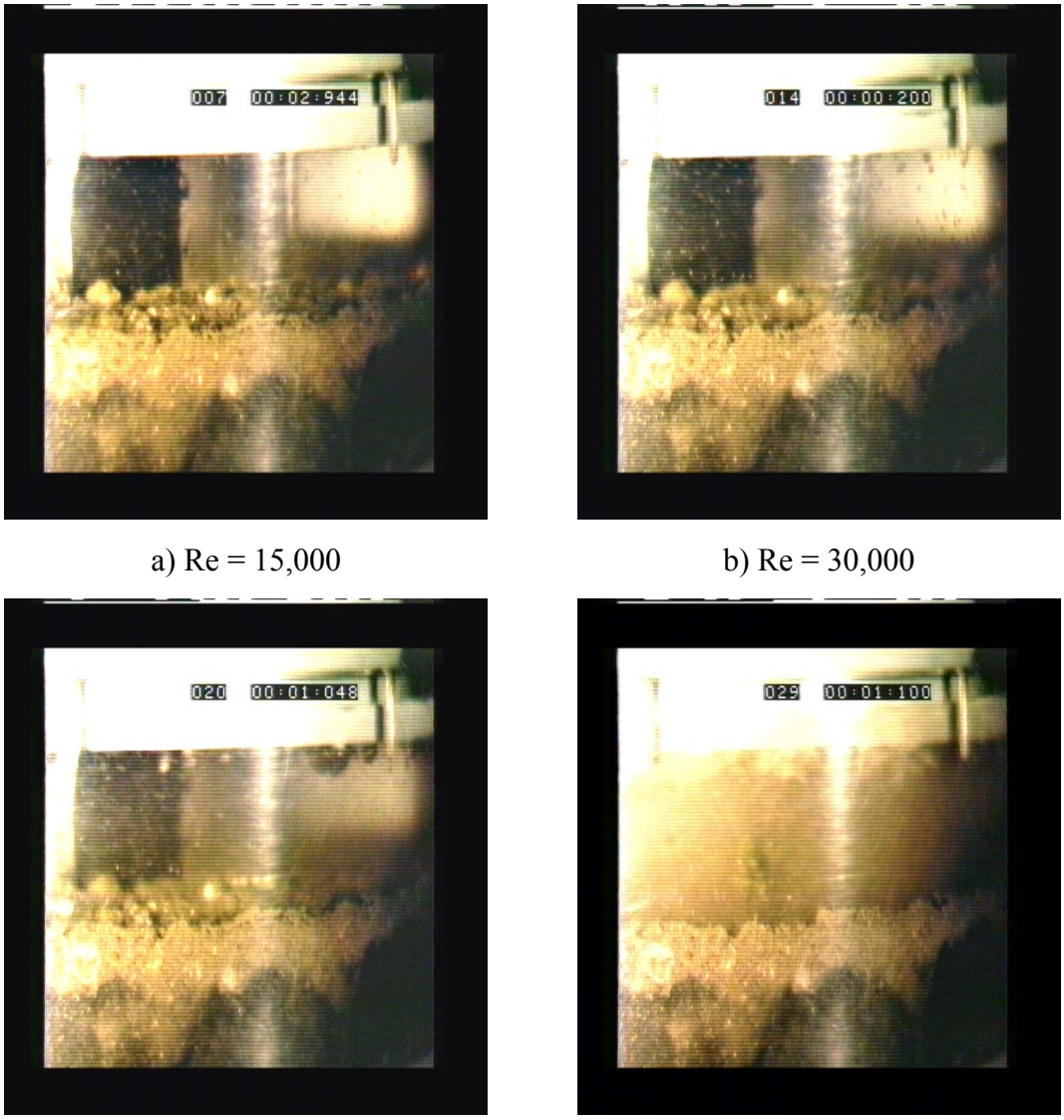

a) Re = 15,000 b) Re = 30,000

c) Re = 45,000 d) Re = 60,000

Figure 7.1- Erosion of a sediment bed

7.1.1 EXPERIMENTAL RESULTS

Results of the tangential velocity profiles at increasing Re are shown in Figure 7.2 for rough bed RB1.

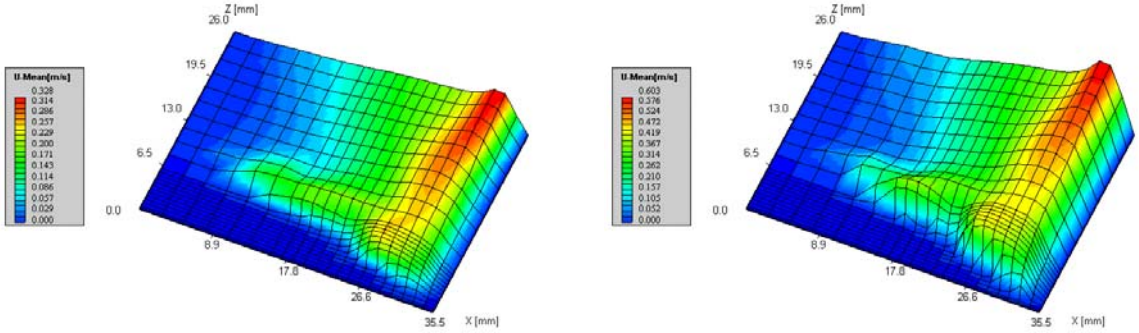

a) Re = 10,000 b) Re = 20,000

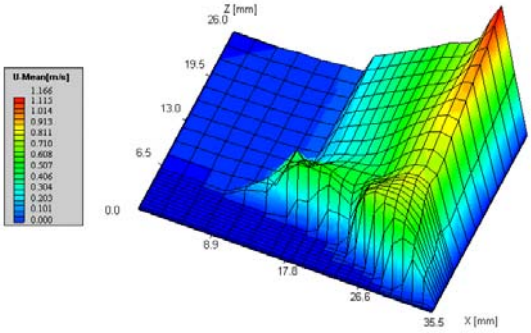

c) Re = 40,000

Figure 7.2- Tangential velocity field; RB1

For the other two test cases (RB2 and RB3), similar profiles are presented in Figures 7.3 and 7.4.

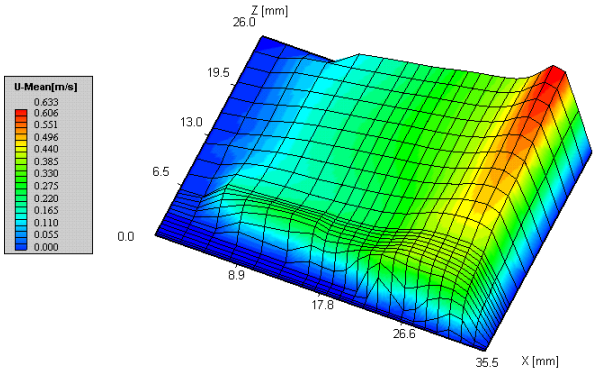

Figure 7.3- Tangential velocity field; RB2; Re=20,000

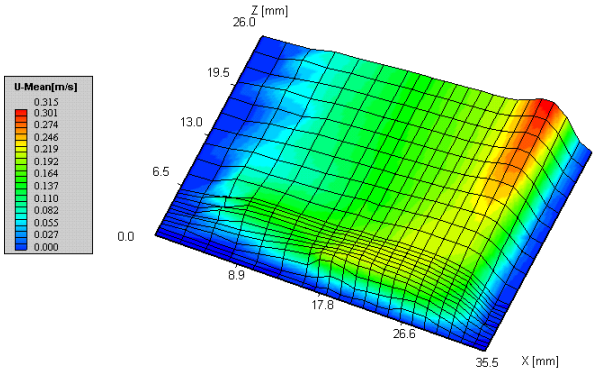

Figure 7.4- Tangential velocity field; RB3; Re=10,000

In Figures 7.2 through 7.4 it is possible to describe the shape of the bed surface, by the location of the zero velocity points, because no data was retrieved if the measuring probe volume is "inside" the bottom surface. In this case, the sediment is thicker near the inner wall of the flume cross section.

In general, the velocity profile shows a similar pattern to that previously described for a smooth surface: the bulk of the flow is pushed outwards and this effect is more evident as the Reynolds number is increased. However, for the same flow Reynolds number, the region of large velocity extends over a smaller cross section area; thus leading to higher maximum velocities in the field. Furthermore, the region of high velocity in the vicinity of the sediment bed is very small in size. These two effects combine to the occurrence of very high shear stresses near the sediment, when compared with those observed over a smooth surface. Even at lower Re, the velocity profile does show very strong gradients in a region confined to the sediment surface. The resulting higher shear stresses should lead to more favourable conditions for bed erosion; in other words, the surface roughness favours erosion.

Comparing Figures 7.2b and 7.3, it is observed that the maximum velocity is similar. The detailed topology of both beds is slightly different, as the location of zero velocity points shows. Only small details in sediment topology may render different shapes to the velocity profiles, but the basic characteristics are similar in both cases. For surface RB3 (Figure 7.4), the maximum velocity is not much different from that to RB1 (Figure 7.2a), both taken at Re = 10,000. Nonetheless the surface porosity, Figure 7.4 shows a reduction of the velocity gradient near the surface.

As far as the vertical component of the velocity is concerned (Figures 7.5 through 7.7), it is observed that a recirculation bubble is formed near the outer ring. The reference line (taken at around 7.5 *mm* from the outer wall) is also shown.

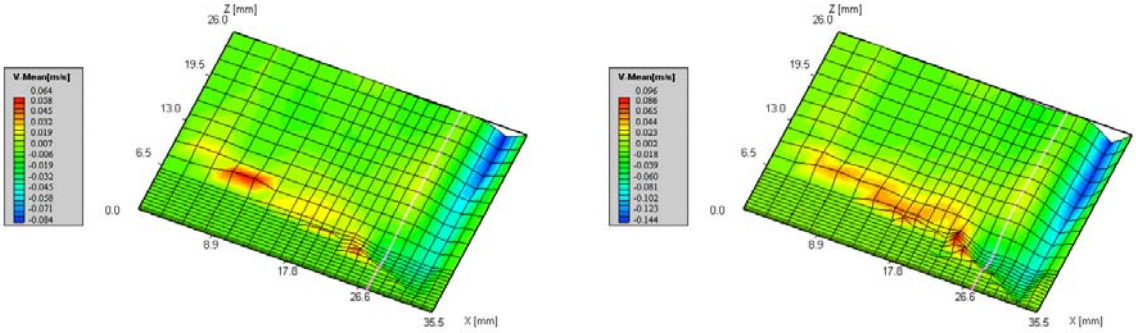

a) Re = 10,000 b) Re = 20,000

Figure 7.5- Axial velocity field; RB1

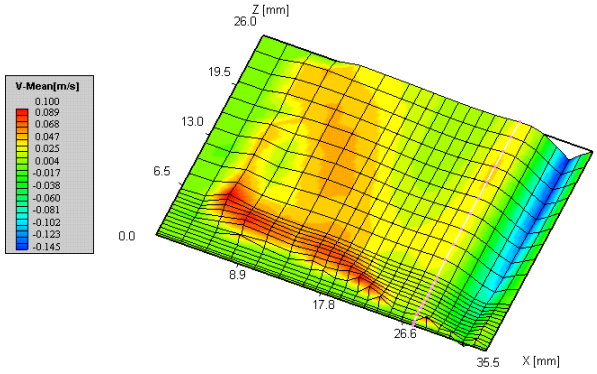

Figure 7.6- Axial velocity field; RB2; Re=20,000

Although the data is very similar for both RB1 and RB2, the recirculation patterns in the latter is extended over a wider area of the flume cross section. This is due to the shape of the "sediment" surface (higher slope in RB1), which drives more effectively the flow upwards, reducing the width of the recirculation pocket.

Results show that the reference line is located through a region of high flow recirculation (alternate upwards/downwards flow direction), for bed RB1. However, the flow is always upwards throughout the entire length of the reference line in RB2. The recirculation is due to both the outward driven flow and that locally induced by the bed topology, which extends over the flume cross section.

In addition, near the sediment bed other smaller recirculation pockets are formed, which is a typical feature of a rough surface. It appears that roughness breaks up the recirculation bubble into various smaller vortices located near the rough surface.

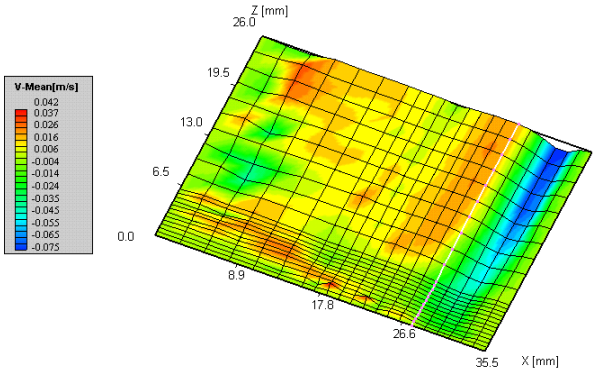

Figure 7.7- Axial velocity field; RB3; Re=10,000

Figures 7.8 through 7.10 show the tangential velocity turbulence profiles.

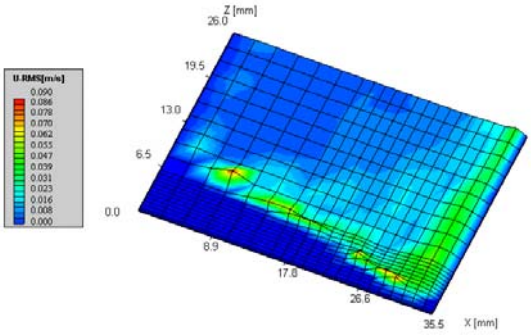

a) Re = 10,000

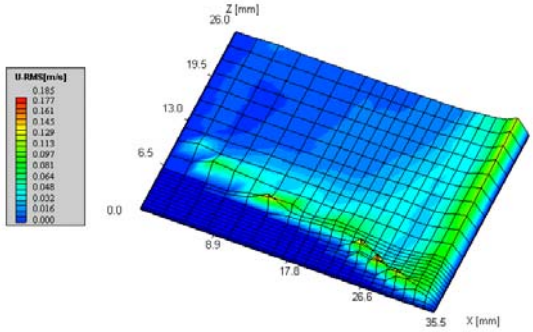

b) Re = 20,000

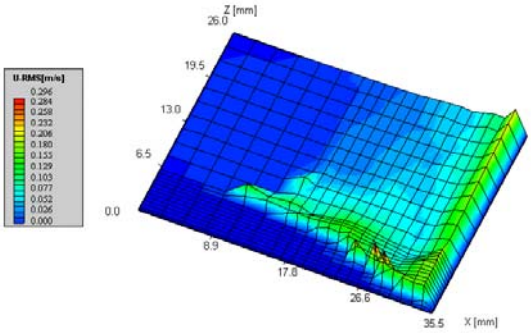

c) Re = 40,000

Figure 7.8- Tangential velocity turbulence field; RB1

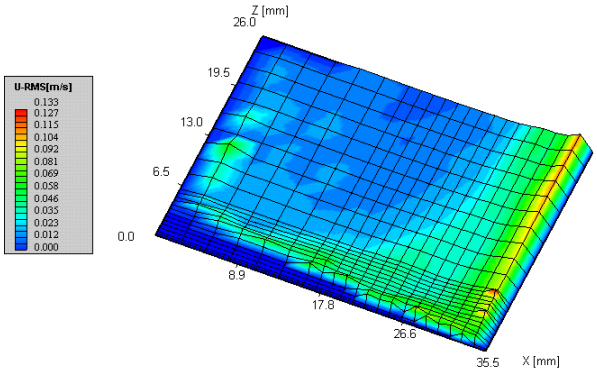

Figure 7.9- Tangential velocity turbulence field; RB2; Re=20,000

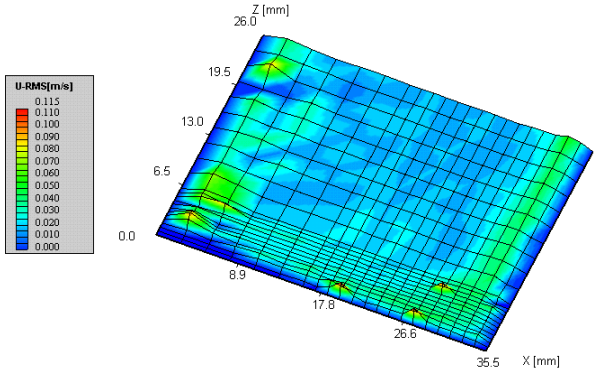

Figure 7.10- Tangential velocity turbulence field; RB3; Re=10,000

The data shows that turbulence levels are much higher than those measured over a smooth surface (Figures 6.7a through 6.7c). For RB1, the turbulence is enhanced by a factor above 100 % at low Reynolds numbers and at around 60 % for the highest Re. In addition, the highest levels of turbulence are located close to the surface, which leads to the conclusion that local roughness is a prime factor in controlling the turbulence structure of the flow. This is opposed to the profiles observed with the flat bed geometry, in which high turbulence levels are primarily located near the outer wall.

Also in Figure 7.8c, it is observed that near the inner wall the flow is of very low turbulence, being nearly laminar. This suggests that the flow structure is controlled by smaller scales rather than the large-scale phenomena that characterise the flow instabilities over smooth surfaces.

An increase in turbulence with Reynolds number can be observed in Figure 7.8, that is related with the reduction of the boundary layer thickness. Typical values of turbulent

intensity were found in the order of 20 %, being approximately twice of those measured on smooth beds.

Figures 7.11 and 7.12 show the isotropic ratio for each one of the test cases evaluated in this study (grey areas are considered non isotropic).

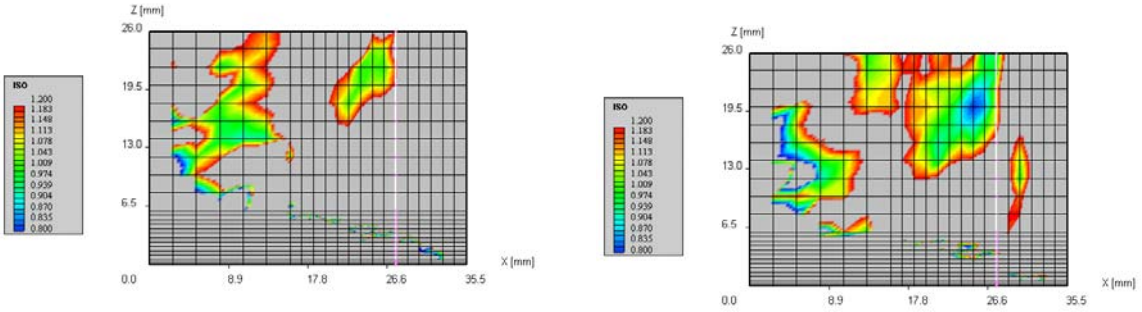

a) Re = 10,000

b) Re = 20,000

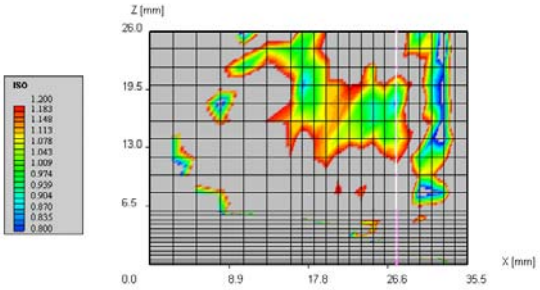

c) Re = 40,000

Figure 7.11- Isotropic ratio; RB1

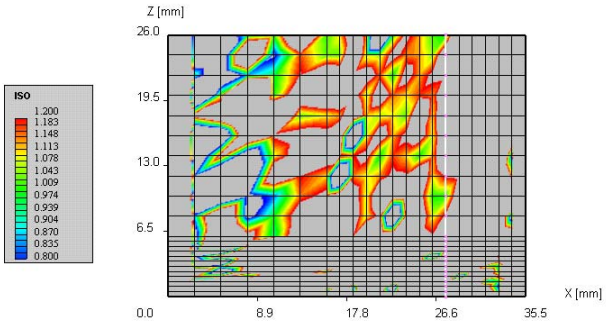

Figure 7.12- Isotropic ratio; RB3; Re=10,000

The results show that for most of the cross section the flow is non isotropic, being the tangential turbulence higher than the crosswise component.

As on a smooth bed, the regions of isotropic turbulence are moved to the outer wall when Re increases (Figure 7.11). It is also observed that, for a flow over rough surfaces, the areas of isotropic turbulence are spread over the entire flume section. Also, the data for RB3 shows large areas of isotropic turbulence even for low Re. Such finding may be expected due to the regular pattern of roughness distribution over the bottom surface of the flume.

Figures 7.13 through 7.15 present the total shear stresses obtained. From these results, it can be observed that the shear stress distribution shows a qualitative pattern similar to that found on a smooth surface (Chapter 6, Figure 6.12). However, the values of the shear stress are much higher than those reported in Chapter 6, due to both turbulent and viscous stresses. Such behaviour is more evident at higher Re (Figure 7.13c).

For most of the cross section of the flume, the shear is approximately zero because of the low local turbulence and uniform velocity profiles. In fact, non zero shear stresses are located in the close vicinity of the "sediment" surface, which highlights the relevance of surface roughness upon the fluid shear. Such enhancement increases the likelihood of erosion.

Because of negative velocity gradients, the shear stress usually shows negative values inside fluid boundary layer over the bottom surface.

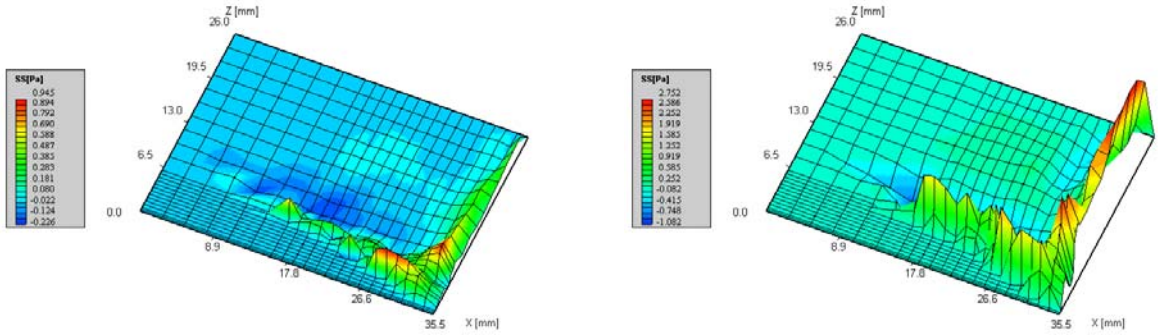

a) Re = 10,000 b) Re = 20,000

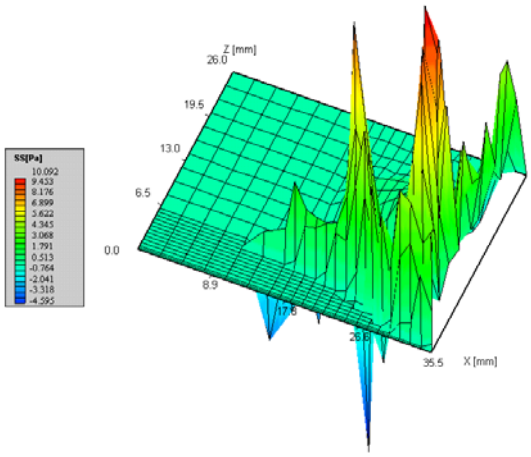

c) Re = 40,000

Figure 7.13- Shear stress field; RB1

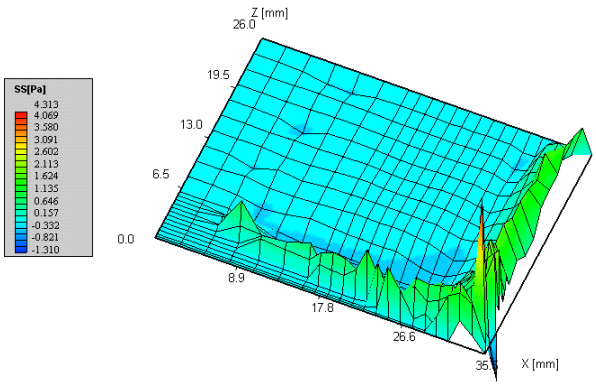

Figure 7.14- Shear stress field; RB2; Re=20,000

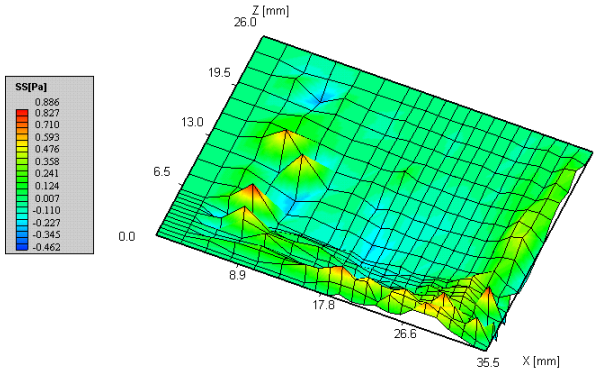

Figure 7.15- Shear stress field; RB3; Re=10,000

7.1.2 BOUNDARY LAYER ANALYSIS

In this section, a detailed analysis of the boundary layer over the four types of surfaces (SB, RB1, RB2 and RB3) is evaluated. This analysis is confined to a single vertical profile at approximately 7.5 *mm* from the outer wall, where the phenomena associated with the sediment erosion is more relevant. This profile is also outside the region of high velocity gradients over the outer wall.

Figures 7.16, 7.17 and 7.18 depict the mean tangential velocity for each one of the surfaces tested, at Reynolds number of 10,000, 20,000 and 40,000, respectively.

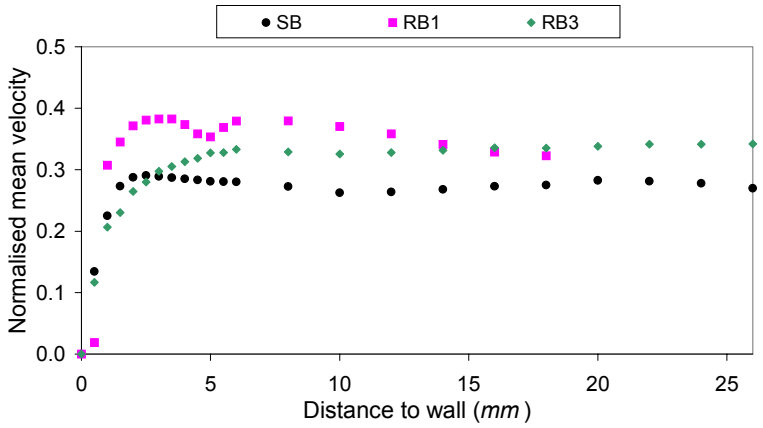

Figure 7.16- Normalised mean tangential velocity; Re=10,000

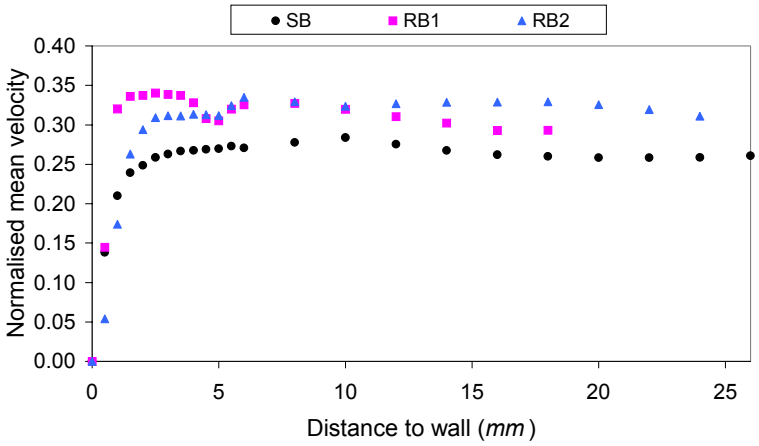

Figure 7.17- Normalised mean tangential velocity; Re=20,000

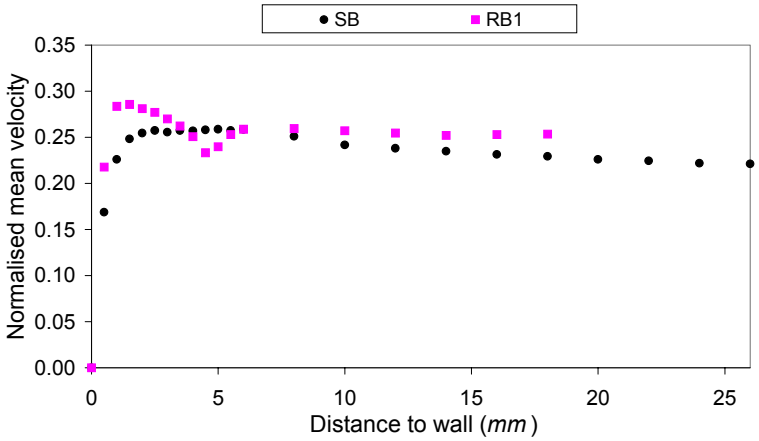

Figure 7.18- Normalised mean tangential velocity; Re=40,000

The velocity profiles for the surfaces RB1 and RB2 show changes in the velocity gradients. This may be related with the cavities existent at the surface, which may cause adverse pressure gradients (Gallagher, 1998).

The data shows that, at higher Re (20,000 and 40,000), the maximum of the mean flow velocity takes place closer to the bottom wall of the rough surfaces. Such reduction of the boundary layer increases the local shear stresses, as shown in Figure 7.19 for Re = 20,000, where data is compared with that obtained on a smooth surface.

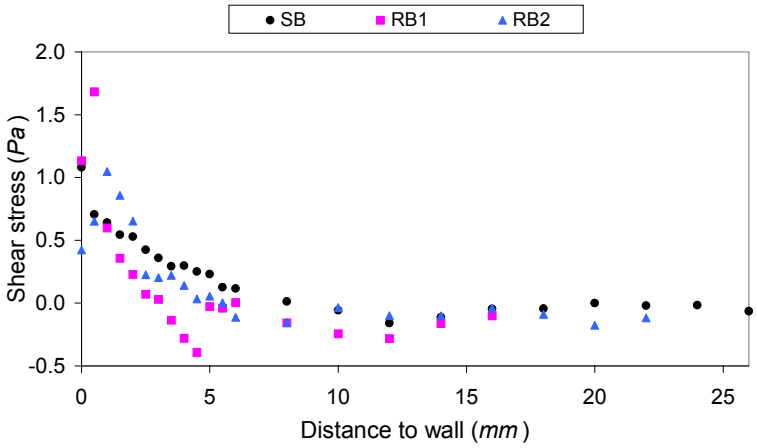

Figure 7.19- Shear stress on a smooth and rough beds; Re=20,000

The shear stress presented includes both the laminar, which is dominant near the interface, and the turbulent components. Laminar shear stress was determined using Equation 3.22, approximating the derivative by a two point approximation, and turbulent component was determined through Equation 3.23, being cross-moments given by the LDA data at that position.

Reductions in the outer region may be caused by local flow recirculation. Figure 7.20 presents the axial velocity field obtained for beds SB and RB1, by truncating the data below 0 *m/s* for a better distinction between the upwards/downwards flow. Regions of downwards flow are identified by the grey areas.

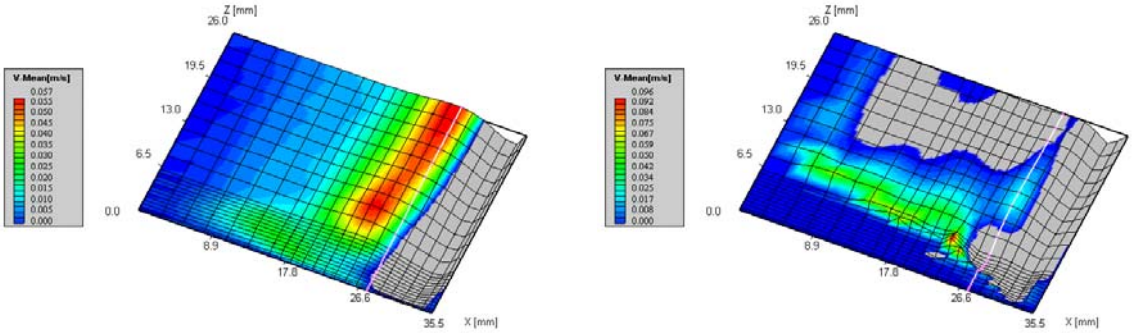

a) SB b) RB1

Figure 7.20- Axial velocity field truncating the scale; Re=20,000

Figures 7.21 through 7.23 show the mean velocity distributions for smooth and rough wall boundary layers, normalised by wall variables, for the various Reynolds numbers.

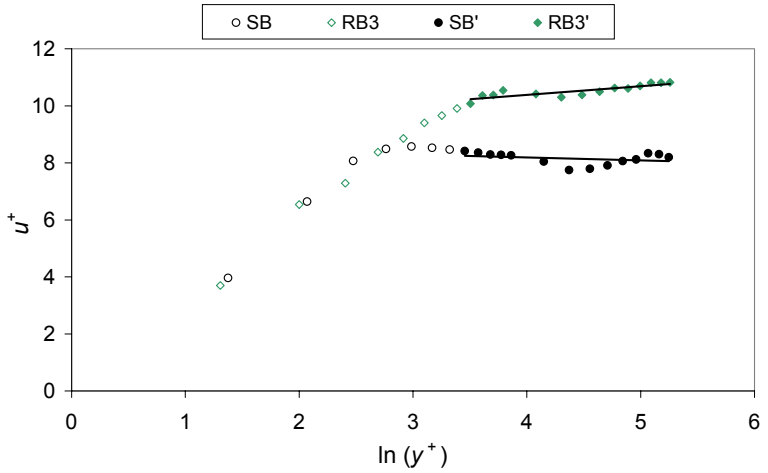

Figure 7.21- Mean velocity profiles; Re=10,000

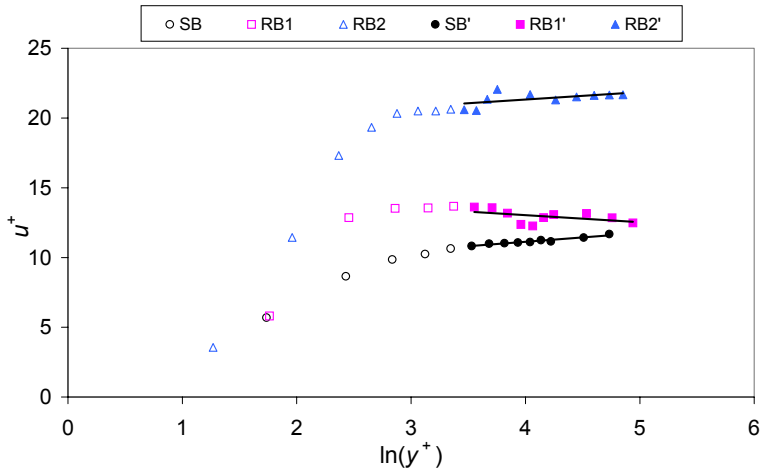

Figure 7.22- Mean velocity profiles; Re=20,000

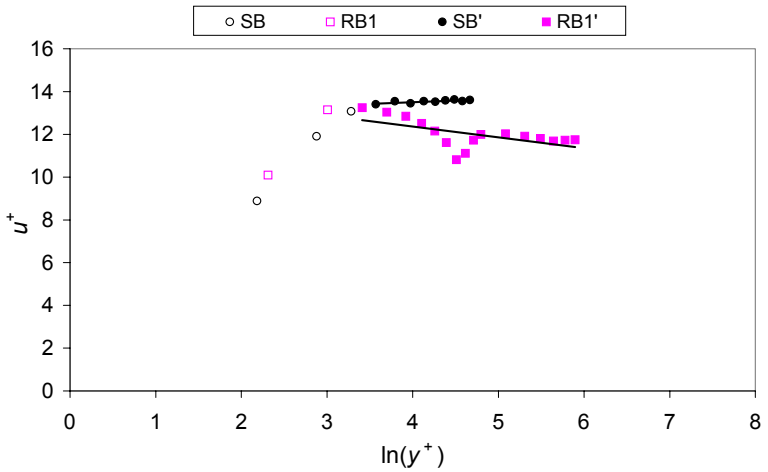

Figure 7.23- Mean velocity profiles; Re=40,000

From Figures 7.21 through 7.23 some insight can be made from the boundary layer. It is observed that the velocity profiles for both rough and smooth beds converge in the laminar sub-layer, which is a typical feature of wall flows. Applying the log-law, the von Kárman constant was found to be much higher than that expected on pipe flows (0.41). Thus, and considering the Equation 6.7, it may be concluded that the mixing length is higher in the flume flow. Furthermore, the high values for the von Kárman constant (and, therefore, the mixing length) appear to be linked to the turbulence enhancement that is observed in this kind of flow.

Table 7.1 presents the von Kárman constant (κ) for each bed.

Table 7.1- von Kárman constant

Re	Surface	κ
10,000	SB	-9.61
	RB3	3.29
20,000	SB	1.54
	RB1	-2.00
	RB2	1.87
40,000	SB	6.40
	RB1	-1.97

The negative values obtained may be due the occurrence of secondary flows and a complex pattern of recirculation zones in the vicinity of the wall, as well as further away from the wall, towards the inner ring, as observed previously in the axial velocity profiles (Figures 6.5a and 7.5b). It suggests that the standard law of the wall may not be applicable in this kind of flow, because the experimental data of u^+ *versus* y^+ in a semi-log diagram does not fall into a straight line over the entire overlap zone, as depicted in Figure 6.1. These results are in line with the not so good results obtained, near the wall, for the numerical simulations (section 6.3).

Because of the secondary flows in a rotating annulus, Sheng (1989) has modified the law of the wall by including the effect of radial pressure gradient. Gust and Southard (1983) also found that, in bed under load, the universal law of the wall is not observed. Thus, a logarithmic layer was found to extend further into the wake region, having a reduced value of von Kárman constant ($\kappa = 0.32 \pm 0.04$), which is related with different momentum transfer processes. Also, Petit (1990) refer that the value of κ may vary, from 0.2 for high concentration of material in suspension, up to the range 0.5-0.8 as a function of channel curvature and in the presence of helicoidal movements. The validity of the classical log-law that describes the overlap region of the mean velocity profile has been questioned by Buschmann and Gad-el-Hak (2003). These authors present other power laws as alternatives, in which coefficients are dependent on the Reynolds number. Such results are in agreement with those reported here.

The shift in the velocity profile (Δu^+) from the smooth wall log-law to the rough surfaces is also shown. In Figures 7.21 and 7.22 that shift is upward, being: -0.57 to RB3, at Re = 10,000; -6.51 and -10.65 to RB1 and RB2, respectively, at Re = 20,000. The upward shift means that the roughness has an effect of decreasing the boundary layer (and subsequently the laminar sub-layer) increasing the flow turbulence. In fact, Figure 7.22 shows a very different profile for both rough beds RB1 and RB2, producing a shift with different magnitude. This confirms that the effects of the surface roughness on the mean flow for the two rough beds are different. Because the surface roughness (average) is very similar in both cases, this observation suggests that it is the local shape of the sediment rather than the actual roughness the factor that controls the velocity profile. A downward shift was obtained in Figure 7.23 ($\Delta u^+ = -1.507$).

Further insight can be gained from Figures 7.24 through 7.26, which show the normalised mean velocity-defect across the boundary layer.

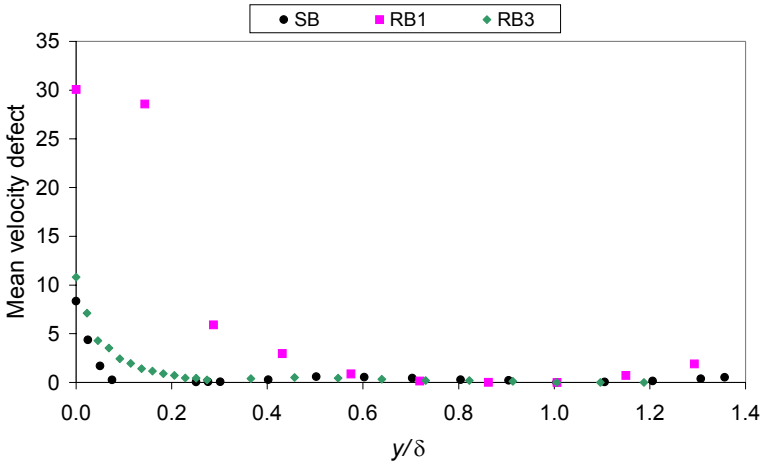

Figure 7.24- Mean velocity-defect; Re=10,000

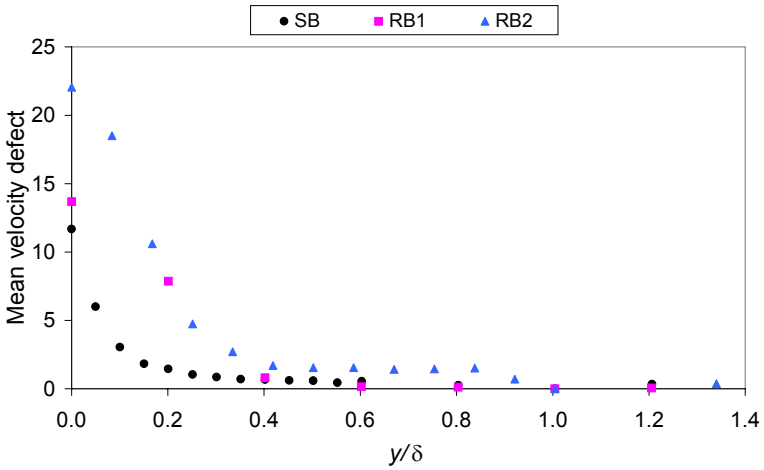

Figure 7.25- Mean velocity-defect; Re=20,000

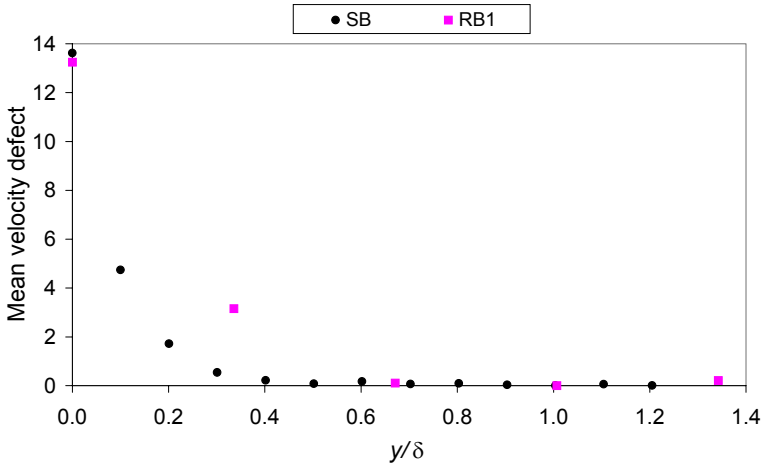

Figure 7.26- Mean velocity-defect; Re=40,000

The velocity-defect plots show that the profiles over rough surfaces are similar to those over a smooth wall in the outer layer, suggesting that surface roughness effects are mainly restricted to the inner wall layer. The deviations in the velocity-defect profiles near the surface suggests that the momentum transport in the fluid is not entirely wall driven and the individual characteristics of the toroidal flow in the flume (secondary flow, recirculation bubbles) may play an important role in momentum transfer in the boundary layer.

It is also observed that, for the uniformly distributed roughness (RB3), the profile is close to that found on smooth beds. Although the average roughness of this surface is higher than that of the other surfaces (irregular roughness), this behaviours suggests that the topology is a far more important factor than the actual mean values of the surface roughness.

Keirsbulck *et al.* (2002) found that, outside the roughness sub-layer (corresponding to about twice the roughness height), the turbulent motions do not depend on the wall roughness, although they are affected in the inner region. In the present study, similar findings can be made in Figures 7.24, 7.25 and 7.26.

Based on the theoretical discussion previously outlined in this text, Table 7.2 presents the characteristics of the different surfaces and the boundary layer parameters for each experimental condition.

The mean roughness height ($\bar{k}$) was based on White (1986) (in a commercial pipe) for SB, mean roughness height (section 5.8) for surfaces RB1 and RB2, and the beads mean diameter for RB3.

The free stream velocity (u_∞) and boundary layer thickness (δ) were determined using the mean tangential velocity profiles. On the other hand, the friction velocity (u^*) and the local skin friction coefficient (c_f) were calculated through Equations 3.35 and 6.11. It must be pointed out that there are some uncertainties in some of the boundary layer parameters, due difficulties in their measurement. As expected, for the same surface, the boundary layer thickness decreases when increasing the flow velocity (Re).

Table 7.2- Boundary layer parameters

Surface	Re	$\bar{k}$ (mm)	u_∞ (m/s)	δ (mm)	u^* (m/s)	c_f $(\times 10^2)$
SB	10,000	1.5×10^{-3}	0.184	19.9	0.022	2.86
	20,000		0.371	9.95	0.032	1.49
	40,000		0.675	4.98	0.050	1.10
RB1	10,000	0.571	0.250	3.48	0.008	0.20
	20,000		0.444	2.49	0.032	1.04
	40,000		0.746	1.49	0.056	1.13
RB2	20,000	0.512	0.437	5.97	0.020	0.42
RB3	10,000	2.275	0.223	21.89	0.021	1.77

From the experimental data, the normalised Reynolds stresses can be retrieved: Reynolds shear stresses ($-\overline{u'^+v'^+}$), perpendicular to the wall; Reynolds normal stresses ($\overline{u'^{+2}}$) parallel and ($\overline{v'^{+2}}$) perpendicular to wall.

The normal stresses $\overline{u'^{+2}}$ are presented in Figures 7.27, 7.28 and 7.29 and the normal stresses $\overline{v'^{+2}}$ are shown in Figures 7.30, 7.31 and 7.32, for the various Reynolds number.

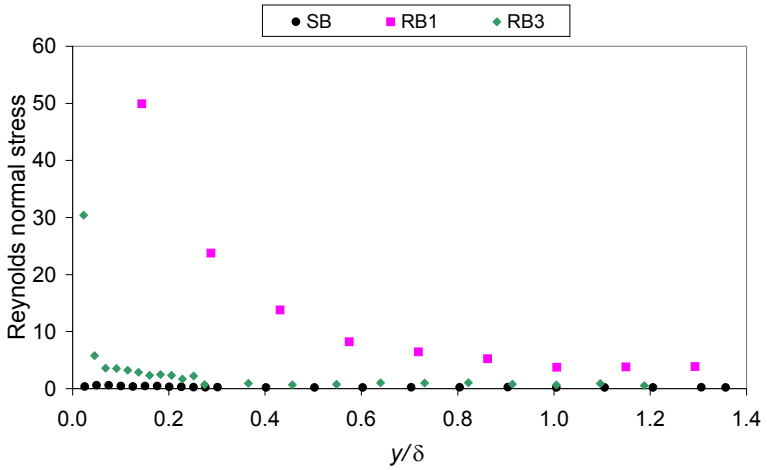

Figure 7.27- Streamwise Reynolds normal stresses; $\overline{u'^{+2}}$; Re=10,000

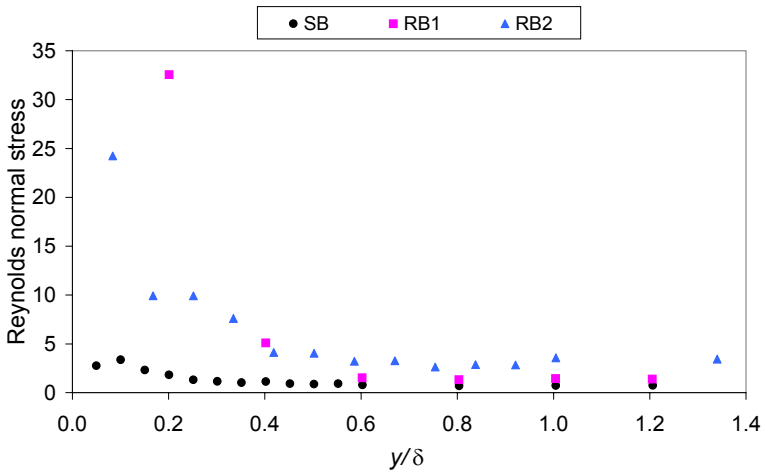

Figure 7.28- Streamwise Reynolds normal stresses; $\overline{u'^{+2}}$; Re=20,000

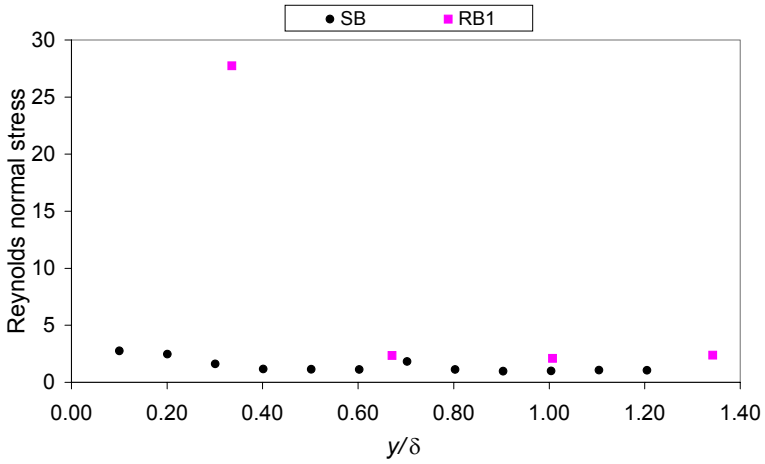

Figure 7.29- Streamwise Reynolds normal stresses; $\overline{u'^{+2}}$; Re=40,000

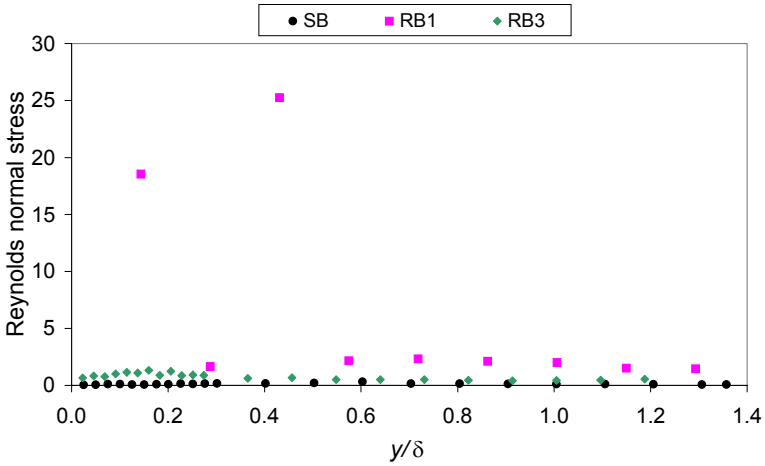

Figure 7.30- Crosswise Reynolds normal stresses; $\overline{v'^{+2}}$; Re=10,000

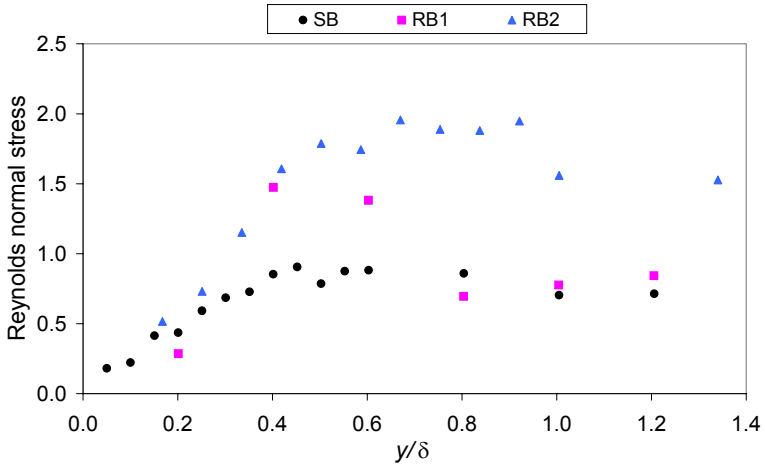

Figure 7.31- Crosswise Reynolds normal stresses; $\overline{v'^{+2}}$; Re=20,000

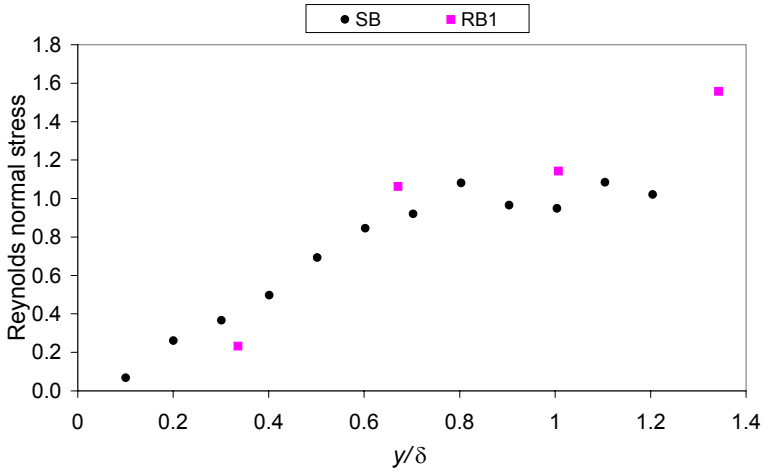

Figure 7.32- Crosswise Reynolds normal stresses; $\overline{v'^{+2}}$; Re=40,000

The normal stresses show considerable sensitivity to the boundary conditions in the vicinity of the surface. Large differences are observed between the smooth wall and the rough surfaces, as well as between the rough surfaces for over half of the boundary layer thickness. These differences are emphasized in the inner layer for $\overline{u'^{+2}}$ stresses, and in the outer layer for $\overline{v'^{+2}}$ stresses. Considerable differences were also obtained by other researchers in different flow configurations (Krogstad and Antonia, 1999). It is observed in Figures 7.27 and 7.30 a good approximation of the artificial sandy bed (RB3) with the smooth bed.

Important differences between the surfaces are also found for the Reynolds shear stresses, as shown in Figures 7.33 through 7.35.

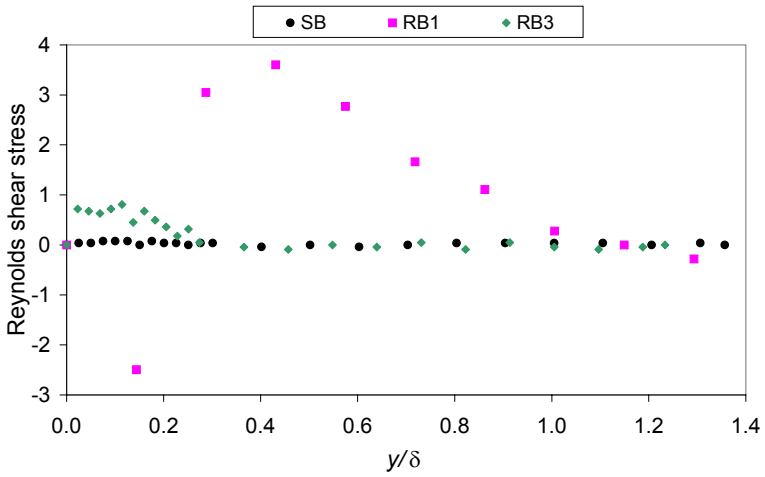

Figure 7.33- Reynolds shear stresses; $-\overline{u'^{+}v'^{+}}$; Re=10,000

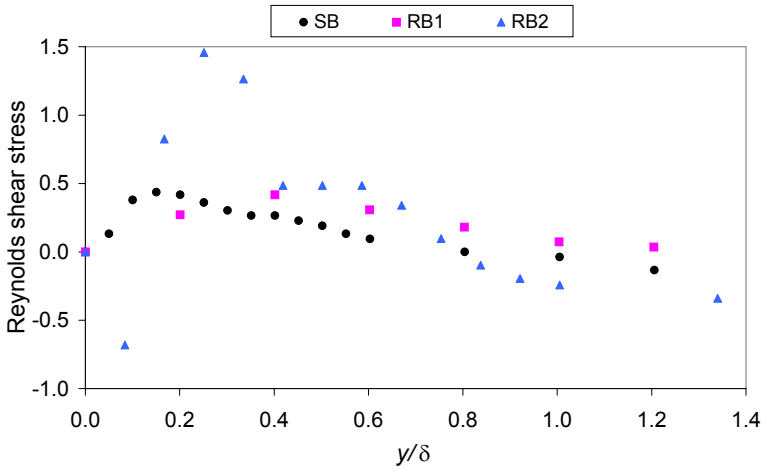

Figure 7.34- Reynolds shear stresses; $-\overline{u'^{+}v'^{+}}$; Re=20,000

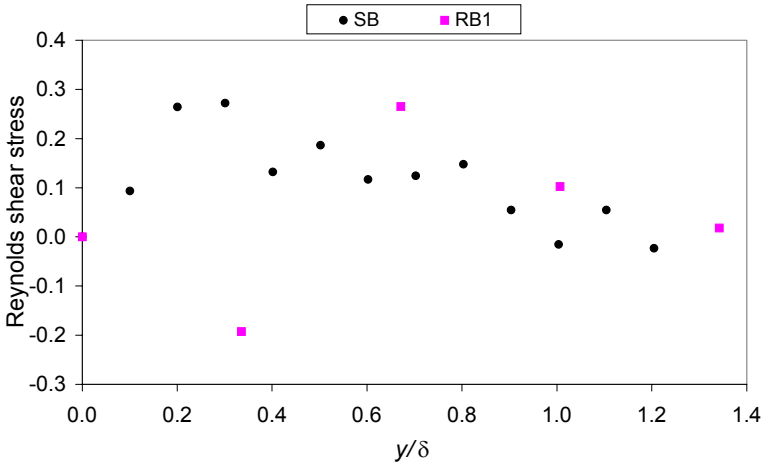

Figure 7.35- Reynolds shear stresses; $-\overline{u'^{+}v'^{+}}$; Re=40,000

From this data, it may be concluded that the turbulent shear stresses are of prime importance in the regions closer to the wall although they approach zero in the laminar sub-layer. In addition, Figure 7.34 shows that, on a flow over a rough surface, the maximum of the shear stress is shifted into a region further away from the wall, when compared with the flow over a smooth surface. This may be due to the enhanced turbulent momentum transfer in the crosswise direction occurring on a rough wall.

Some of these differences may be also due to possible measurement errors in the region very close to the wall, for the rough beds. Occasionally, the existence of orifices makes the measurement with the laser technique difficult. This problem was also pointed out by Krogstad and Antonia (1999), who referred authors that, during their measurements in rough walls, required the use of a flying hot wire technique. However, these measurement uncertainties may only partially explain the differences observed very close to the wall.

It should be referred that in Figures 7.31 and 7.34, $\overline{v'^{+2}}$ and $-\overline{u'^{+}v'^{+}}$ are largest for the bed RB2, implying a much stronger momentum transport for this surface. The same observations are also made for bed RB1, in Figures 7.30 and 7.33. Comparing both Reynolds normal stresses with turbulent kinetic energy (k^{+}) plots (Figures 7.36, 7.37 and 7.38), it may be stated that in all cases $\overline{u'^{+2}}$ has a dominant contribution to k^{+}.

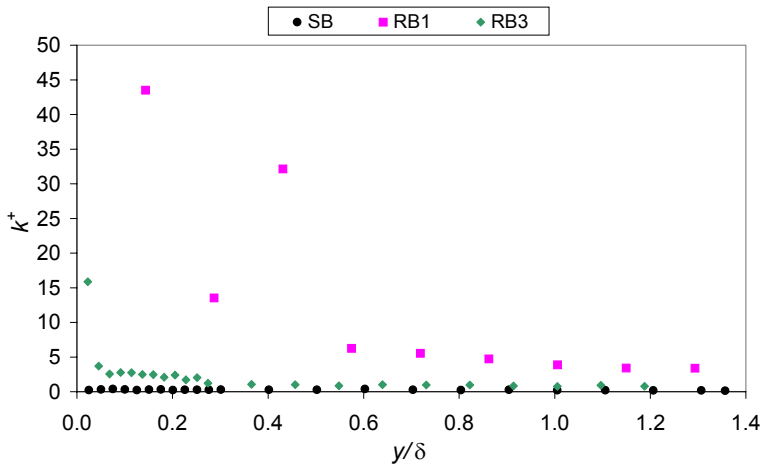

Figure 7.36- Turbulent kinetic energy; Re=10,000

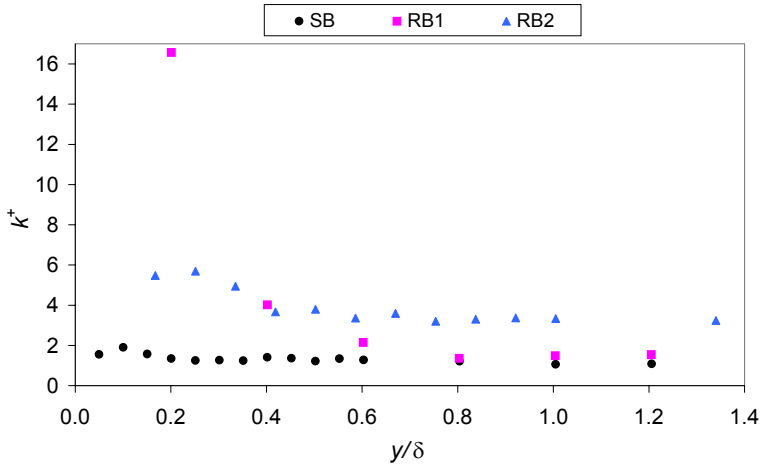

Figure 7.37- Turbulent kinetic energy; Re=20,000

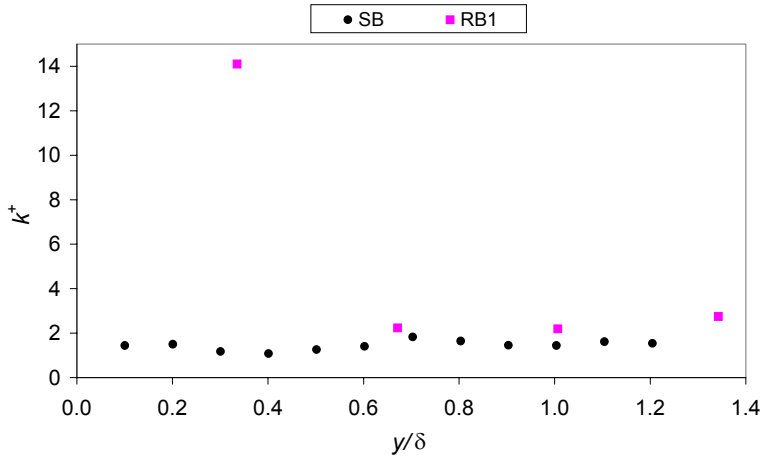

Figure 7.38- Turbulent kinetic energy; Re=40,000

The turbulent kinetic energy is higher for the rough beds when compared with that on a smooth surface, corresponding at larger eddies. In Figure 7.37, the higher values for RB2 may be related with high value of the von Kárman constant observed when compared with that for a smooth bed.

The profiles for the production (P^+) and the rate of dissipation (ε^+) of mean turbulent energy for all the surfaces considered are presented, for the various Reynolds numbers. Thus, Figures 7.39 and 7.40 present those variables at Re = 10,000.

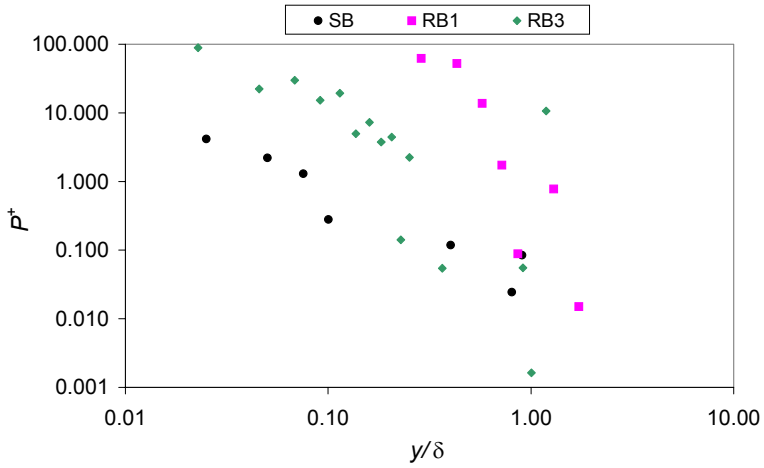

Figure 7.39- Rate of production of mean turbulent energy; Re=10,000

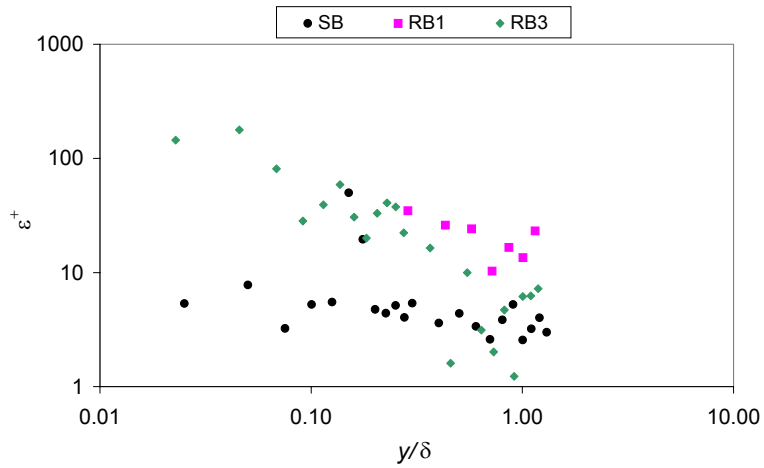

Figure 7.40- Rate of dissipation of mean turbulent energy; Re=10,000

Although in Figure 7.39 all data shows a similar trend, turbulent energy production is clearly dependent on the surface. The RB1 surface presents high values. The same behaviour was observed for the dissipation of turbulent energy (Figure 7.40).

The production and dissipation of turbulent energy at Re = 20,000 and Re = 40,000 is shown in Figures 7.41 through 7.45.

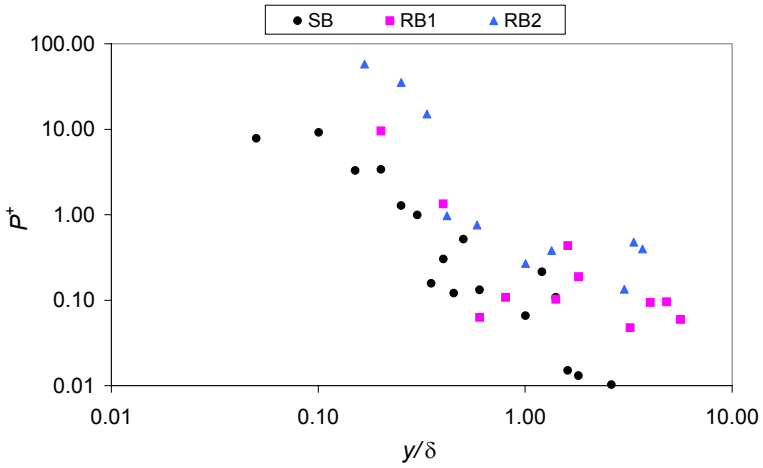

Figure 7.41- Rate of production of mean turbulent energy; Re=20,000

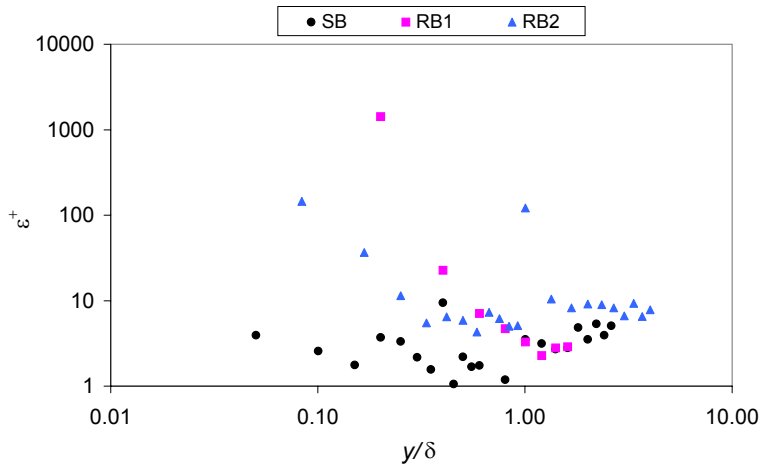

Figure 7.42- Rate of dissipation of mean turbulent energy; Re=20,000

A comparison of the dimensionless production/dissipation turbulent energy is made in Figure 7.43 taking the surface RB2, as an example.

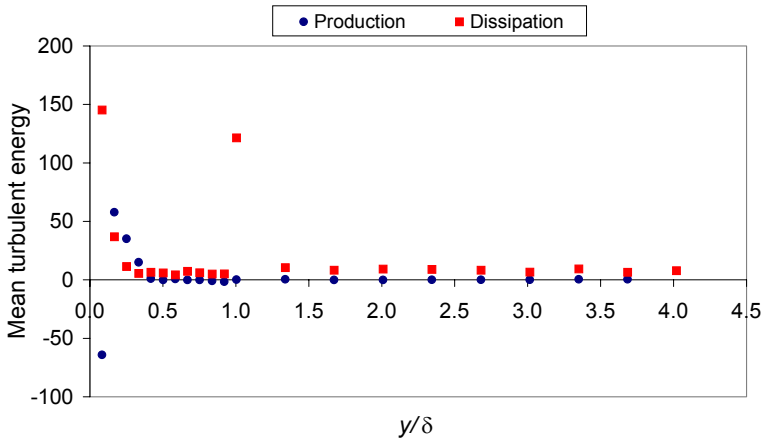

Figure 7.43- Rate of production/dissipation of mean turbulent energy; RB2

It is observed a higher rate of energy dissipation through the boundary layer, except in some regions close to the wall, where a higher energy production is observed. Energy production decreases to a position where energy dissipation is approximately equal to energy production. This means that the energy production takes place in other regions of the flow field. Similar observations were made for the other surfaces, even at higher Reynolds number. It is also observed in Figure 7.43 a strong negative energy production in the vicinity of the wall, what means that the fluid is non accelerated, occurring an extraction of energy from the turbulent vortices to the mean flow motion, decreasing the turbulence (the mean motion gives a negative contribution to the turbulence energy). In this experimental work, the higher production of turbulent energy does not correspond to a proportionally higher dissipation. Laufer (1954) has shown that, in fully developed turbulent pipe flow, for most of the tube cross section the rate of energy production at a point is approximately balanced by the rate of energy dissipation. In addition, both P and ε show a sharp maximum near the edge of the laminar sub-layer. A similar pattern is observed in the present research.

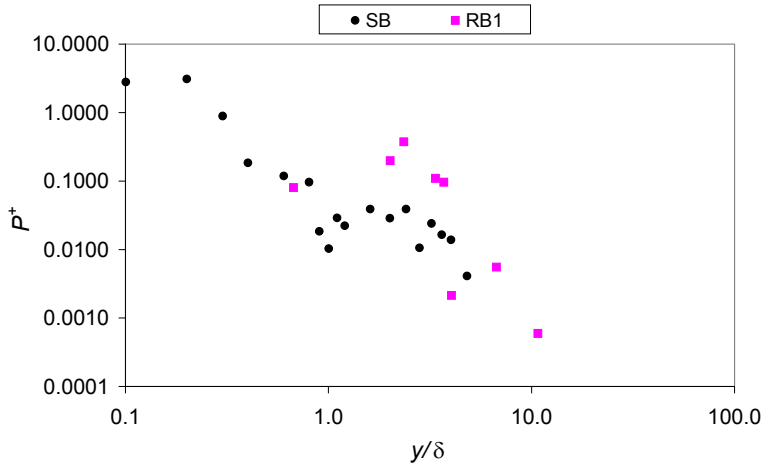

Figure 7.44- Rate of production of mean turbulent energy; Re=40,000

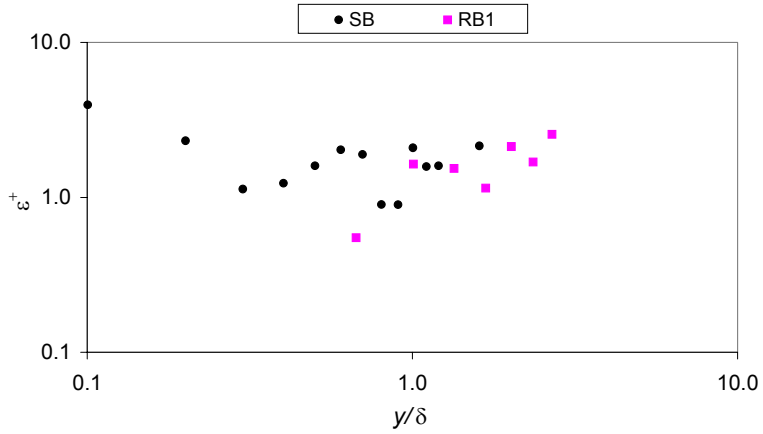

Figure 7.45- Rate of dissipation of mean turbulent energy; Re=40,000

The enhanced production rate throughout the layer for RB2 (Figure 7.41) is primarily due to an increase in the magnitude of the Reynolds shear stress (Figure 7.34). Figure 7.42 shows a greater energy dissipation for the rough beds, which results from the existence of larger eddies that are broken into smaller eddies, dissipating energy in the process.

It is observed that both the production and dissipation of mean turbulent energy near the wall are affected by the surface geometry. Thus, any turbulence model which does not take into account the surface roughness geometry will not be able to properly predict the transport characteristics of the flow.

From all these observations, the turbulent transport mechanisms near the wall strongly depend on the surface topology. This generates a highly complex flow pattern of reduced boundary layer thickness, high turbulence intensity and shear stress and multiple recirculation pockets. The data shows that the local shear stress is strongly enhanced, which leads to more favourable conditions for sediment erosion to occur. It was concluded that the higher momentum transfer in the crosswise direction in a flow over a rough surface shifts the maximum of the Reynolds stresses away from the surface. Thus, the characterisation of the roughness by simply analysing its effect on the mean velocity profile becomes inadequate.

Concerning the skewness (***S***) and flatness (***F***) obtained for smooth and rough walls boundary layers, Figures 7.46 and 7.47 show the data for the tangential velocity component $\boldsymbol{S}_u$ and $\boldsymbol{F}_u$, respectively, at Re = 10,000.

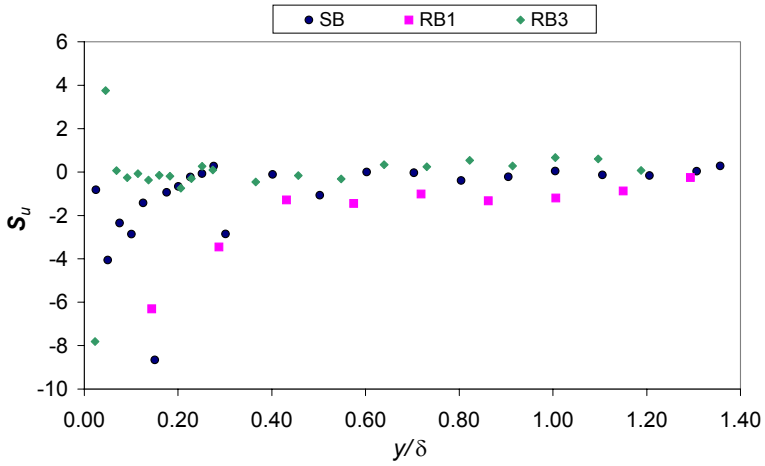

Figure 7.46- Skewness; Re=10,000

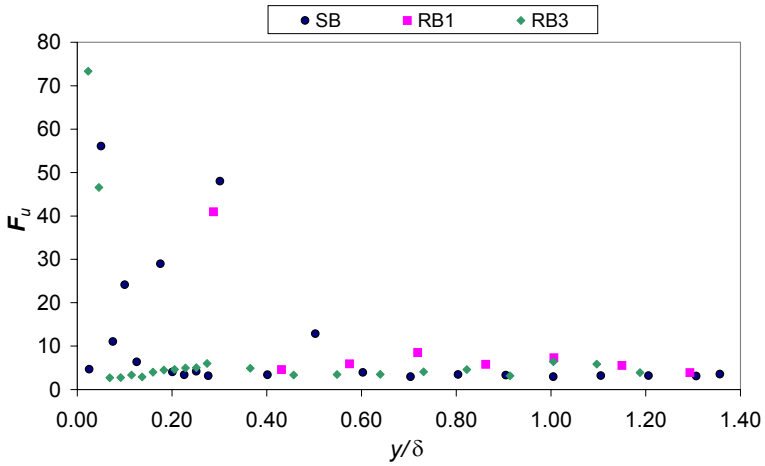

Figure 7.47- Flatness; Re=10,000

Figure 7.46 shows, in the near wall region, high negative values for RB3, when compared with those for SB, suggesting the dominance of ejection events (frequent and energetic movements of fluid vertically, upwards). Different results were found by Keirsbulck *et al.* (2002), where the sweep events (high velocity parcels of water moving downwards associated with moving eddy structures) dominated in the near-wall region. Sweep events are observed mostly on RB3, by the occurrence of positive values. Ejections and sweeps are two transport modes near the wall, and the last ejection (from various close to each other) is immediately followed by a strong sweep (Sechet and Le Guennec, 1999). For $y/\delta > 0.4$ data is not much different for the three beds; the influence of the roughness is emphasized as the distance from the wall decreases. Data for RB1 is more similar to that of SB. In general, close to the wall, ejections are the major events contributing to the fluid movement, although some sweeps may also be involved. Concerning the flatness (Figure 7.47), great differences are also observed to the three beds in the region close to the wall.

For regions far from the wall, it is observed that both factors present some deviations from that usually expected (Hinze, 1987): 0 for the skewness and 3 for the flatness, if a Gaussian velocity distribution was valid.

7.2 INFLUENCE OF ENTRAINED PARTICLES

The present section reports the data concerning the contribution of entrained particles upon the main flow configuration and the turbulence. As previously mentioned, the particulate beds are made of dispersed glass beads, initially deposited in the flume. Bead entrainment occurs when the force produced by the fluid exceeds that of the resisting forces of the beads in the bed.

7.2.1 FLOW OVER A DEFORMING PARTICLE LAYER

Due to the particular characteristics of the interface fluid/bed, it is necessary some detailed description of the whole process of data retrieving (average and turbulent velocities) for the current setup.

During the course of the experiments, it was possible to observe the simultaneous formation of three similar dunes, equally spaced along the perimeter, which are continuously deformed by the moving fluid. Assuming that the flume perimeter is approximately 300 *mm*, the distance between consecutive dunes is approximately 100 *mm*. The macroscopic motion of these large-scale formations is characterised by the continuous entrainment and deposition of individual particles by the fluid moving above the bed, as shown in Figure 5.26. The formation of these dunes may be related with the existence of secondary flows typical from the flume. As referred by Torfs *et al.* (1994), their formation depends strongly on the shape of the flume cross-section. Their quantity and stability depends also on flow depth (Engelund, 1975). On the other hand, in tests carried out by Bennett and Best (1996) using a recirculating flume (10 *m* long and 0.3 *m* wide) and glass spheres of 220 μm, it was observed the formation of ripples ranging from 5 to 25 *mm* in height and 70 to 120 *mm* in length. The mean flow depth and velocity was 0.1 *m* and 0.4 *m/s*, respectively.

Although, the quantity of the various beads inside the flume was similar, the height of the dunes was different: 15, 11 and 8 *mm* for different size beads P1, P2 and P3, respectively (Chapter 5). For particles P4, it was not possible to observe any dune because the beads were evenly dispersed in the flume at higher Reynolds number (Re = 40,000) and virtually did not move at lower velocities (Re = 20,000). These differences are related with the settling velocity of the particles, which is very small for the beads P1 (0.021 *m/s*) and high for particles P4 (0.252 *m/s*), when compared with the mean velocity of the flow. The settling velocity was determined by the formulation of Gibbs *et al.* for spheres (Soulsby, 1997). Due to the difference in height of the dunes and because the distance from the basis of the dune to the measuring point is changing with time, the curves presented will have different time lengths.

Prent and Hickin (2001), in their field studies, have found dune lengths with approximately 12-17 times dune height. A review of other relationships obtained by various researchers is made by these authors. They emphasize that the size and shape of bedforms depends on the forces exerted by the flow. On the other hand, the water depth is a limiting factor of dune growth, being, therefore, an important parameter in the examination of the dunes behaviour.

Raudkivi (1997) correlated laboratory results obtained by other researchers in flow depths between 0.25 and 0.4 *m*. These results show that no dunes were obtained using sand grains finer than 150 μ*m* and at velocities higher than around 1.5 *m/s*. When the particle diameter increases, there is a linear relationship between that diameter and the fluid velocity required to form the dunes: above around 800 μ*m* and below 0.4 *m/s* there is no particle motion. Furthermore, the dunes formation takes place only above 0.4 *m/s*. At the early stages, the sands display small features (ripples), merging into dunes, whose wavelength is related to flow depth. Raudkivi (1997) refers that it is difficult to determine the wall shear stress from data in small flumes whether the feature is a ripple or a dune; data may be affected when the water depth is less than 50 *mm* (very shallow water depth). The author also presents relationships between the ripple length and the grain diameter. In fact, it was found that results presented by Raudkivi (1997) cannot be directly applied to the current research (for the beads tested), where water depth is 49 *mm*. However, in testing beads P4 no movement was observed in the same way as in his work.

For each measuring point, the data consisted of a time series long enough to accommodate the entire rotation of the bed. This time length varies with the particle size and the rotation speed of the lid.

Figure 7.48 shows a frame from a video movie depicting the behaviour of a deforming bed.

Figure 7.48- Typical deforming bed

For beds made up of the smaller beads, it was also observed the movement of these beads from the outer wall of the flume to the inner, because of the secondary flows. Similar behaviour was found by Besley and Delo (1990) on eroded mud, in experiments using a sediment bed on a carousel flume.

Figure 7.49 shows a typical time series for the instantaneous velocity (beads P3, at Re = 40,000 and at 18 *mm* distance from the basis of the dune). From this data it is observed that the mean velocity has a periodic behaviour due to the particle movement; therefore, the mean velocity has to be calculated along the time as a moving average, which is also shown in the same figure. Furthermore, the higher order moments (RMS) can also be retrieved from this data, as a function of time. It should be emphasized that, in knowing the perimeter of the flume, a time scale can be converted into a position scale.

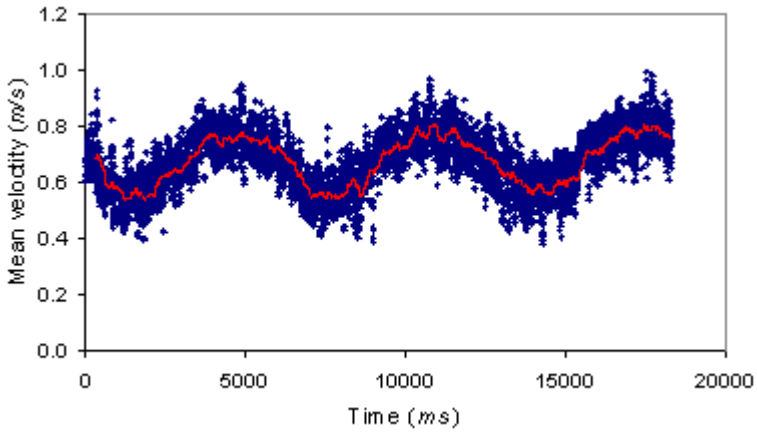

Figure 7.49- Mean tangential velocity along the time

Extending this procedure for all the measuring points across a vertical direction, velocity profiles along the moving bed can be obtained. Figure 7.50 presents the mean tangential velocity profiles for beads P3, at Re = 40,000, at a few selected positions from the basis of the dune (distances of 1, 3, 7, 9 and 16 *mm*), for the sake of simplicity.

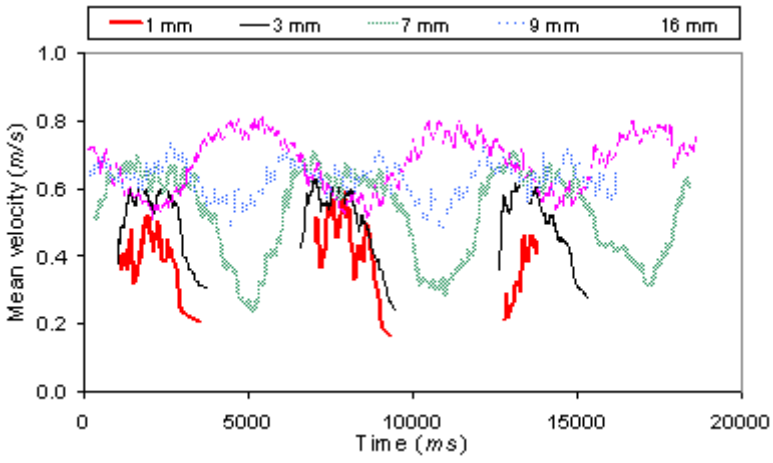

Figure 7.50- Mean tangential velocity profiles at different positions

This figure was obtained by plotting the moving average of the tangential velocity, for each position. From Figure 7.50, it is possible to observe the effect of the moving bed. The broken lines referring to positions closer to the surface are due to the absence of any data, as the moving bed periodically "submerges" the probe volume.

From the figure, it can be observed that a peak of the first dune occurs at ≈ 5s. Due to the close proximity of the measuring point to the surface, velocity here is lower than at regions in between two consecutive dunes (at ≈ 2s). As the measuring point is moved upwards, the effect of the boundary layer near the lower wall is reduced and the velocity is primarily controlled by the available cross section area (local gap between the "sediment" and the upper driving lid), which is reduced on top of a crest. Therefore, the average velocity is higher at that location than in other regions.

7.2.2 VELOCITY DATA

Taking the data from all the measuring points at a certain position in time allows the construction of vertical velocity profiles. Of all the possible positions, five of them were systematically taken and, as represented in Figure 5.26, they are referred to positions A, B, C, D and E. Positions A and E are physically equivalent.

The results obtained for each set of beads tested are shown as follows. Figure 7.51 presents the mean tangential velocity at positions A, B, C, D, and E (along the dune), for beads P1, at Re = 20,000. The distance to wall refers to the distance from the local dune surface.

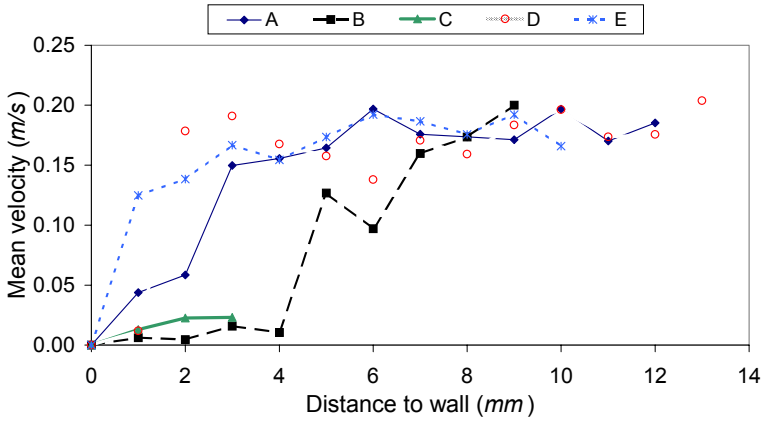

Figure 7.51- Mean tangential velocity; beads P1; Re=20,000

Local averages are based on samples of limited size centred around each one of the positions referred (A, B, C, D, E). Therefore, certain statistical uncertainty is linked to the data, particularly for the higher order velocity moments (see Chapter 5). However, it can be observed that, as expected, positions A and E are similar indeed. Positions B and D are quite dissimilar: B is downstream of the dune and D is a position upstream of that. Due to the flow development, the boundary layer for position B is much larger than that of D and, therefore, the velocity profile shows a region close to the surface of very low gradients (thus lower, shear stresses). However, there is no observation of reverse flows, although it

is in a region of adverse pressure gradients. This fact is not entirely surprising because it is known that moving surfaces delay flow separation. The higher shear stresses in position D are responsible for the particle separation and subsequent entrainment into the main flow, which is the prime mechanism for dune motion.

Figures 7.52 and 7.53 present the tangential velocity turbulence and the total shear stresses, respectively, for these particles, along the length of the dune.

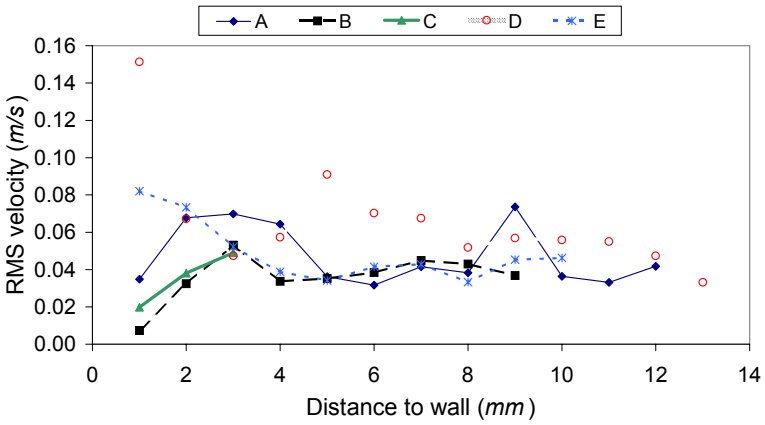

Figure 7.52- Tangential velocity turbulence; beads P1; Re=20,000

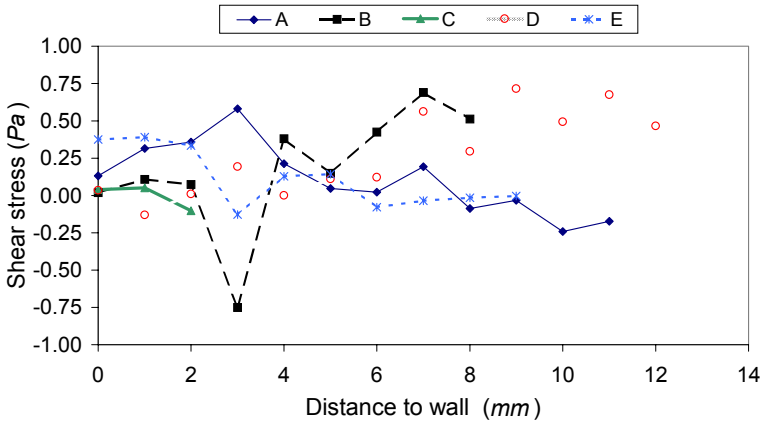

Figure 7.53- Shear stress; beads P1; Re=20,000

The wall shear stress is higher in positions A and E. At a position of 1 *mm* from the wall and at position D the total shear stress value is not much high because, although its laminar contribution is considerable, the turbulent component is greater and with an opposite signal.

Figures 7.54 and 7.55 show the mean and turbulent velocities, respectively, for particles P2 at Re = 20,000.

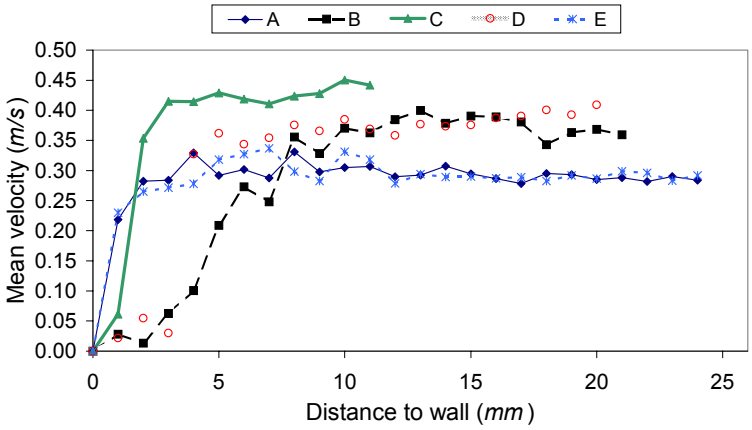

Figure 7.54- Mean tangential velocity; beads P2; Re=20,000

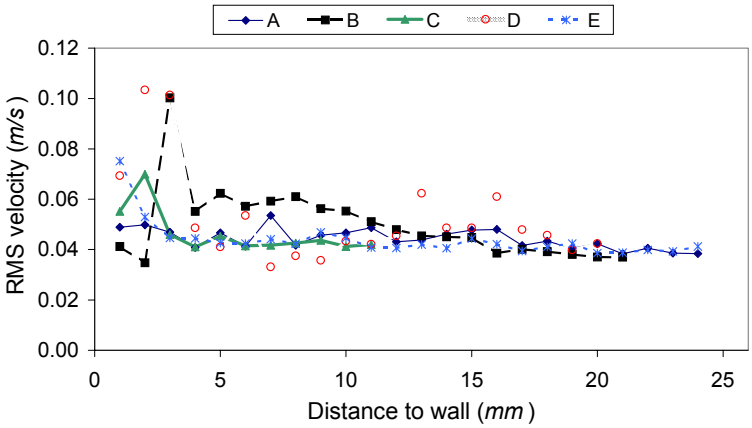

Figure 7.55- Tangential velocity turbulence; beads P2; Re=20,000

The profiles to these beads at Re = 40,000 are depicted in Figures 7.56 through 7.58.

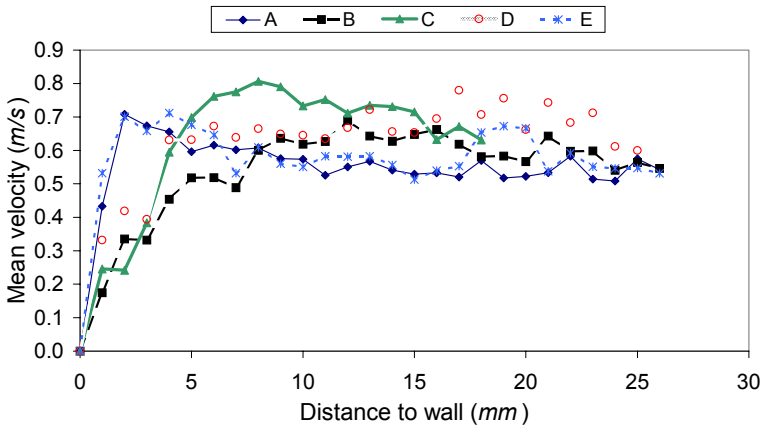

Figure 7.56- Mean tangential velocity; beads P2; Re=40,000

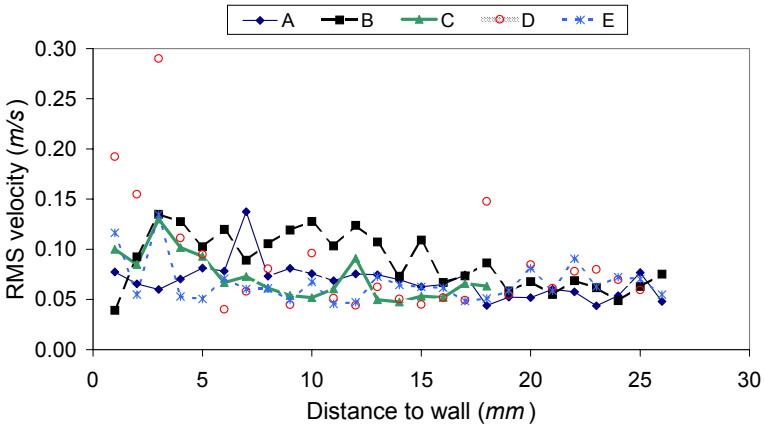

Figure 7.57- Tangential velocity turbulence; beads P2; Re=40,000

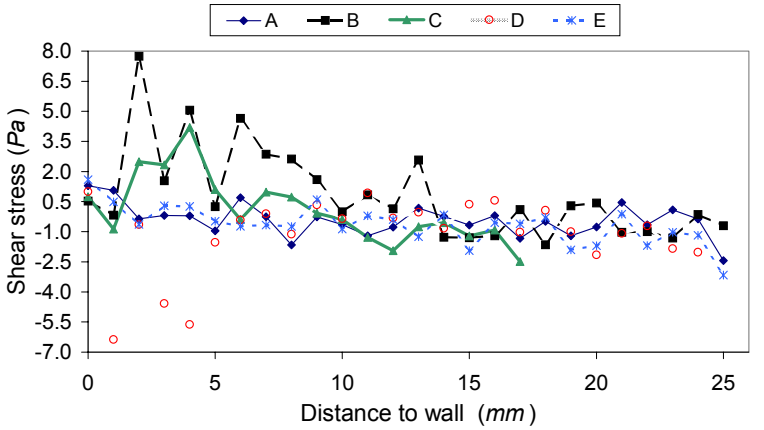

Figure 7.58- Shear stress; beads P2; Re=40,000

From the previous data, no flow separation is observed downstream of the moving dunes (positions A and B). This may be due to the fact that the dune amplitude to wavelength ratio is small, reducing the possibility of flow separation downstream. Another contributing factor is likely to be the bed deformation, which reduces the risk of flow separation. Further evidence on this will be shown subsequently. Detailed measurements of individual dunes, made by Kostaschuk and Ilersich (1995) in an estuary, also showed an absence of lee-side flow separation. The authors attributed these results to a predominance of bed material movement in suspension rather than as bedload.

The mean and RMS velocities and shear stresses for beads P3, at Re = 20,000, are presented in Figures 7.59, 7.60 and 7.61, respectively.

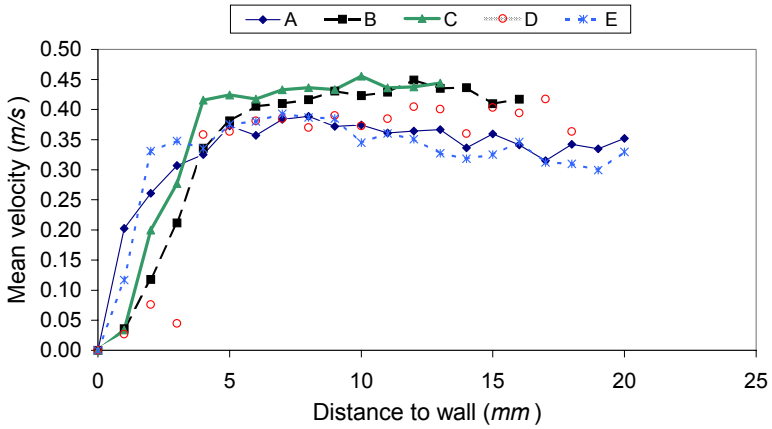

Figure 7.59- Mean tangential velocity; beads P3; Re=20,000

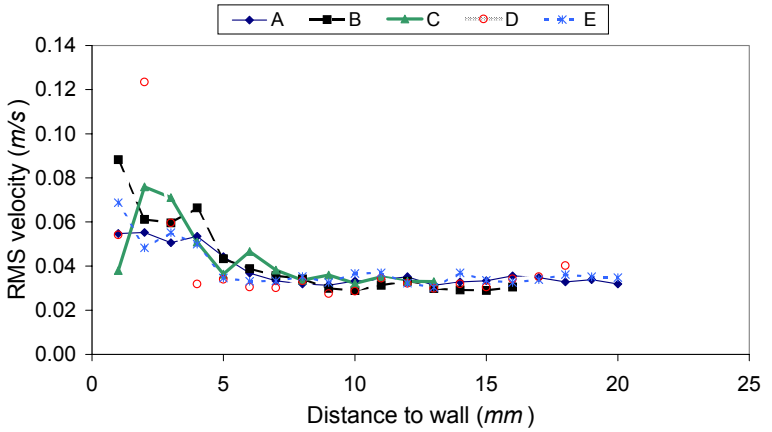

Figure 7.60- Tangential velocity turbulence; beads P3; Re=20,000

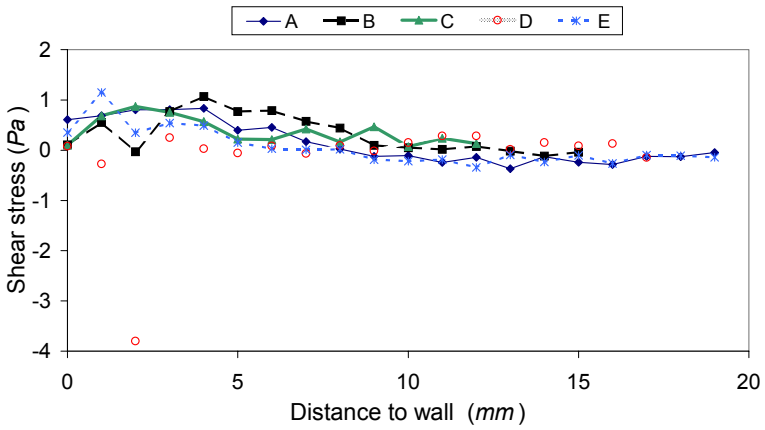

Figure 7.61- Shear stress; beads P3; Re=20,000

Comparing the figures detailing the mean velocity (Figures 7.51, 7.54, 7.56 and 7.59), a similar pattern occurs: the highest velocity gradients (shear stress) are observed on the upstream face of the dune.

The turbulent velocities (Figures 7.52, 7.55, 7.57 and 7.60) show some interesting features: from the particle size and density ratio (particle to fluid density) the system of particles P3 is that in which the response in the frequency domain of particles to fluid velocity is damped. Comparing particles P1, P2 and P3 (same Re) it may be observed that turbulence levels are higher for the P1 (smaller particles). It should be referred that the same Re is achieved at a lower velocity for the system with particles P1, though the turbulence intensity is higher than with the others. This observation is certainly due to the fact that, as a result of lower density ratio on P1, a large concentration of particles are entrained into the fluid. Therefore, it can be concluded that particle concentration is an important factor in controlling flow turbulence. In addition, for particles P1 the flow turbulence remains at higher levels into regions further from the surface. This may be due to the momentum transport into regions further away from the surface by the large number of particles entrained into the flow.

Figures 7.62 through 7.64 show the velocity profiles for particles P3 at Re = 40,000.

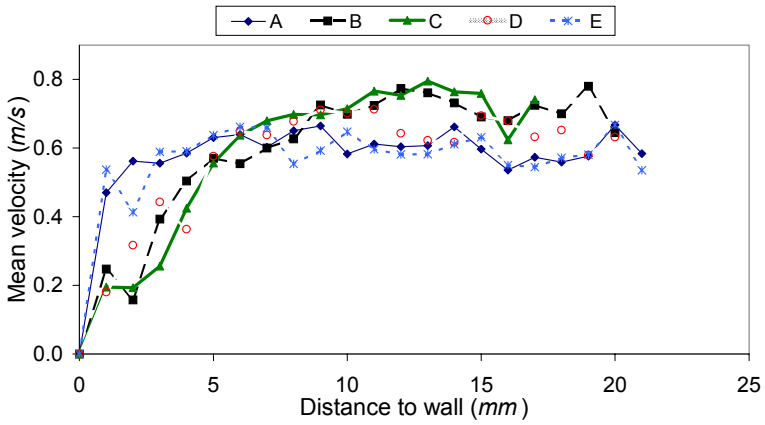

Figure 7.62- Mean tangential velocity; beads P3; Re=40,000

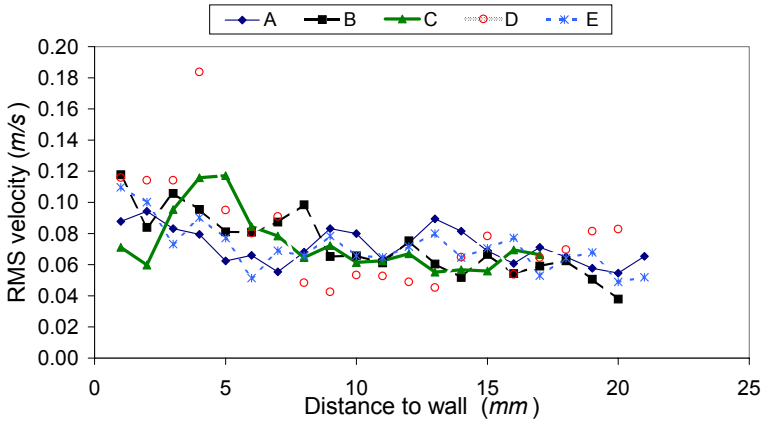

Figure 7.63- Tangential velocity turbulence; beads P3; Re=40,000

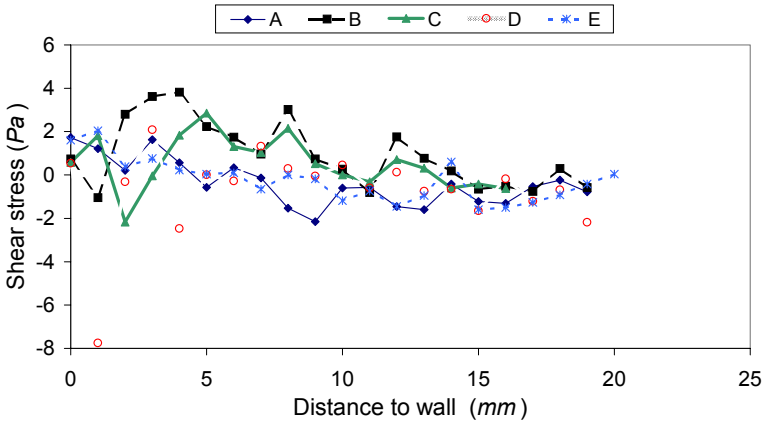

Figure 7.64- Shear stress; beads P3; Re=40,000

It is observed that the crest of the dunes is the region that shows the lower velocity gradients, although the cross section area is smaller. This observation is in agreement with the hypothesis previously put forward of bed deformation reducing the local stresses. This fact yields an interesting characteristic to the flow. Figure 7.62 shows that the velocity is higher just above the sediment at the throat of the dunes than right above its crest. This is observed for all distances within 14 *mm* from the throat, which is equivalent to 6 *mm* above the crest (dune height is 8 *mm*). The mean velocity is approximately the same at that position (14 *mm* above the throat and 6 *mm* above the crest). Because the velocity at the top of the flume is the same (boundary condition), due to mass conservation the flow velocity in the regions closer to the rotating lid must be inverse to those near the sediment: the flow velocity is higher above the crest and lower above the throat. It takes place for all the positions above the one previously referred. This means that from the crest dune surface up to 6 *mm* above, the wall dominate the lid effects, decreasing the velocity at the crest. Above that position, the lid effect as well as the small gap exert higher influences, increasing the velocity. These results are in agreement with Figure 7.50. As a consequence, a periodic oscillation occurs along the flume perimeter in which the flow is driven upwards upstream of the dune and downwards downstream the crest of the dune. This mechanism is the main factor for particle entrainment and deposition, as sketched in Figure 5.26.

An important conclusion is that erosion should occur in regions facing upstream the flow motion. The higher shear stresses in position D, observed at around 1 *mm* from wall distance in Figures 7.58, 7.61 and 7.64, are responsible for the particle drag and subsequent entrainment into the main flow, which is the driving mechanism for the bed deformation and motion. Although this is the total shear stress, the turbulent contributions are much higher; this is related with the enhancement of turbulent momentum transfer due to particle entrainment.

In addition, the regions near the crest (position C) always exhibit a lower shear stress than near the throat (position A). It must be pointed out that the surface deformation is stronger near the crest than in other regions along the dune surface, because particle entrainment and motion (lowering the local shear stress), which is in agreement with the flow patterns above described. The same conclusions can be made by observing Figures 7.65 and 7.66, which show the local wall shear stress for the five different positions along the dune, at Reynolds numbers of 20,000 and 40,000, respectively.

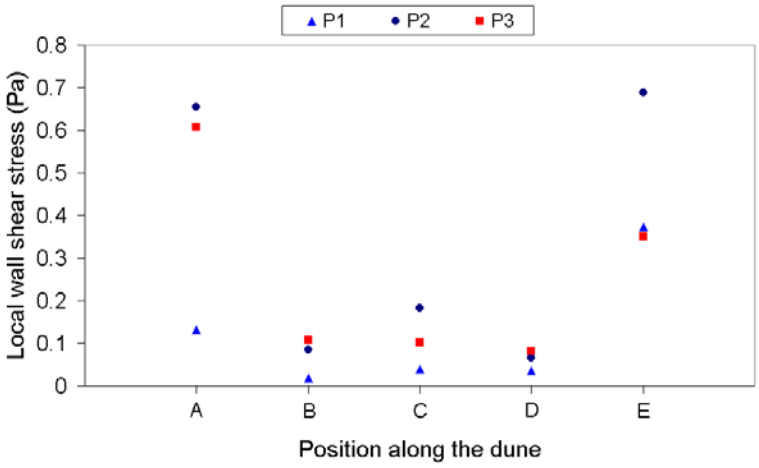

Figure 7.65- Variation of the local shear stress over a sandy dune; Re=20,000

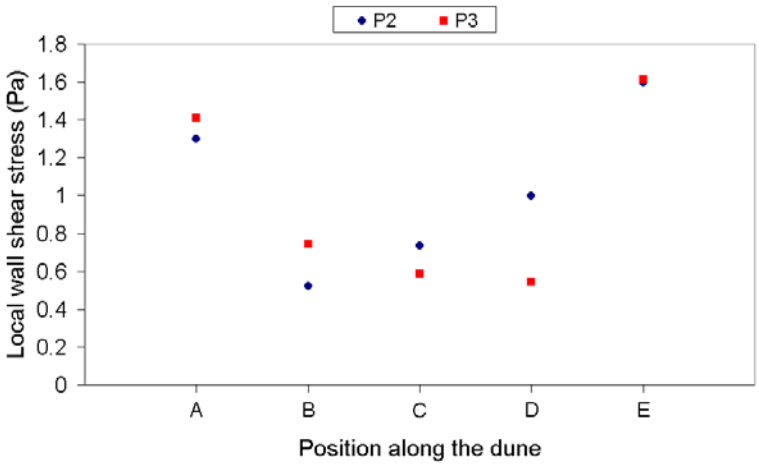

Figure 7.66- Variation of the local shear stress over a sandy dune; Re=40,000

This behaviour also prevents the formation of a recirculation bubble (or reverse flow) over the downstream side of the dune.

7.2.3 DISCUSSION

Figures 7.67 and 7.68 show the effect of particle size upon fluid turbulence for different Reynolds numbers. These second order moments were calculated as an average over the entire time series. This is a reasonable approach because the data spread remains fairly constant throughout the duration of the experiments (Figure 7.49).

The data shows that turbulence near the surface is of at similar level, although higher when compared with that of a solid rough wall. However, for regions further apart from the surface, the flow turbulence remains at a much higher level. This may be due to the fact that the bed deformation is made up of a succession of particles entrained into the main flow, transport over the dune, and their subsequent deposition. This whole process enables the transportation of energy into regions further away from the bed surface, increasing the flow turbulence.

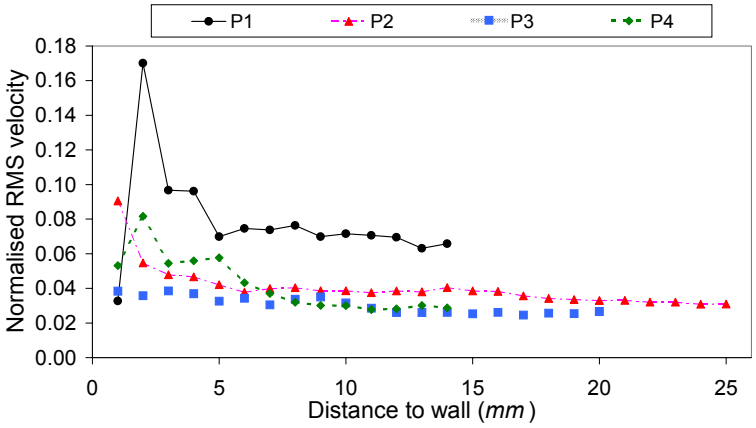

Figure 7.67- Tangential velocity turbulence; beads P1, P2, P3 and P4; Re=20,000

It is observed that, near the surface, turbulence is higher for larger particles. However, as smaller particles (P1) are easily entrained into the fluid, they enhance turbulence further away from the wall, resulting, as mentioned above, in higher turbulence than with larger particles. This is in agreement with that discussed by Azzopardi and Teixeira (1994). The data also shows the effect of particle concentration in the flow (that is bigger to the smaller particles as a result of lower density ratio), a factor which is known to affect the turbulence of the continuous phase.

When the particle concentration is approximately constant (Figure 7.68) the fluid turbulence increases in the presence of larger particles, because of the velocity slip between the phases.

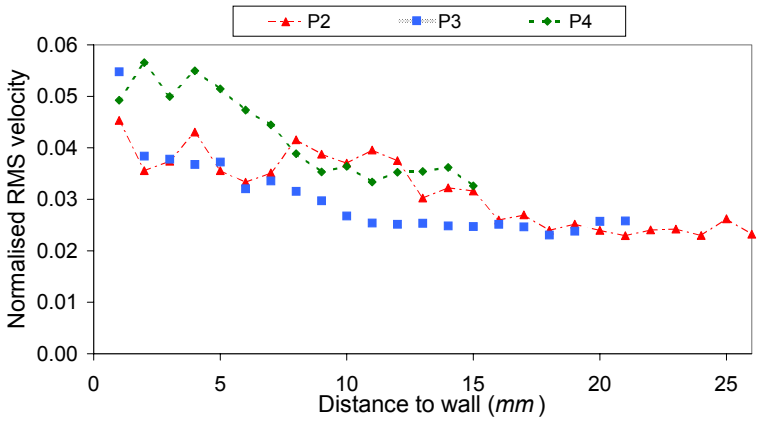

Figure 7.68- Tangential velocity turbulence; beads P2, P3 and P4; Re=40,000

The effect of fluid Reynolds number is shown in Figure 7.69 for particles P3. It can be observed that by increasing the fluid velocity, enhancement of turbulence is stronger near the surface. In such conditions, boundary layer thickness reduces and so does the laminar

sub-layer. Thus, roughness effects are expected to be stronger near the surface at such high Reynolds number. Similar behaviour was found for beads P2.

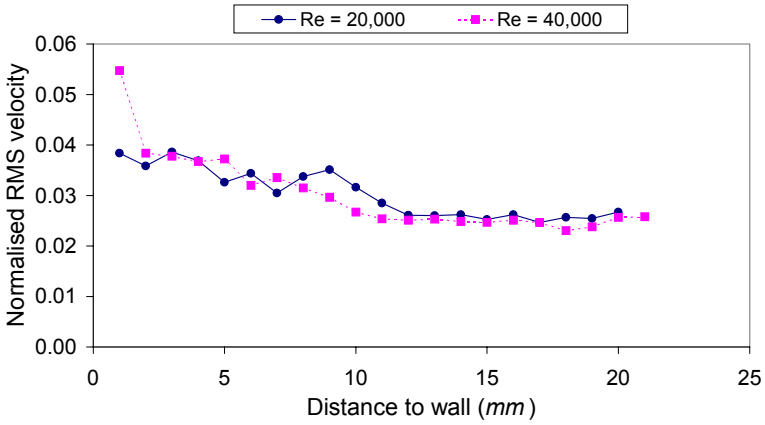

Figure 7.69- Tangential velocity turbulence; effect of Reynolds number; beads P3

It will be interesting to assess the effect of the particle size upon the velocity profile and the turbulence, for the various positions along the dune (A, B, C and D). Figures 7.70 through 7.73 show the effect of the particle size upon the velocity profile at Re = 20,000.

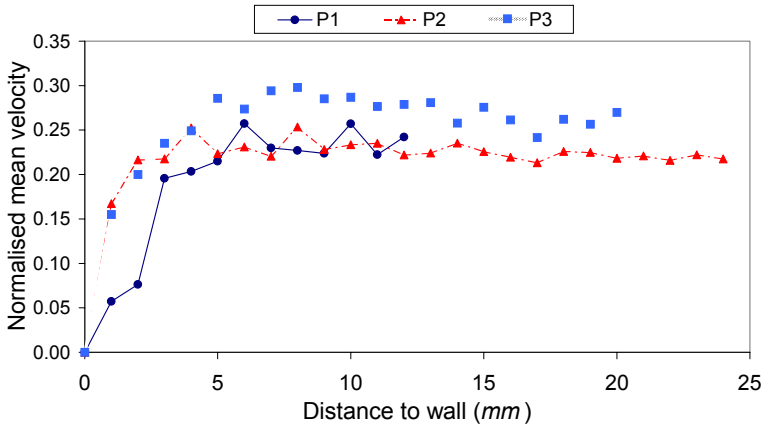

Figure 7.70- Normalised mean tangential velocity at position A; beads P1, P2 and P3; Re=20,000

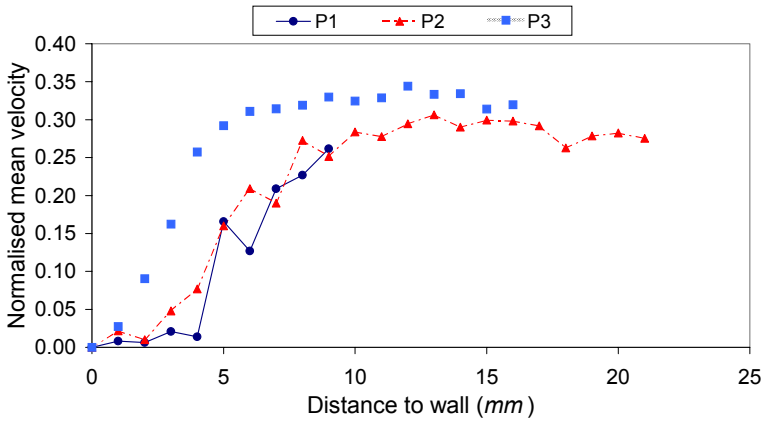

Figure 7.71- Normalised mean tangential velocity at position B; beads P1, P2 and P3; Re=20,000

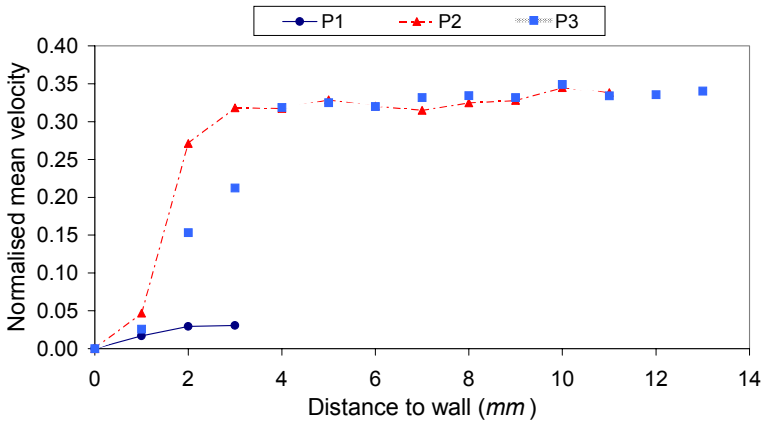

Figure 7.72- Normalised mean tangential velocity at position C; beads P1, P2 and P3; Re=20,000

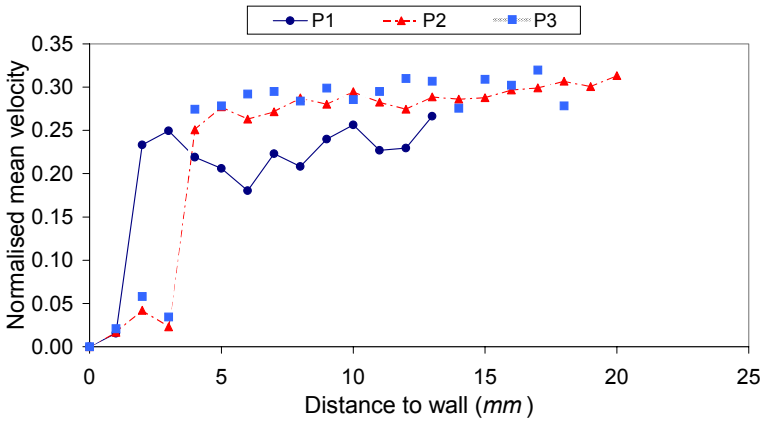

Figure 7.73- Normalised mean tangential velocity at position D; beads P1, P2 and P3; Re=20,000

At the dip between dunes (position A), the smaller particles show a lower velocity gradient than that observed with larger particles. It appears that with the larger beads (because the concentration is much smaller) the flow reattaches to the surface over a shorter distance. This effect is clearly observed on the downstream slope (B) where the shear stress for particles P1 is nearly zero close the surface. Even at the crest of the dune a certain amount of slip appears to be present. It may be concluded that particles P1 form a more deformable bed than larger particles.

In this comparison, both particles P2 and P3 have a similar density ratio; therefore, and apart from the particle size, they are closer to each other than P1 was to P3. Thus, it is reasonable to expect a very similar pattern for the velocity profiles along the dune between these two particles for both the mean velocity and the turbulence, which is evident from the data. At higher velocities (Re = 40,000) a similar behaviour was found.

It is obvious that the fluid turbulence near the sediment is influenced by the particle size/sediment roughness. In fact, a sediment made of larger particles shows higher turbulence levels, as shown in Figure 7.67. Because the flow is periodic due to the surface configuration, one may question if this pattern is constant through the entire dune cycle. Figure 7.74 shows the turbulence level at position D for beads P1, P2 and P3.

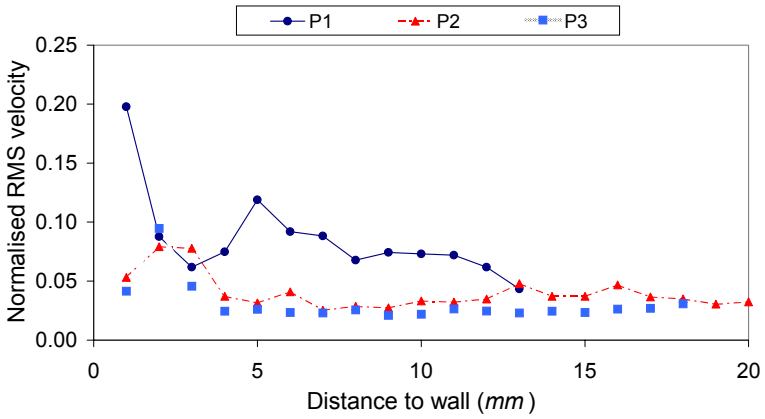

Figure 7.74- Tangential velocity turbulence at position D; beads P1, P2 and P3; Re=20,000

The data shows that, at this location, the fluid turbulence for beads P1 is much higher than that for the other particles. This observation is at odds with the average values over the dune cycle. Such pattern can provide further insight into the mechanisms of turbulence generation. Position D is identified with the location where, due to fluid shear, particles are entrained into the main flow. Because of their size and density, particles P1 are easily entrained than the others and, at higher velocities, it can be concluded that turbulence enhancement by particle entrainment into the flow primarily occurs during the ejection process and not during the transport by the carrier fluid. It is during that period that the velocity slip is much higher.

Referring the shear stresses profiles, an example is shown, for position D, in Figure 7.75.

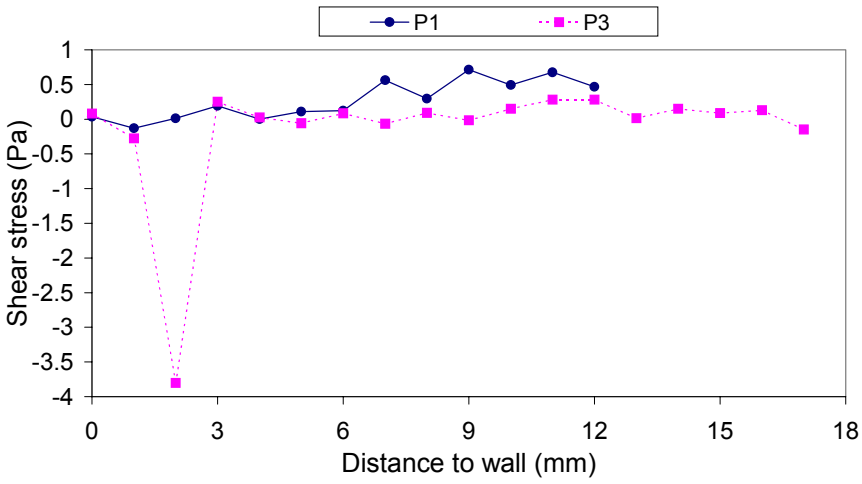

Figure 7.75- Shear stress at position D; beads P1 and P3; Re=20,000

It is observed much higher shear stress for the bigger particles in the vicinity of the wall. Far away from the wall, the shear stresses increase for the smaller particles.

The influence of Reynolds number upon the velocity profile, for the various positions over the dune, is shown in Figures 7.76 through 7.79. Results refer to the particles P3.

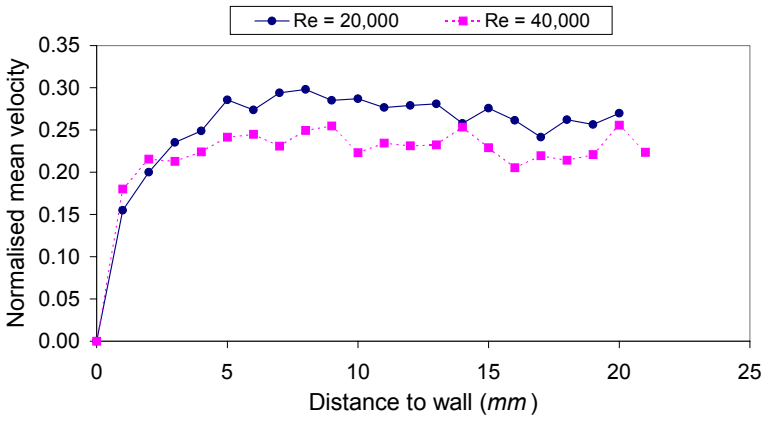

Figure 7.76- Normalised mean tangential velocity at position A; beads P3

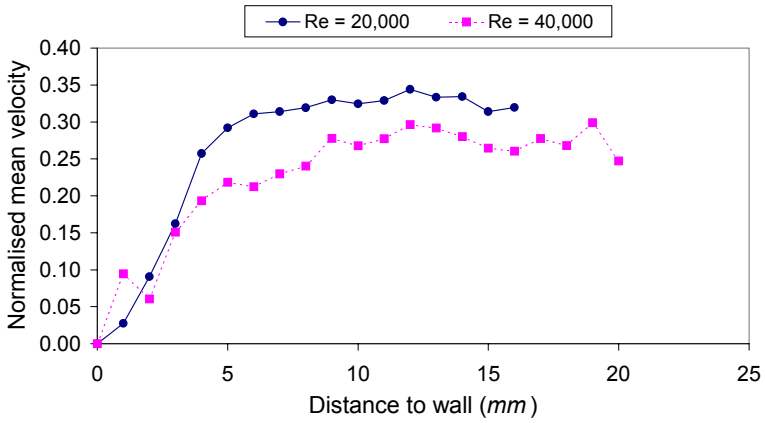

Figure 7.77- Normalised mean tangential velocity at position B; beads P3

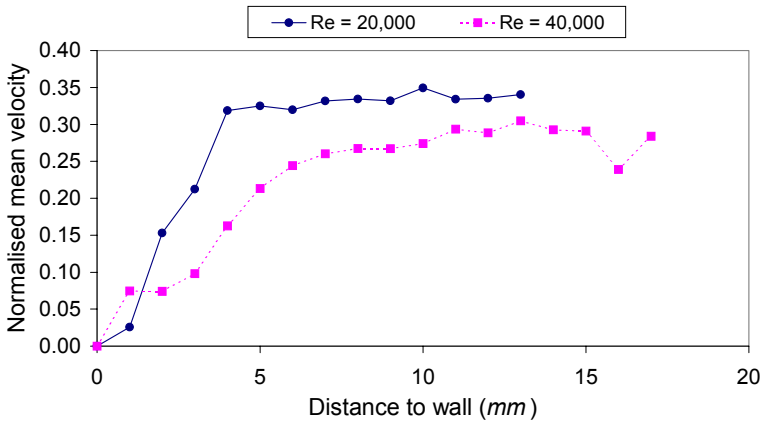

Figure 7.78- Normalised mean tangential velocity at position C; beads P3

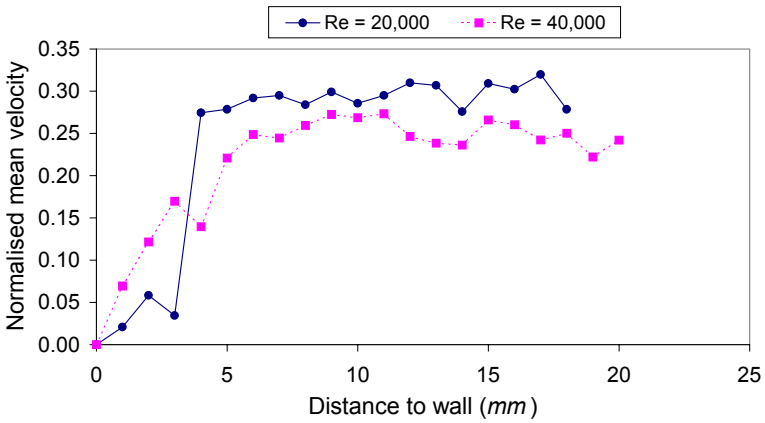

Figure 7.79- Normalised mean tangential velocity at position D; beads P3

Figures 7.76 through 7.79 show that, downstream of the dune, the bed deformation should be reduced, therefore once the velocity is normalised, the velocity profiles should be very similar for both positions A (Figure 7.76) and B (Figure 7.77). The entrainment of particles into the main flow will slow the mean flow due to momentum exchange between the phases. This effect is more evident in positions C and D, particularly at higher Reynolds, where such interaction will be stronger.

Figure 7.80 shows higher stresses at high Re, as a function of the wall distance. In addition, close to the wall the turbulence is always higher at low Reynolds number and the profiles merge far from the wall.

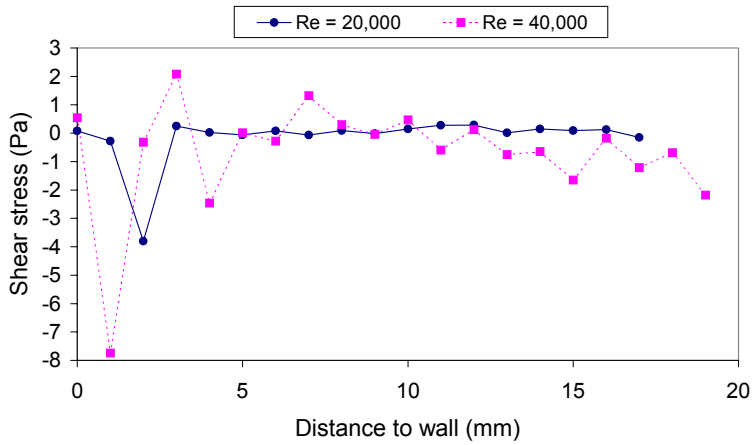

Figure 7.80- Shear stress at position D; beads P3

Similar behaviour was found for particles P2.

Finally, results comparing the tangential and turbulence velocities and shear stress profiles between rigid and deformable beds are shown at Re = 20,000.

Figures 7.81 through 7.83 compare the solid surfaces with those made of particles P1 at the most important positions.

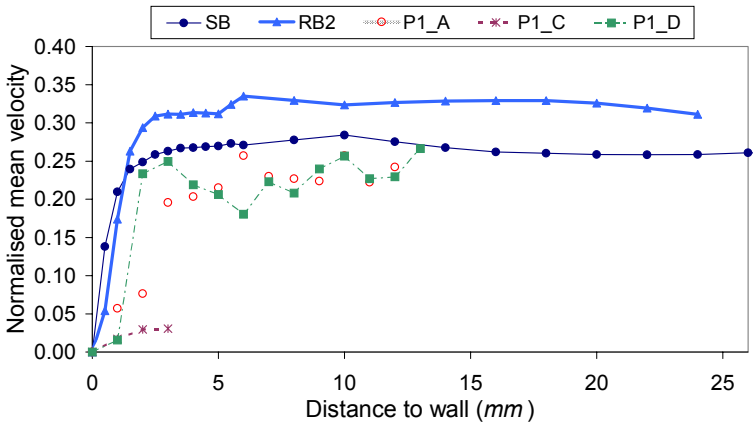

Figure 7.81- Normalised mean tangential velocity; SB, RB2 and beads P1; Re=20,000

In Figure 7.81, P1_A, C and D refer to the P1 particle system at positions A, C and D. The same nomenclature is used in the following figures. Although the mean velocity is normalised for each set of experiments, there are differences. Firstly, as opposed to the fixed bed systems, velocity profiles do change along the streamwise direction, even if the average surface roughness is of the same order of magnitude for RB2 and P1_x data sets. The difference may be due to surface deformation and such an occurrence reduces the

surface shear stress (Figure 7.83). This is always lower, regardless of the position along the dune.

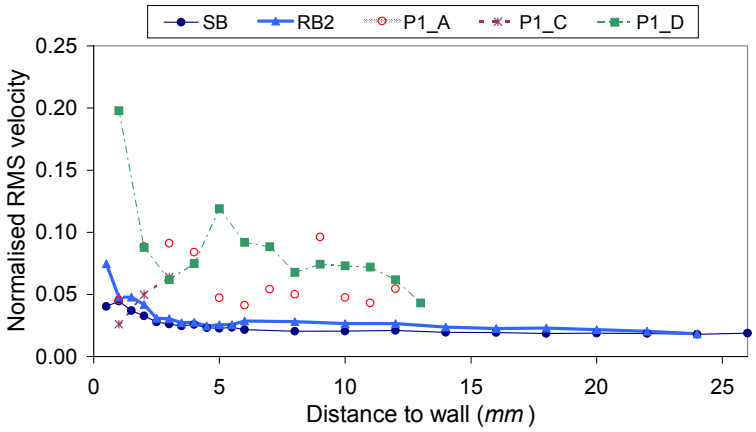

Figure 7.82- Tangential velocity turbulence; SB, RB2 and beads P1; Re=20,000

The data for the RMS of the tangential velocity component presented in Figure 7.82 shows a reduction on turbulence near the surface of the deformable bed, for positions A and C. It was previously discussed that turbulence is enhanced upstream (position D) of the dune, certainly due to the reduction of the boundary layer thickness.

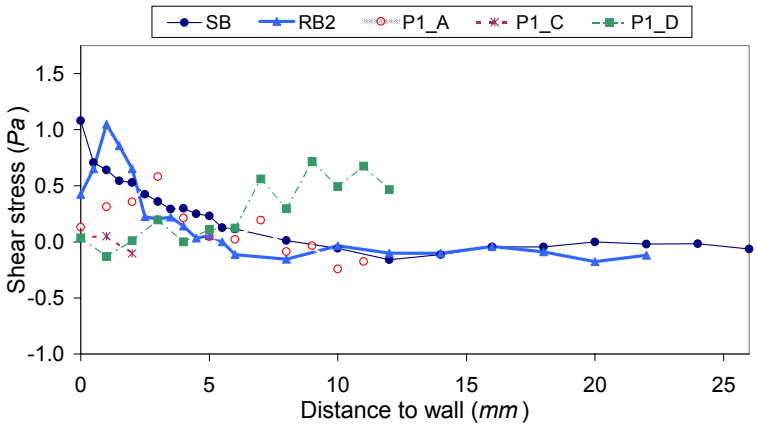

Figure 7.83- Shear stress; SB, RB2 and beads P1; Re=20,000

Figures 7.84 through 7.86 show the profiles for beads P3, at Re = 20,000.

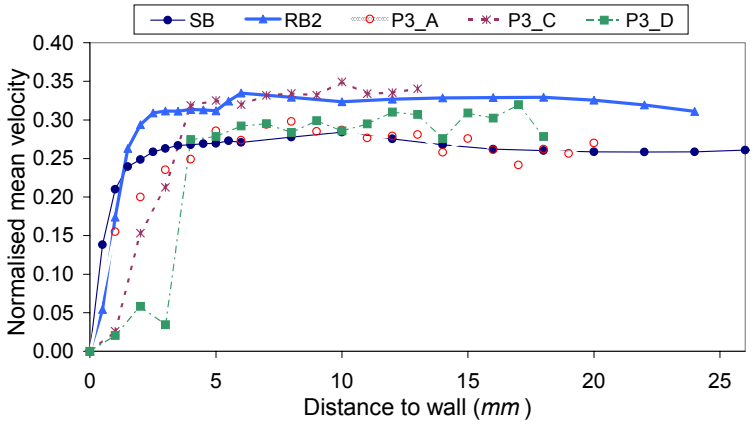

Figure 7.84- Normalised mean tangential velocity; SB, RB2 and beads P3; Re=20,000

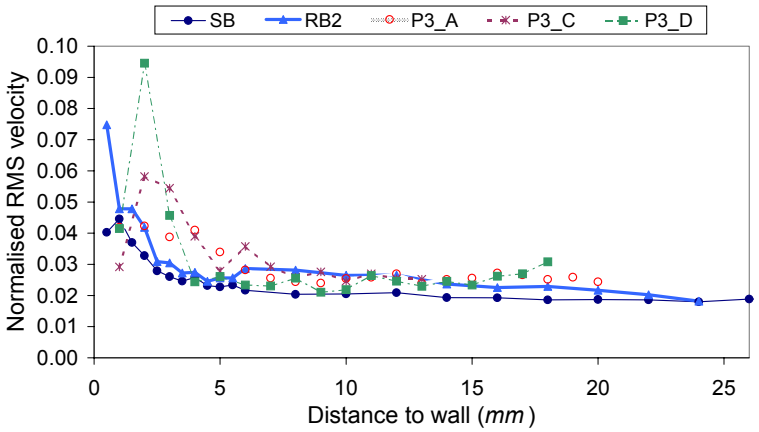

Figure 7.85- Tangential velocity turbulence; SB, RB2 and beads P3; Re=20,000

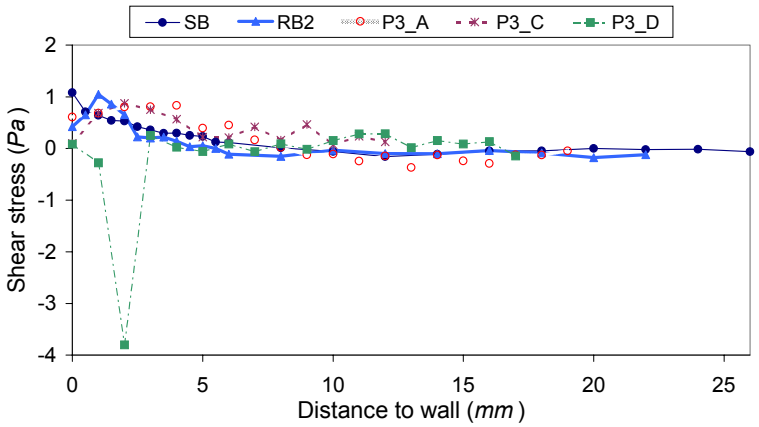

Figure 7.86- Shear stress; SB, RB2 and beads P3; Re=20,000

The effects of bed deformation and related reduction in the surface shear stress are clearly of low magnitude for larger particles. It is evident that, for these systems, the velocity profiles near the surface are much closer to those observed on a solid rough bed than those with particles P1 system.

A comparison of the various systems tested at higher Reynolds number (Re = 40,000) was made and similar patterns to those discussed for Re = 20,000 were observed, though turbulence reduction in the vicinity of the bed downstream of the dune is less effective.

Figure 7.87 aims to show together the surface roughness effects and those from entrained particles to the fluid turbulence.

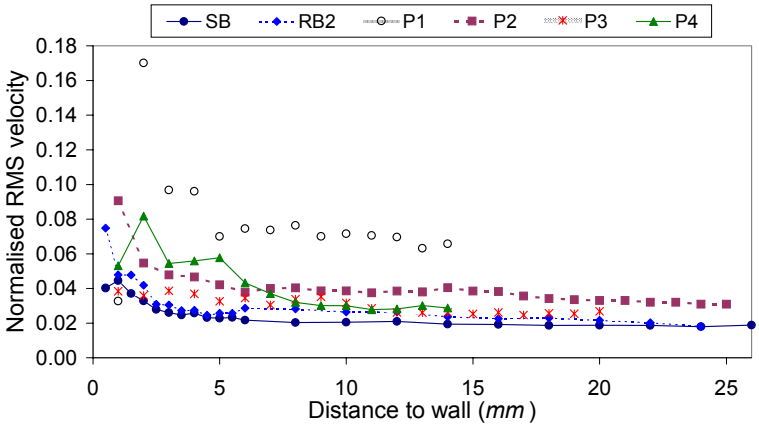

Figure 7.87- Tangential velocity turbulence; SB, RB2 and beads P1, P2, P3 and P4; Re=20,000

The contribution of particles is to enhance the flow turbulence, as compared with a solid rough wall, though the increase is small for larger beads. However, for particles P1 the effect of concentration is very strong.

7.2.4 SUMMARY

From the experiments reported in this section some concluding remarks can be made at this stage. First and foremost, the use of glass/polymer beads seems to be an effective way of simulating a moving bed. Some of the features observed in an eroding sediment are duplicated in this artificial system: entrainment of particles into the main flow, transport and subsequent deposition. Furthermore, as the resulting bed moves, its behaviour is similar to that of a deforming sediment in which the shear stress at the interface is lower than that on a rigid surface. The flow patterns along the moving surface have been identified and described based upon the information retrieved from the velocity time series data. From this, it has been found that the upstream face of the bed formation is that more prone to erosion, due to the higher shear stress in this region. Downstream, the opposite is observed: lower velocity gradients in which the shear stress approaches zero.

The particle size, which increases local roughness, enhances turbulence near the interface. In addition, higher turbulence levels are observed further way from the wall (when compared with a solid rough surface) due to momentum transport by the entrained particles. If the conditions are appropriate (that is lower density ratio and smaller particles) a very high concentration of particles can be observed. It was also found that turbulence increases with particle concentration in the flow.

The flow Reynolds number has been observed to be directly linked with turbulence levels and, more interestingly, due to changes in boundary layer thickness, the turbulence profile across the flow cross section is different.

7.3 INFLUENCE OF SURFACE WAVES

It is understood that surface waves in the fluid above the sediment may modify the flow field properties into positions far from the surface. However, the effect of waves on the erosion and movement of sediments is complicated, depending on the waves properties and the muddy bed (Roberts *et al.*, 2000). These authors studied the effect of tidal cross-shore and long-shore currents and waves on mudflats. They found that mudflats are greatly influenced by those factors, being their shape dependent on a complex interaction with the morphology and hydrodynamics of the surrounding estuary.

The effect of surface waves upon the flow patterns and their contribution to the turbulence field near the interface is investigated in this section.

The various geometric configurations for the surface waves have been discussed previously. The tangential velocity fields are presented in Figure 7.88 for each one of the lids tested, at Re = 20,000. Figure 7.89 shows the effect of the Reynolds number in that velocity profile.

At the same Reynolds number, a similar behaviour in the tangential velocity field using lids L2, L3 and L4 is observed, although for lid L2 the maximum velocity is extended to the inner ring. Using lid L1, higher velocities are observed, even in the region close to the inner ring.

Increasing the Reynolds number, it is observed a proportional increase in the velocity through the entire flume section, being expanded towards the inner wall (Figures 7.89a, 7.88b and 7.89b).

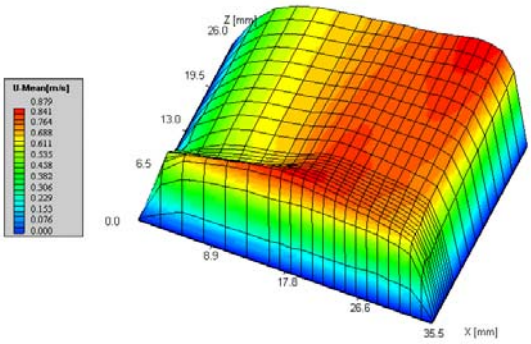

a) L1

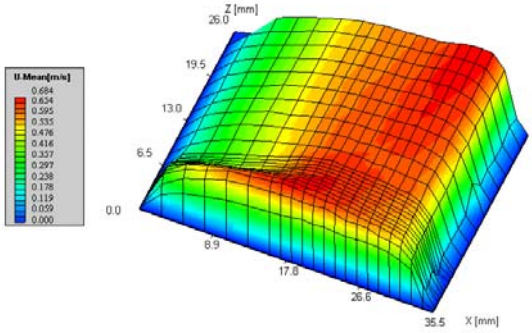

b) L2

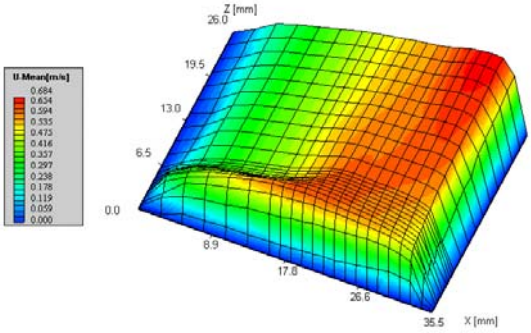

c) L3

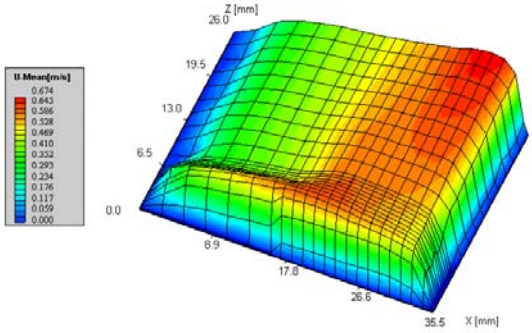

d) L4

Figure 7.88- Tangential velocity field; wavy lids; Re=20,000

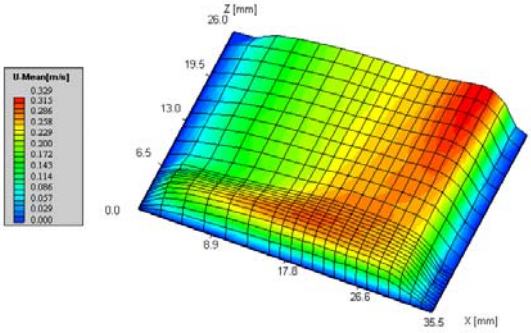

a) Re = 10,000

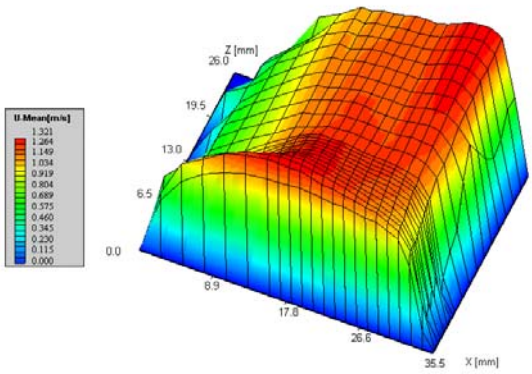

b) Re = 40,000

Figure 7.89- Tangential velocity field; L2

The tangential velocity field for lid L1 at Re = 40,000 presented stronger velocity gradients towards the bottom and the outer walls.

Figures 7.90 and 7.91 depict the axial velocity field for each case.

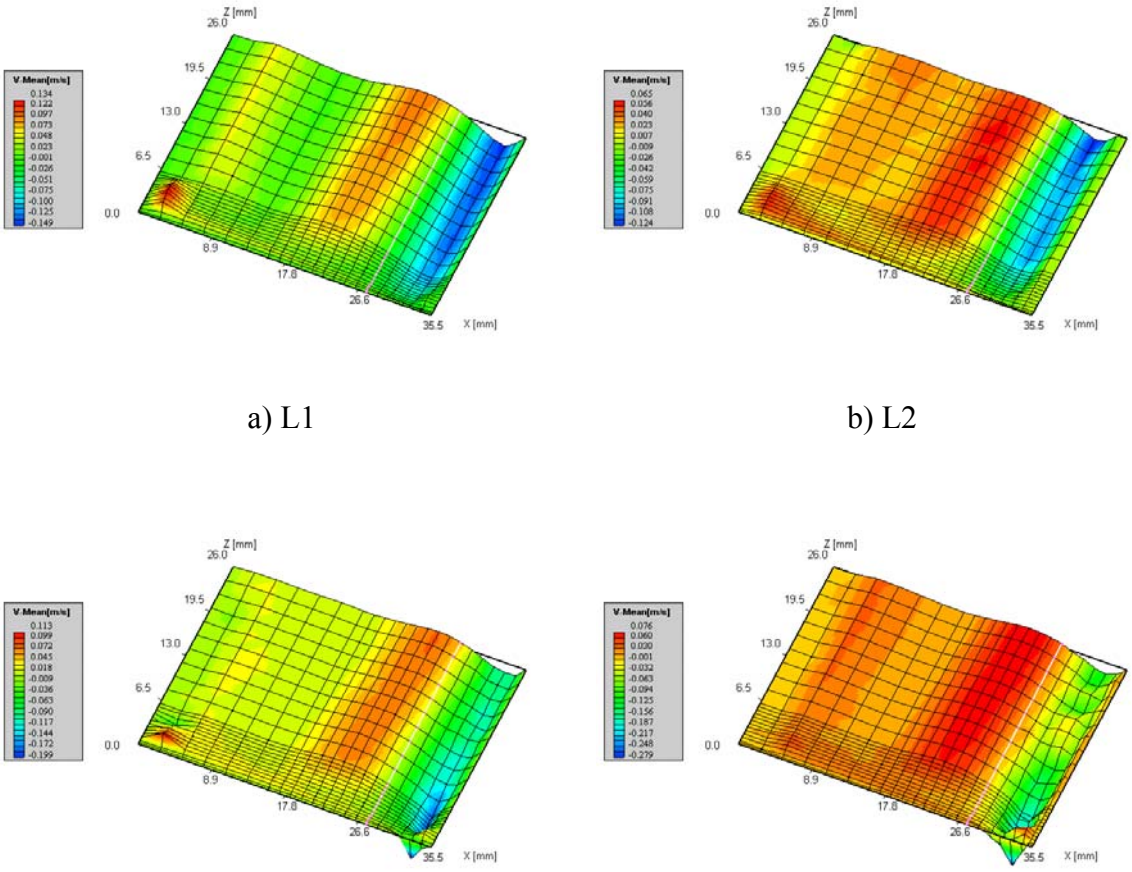

a) L1 b) L2

c) L3 d) L4

Figure 7.90- Axial velocity field; wavy lids; Re=20,000

Comparing the data at Re = 20,000, Figure 7.90 shows that lid L1 produces a similar effect as lid L3, while lids L2 and L4 have similar profiles. It may be concluded that wavelength is the most important factor affecting the flow field. For lid L2, when Re increases, a proportional increase in the downward flow close to the outer wall occurs.

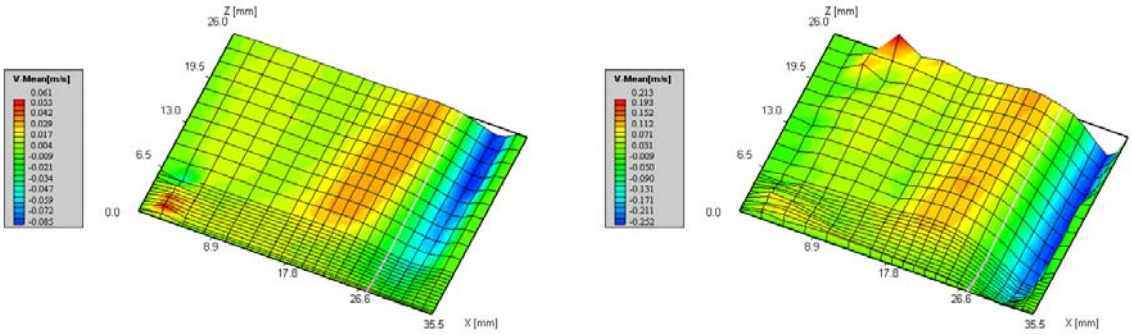

a) Re = 10,000 b) Re = 40,000

Figure 7.91- Axial velocity field; L2

The turbulence intensity is shown in Figures 7.92 and 7.93.

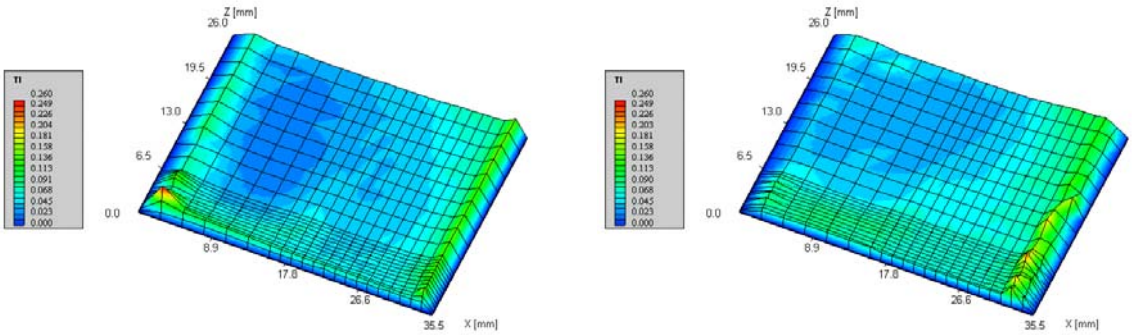

a) L1 b) L2

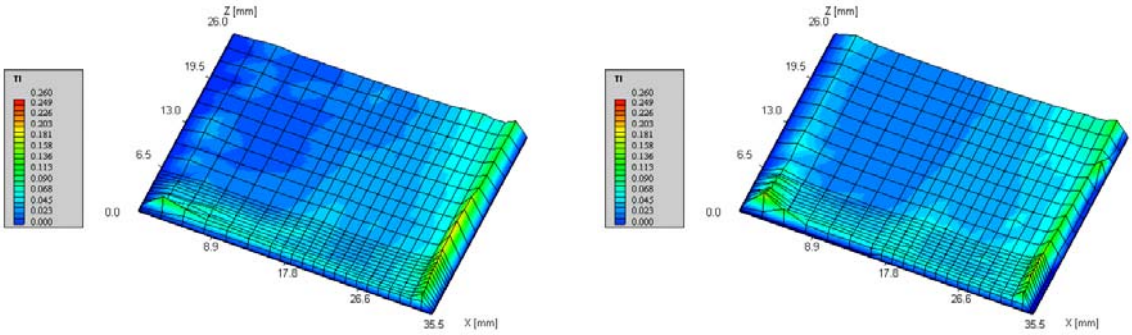

c) L3 d) L4

Figure 7.92- Turbulence intensity; Re=20,000

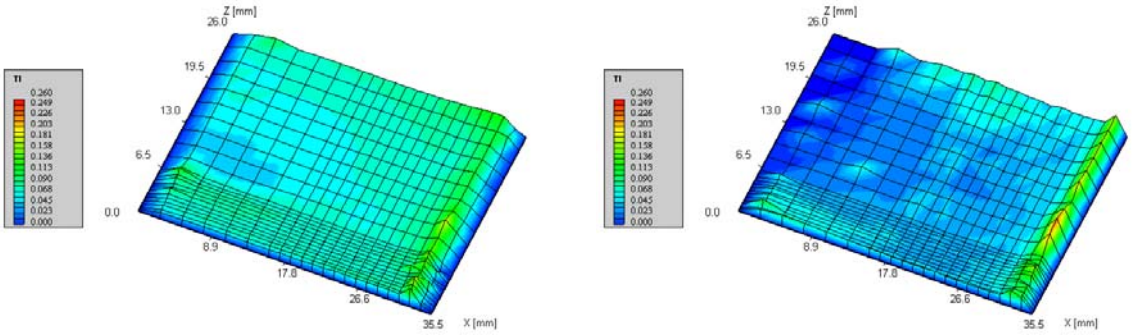

a) Re = 10,000 b) Re = 40,000

Figure 7.93- Turbulence intensity; L2

The data shows that the turbulence intensity is always higher near the outer wall, although it is also evident near the inner wall for lid L1 and, to a smaller extent, also with lid L2. These two configurations are characterised by a high wave amplitude, when compared with the other two. The increase in wave amplitude effectively reduces the available channel area for the main flow in the flume and, in consequence, the secondary flows are more intense (Figure 7.90a,b). Therefore, the flow shows a stronger influence of the surface phenomena which leads to an increase in turbulence near the inner wall. In short, the surface waves balance the centrifugal forces generated by the flow rotation. This may explain the fact that the velocity profiles (Figures 7.88a through 7.89b) are flatter through the flume cross section, when compared with a standard flume (Figure 6.4). Also, for lid L1 a velocity close to zero was found over a smaller area. By increasing the velocity, there are more differences in the turbulence intensity between the regions close to both walls.

In order to obtain more meaningful data, a 2D analysis is carried out for a vertical profile located 7.5 *mm* off the outer wall. Because the fluid gap is not constant throughout the entire experimental programme, the flow mean velocity is adjusted in order to keep dynamic similarity (constant Reynolds number). Therefore, velocity profiles are always normalised through the maximum fluid velocity.

Figure 7.94 compares the normalised mean tangential velocity for both with (SB-L1, SB-L2) and without (SB) surface waves at Re = 10,000. The shear stresses and the turbulence velocity are shown in Figures 7.95 and 7.96, respectively.

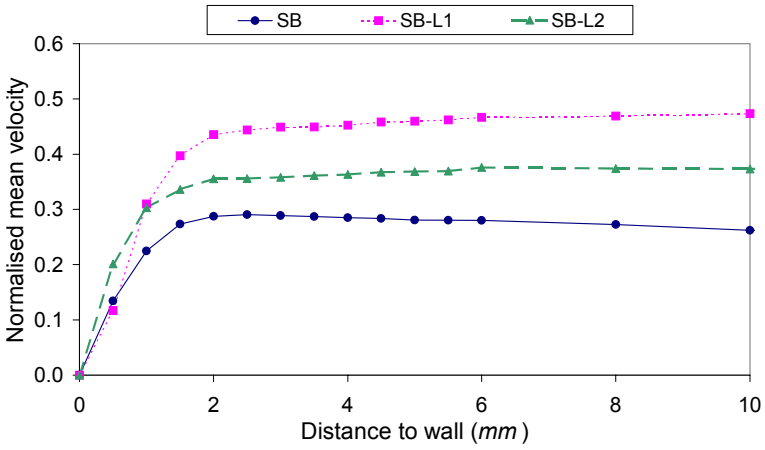

Figure 7.94- Normalised mean tangential velocity; wavy lids effects; Re=10,000

The presence of waves has the effect of increasing the mean velocity near the sediment surface. This behaviour may be due to the strong vertical component of the momentum resulting from the shape of the top surface. In this region of the flow cross section (close to the outer wall of the flume), the downwards velocity is higher than that observed in the absence of waves, pushing the flow towards the bottom surface and increasing the local tangential velocity.

It should be stressed that the data from lid L1 (higher amplitude, lowest wavelength) clearly shows a much higher velocity. This is due to the reduction in the effective channel size, which results from such configuration of amplitude/wavelength: most of the main flow is confined to the free space between the lower part of the lid and the sediment surface. However, the calculation of the local shear stress at the interface shows that, when the wavelength is increased (lid L2), the wall shear increases from 0.513 *Pa* up to 0.884 *Pa*. In this case, because of the increased wavelength, the main fluid flow is not confined to the free space and is also driven by the upper surface (crest) of the lid. This yields an oscillatory vertical motion of the flow, which, in turn, increases the surface shear. This hypothesis is confirmed by the measurements of the vertical component of turbulence, which shows a higher value in most of the measuring section for lid L2.

As a consequence of the higher velocity gradients near the sediment surface when using wavy lid L2, the resulting shear stresses (including both the laminar and turbulent components) are also higher (Figure 7.95).

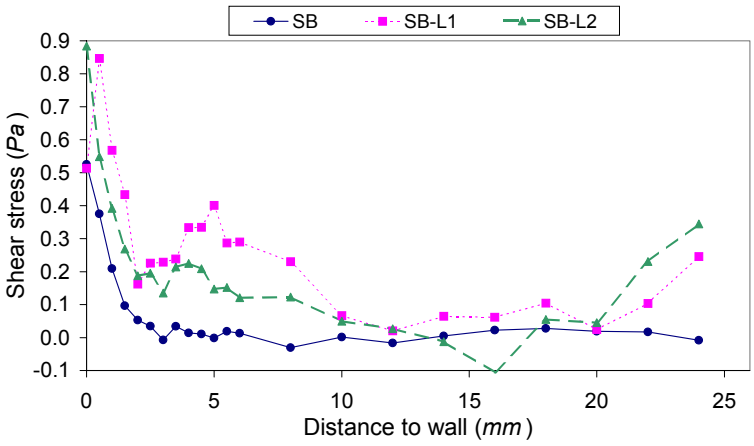

Figure 7.95- Shear stress; wavy lids effects; Re=10,000

Another interesting feature is that, in the absence of waves, the local shear stresses are negligible except in the regions very near the wall. In this case, it is clearly a wall driven shear. On the other hand, when surface waves drive the flow, shear stresses are not negligible even in the flow main stream. Therefore, it can be concluded that the shear stress is a surface phenomenon but it is also affected by the momentum transport from the surface due to the wave motion.

The analysis of the flow shear stress shows that in the regions near the surface, the contribution of the laminar shear dominates, as the turbulent contributions are negligible. However, for regions further away from the bottom surface, the turbulent stresses dominate.

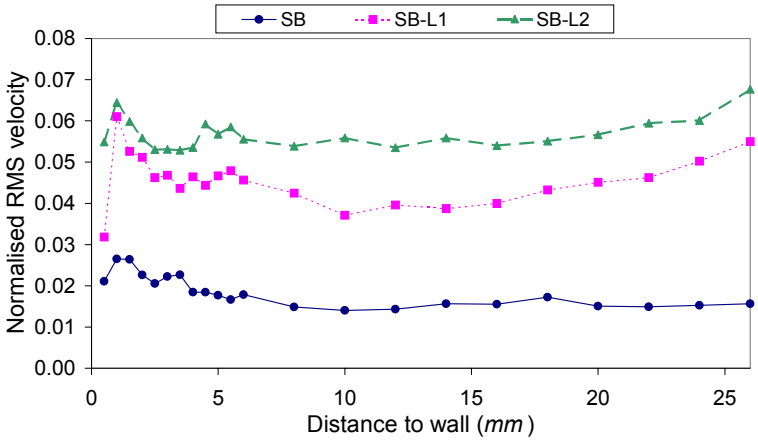

Figure 7.96- Tangential velocity turbulence; wavy lids effects; Re=10,000

The turbulence levels are always higher in the presence of surface waves, when compared with those of a smooth surface (Figure 7.96). In addition, the local turbulence level

increases towards the wavy lid, contrary to the trend observed when waves are not present. These higher levels are due to the flow oscillations generated near the liquid surface.

Another meaningful conclusion is that turbulence increases with the wavelength. In this case the flow oscillates over a wider region of the main flow. Because turbulence is a time averaged quantity, these oscillations are accounted into the RMS value of the velocity.

The mean and turbulent velocities and the shear stress results of the four different lids are compared with the smooth case in Figures 7.97, 7.98 and 7.99, for Re = 20,000.

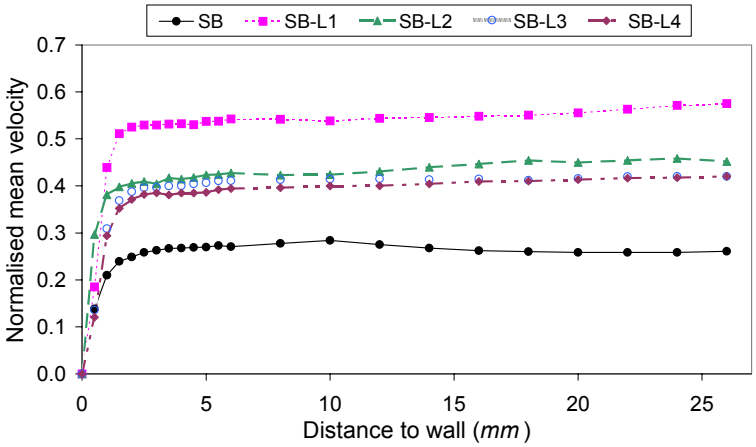

Figure 7.97- Normalised mean tangential velocity; wavy lids effects; Re=20,000

The trends previously discussed for low Reynolds numbers are also observed at Re = 20,000. Again, the effect of wavelength is to decrease the mean velocity near the bottom surface although the effects are weaker for lower wave amplitudes (lids L3 and L4). For these lids, no significant effect is observed on the velocity profile, yielding a lower wall shear stress.

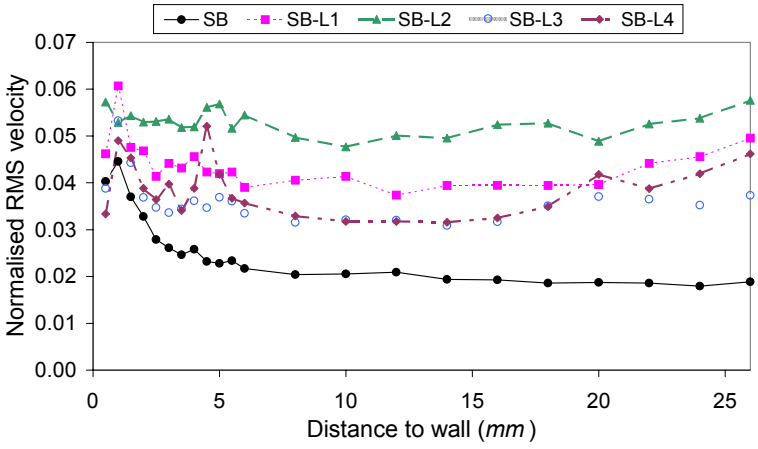

Figure 7.98- Tangential velocity turbulence; wavy lids effects; Re=20,000

Figure 7.98 shows the effect of wave characteristics upon the flow turbulence. The behaviour observed for Re = 10,000 is also found for higher Reynolds numbers. Figure 7.98 also shows the effect of the wave amplitude upon flow turbulence. The reduction of the amplitude in surface waves decreases the flow oscillations, hence the turbulence.

In general, it is observed that when surface waves drive the flow, the turbulence is always high and, in some cases, nearly constant through the flow field. This means that this turbulence is generated from the surface waves and is not related with the sediment surface.

Figure 7.99 shows the effect of wave geometry upon the flow shear stress. The trends discussed for low Reynolds numbers also apply for the condition reported here.

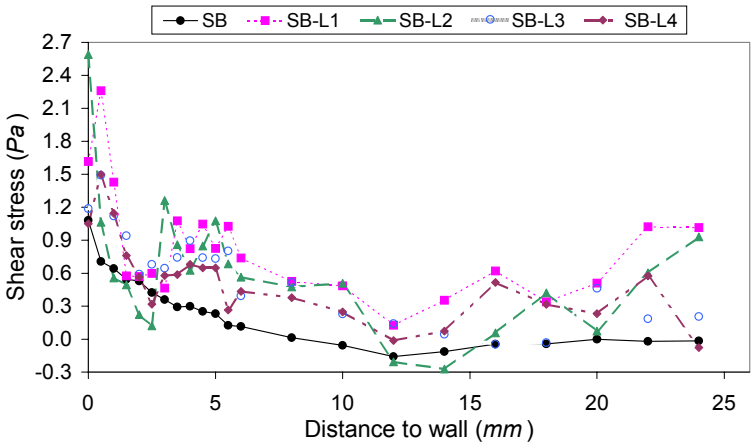

Figure 7.99- Shear stress; wavy lids effects; Re=20,000

Again, the wall shear stress is higher using lid L2 (2.590 *Pa*), following the lid L1 (1.616 *Pa*). The wall shear stress to lids L3 and L4 are similar and not much different from that to smooth bed (1.187, 1.050 and 1.081 *Pa*, respectively).

The comparison for a high Reynolds number (Re = 40,000) for lids L1 and L2 and for a smooth lid is shown in Figures 7.100 through 7.102.

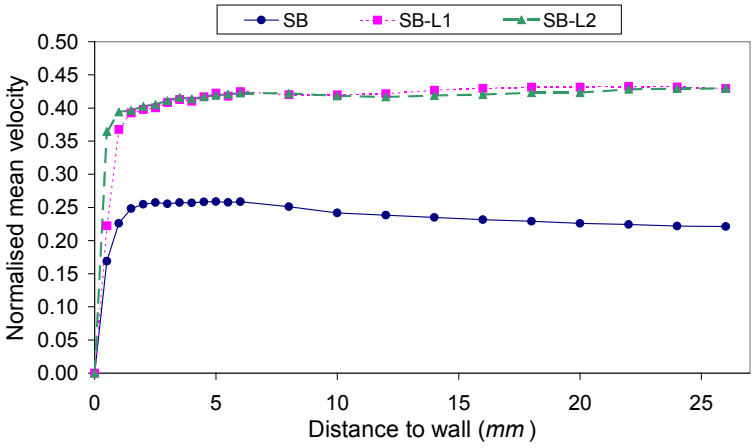

Figure 7.100- Normalised mean tangential velocity; wavy lids effects; Re=40,000

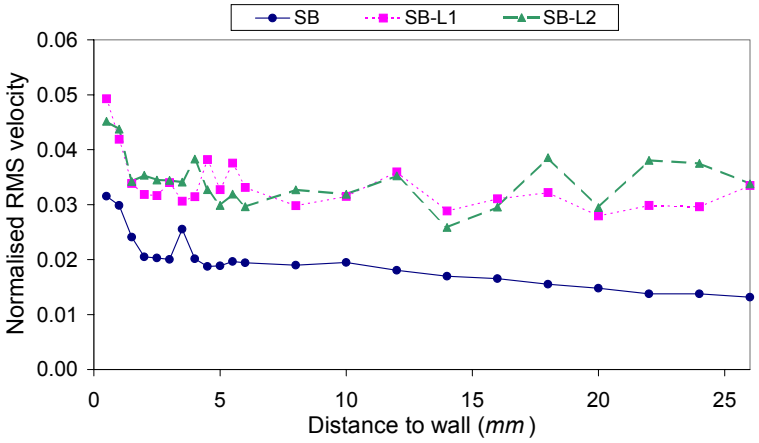

Figure 7.101- Tangential velocity turbulence; wavy lids effects; Re=40,000

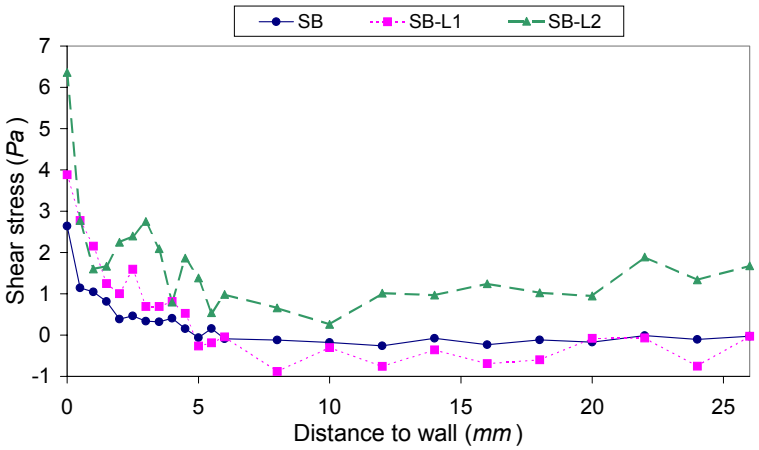

Figure 7.102- Shear stress; wavy lids effects; Re=40,000

When the Reynolds number increases, an increase in the wall shear stress is also observed, being 2.641, 3.885 and 6.361 *Pa* for SB, SB-L1 and SB-L2, respectively.

By increasing the Reynolds number it may be concluded that, as opposed to that observed at low flow velocities, the results for the mean and the RMS velocities (Figures 7.100 and 7.101, respectively) are very similar for lids L1 and L2. This suggests that the effect of wavelength is stronger at low Re, which can be related with the reduction of boundary layer thickness at higher velocities.

7.3.1 MULTIPLE FACTORS

Wavy flow over a rough bed

The velocity fields resulting from the simultaneous use of rough bed RB1 and wavy lid L1 (RB1-L1) are shown in Figures 7.103 through 7.105, for the tangential, axial and turbulence velocity, at Re = 20,000.

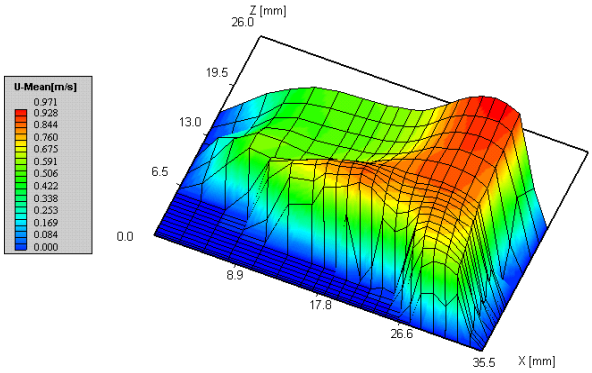

Figure 7.103- Tangential velocity field; combined effect RB1-L1; Re=20,000

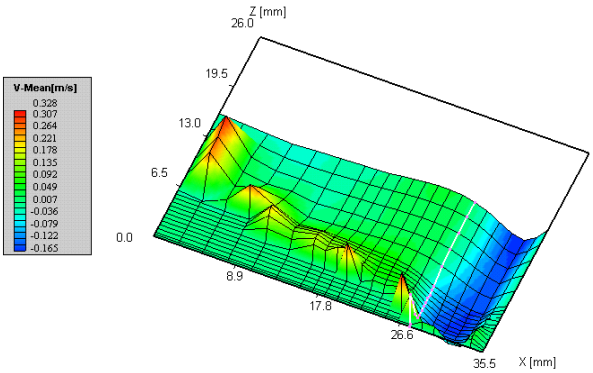

Figure 7.104- Axial velocity field; combined effect RB1-L1; Re=20,000

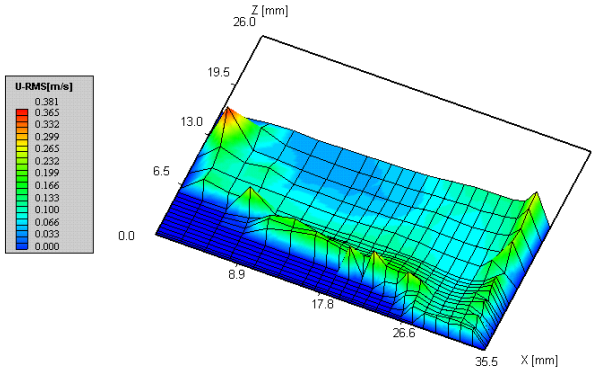

Figure 7.105- Tangential velocity turbulence; combined effect RB1-L1; Re=20,000

Comparing Figures 7.103 and 7.104 with Figures 7.88a and 7.90a, the influence of surface roughness is evident, increasing the tangential as well as the axial velocities. By introducing the surface roughness into the flow, the size of the recirculating vortices is increased as the upwards velocity occurs closer to the inner wall. Furthermore, these effects are emphasized when Re increases.

Similarly to the smooth bed, the vertical profiles obtained at 7.5 *mm* from the outer ring using the rough bed with (RB1-L1) and without (RB1) the wavy lid are shown in the following figures. Results for the normalised mean velocity, the shear stresses and the tangential velocity turbulence profiles are shown in Figures 7.106 through 7.108, at a low Reynolds number (Re = 10,000).

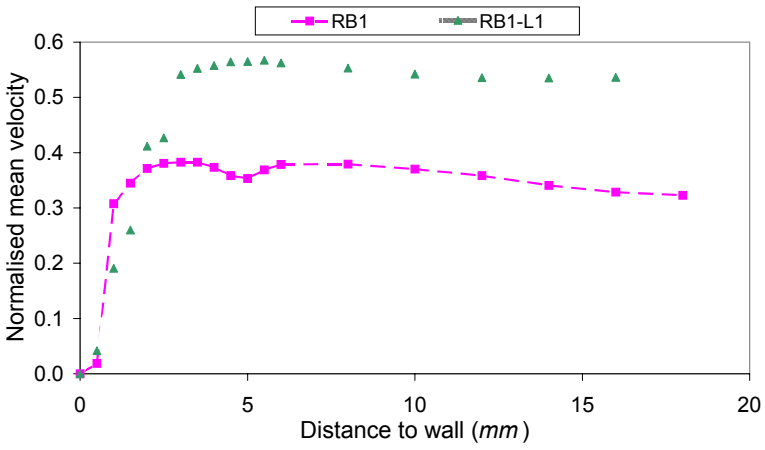

Figure 7.106- Normalised mean tangential velocity; wavy lid effect on a rough bed; Re=10,000

The data in Figure 7.106 shows that the presence of surface waves increases the mean velocity in the vicinity of the wall. Comparing with data from Figure 7.94, the trend reported here is very similar. In addition, it is also found that the whole velocity profile is moved outwards from the wall.

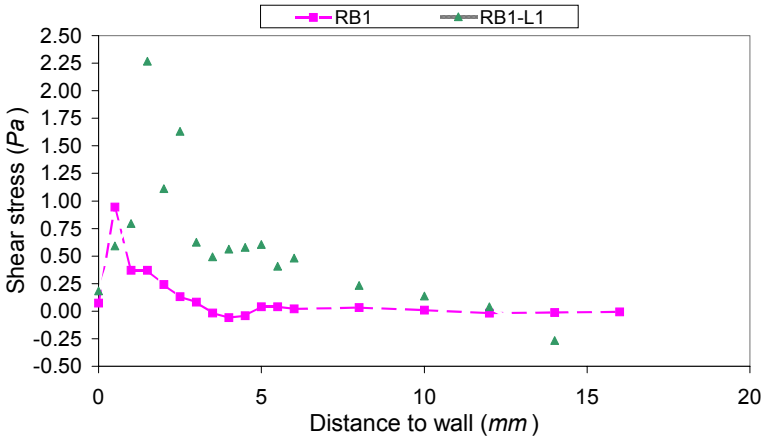

Figure 7.107- Shear stress; wavy lid effect on a rough bed; Re=10,000

Because the velocity gradient near the bottom surface is very similar in both conditions, the shear stress in this region (dominated by wall effects), when surface waves are present, is in close agreement to that found when they are absent (Figure 7.107).

Therefore, the shear stress at the interface is governed by the sediment surface morphology. Waves appear to affect the region above the sediment where the shear stresses are dominated by turbulence shear (Figure 7.108).

When sediment roughness is considered, the presence of waves does not appear to be relevant to the conditions concerning the onset of erosion, although they may be of great relevance to the dispersion of entrained sediments into the main flow, once they are eroded from the bed.

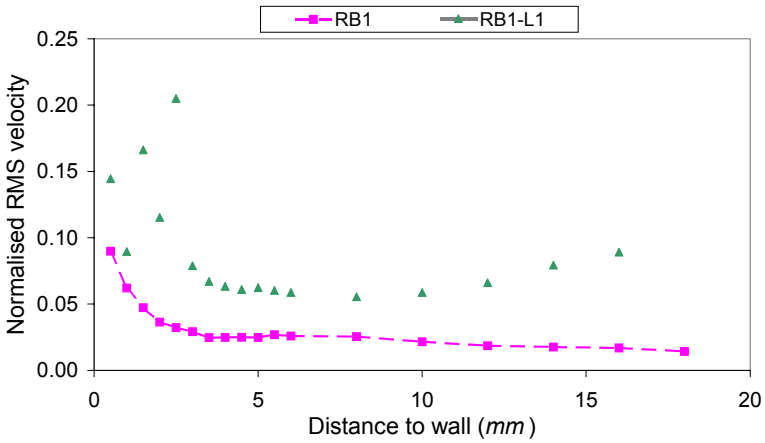

Figure 7.108- Tangential velocity turbulence; wavy lid effect on a rough bed; Re=10,000

In Figures 7.109 through 7.114 results are presented for increasing Reynolds numbers (20,000 and 40,000). The data includes mean velocities, tangential velocity turbulence and shear stresses.

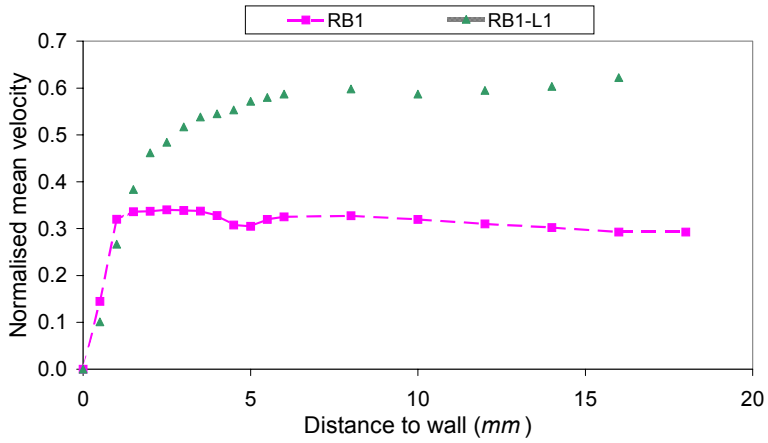

Figure 7.109- Normalised mean tangential velocity; wavy lid effect on a rough bed; Re=20,000

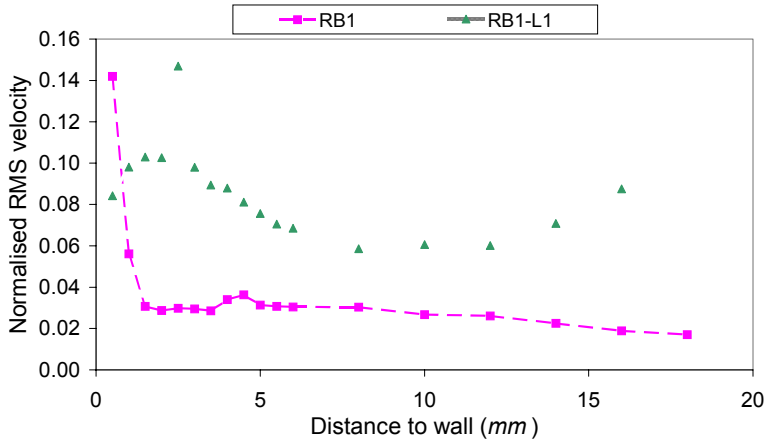

Figure 7.110- Tangential velocity turbulence; wavy lid effect on a rough bed; Re=20,000

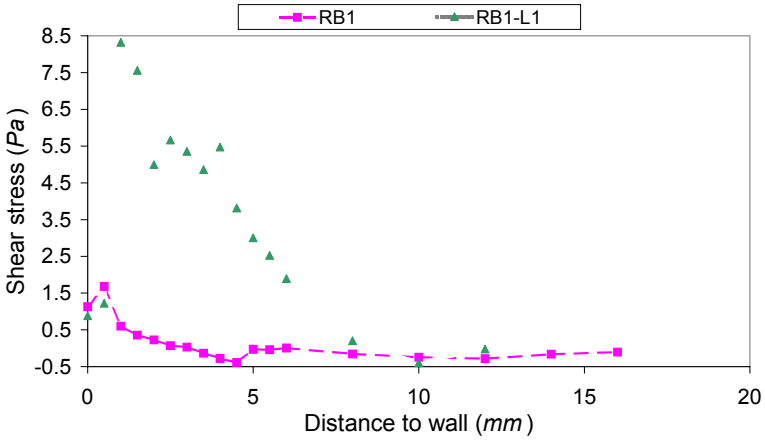

Figure 7.111- Shear stress; wavy lid effect on a rough bed; Re=20,000

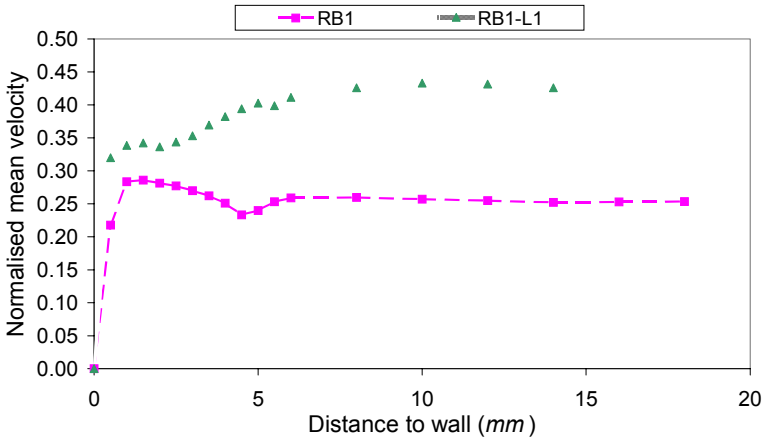

Figure 7.112- Normalised mean tangential velocity; wavy lid effect on a rough bed; Re=40,000

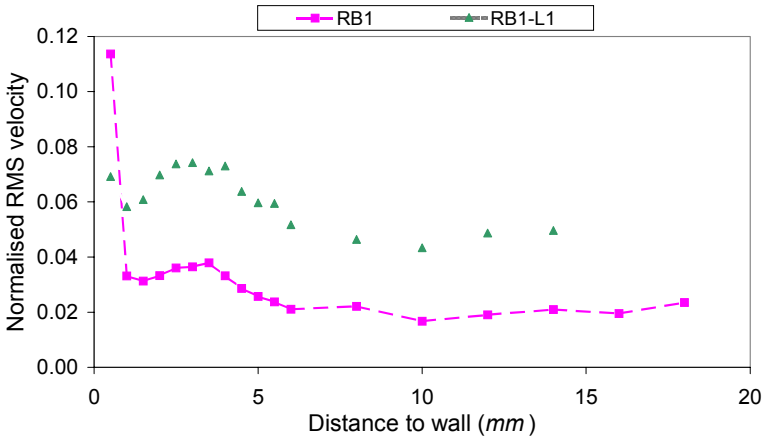

Figure 7.113- Tangential velocity turbulence; wavy lid effect on a rough bed; Re=40,000

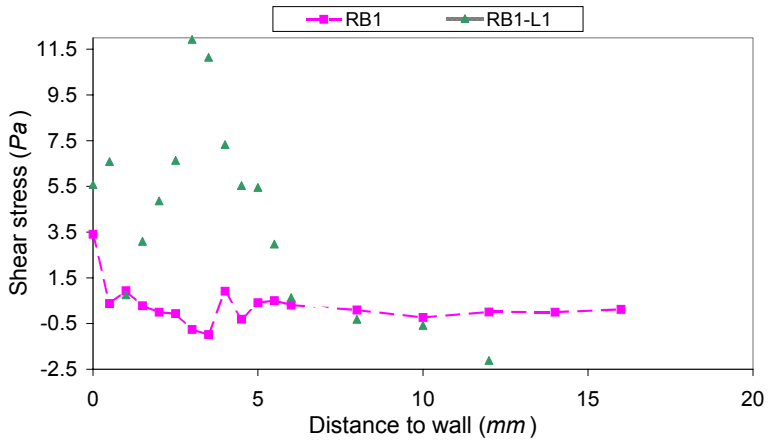

Figure 7.114- Shear stress; wavy lid effect on a rough bed; Re=40,000

By observing the velocity profiles (Figures 7.109 and 7.112) it may be concluded that the mean velocity (in the region adjacent to the bottom wall) is shifted towards the wall due to the reduction of the boundary layer thickness, although the velocity gradient is similar both with and without waves. Therefore, the shear stresses (Figures 7.111 and 7.114) at the sediment interface are similar in both cases, although an increase in the shear stress with the Reynolds number is observed. In addition, the laminar component of the shear stress increases near the wall although it is limited to a smaller region in the vicinity of the interface.

In the regions further away from the interface, the turbulent stress dominates the laminar component and the total shear stress in the presence of waves deviates from that when waves are not present due to their contribution to the turbulent shear (Figures 7.110 and 7.113).

In this case, the reduction of the boundary layer thickness with increasing Reynolds number is also in accordance with the reduction of that narrow region, close to the sediment interface, where the shear is dominated by the surface roughness.

Wavy flow over particles

Results presented below show the interference of surface waves with particles present in the flow. A comparison of the profiles obtained using the wavy lid (P3-L1) or not (P3), is made, at the usual radial distance.

It is important to stress that, in these conditions and during the experiments at various flow velocities, it was not possible to observe any dune inside the flume, because the beads were evenly dispersed. This observation is in agreement with the suggestion previously outlined that the turbulent shear associated with the waves is of great relevance to the dispersion of entrained particulate matter into the main flow. This occurrence did not take place in the absence of surface waves (section 7.2). Similar observations were made by Raudkivi (1997), in which strong interaction between fluid and surface waves may lead to such features as antidunes. In fact, looking at the axial velocity fields, using a flat lid (Figure

7.20a) the recirculation bubble is located close to the outer wall (favours dune development), as sketched in Figure 6.6. In the presence of a wavy lid, that bubble is larger and moves towards the inner ring, as shown in Figure 7.115.

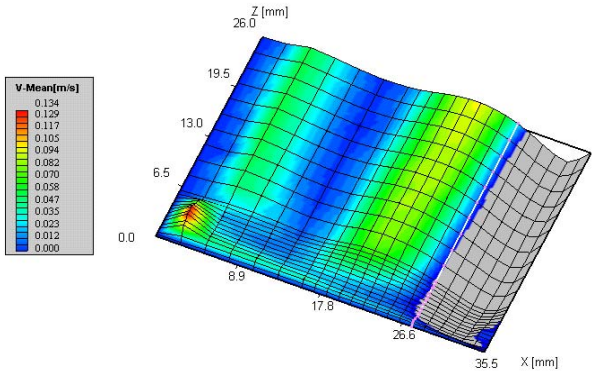

Figure 7.115- Axial velocity field truncating the scale; L1; Re=20,000

Figure 7.115 shows a strong upwards flow close the inner wall. All these conditions contribute to the absence of dunes. The recirculation pattern inside the flume, using the wavy lid, is sketched in Figure 7.116.

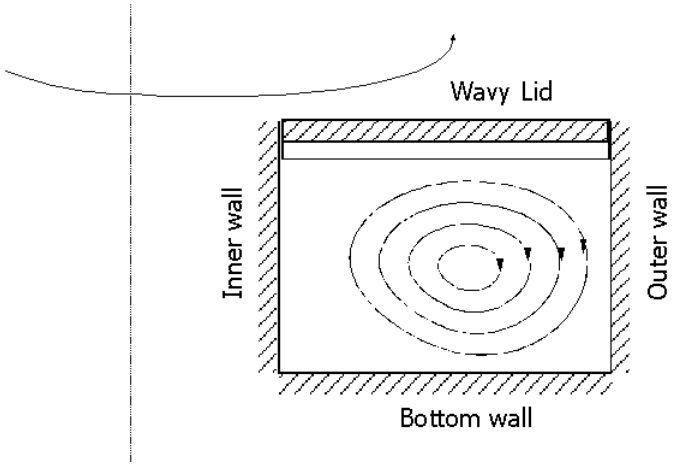

Figure 7.116- Recirculation pattern in a flume; wavy lid

The turbulence profiles at Re = 20,000 and 40,000 are depicted in Figures 7.117 and 7.118, respectively.

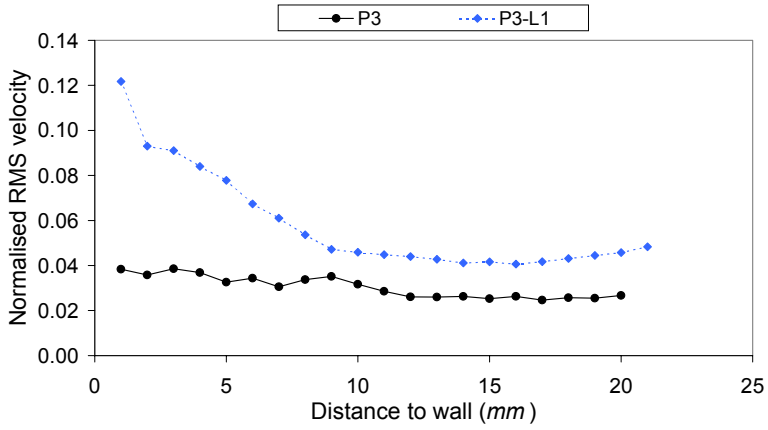

Figure 7.117- Tangential velocity turbulence; wavy lid effect on a deformable bed; Re=20,000

In Figure 7.117 the data shows that turbulence levels are considerably higher than those measured in the absence of waves. This observation is particularly evident in the region close to the wall. Further from the surface, the profile appears to level off, a feature that does not occur at higher Reynolds number (Figure 7.118).

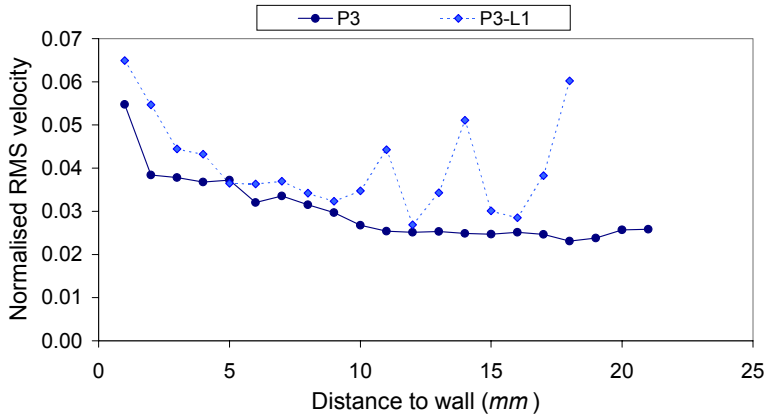

Figure 7.118- Tangential velocity turbulence; wavy lid effect on a deformable bed; Re=40,000

The increase in turbulence is clearly linked with particle entrainment into the main flow and this is in agreement with early observations concerning the high shear stresses in the region immediately above the bed. By increasing the Reynolds number (Figure 7.118), the difference between a wavy and a smooth surface is less evident because, at such high Reynolds numbers, the mechanism of entrainment and dispersion is already very strong even in the absence of waves at the liquid surface (see section 7.2).

7.3.2 DISCUSSION

From all the results presented, some conclusions can be drawn.

The presence of waves increases the vertical component of the momentum, increasing the mean tangential velocity in the vicinity of the sediment surface, yielding an increase in shear stress near the sediment. In addition, the high shear stress (when compared with the case of no waves) above the region of strong gradients (further away from the sediment surface) shows that in such regions, the shear is dominated by turbulence.

The data also shows that an increase in wave amplitude (for both wavelengths) increases the flow mean velocity, hence the shear stress at the sediment surface. Furthermore, the turbulence levels also increase.

The decrease in wavelength shows that the average cross section for the main flow is reduced which, in turn, increases the velocity gradient near the sediment and the shear stress. On the other hand, the increase in wavelength increases the amplitude of the flow oscillations into the main flow and the local turbulence, as this quantity is a time average property.

The data, integrating the simultaneous influence of surface waves and sediment roughness, shows some important features when compared with that on a smooth sediment. Due to the high surface roughness, the flow properties in the immediate vicinity of the sediment surface are controlled by the wall. In such circumstances, the surface shear stress does not show significant deviations to that observed in the absence of waves. However, in the region of turbulence dominated shear, the presence of waves do show an important contribution to the flow patterns. It may be concluded that surface waves may not be very significant in terms of initiating the erosion process (sediment surface properties are more important) but they do contribute to the dispersion of entrained matter into the main flow. The increase in Reynolds number, extends the region of turbulence dominated shear at the expense of the reduction of the laminar shear. This is linked with the reduction of the boundary layer thickness.

This effect of wave driven particle dispersion was confirmed by the experiments with suspended particles. In this case, even at low Reynolds numbers, the entire particle population is dispersed into the flow, increasing the local turbulence.

Putting together all the contributions analysed, Figures 7.119 and 7.120 show such effects, at Re = 20,000 and Re = 40,000, respectively.

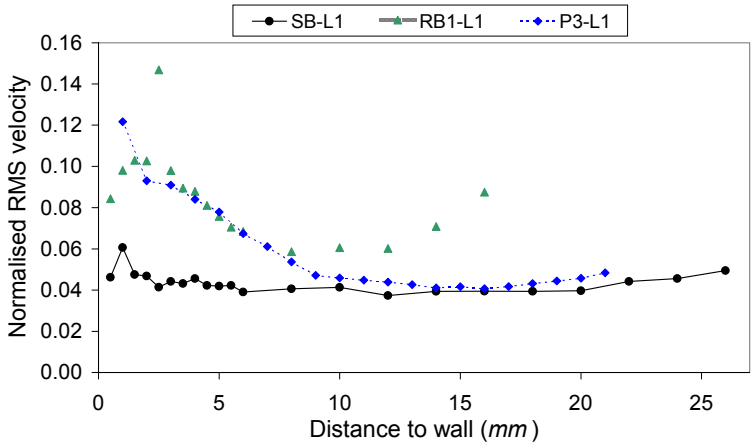

Figure 7.119- Tangential velocity turbulence; wavy lid effect on a smooth, a rough and a deformable bed; Re=20,000

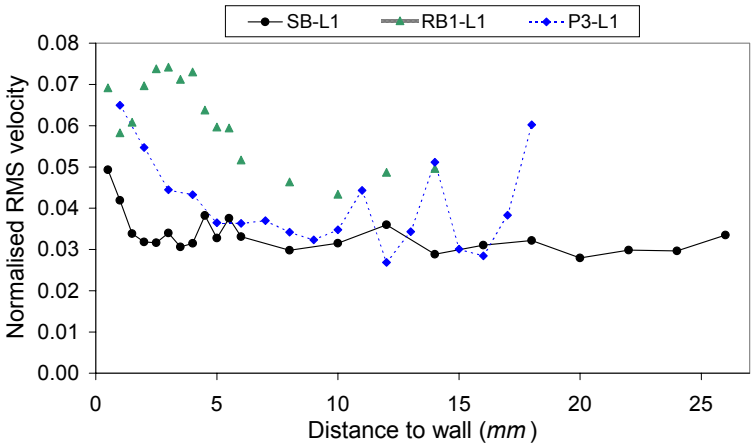

Figure 7.120- Tangential velocity turbulence; wavy lid effect on a smooth, a rough and a deformable bed; Re=40,000

It can be concluded that, using a rough bed, the turbulence is enhanced far from the surface and is higher than that obtained to the other conditions, particularly at Re = 40,000. The same observations did not occur without the wavy lid, in Figure 7.87, where turbulence was higher for the deformable bed. Furthermore, Figure 7.120 shows oscillations when using the spherical beads, which are related with flow oscillations induced by the wavy lid.

7.4 TWO-FLUID BED

As referred in Chapter 5, one of the simulated beds consisted in using two immiscible liquid layers, in which the lower fluid is highly deformed under a shear stress.

Because the sediment beds are known to deform, under the effect of fluid shear, James and Jones (1992) have used a combination of fluids to simulate the deformable interface. However, the combination of fluids used is not appropriate because the very high viscosities yield a highly laminar flow on the top fluid. Figure 7.121 shows the normalised velocity profile in the vicinity of the interface. Because of the present fluids combination, the Reynolds number is low, though the range could be extended into the laminar-turbulent transition. Nonetheless, the data suggests that, assuming a non-deformable interface, the shear stress is much higher (29.9 *Pa*) than that expected for a rigid interface (Figure 7.19). This suggests that such hypothesis is not applicable and the lower layer fluid, such as depicted in Figure 7.122, exhibits a strong deformation. Such deformation (visually observed during the course of the experimentation) yields a reduction of the actual shear stress at the interface. For this combination of fluids, no optical access could be made into the lower fluid for direct LDA measurements, in order to directly measure the velocity.

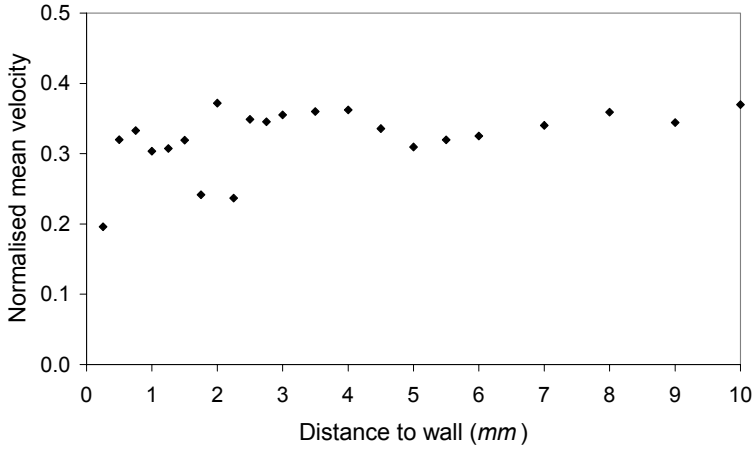

Figure 7.121- Mean tangential velocity; two-fluid bed; Re=2,500

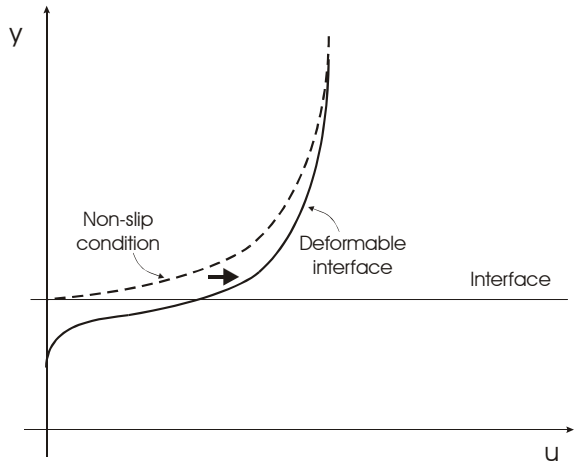

Figure 7.122- Velocity profile modification at a deformable interface

The velocity profile was compared with other data, as shown in Figure 7.123.

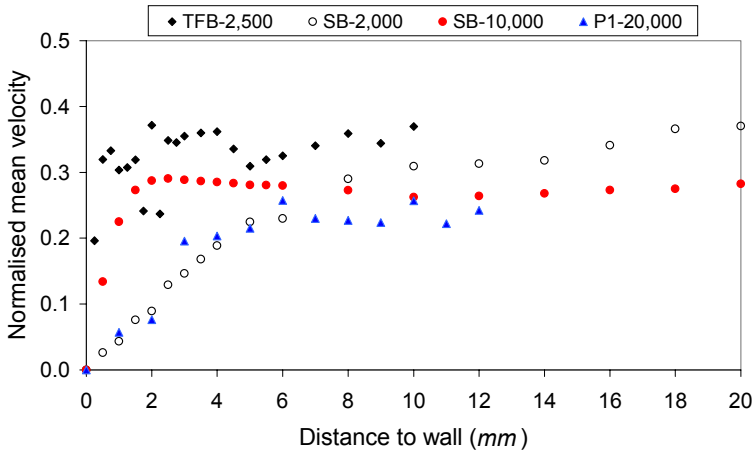

Figure 7.123- Mean tangential velocity; two-fluid (TFB), rigid (SB) and deformable (P1) beds

Figure 7.123 shows that, for similar Re, the rigid surface (SB-2,000) exhibits a much lower wall shear stress than that expected for the two fluid combination if the non deformation of the lower fluid is assumed. Even at much higher velocities (SB-10,000), the data still shows a lower shear at the surface. On the other hand, the data for a fully deformable bed (P1) shows a very low wall shear stress. Therefore, although no velocity data is available for the lower fluid, there is enough evidence suggesting that a considerable deformation occurs at the interface.

Figure 7.124 shows the turbulence velocity normalised. Results are lower than those found in other beds.

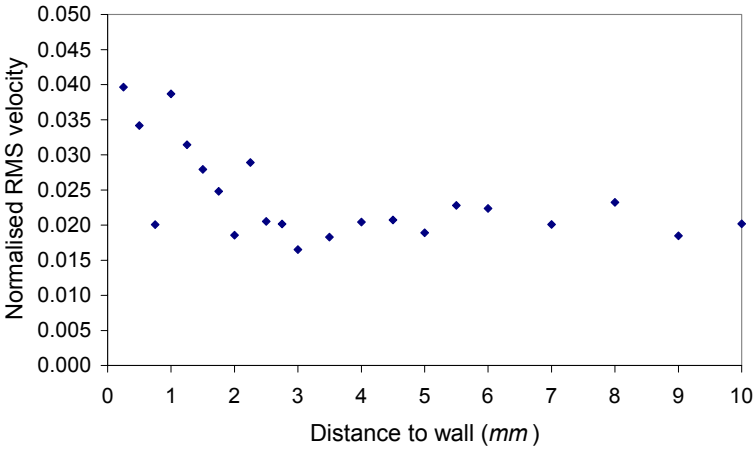

Figure 7.124- Tangential velocity turbulence: two-fluid bed; Re=2,500

7.5 CONCLUDING REMARKS

The contribution of surface roughness, particles entrainment and surface waves to the turbulence was investigated in the previous sections along this chapter. Figures 7.87 and 7.119 presented the turbulence profile, at Re = 20,000, for each factor. It may be concluded that both the surface roughness and topology increase turbulence very close to the wall. Also, the concentration of suspended particles is the main factor affecting the fluid turbulence in the vicinity of the bottom surface. The presence of surface waves proved to be important, particularly in regions away from the wall.

CHAPTER 8

FLOW OVER NATURAL SEDIMENTS: RESULTS AND DISCUSSION

This chapter reports measurements in natural sediments, with the purpose of investigating seasonal and sampling site effects. For this purpose, data obtained in different estuaries is compared. The data is used to calculate the critical shear stress and a comparison between simulated and natural beds is made.

Because of the high beam intensity in the measuring probe volume, the LDA could operate and provide meaningful data at a fairly high concentration of suspended particles. In this way, measurements of velocity profiles and turbulence could be carried out beyond the onset of erosion. However, for the highest Reynolds number tested with each sample the data is untrustworthy because of the very high turbidity inside the mini flume, which led to very low data rates. All data reported in this chapter refers for a vertical profile located at 7.5 *mm* from the outer wall.

8.1 SEASONAL EFFECTS

In order to investigate the seasonal influence on the sediment erosion, Figure 8.1 shows the normalised mean tangential velocity for samples collected close to the river water: C12 (Autumn), C16 (Winter), C18 (Spring) and C20 (Summer). The mean velocity was normalised by the maximum velocity inside the flume, at the outer edge of the driving lid. Results were taken at Re = 20,000. The normalised tangential velocity turbulence is presented in Figure 8.2.

The tangential velocity profiles in Figure 8.1 show differences near the surface, depending on the season. Thus, the surface shear stress for sample C12 is the highest (0.433 *Pa*), although the data for samples C18 and C20 (0.026 and 0.028 *Pa*, respectively) is similar. The Winter season sample (C16) presents a value in between (0.119 *Pa*).

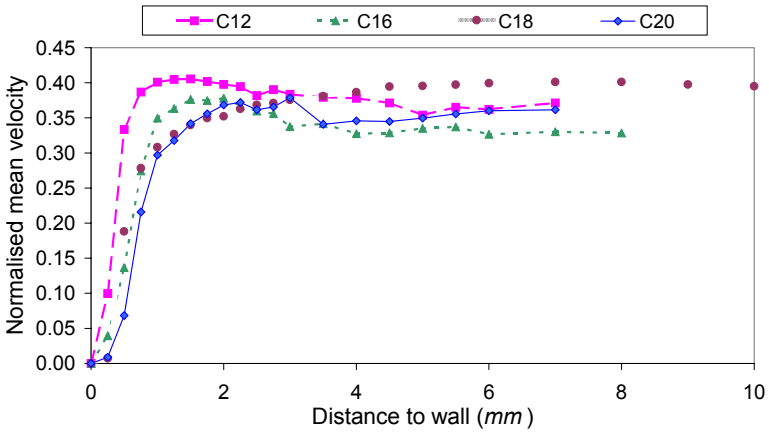

Figure 8.1- Mean tangential velocity: seasonal effects; samples close to the water

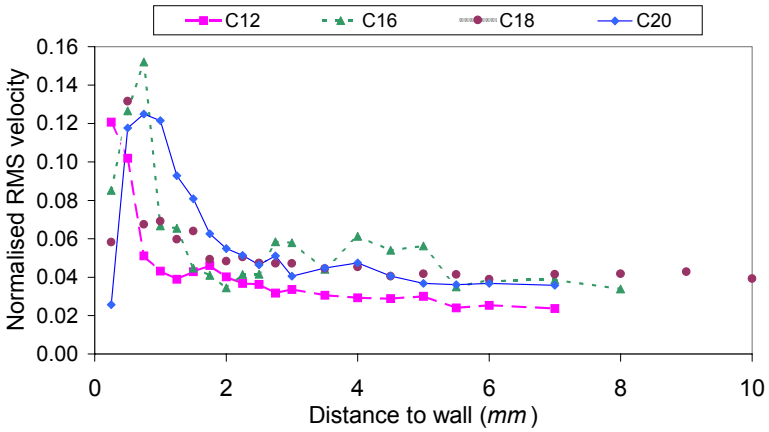

Figure 8.2- Tangential velocity turbulence: seasonal effects; samples close to the water

These shear stress values are directly related with the particle size and the water content of each sample. In fact, as referred in Table 5.19, samples C18 and C20 are sandy and non-cohesive, showing a low percentage of water (Figure 5.21) and a large particle size diameter (Table 5.22). These factors reduce cohesiveness, yielding a lower wall shear stress. However, using Table 5.24 it is possible to evaluate more correctly the sediments cohesiveness. As mentioned in Chapter 5, the cohesiveness of sediments increases with decreasing particle size, i.e. how muddy the sample is. By careful analysis of Table 5.24, it may be concluded that sample C13 is the most cohesive, which is in agreement with visual results (Table 5.19). In general, the Cávado samples are not much cohesive, being, in this way, the grain size distribution a more relevant parameter than the biological processes (Mitchener and Torfs, 1996).

Because natural muds are non uniform, a cohesiveness classification solely based upon the particle size distribution is not complete (Torfs, 1995). Using the Flemming (2000) classification of muddy sediments (gravel-free) and looking at Table 5.24, most part of

Cávado samples are classified as muddy sand (25-50 % mud), though samples C13 and C16 may be identified as sandy mud (50-75 % mud).

The turbulence data presented in Figure 8.2 shows a similar trend for all the profiles, although in the close vicinity of the surface the slightly muddy samples (C12 and C16) do show higher turbulence

For each sample, the wall shear stress as a function of the Reynolds number, is presented in Figure 8.3.

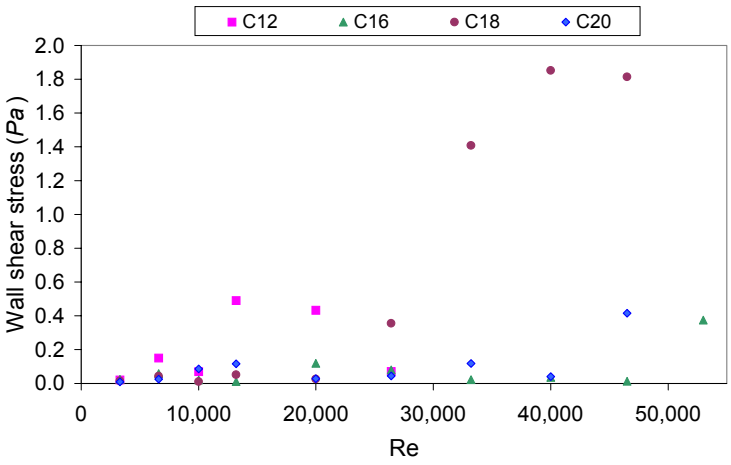

Figure 8.3- Wall shear stress: seasonal effects; samples close to the water

The shear stress values are of the same order of magnitude as those directly measured using contact probes (Graham *et al.*, 1992) or other instruments (Williamson and Ockenden, 1996; Tolhurst *et al.*, 2000a; Black *et al.*, 2002). Such value of the shear stress at the interface will represent the threshold for erosion. At low Reynolds number, the wall shear stress is similar for all the samples, but, at higher velocities, the differences become more evident as the deformation and subsequent destruction of the surface by erosion comes into play. Oscillations are observed in the local shear stress, suggesting that the sediment is eroded in layers, until a critical value is reached just before a layer is depleted. This means that there are variations in the cohesive properties, with depth. According with the Parchure and Mehta (1985) classification, these are stratified beds, which are formed by deposition of the suspended sediment under low flow velocities. This is easily justified because Cávado is considered a microtidal (< 2 *m*) estuary, having therefore relatively quiescent conditions and low energy (Kniskern and Kuehl, 2003). Also, the erosion threshold is significantly affected by small changes in composition when the sediment consists of a mud/sand mixture (Mitchener and Torfs, 1996). Thus, for the Cávado estuary, the grain size is a controlling parameter of erodibility.

As shown in Table 5.24, the samples tested present different percentages of mud and, as stated by Torfs *et al.* (1994), small increments in the percentage of mud may yield significant increases in the critical shear stress of the mixture.

Taking into account Figure 8.3, the critical shear stress (τ_{cr}) was determined for each sample. This parameter was inferred from the wall shear stress profile, corresponding to

the wall stress immediately before its first decrease (meaning that some sediment has been eroded). Results are shown in Table 8.1.

Table 8.1- Critical shear stress; samples near the water line

Sample	τ_{cr} (Pa)
C12	0.150
C16	0.058
C18	0.043
C20	0.116

There are various factors affecting the stability of the sediment bed, its erosion and, consequently, the critical shear stress, as detailed in Chapter 2. Some of those factors have already been quantified in Chapter 5 and Annex C, such as sediment salinity (Figure 5.22), particle size (Tables 5.22 and 5.23), temperature, pH (Table 5.20), water content (Figure 5.21). In addition to these factors, biological activity plays an important role (Black *et al.*, 2002).

It has been found that the biological activity varies throughout the year (Kornman and Deckere, 1998), affecting the sediment erodibility. Thus, in parallel with this work it was determined, throughout the year, the quantity of diatoms (Soares, 2004) in the vicinity of each one of the samples collected. The existence of brown stains on the sediment surface is an indication that diatoms are present (Paterson, 2001). Riethmüller *et al.* (1998) also related the erosion shear stress to tidal flat surface colour. Through optical reflectance spectra measurements, they found a dependence of erosion shear stress on both the amount of fine-grain fraction (below 63 μm, not covered by diatoms) and *chlorophyll a* concentration of benthic diatoms (brown algae or green macroalgae) present on the sediment surface.

Table 8.2 presents the percentage of diatoms (that produce EPS) determined for each season, for both places close and far from the river water, in the close vicinity of the sampling site.

Table 8.2- Percentage of diatoms per season and sampling site (Soares, 2004)

Season	Autumn		Winter		Spring		Summer	
	Close	Far	Close	Far	Close	Far	Close	Far
Diatoms (%)	13.0	19.0	22.0	25.8	19.4	25.8	27.6	29.4

It must be stressed that the correspondence between the brown stains observed at the surface of the sediment and the percentage of diatoms was not always evident because of the sand content. Also, the quantity of sand observed at the estuary surface was always higher in the regions close to the river water than further away. On the other hand, the

weather conditions in the days before sampling appears to be correlated with the percentage of diatoms. For example, because heavy rainfall preceded the Autumn sampling, a small quantity of brown stains was observed although the sediment surface did not present a large quantity of sand. In such case, the presence of diatoms could be affected by rainfall. However, when sampling three days later (samples C14 and C15), the field presented a much higher quantity of brown stains. This occurrence may be related with the sunny spell prior to sampling, which suggests that the recovery of sediment stability is fast Paterson *et al.*, (2000).

In both Winter and Spring the quantity of brown stains was small close to the river water (it was observed a large quantity of sand, maybe pebble, in this region) and high in the regions further away (muddy surface). However, the weather conditions prior to the collection were different: it was sunny in Winter and rainy in Spring (even during the sampling process). This fact justifies the relatively low percentage of diatoms observed in Table 8.2 in Spring. This table also always shows a lower percentage of diatoms in the site close to the river, not depending on the season. Because sampling was carried out in a slope, the concentration of diatoms was easily reduced.

The Summer sampling took place in a hot and dry day, and the highest quantity of sand at the surface (at any place) was observed. Therefore, the brown stains were practically non observable. However, the percentage of diatoms was the largest (for both sites), as observed in Table 8.2.

Crossing the information from Tables 8.1 and 8.2, it is observed that the critical shear stress was higher for sample C12 (Autumn), corresponding to the lowest quantity of diatoms. This quantity was the largest when sampling C20 (Summer). This means that other factors rather than the biological activity may dominate. In fact, although a low percentage of diatoms is associated with sample C12, this sample has the lowest pH value and a very low salinity, increasing the critical shear stress, as mentioned in Chapter 2.

Parchure and Mehta (1985) showed that the influence of salinity on erosion becomes important when it is below 10 *ppt*, and particularly when it is less than 2 *ppt*. In fact, for samples C12 and C18 that values are 0.33 and 8.19 *ppt* (Figure 5.22), respectively. This suggests that the erosion, particularly for sample C12, is greatly affected by the sediment salinity.

Although salinity may increase critical shear stress for sample C18, it has the lowest water content (because of the high percentage of sand), which decreases the critical shear stress. On the other hand, although sample C16 presents a high water content, its critical stress is lower than that found for sample C12 because its pH value is higher.

For sample C12, a maximum in the wall shear stress is linked to the initiation of the process itself, subsequently decreasing. Sample C18, which is very sandy, presents a large increase above Re = 26,400. This means that the sediment cohesiveness increased in depth, although oscillating in the early stages of the erosion process. This is an indication that there is a large quantity of sand at the surface, resulting in a lower shear stress, followed by a layer of mud (which increases that value), and by another layer of sand. The data suggests that the erosion process is not a continuous event; it is rather a step-by-step process of sediment depletion.

It has to be stressed that, once erosion is initiated, the exact location of the sediment interface becomes difficult to assess, due the presence of bedforms. Obviously, this will

affect the determination of the wall shear stress and, therefore, the critical shear stress retrieved from the velocity data.

Results concerning samples collected far from the water line are shown in Figure 8.4,

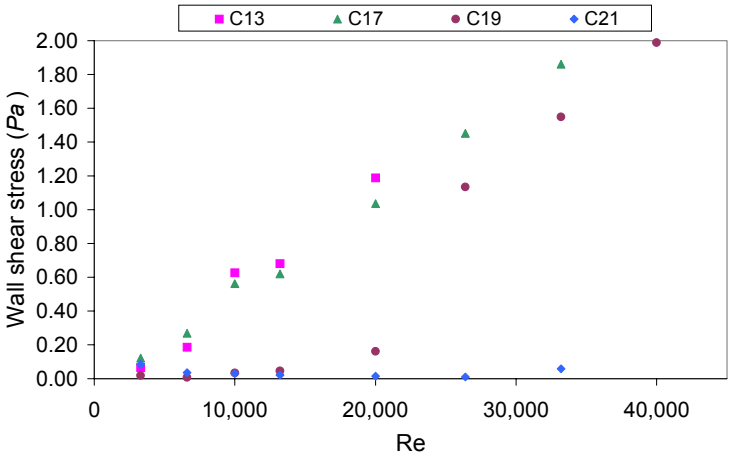

Figure 8.4- Wall shear stress: seasonal effects; samples far from the water line

and the resulting critical shear stresses are listed in Table 8.3.

Table 8.3- Critical shear stress; samples far from the water line

Sample	τ_{cr} (Pa)
C13	0.681
C17	0.621
C19	0.046
C21	0.031

Comparing Table 8.3 with Table 8.2, a higher percentage of diatoms correlated with the lowest critical shear stress (C21) and, conversely, a lower quantity of diatoms associated with the highest shear stress (C13) is observed. Such as with the previous 4 samples, the biological activity appears to have a negligible effect. This is evident by comparing, for example, samples C17 (Winter) and C19 (Spring), which present exactly the same percentage of diatoms and, nevertheless, exhibit a very different critical shear stress. The much higher value obtained for sample C17 is related with its higher water content as well as with a lower pH.

Both samples C13 and C17 show a similar water content and the same pH. However, the higher critical stress for C13 is due its very low salinity. Figure 8.4 shows a similar profile for both samples. Besides, samples C19 and C21 also have a similar water content, although lower than the previous two. Their differences in critical shear stress are related

with both the effect of salinity in sample C19 and its lower pH, increasing the critical stress.

These results confirm the previous assessment that, for the Cávado estuary, the sediment particle size is more important than the sediment biology. Particle size greatly affects the water content, enabling or disabling its retention. In addition, pH and salinity proved to be of high relevance in sediment stability.

In the same manner, measurements made on a macrotidal (10-14 *m*) mudflat by Mitchener and O'Brien (2003) have shown that, in spring tide conditions, the sediment water content is the major factor controlling the surface strength, while the biological processes have secondary influences. In addition, the authors found a seasonal trend of increasing sediment strength with monthly mean air temperature. Furthermore, de Brouwer (2002) identified a seasonal deposition of sediment mediated by benthic diatoms (biofilms favour deposition), in which sediment erosion was observed with their absence.

Also, Kornman and Deckere (1998) determined the erosion threshold in the period of March-August and reported that it was considerably higher in April and May. Furthermore, they observed that, within a period of two weeks, large variations in the erosion threshold took place. It suggests that collecting and analysing one sample per season is not meaningful, but measurements on a much shorter time basis are needed, particularly in Spring and Summer (when the quantity of diatoms is higher). At any rate, in the case of Cávado estuary, it was concluded that it does not make great difference.

As far as the sediment chemical composition is concerned, this was found to be approximately constant throughout the year (Figure 5.18).

In order to assess the influence of temperature in the fluid characteristics and subsequent erosion, various rheology tests and measurements of apparent viscosity were carried out on samples collected at different seasons, at the Cávado estuary (Annex C, Figure C.4). It was concluded that the influence of temperature in the rheological properties of the fluid is negligible. Temperature variations practically do not interfere with the flow conditions above the bed, but appear to be a non negligible factor on the sediment stability.

The data suggests that the erosion process mainly depends on the mud characteristics and composition and on the weather conditions, changing the surface shear stress. For the Cávado estuary, the weather conditions prior the collection becomes a key factor, probably more important than any large scale variations throughout the year.

8.2 SAMPLING SITE EFFECTS

To investigate the influence of the collection site location, comparisons are made for samples taken in the same season (same day), but at different distances from the shoreline. Thus, the sediment was exposed to the sun for different periods of time.

Winter samples, C16 (close) and C17 (far), and Spring samples, C18 (close) and C19 (far) are compared in Figures 8.5 and 8.6 for the mean tangential velocity and flow turbulence, respectively. The data refers to Re = 20,000.

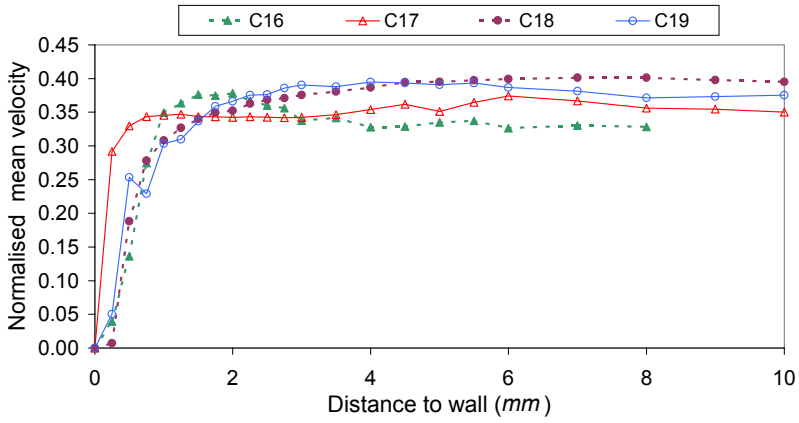

Figure 8.5- Mean tangential velocity: sampling site effects

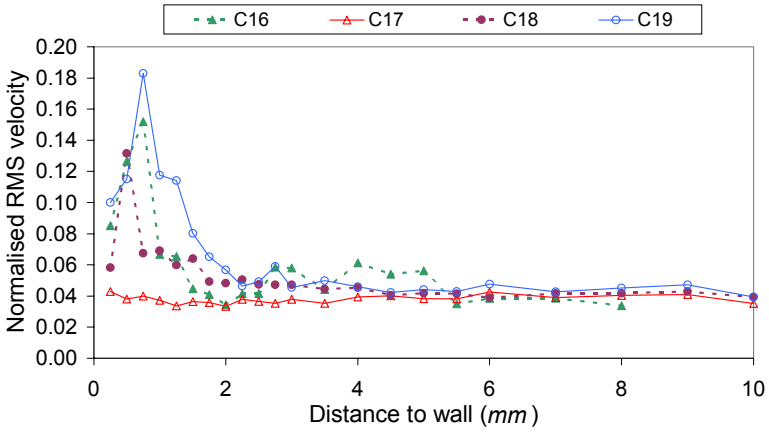

Figure 8.6- Tangential velocity turbulence: sampling site effects

The velocity profiles for the Spring samples are similar, although the wall shear stress is higher for sample C19 (0.162 *Pa*). Such differences in shear stress are related with the sediment composition, which is sandy and has a much lower water content in sample C18 (see Table 5.19 and Figure 5.21). Although for sample C18 the particle size is larger (Tables 5.22 and 5.23), lower turbulence (Figure 8.6) is observed. This means that other factors, such as topology, rather than the sediment roughness exhibit larger influences.

It was stressed by Tolhurst *et al.* (2000a,b) that results can be significantly influenced by user bias in site selection for sample collection, mainly when there is significant spatial variation such as of diatom patches, sediment irregularities, sand burrows. In fact, this point of view can also be applied for the sampling campaigns at the Cávado. Obviously, when evaluating parameters such as seasonality or sampling site, this fact makes the comparison of results more difficult. This is true because there are many simultaneous factors affecting the results and it is not easy to isolate them in order to determine which one is dominant.

For the Winter samples, a wider variation of wall shear stress was found (C16 and C17 in Figure 8.7). Such differences are related with differences in composition.

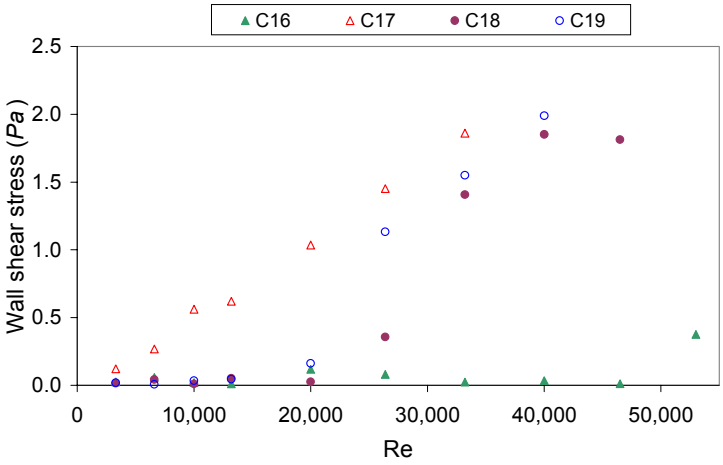

Figure 8.7- Wall shear stress: sampling site effects

From the data shown in Tables 8.1 and 8.3, a higher critical shear stress for both samples collected far from the river water (comparing C16 with C17 and C18 with C19) is observed, which may be due to the higher sediment water content in both cases. On the other hand, close to the river water (C16 and C18) the sediments were sandy and non cohesive (see Table 5.19), yielding a lower capacity for water retention. However, although large differences in water content are observed between C18 and C19 (see Figure 5.21), their critical shear stress was not much different, which may be related with the strong influence of salinity in sample C18.

The large differences in critical shear stress between samples C16 and C17 were mainly due the water content because they have the same pH value and are not influenced by salinity (above 10 *ppt*).

Parchure and Mehta (1985) have shown that the sediment shear strength increased with depth, being influenced by the type of sediment, period of bed consolidation and salinity. Such bed shear strength behaviour was also reported by Besley and Delo (1990).

It is observed in Figure 8.7 that, particularly for sample C17, the wall shear stress always increases with Re. This is a typical behaviour of a rigid surface, in which there is no deformation of the surface. It means that sediment particles are entrained into the fluid with a very small bed deformation. This is an indication that, for this sample, sediment shear strength increases with depth. A similar behaviour was observed for sample C19, although less evident at the early stages of the erosion process. In addition to the oscillations in wall shear stress at low Re, sample C18 shows a decrease in the later stages of the erosion process, meaning that a higher deformation of the sediment occurred. Changes in composition with depth for sample C16 justifies the oscillations obtained with Re. Observing the profile for this sample and comparing with that obtained for C13 (Figure 8.4), it may be concluded that, although both samples have similar percentage of mud on the top 2 *mm* (see Table 5.24), their wall shear stress is very different. However, as shown in Figure 5.21, the water content is not much higher for sample C13. This may be due the

muddy characteristics of sample C13 (resulting in water turbidity much earlier) and the existence of sand in sample C16 (decreasing the wall shear stress) (see Table 5.19). Therefore, changes in sediment composition with depth are a key factor affecting erosion.

The exposure time is another factor that may greatly affect the sediment stability (Amos *et al.*, 1988; Mitchener and O'Brien, 2003), due to drainage and desiccation. Widdows *et al.* (2000) found a reduction in sediment erodibility on the upper shore because of prolonged air exposure/dehydration during the low tide. Although samples close to the river water were always collected first, the others were always hydrated due to water retention, because of the sediment shape, as referred in Chapter 5.

It may be concluded that, in the Cávado estuary, more important than the seasonal effects is the sampling site, because the sediment properties greatly depend on the place where sampling is made. It was also found in other estuaries (de Brouwer *et al.*, 2000; Widdows *et al.*, 2000) that spatial differences in sediment structure, even on short distances, have a considerable effect on biological and physical processes.

8.3 COMPARISON BETWEEN DIFFERENT ESTUARIES

It was just reported that sediment properties depend on the sampling site. Thus, for two different estuaries it is not surprising that larger differences are obtained. In this way, samples collected in April in both the Cávado (C19) and Westerschelde (W) estuaries are compared. The physical aspect of both samples was different: while sample from Cávado presented some sand particles at the surface (particle size diameter is 37.47 μm), the other was very cohesive due to its small grain size (12.57 μm) and high water content (62.23 %) (see Annex C, Table C.3 and Figure C.12).

Although measurements in the Westerschelde sample were carried out two days after collection, its water content is much higher than in any of the Cávado samples. Therefore, the results from different samples are linked to the composition of the mud, and not due the evaporation. It must be stressed that, because of the different sediment properties, it is possible that in the Westerschelde the biological activity becomes a more important factor than that it was found to the Cávado. However, when measurements took place (48 *h* after) it is expected that the biological activity has disappeared. In this way, its effect upon the critical shear stress is diminute.

The cohesiveness (given by the percentage of mud) is much higher for Westerschelde sample (see Tables 5.24 and C.5). Flemming (2000) classification indicates that the sediment type in the Westerschelde is mud (> 95 % mud). As a result, the wall shear is higher for this estuary (Figure 8.8).

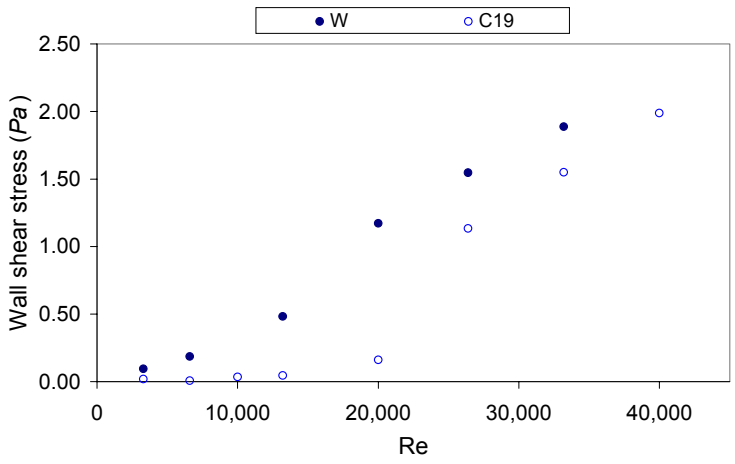

Figure 8.8- Wall shear stress: estuaries comparison

It is observed that, for the Westerschelde sample, the shear stress on the surface increases with the Reynolds number, suggesting that the sediment cohesiveness and strength increases with depth. In fact, for this estuary the sediment is uniform in depth, not showing sand on the deeper layers (this is evident in Annex C, Figure C.10 and Table C.3). Because the sediment particles for W sample are smaller, the suspended matter concentration is larger on this sample due the higher entrainment of particles and their higher settling times. Thus, high turbidity inside the flume occurs in the early stages. Hence, the suspended matter concentration resulting from the erosion tests was approximately twice for this sample.

From Figure 8.8 the critical shear stress for sample W is 0.483 *Pa*, which is over 10 times higher than that for sample C19 (0.0456 *Pa*). This could be related with the higher water content in that sample (see Figure 5.21 and Annex C, Figure C.12).

These results are in agreement with those obtained by Alvarez-Hernandez (1990) and Torfs *et al.* (1994), who found that critical shear stress increased with an increasing content of fine particles. And when the clay content is higher, it is harder to erode the bed material. Also, water salinity was found to be much higher in Westerschelde estuary (see Figure 5.15) and, consequently, the presence of salt in the correspondent sample is higher, affecting the erosion process.

Observing the tangential velocity profiles for both samples at different Re (Figure 8.9), higher velocities were obtained on Cávado sample.

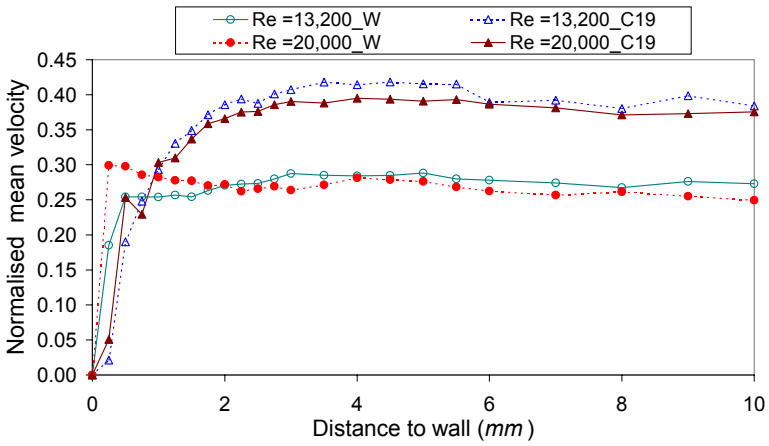

Figure 8.9- Mean tangential velocity: estuaries comparison

For a more detailed analysis in the sediment behaviour with the Reynolds number, Figures 8.10 and 8.11 show the normalised mean axial velocity profiles for samples C19 and W, respectively. This data may provide information concerning the deposition and transport of sediment in the vicinity of the bed. The positive and negative velocities correspond to an upward and downward flow, respectively.

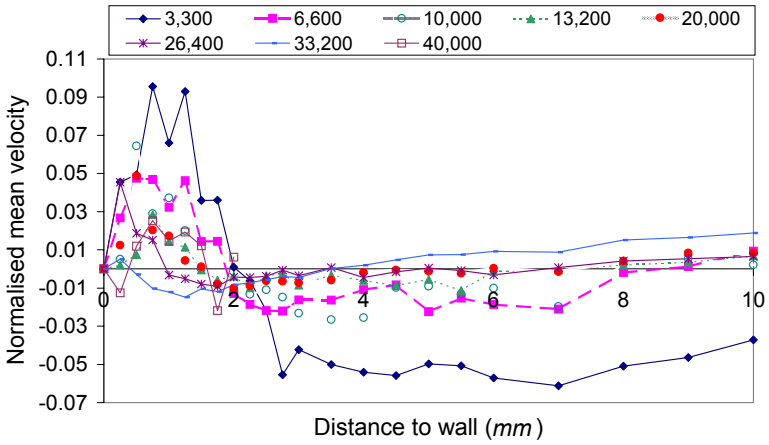

Figure 8.10- Mean axial velocity; sample C19

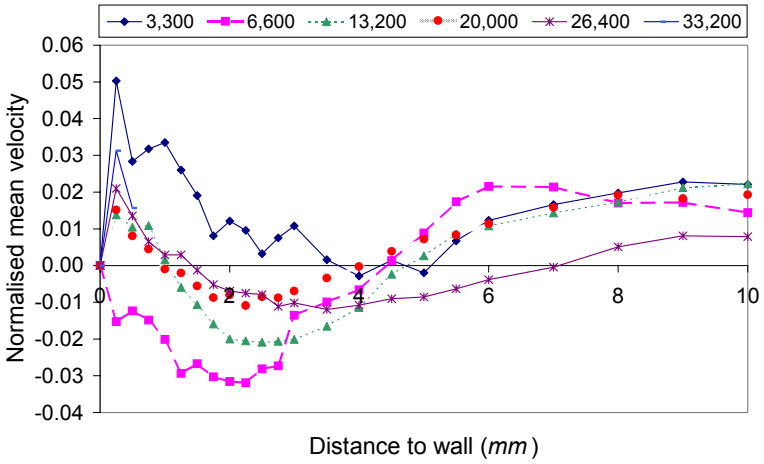

Figure 8.11- Mean axial velocity; sample W

These figures show that, close to the bottom, the flow is essentially upwards, suggesting that particles are easily dragged and entrained into the main flow. That upward flow is also observed far from the wall, particularly for the Westerschelde sample, which is in agreement with the observed higher concentration of suspended matter, as previously referred.

Comparing the chemical composition of the sediments, the major differences observed among the three estuaries concern the higher contents of calcium (Ca) in the W sample (Figure C.7), which may result from the water treatments, and a lower quantity in aluminium (Al).

For the Gironde sediments (Table C.4), their classification is (according to Flemming, 2000): sandy mud at top shore (75-95 % mud); mud at mid shore (> 95 % mud); sand at low shore (< 5 % mud). Comparing the particle size (Annex C, Figure C.11), the sample from the Gironde had the smallest particle size, while the opposite is observed for sample C19.

As mentioned by Young and Southard (1978), cohesion and erosion resistance in sediments depend on several factors, such as grain size, water content, mineral and organic composition and depositional history. Their contribution differs, depending on the type of estuary, sampling site and seasonal and weather conditions. Thus, it is not surprising when results differ significantly from those obtained by other authors, because of the influences of sediment type and bed preparation procedure, temperature and measuring technique (Parchure and Mehta, 1985) are difficult to account for.

8.4 COMPARISON OF SIMULATED AND NATURAL BEDS

In this section, the results obtained on natural sediments are used to find an appropriate simulated bed to duplicate, in laboratory, the conditions relevant to marine sediment

erosion. For that purpose, results obtained on artificial (both rigid and deformable) beds are compared with those obtained in natural sediments.

The presence of surface waves is also evaluated, comparing results obtained on both artificial and natural beds.

Although measurements were carried out at various Reynolds number (covering different stages of the erosion process), this section will report primarily the data concerning Re = 20,000, corresponding to conditions that, in general, sediment erosion is occurring.

8.4.1 RIGID AND DEFORMABLE BEDS

The possible approaches to fixed beds are: smooth surface (was set as a basis for subsequent comparisons with more complex surface structures); rough bed RB1 (resulting from a mud sample collected in mid May); sand roughness bed, RB3. The deformable bed yields the entrainment of particles into the flow.

The sediment samples considered are those collected at end of April (samples C18 and C19 from Cávado and that from the Westerschelde (W)).

- Rigid surfaces

One obvious way of conducting the erosion tests in laboratory would be by accurately duplicating the sediment morphology on a solid surface, as referred in Chapter 5. Figure 8.12 shows the mean tangential velocity profile for the various surfaces considered and the three natural sediments, for comparison. The results show that the profiles on a natural sediment are similar in shape to those on rigid surfaces, though that on RB1 shows a better approximation.

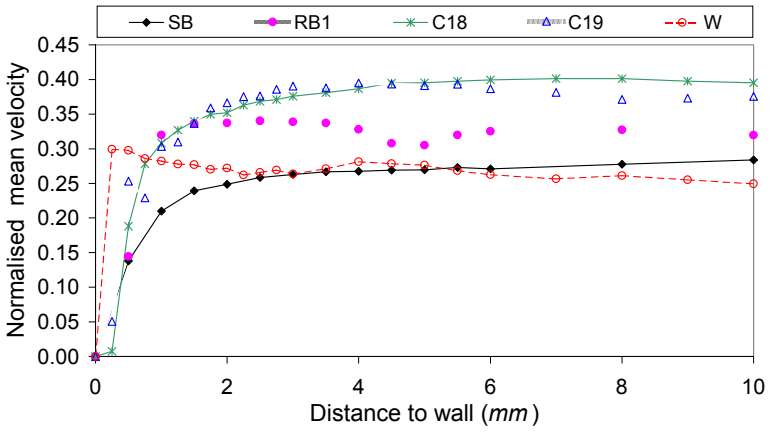

Figure 8.12- Mean tangential velocity: surface roughness; Re=20,000

Clearly, the surface roughness is a crucial parameter in duplicating the natural sediment. However, a detailed observation of the velocity profile close to the surface shows important deviations, which are evident by computing the wall shear stress. Data from the Cávado natural sediments always shows lower shear stresses than those on a rigid surface.

In fact, the wall shear stress for samples C18 and C19 is 0.026 and 0.162 *Pa*, respectively, although the shear stress on a rigid surface varies between 1.081 for a smooth surface (SB) and 1.133 *Pa* for RB1. Also, Mitchener and Torfs (1996) found lower critical shear stresses for erosion in natural sediments, comparing with those on an artificial bed (mud/sand mixtures). In addition, de Jonge and van den Berges (1987), assessing the influence of surface roughness on fluid velocity, obtained lower current velocities using natural sediments when compared with those obtained using a smooth PVC bottom plate. The authors argued that, because of the increase in surface roughness, the energy dissipation to the bottom sediment would increase.

This behaviour suggests that the bed deformation is an important feature, which cannot be reproduced by a rigid surface. In addition, sample C18, which is non cohesive (mostly loose sand with a very limited capacity for water retention as shown in Table 5.19 and Figure 5.21), shows a very small shear stress because of its surface deformation; sediments can become easily loose. The sample from Westerschelde (W) is very cohesive due to its small particle size diameter and high water content as previously referred. As a result, the wall shear stress (1.172 *Pa*) is very close to that observed over the rigid surface, which is certainly due to its very small surface deformation.

The effect of surface roughness is further highlighted upon the turbulence levels near the surface (Figure 8.13). It can be observed that the data from the natural sediments (C18 and C19) is very close to that of the solid surface RB1, which suggests that the turbulence is controlled by the surface characteristics. On the other hand, the data from the natural sediment, W, is very similar to that on a smooth surface (SB). In fact, due to its small grain size, the Westerschelde sample shows a very smooth surface with no visible sand grains.

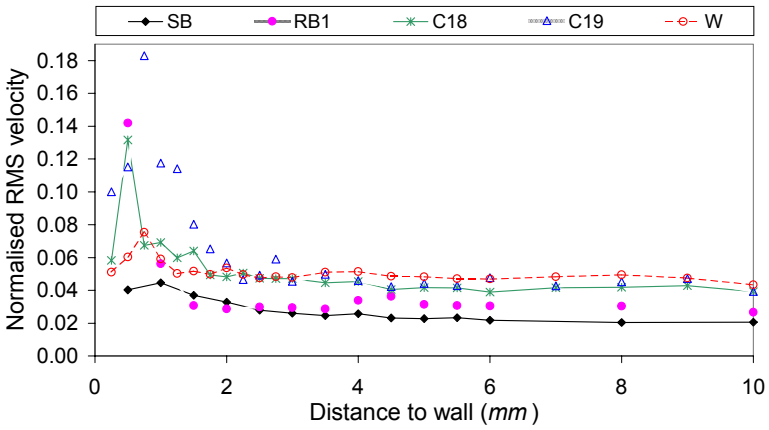

Figure 8.13- Tangential velocity turbulence: surface roughness; Re=20,000

A regular pattern for surface roughness was tested in the form of a sandy bed (RB3), at Re = 10,000. The results are shown in Figure 8.14 and confirm some of the hypothesis put forward.

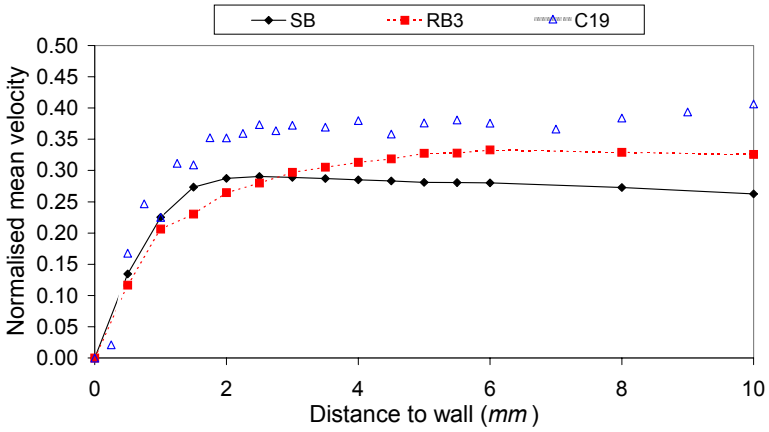

Figure 8.14- Mean tangential velocity: surface roughness; Re=10,000

As with other rough surfaces (Figure 8.12), the shear stress is similar (0.457 *Pa*) to that on a smooth bed (0.526 *Pa*) and much higher than that of the natural sediment, C19 (0.034 *Pa*). Because of the lower shear on the surface, the natural sediment is less likely to deform and shows a lower stress than that at Re = 20,000. The similarities between a sandy roughness and smooth walls are shown in Figure 8.15 where the dimensionless velocity is plotted *versus* dimensionless wall distances. Near the surface vicinity, all the data collapses into the same line, converging into the laminar sub-layer.

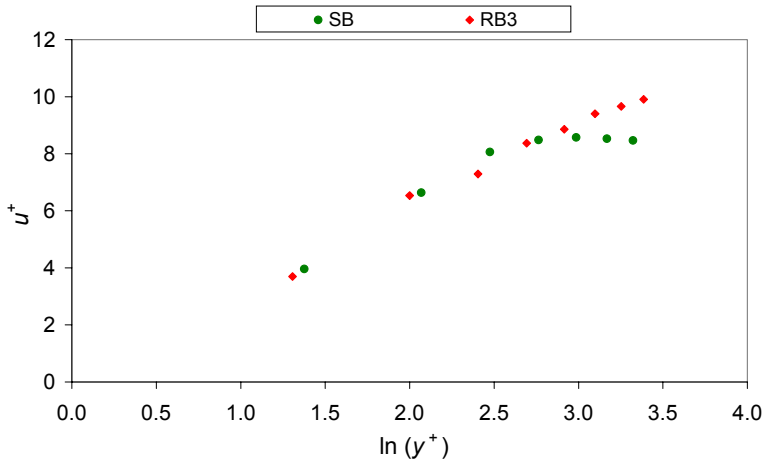

Figure 8.15- Mean velocity profile: sandy surface roughness; Re=10,000

- Deformable beds

Results obtained in section 7.4 for the deformable two-fluid bed suggest that the use of this type of bed is not an appropriate option to duplicate the sediments erosion due to the very high deformation at the interface. Such behaviour was not observed on natural sediments.

The use of various glass beads as a sediment bed yielded a variety of behaviour, as shown in section 7.2. It was found that the small/light particles (P1) were easily entrained by the moving fluid, while particles P2 and P3 were continuously deformed by the fluid shear. Due to such deformation of the sediment structure, the shear stress varies along the dune perimeter, as shown in Figure 7.65. Nonetheless, it was observed that the shear stress is always lower than that over a fixed surface (either smooth or rough).

The local fluid turbulence is compared in Figure 8.16.

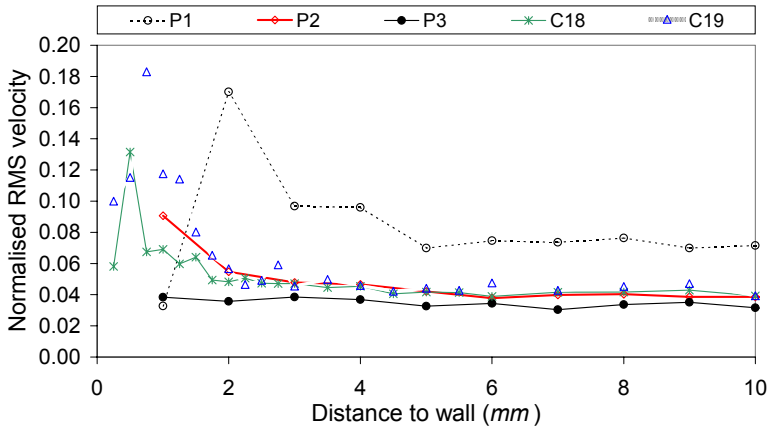

Figure 8.16- Tangential velocity turbulence: deformable bed; Re=20,000

This data shows that the fluid turbulence is governed by the local wall roughness, as the data follows that from a solid rough wall sediment surface. However, particles P1 (the smallest in size) show that the turbulent structure of flow field is mostly influenced by the presence of particles inside the fluid and is not entirely driven by wall properties. It is also observed that particles P2 are those yielding a more similar turbulence profile to that of the sediment.

Comparing Figures 8.16 and 8.13, it should be stressed that, for not much cohesive sediments, a deformable bed using particles P2 should duplicate, in laboratory, the sediment erosion conditions. Furthermore, the wall shear stress for such particles (see Figure 7.65) are not much different (at positions B, C and D of the dune) from those found in samples C18 and C19.

8.4.2 PRESENCE OF SURFACE WAVES

Firstly, results are shown in Figure 8.17 comparing the mean tangential velocity for the various types of wavy lids on smooth beds with the sediment samples.

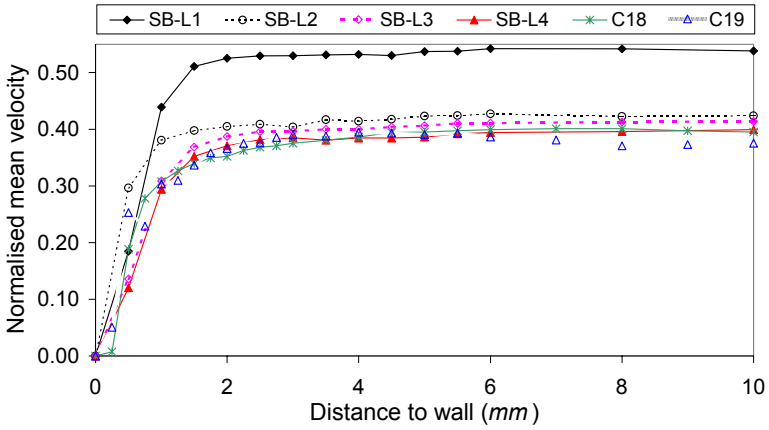

Figure 8.17- Mean tangential velocity: sediments without surface waves; Re=20,000

Some similarities are observed between the sediments and the profiles for lids L3 and L4. Although lid L1 increases the flow mean velocity near the bottom surface and the wall shear stress increases with lid L2 (as justified in section 7.3), the flow turbulence near the sediment surface is not affected by the flow conditions near the free stream, as shown in Figure 8.18. This is in accordance with previous observations that the turbulent structure is a wall driven mechanism.

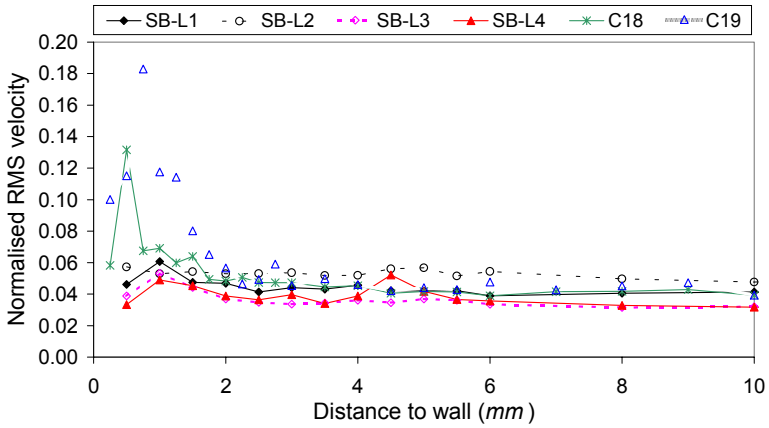

Figure 8.18- Tangential velocity turbulence: sediments without surface waves; Re=20,000

As previously referred, samples C14 and C15 were eroded using lids L1 and L2, respectively. Their tangential velocity profiles at Re = 20,000 are plotted in Figure 8.19, together with the same lids used on a smooth bed flume.

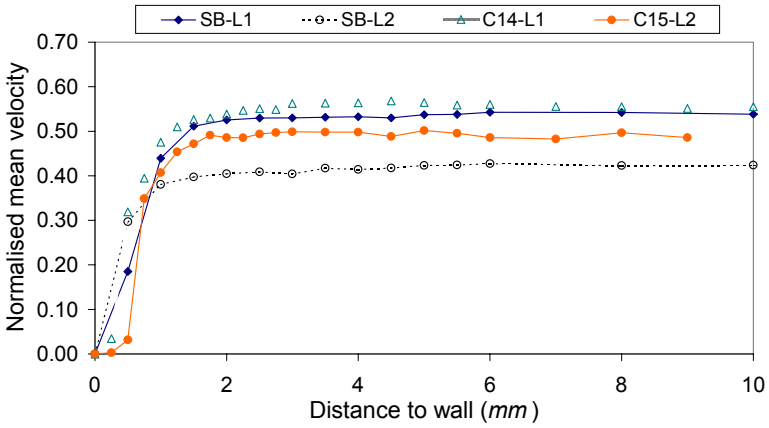

Figure 8.19- Mean tangential velocity: sediments with surface waves; Re=20,000

Although the profiles using lid L1 are similar, the wall shear stress is much higher using a rigid bed (1.616 *Pa* to SB and 0.105 *Pa* to C14). This is in agreement with previous observations, in which the bed deformation yields lower shear stress. Similarly, lid L2 shows a much lower wall shear stress on a sediment sample (0.010 *Pa* to C15 and 2.590 *Pa* to SB).

Although the wall shear stress on natural sediments, at Re = 20,000, is lower with lid L2 (which was not observed in artificial beds), Figure 8.20 shows a different trend for other velocities.

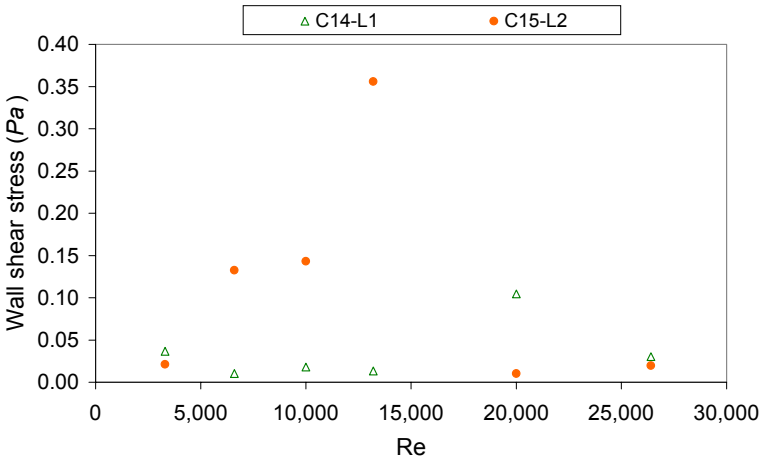

Figure 8.20- Wall shear stress: sediments with wavy lids

In fact, this figure shows a much higher wall shear stress using lid L2 at Re = 13,200. Also, the critical shear stress was found to be higher for this lid (0.018 and 0.143 *Pa* using lids L1 and L2, respectively). Particularly for lid L2, it is evident a strong bed deformation because of the sharp decrease in the wall shear stress. Comparing with other results from sediments without the wavy lids, such as in Figure 8.8, it is observed that the wavy lids are

associated at lower wall shear stress. As referred, this is due to the higher surface deformation, resulting in an increase in the flow turbidity in the early stages because of sediment transport.

Laboratory experiments in mud beds under waves showed an initial break up of bed structure, due to a build up of excess pore pressure under waves. Subsequently, the stress decreased and inter-floc rearrangement occurs, followed by an increase in bed density (Maa and Mehta, 1987). In case of layered beds (in sand/mud mixtures), this may cause mixing of the sediment. In addition, waves can resuspend bed material being transported as suspended load (fines) or bedload (sands), increasing turbidity inside the mini flume.

Concerning the fluid turbulence, the effect of the wavy lids on the sediment samples shows higher levels when compared with data in Figure 8.18. That effect is observed in Figure 8.21, which shows the tangential velocity turbulence, over sediment samples with (C14-L1 and C15-L2) and without (C12) the wavy lids. As mentioned in Chapter 5, all the three samples were collected at the same time of the year (difference of three days, only) and close to the river water. Therefore, they should have the same physical properties (see Table 5.19) and, in this way, the comparison is meaningful.

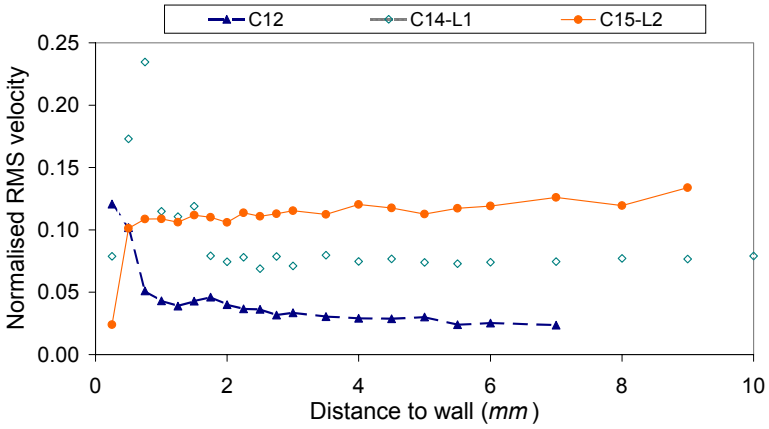

Figure 8.21- Tangential velocity turbulence: sediments with and without surface waves; Re=20,000

Although the turbulent structure proved to be a wall driven phenomena, this figure shows that the strong entrainment of sediments caused by the wavy lids greatly influences the turbulence, which is in agreement with results reported for the smaller particles in the deformable bed tests (Figure 8.16). The higher bed deformation due to a wavy surface is observed in Figure 8.22, which shows lower wall shear stress for samples C14-L1 and C15-L2 (0.105 and 0.010 *Pa*, respectively) when compared with sample C12 (0.433 *Pa*).

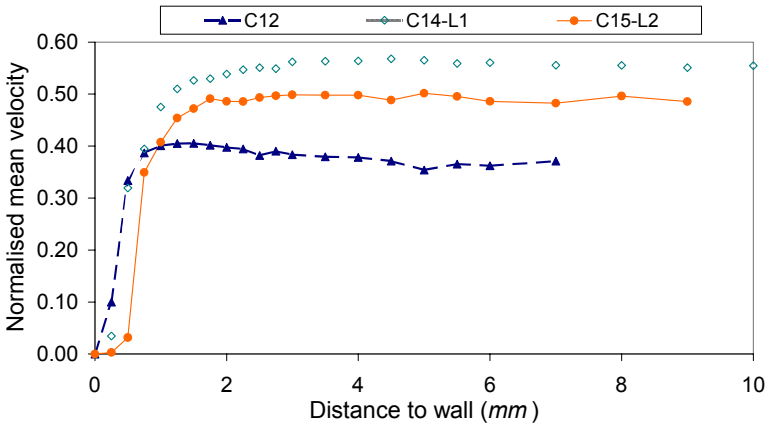

Figure 8.22- Mean tangential velocity: sediments with and without surface waves; Re=20,000

Tests were also carried out combining the effects of the artificial bed, using lid L1 on both a rough (RB1) and a deformable (with particles P3) beds. The data is presented in Figure 8.23.

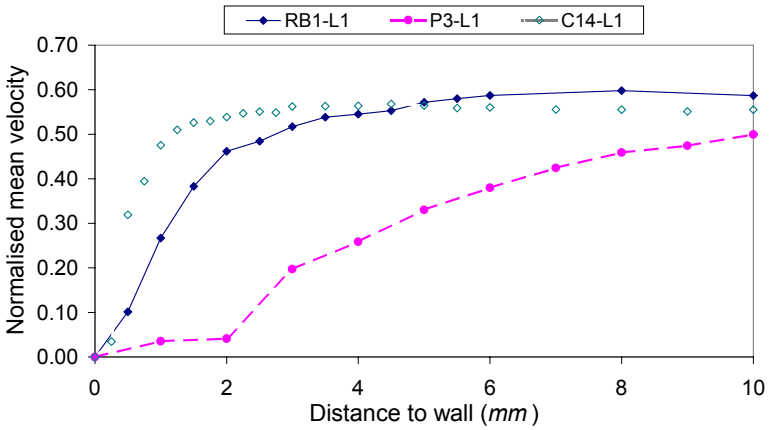

Figure 8.23- Mean tangential velocity: combined effects; Re=20,000

The wall shear stress is higher for the rigid surface (0.883 *Pa*), as expected. Using the natural sediments, the shear stress is lower than that with the particles (0.105 and 0.156 *Pa* to C14-L1 and P3-L1, respectively), meaning that deformation is higher for the first case. Thus, Figure 8.24 presents higher turbulence for the natural sample, close to that on the sediment surface. Comparing the experiments for the various particles size (deformable beds), this suggests that probably the sediments entrained are smaller than particles P3.

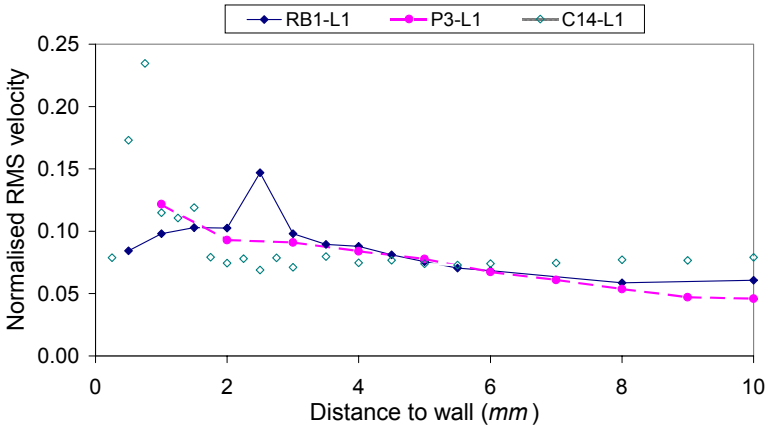

Figure 8.24- Tangential velocity turbulence: combined effects; Re=20,000

Data from the solid surface RB1 is in closer approximation to that on natural sediments in the absence of surface waves (Figure 8.25) than in their presence (Figure 8.24), because of the lower sediment entrainment.

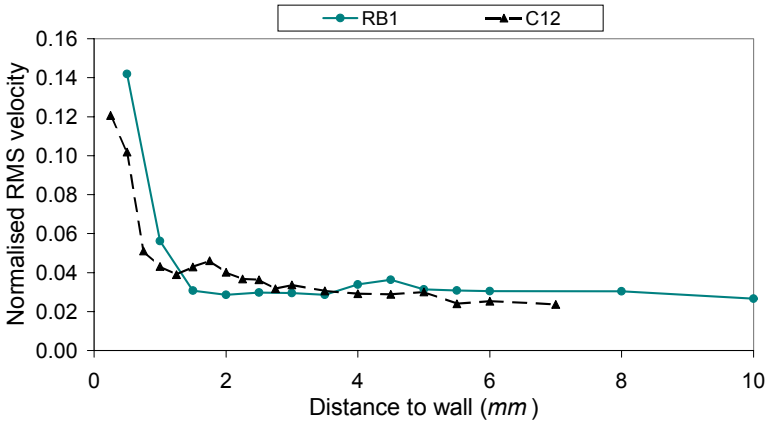

Figure 8.25- Tangential velocity turbulence: absence of surface waves; Re=20,000

8.4.3 FINAL DISCUSSIONS

Various alternatives for an artificial sediment were investigated and assessed as alternatives to the natural sediments, using direct velocity data. This approach proved successful in identifying the most appropriate options and its chief limitations. From the observations previously discussed, the main conclusions may be summarised as follows:

- Except for very cohesive sediments, the sediment deformation plays an important role in the shear stress at the interface.

- For low Reynolds number, well below the onset of erosion, the natural sediment behaves as a rigid surface.
- Rigid sandy beds show similarities with a continuous rigid surface suggesting that surface porosity is of reduced relevance.
- Rigid surfaces, which are exact replicas of the sediment morphology and roughness, may be appropriate for highly cohesive sediments. For non cohesive sediments, a simulated deformable bed using particles with properties such as P2 in a fluid having the solution of glycerine characteristics, should be adequate.
- Turbulence is a wall driven phenomena, except in the presence of large concentration of suspended particles. However, a wide range of experiments on natural sediments has shown such occurrence only by using wavy lids.

CHAPTER 9

CONCLUSIONS AND FUTURE WORK

The conclusions and suggestions into how future work could be developed are a direct outcome of the present thesis. Here they are outlined.

9.1 CONCLUSIONS

In this work, some of the physical mechanisms leading to erosion process have been studied experimentally. The erosion of a sediment bed depends on the near-bed fluid flow and the resistance and composition of the sediment. The aim was to examine the influence upon the flow turbulence, of the sediment surface roughness, entrained particles, a deformable bed and of surface waves. In addition, the comparison with data from natural sediment enabled the assessment of a suitable sediment bed for erosion studies. For that, velocity profiles were taken in natural sediments and, with these results, it was possible to validate the approach in defining the simulated bed.

The work carried out in the present research has provided an insight into the interface interactions, thus enabling a better understanding of the erosion mechanisms. It enabled also the characterisation of sediments from three estuaries. With additional study, these results may be incorporated into accurate sediment transport models. Finally, the experimental data obtained in a mini flume is important for validation of models for curved flows with strong curvature.

Although concluding remarks have been detailed throughout the thesis, the following general conclusions can be drawn from this study:

- The laser technique proved to be a capable tool to measure the velocity and, thus, the shear stress at the sediment interface. The value measured in this way is in agreement with other techniques. This technique is non intrusive and requires no calibration. In addition, the data can be used to infer on the structure of the mud through its depth.
- The particles entrainment into the flow greatly affect the turbulence in the vicinity of the interface. However, if the suspended sediments are in high concentration, the

flow turbulence structure is influenced into regions outside the boundary layer, due to momentum transport by those particles.

- In general, flow turbulence is a wall driven mechanism. Surface waves and high concentration of entrained particles are exceptions.
- The phenomena associated with surface sediment deformation has proved to be the main flow characteristic that influences the wall shear stress.
- The use of a two layer fluid bed highlights the relevance of surface deformation to the shear stresses. However, a quantitative analysis requires detailed measurements inside the lower fluid. Nonetheless, the available data suggests this approach yields unrealistic high deformation at the interface.
- Although surface roughness is important, the soil topology is the single most important parameter that affects the flow structure near the sediment. In fact, the results have shown that the simulated bed which duplicates the sediment morphology and roughness is an acceptable replica for natural samples. This feature is an important factor in defining the shear stress and flow field in the vicinity of the sediment.
- The shape of the bed shear stress distribution, which is dependent on the type of flume (shape and scale), influences the development of bedforms or other erosion patterns. These effects are very important in extrapolating the laboratory data into realistic field conditions.
- For the Cávado estuary, more important than the seasonal effects or concentration of diatoms on the erosion, is the influence of seemingly random events such as the occurrence of rain before the collection and the sampling site.
- Although the factors affecting sediments erosion are approximately the same for any estuary, as described in the literature review (Chapter 2), the erosion mechanisms are different and typical for each one, due the specific properties such as sediment grain size, cohesion, estuary slope, sediment irregularities. Therefore, results between estuaries are difficult to compare and each one needs a comprehensive evaluation of all factors involved in erosion.

9.2 SUGGESTIONS FOR FUTURE WORK

Although this work has provided a better understanding of the erosion mechanisms and some physical factors contributing to that process, it also opened lines for further research. Some suggestions are given below.

- To investigate other factors affecting sediments erosion, such as biological effects, and to relate them with the LDA results obtained in this work.
- To evaluate in real time the suspended matter concentration in the fluid as the erosion progresses. Techniques based upon the light attenuation could be valuable.

- To use a more accurate high speed video camera in order to accurately observe the mass transfer at the onset of erosion, and to make possible the analysis of the eroded flocs (size, shape and fractal dimension).
- For a better characterisation of the secondary flows inside the mini flume it is also important to quantify the radial velocity component. To do that, the rig should be modified in order that the optical access into the flume could be either from the bottom or from the top of the flume.
- Most of the limitations in this work are related with the shape of the flume. Therefore, the use of a straight channel would remove the major cause of secondary flows and would provide a simpler flow to investigate the fluid-sediment interaction.
- The present study has been limited to uniform flow conditions. However, in the field the flow conditions can be very unsteady due the effect of the tidal waves, which determine the motion of the sediment. Therefore, it is suggested laboratory tests in oscillatory flows. The unsteady conditions could include sudden events like floods.
- Clearly the flow simulation is open to improvement. Therefore, the use of adequate turbulence models and/or wall functions should be improved. In this way, the flow model could be used for two purposes: 1) to calculate the surface shear stress at the interface and correlate it with the total torque driven by the rheometer; 2) to accurately investigate sediment transport and deposition.

ANNEX A - RHEOMETER CHARACTERISTICS

Various measuring *bobs* are available for measuring the viscosity with the Physica Rheolab MC 1. Each one is suitable for a certain range of viscosities. For low viscosity fluids the Z1 *bob* (according to DIN 53453) is the most appropriate. Figure A.1 and Table A.1 present, respectively, its geometry and characteristics (Rheolab MC 1, 1998).

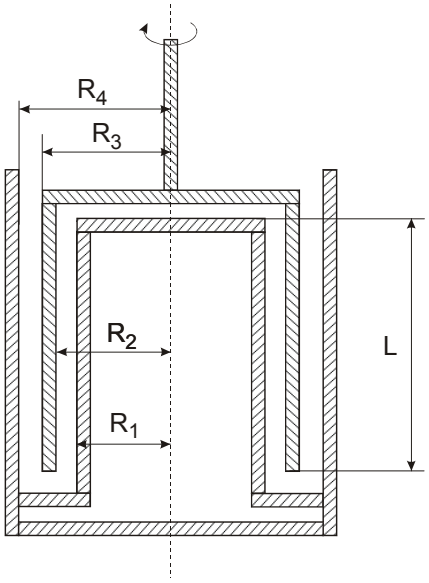

Figure A.1- Measuring geometry of Z1 (DIN 53453)

The most relevant technical data for the Physica MC 1 rheometer is presented in Table A.2.

Table A.1 - Z1 DIN measuring system characteristics

Characteristics	Standard values
Shear rate range (s^{-1})	0-4,031
Shear stress range (*Pa*)	0-67
Viscosity range (*Pa.s*)	0.001-1.3
Sample volume (*ml*)	22.5
Shear rate factor (*min/s*)	5.039
Shear stress factor (*Pa*)	0.067
Inner radius of measuring *bob* R_2 (*mm*)	22.75
Outer radius of measuring *bob* R_3 (*mm*)	23.5
Inner radius of measuring *cup* R_1 (*mm*)	22.25
Outer radius of measuring *cup* R_4 (*mm*)	24
Length of measuring *bob* L (*mm*)	111
Ratio of radii	1.021
Resistance coefficient	1

Table A.2- Technical data referent to rheometer MC1

Property	Value
Torque range (*mNm*)	0.05 - 50
Torque resolution (*mNm*)	0.01
Speed range (*rpm*)	0.3 – 1,200
Temperature range (*ºC*)	-19.9 - 180
Shear rate range (s^{-1})	$0.9 - 4\times10^{3}$
Shear stress range (*Pa*)	$0.7 – 3.4\times10^{4}$
Viscosity range (*Pa.s*)	$1\times10^{-3} - 3\times10^{3}$

ANNEX B - REFRACTIVE INDEX COMPENSATION FOR LDA CROSSING ANGLES

The crossing angles corrections were obtained from the transmitting conditions of the LDA optical configuration (without any corrections), which are presented in Table B.1.

Table B.1- LDA optical properties without corrections

Output property	Green (Horizontal)	Blue (Vertical)
Beam spacing (*mm*), (S_b)	75	78
Number of fringes, (N_{fs})	37	39
Fringe spacing (μm), (S_{fs})	2.142	1.955
Beam half angle (º), (θ)	6.897	7.171
Probe volume (*mm*)		
Height, (h_{mv})	0.081	0.077
Width, (d_{mv})	0.080	0.076
Length, (l_{mv})	0.667	0.609

The crossing angle corrections will be calculated for both the vertical and horizontal beams (their wavelength is 488 *nm* and 514.5 *nm*, respectively). It will be considered, as an example, an experiment using the quartz flume and a solution of glycerine.

B.1- Determination of angle corrections for the vertical beams

Being α_1 the beam cross angle (2θ from Table B.1) and d_g, d_w and d_q the glass thickness, the distance inside the water and the quartz thickness, respectively, it was possible to calculate the actual beam crossing angle (α_5), according to Figure B.1. The distance inside the water is the distance between the glass box wall and the flume wall, and takes the value of 29 *mm*. The refractive indexes of the air (n_a), glass (n_g), water (n_w), quartz (n_q) and solution of glycerine (n_{sg}) are presented in Table 5.1. The relationship between the traverse displacement (d_T) and the real distance moved by the probe volume inside the flume (d_r) was also determined.

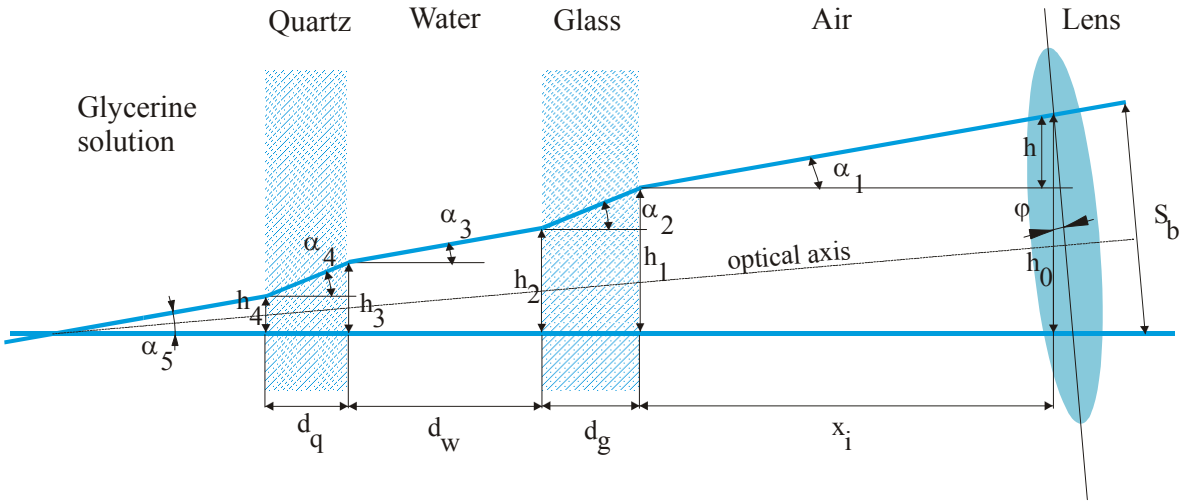

Figure B.1- Schematic representation of the vertical beams crossing the different media

All the unknown variables existent in Figure B.1 are determined, using geometric optics laws, such as follows:

$\alpha_1 = 2\theta$ and $h_0 = S_b \cos\varphi$

φ is the beams tilting angle, as referred in section 5.1.2.

By Snell's law:

$$\alpha_2 = \sin^{-1}\left(\frac{n_a \cdot \sin\alpha_1}{n_g}\right)$$

$$\alpha_3 = \sin^{-1}\left(\frac{n_g \cdot \sin\alpha_2}{n_w}\right)$$

$$\alpha_4 = \sin^{-1}\left(\frac{n_w \cdot \sin\alpha_3}{n_q}\right)$$

$$\alpha_5 = \sin^{-1}\left(\frac{n_q \cdot \sin\alpha_4}{n_{sg}}\right)$$

Without traverse displacement:

$h_4 = 0$

$h_3 = d_q . \tan\alpha_4$

$h_2 = h_3 + d_w . \tan\alpha_3$

$$h_1 = h_2 + d_g.\tan\alpha_2$$

$$x_i^{\,0} = \frac{h_0 - d_q.\tan\alpha_4 - d_w.\tan\alpha_3 - d_g.\tan\alpha_2}{\tan\alpha_1}$$

$$h = x_i^{\,0}.\tan\alpha_1$$

Relationship between the traverse displacement (d_T) and the real distance travelled by the beams (d_r):

Being:

$$0 \le d_T \le 27$$

$$x_i = x_i^{\,0} - d_T$$

$$d_r = \frac{h_0 - d_q.\tan\alpha_4 - d_w.\tan\alpha_3 - d_g.\tan\alpha_2 - x_i.\tan\alpha_1}{\tan\alpha_5}$$

resulting (after traverse displacement):

$$h'_4 = d_r.\tan\alpha_5$$

$$h'_3 = h_4 + d_q.\tan\alpha_4$$

$$h'_2 = h_3 + d_w.\tan\alpha_3$$

$$h'_1 = h_2 + d_g.\tan\alpha_2$$

$$h' = x_i.\tan\alpha_1$$

B.2- Determination of angle corrections for the horizontal beams

Firstly, it was determined the beam half angle resulting from the beams tilting (α_1) as well as h_0, according to Figure B.2.

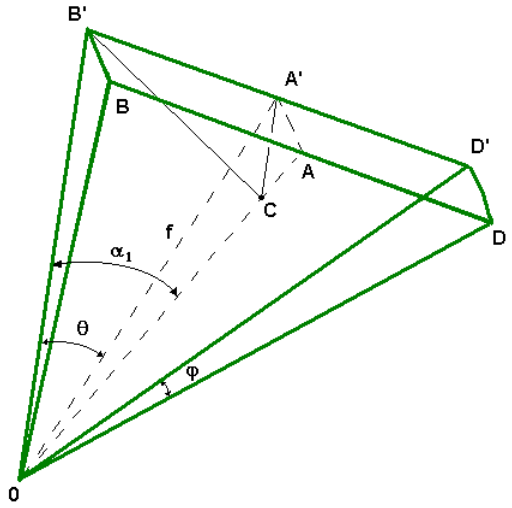

Figure B.2- Schematic representation for determination of α_1 and h_0 applied on horizontal beams corrections

Being $\theta = 6.897$ and f the focal length (310 *mm*),

and

$$\overline{OA} = \overline{OA'} = f$$

$$\overline{B'C} = f\sqrt{(\tan\theta)^2 + (\sin\varphi)^2}$$

$$\overline{OB'} = \frac{f}{\cos\theta}$$

$$\sin\alpha_1 = \frac{\overline{B'C}}{\overline{OB'}}$$

$$\alpha_1 = \sin^{-1}\left(\cos\theta \cdot \sqrt{(\tan\theta)^2 + (\sin\varphi)^2}\right)$$

obtaining:

$\alpha_1 = 9.937°$ and $h_0 = \overline{B'C} = 53.88\ mm$.

Using α_1 and h_0 previously obtained, it was possible to determine the corrected beam half angle (α_5), according to the scheme in Figure B.3. It was also possible to calculate the relationship between the traverse displacement and the real distance travelled by the beams inside the flume.

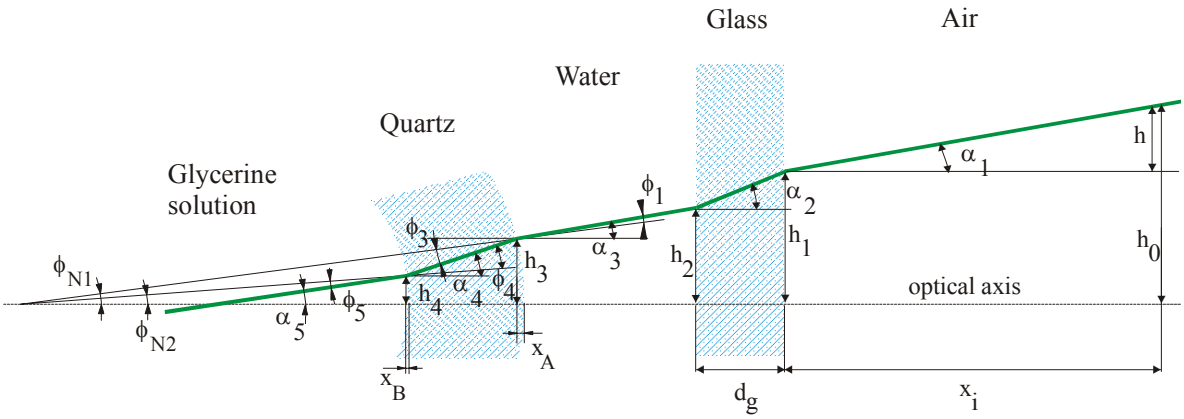

Figure B.3- Schematic representation of the horizontal beams crossing the different media

Again, all the unknown variables present on this figure are determined.

By Snell's law:

$$\alpha_2 = \sin^{-1}\left(\frac{n_a \cdot \sin\alpha_1}{n_g}\right)$$

$$\alpha_3 = \sin^{-1}\left(\frac{n_g \cdot \sin\alpha_2}{n_w}\right)$$

Without traverse displacement:

$h_4 = 0;\ x_B = 0$

estimate $x_i^{\,0}$

$h = x_i^{\,0}.\tan\alpha_1$

$h_1 = h_0 - h$

$h_2 = h_1 - d_g.\tan\alpha_2$

$h_3 = h_2 - d_w.\tan\alpha_3$

$$x_A = \frac{2\left(r_{iq} + d_q\right) - \left[\left(2\left(r_{iq} + d_q\right)\right)^2 - 4{h_3}^2\right]^{0.5}}{2}$$

being r_{iq} the internal radius of the quartz flume,

$$\phi_{N1} = \tan^{-1}\left(\frac{h_3}{r_{iq} + d_q - x_A}\right)$$

$$\phi_1 = \alpha_3 - \phi_{N1}$$

Applying again the Snell's law:

$$\phi_3 = \sin^{-1}\left(\frac{n_w \cdot \sin(\phi_1)}{n_q}\right)$$

$$\alpha_4 = \phi_{N1} + \phi_3$$

$$h_3'' = (d_q - x_A)\tan\alpha_4$$

$x_i^{\,0}$ is estimated in order to get $h_3 = h_3''$

Relationship between the traverse displacement (d_T) and the real distance travelled by the beams (d_r):

Being:

$$0 \le d_T \le 27$$

$$x_i = x_i^{\,0} - d_T$$

$$d_r = \frac{h_0 - (d_q - x_A')\tan\alpha_4' - d_w \tan\alpha_3 - d_g \tan\alpha_2 - x_i \tan\alpha_1}{\tan\alpha_5} + x_B'$$

in which,

$$h' = x_i \tan\alpha_1$$

$$h_1' = h_0 - h'$$

$$h_2' = h_1' - d_g \tan\alpha_2$$

$$h_3' = h_2' - d_w \tan\alpha_3$$

$$x_A' = \frac{2(r_{iq} + d_q) - \left[(2(r_{iq} + d_q))^2 - 4h_3'^2\right]^{0.5}}{2}$$

$$\phi'_{N1} = \tan^{-1}\left(\frac{h'_3}{r_{iq} + d_q - x'_A}\right)$$

$$\phi'_1 = \alpha_3 - \phi'_{N1}$$

Using the Snell's law:

$$\phi'_3 = \sin^{-1}\left(\frac{n_w \cdot \sin(\phi'_1)}{n_q}\right)$$

$$\alpha'_4 = \phi'_{N1} + \phi'_3$$

$$h'_4 = h'_3 - (d_q - x'_A)\tan\alpha'_4$$

$$x'_B = \frac{2r_{iq} - \left[(2r_{iq})^2 - 4h'^2_4\right]^{0.5}}{2}$$

$$\phi_{N2} = \tan^{-1}\left(\frac{h'_4}{r_{iq} - x'_B}\right)$$

$$\phi'_4 = \alpha'_4 - \phi_{N2}$$

Finally, by the Snell's law:

$$\phi_5 = \sin^{-1}\left(\frac{n_q \cdot \sin(\phi'_4)}{n_{sg}}\right)$$

$$\alpha_5 = \phi_{N2} + \phi_5$$

$$h''_4 = (d_r - x'_B)\tan\alpha_5 = h'_4$$

ANNEX C - PHYSICAL AND CHEMICAL SAMPLE CHARACTERISATION

This annex reports a comprehensive list of the results concerning the sample characterisation. They include erosion tests, fluids characterisation and sediment samples analysis. The results refer to the three estuaries for all but those samples already discussed in the main text.

C.1- Erosion tests

Figure C.1 shows the torque *versus* the rotation speed during the erosion of samples C1 and C2. Both samples were collected in the same day.

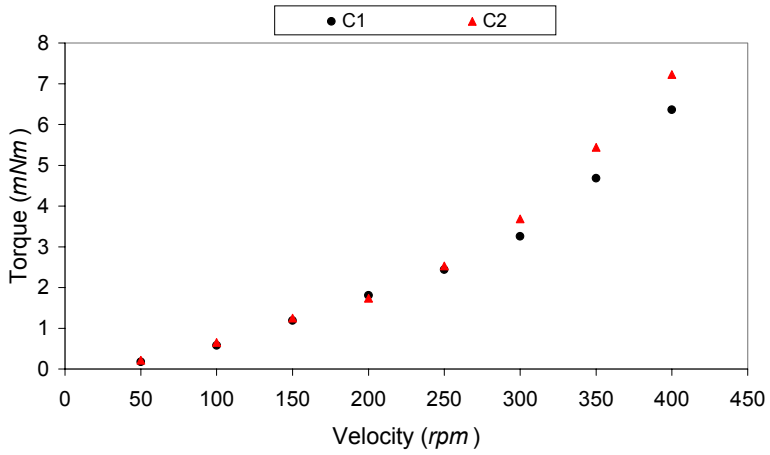

Figure C.1- Torque for samples C1 and C2

It is observed that the critical velocity is in the range of 250 *rpm* for both.

Figure C.2 shows the results for the samples taken from Cávado estuary.

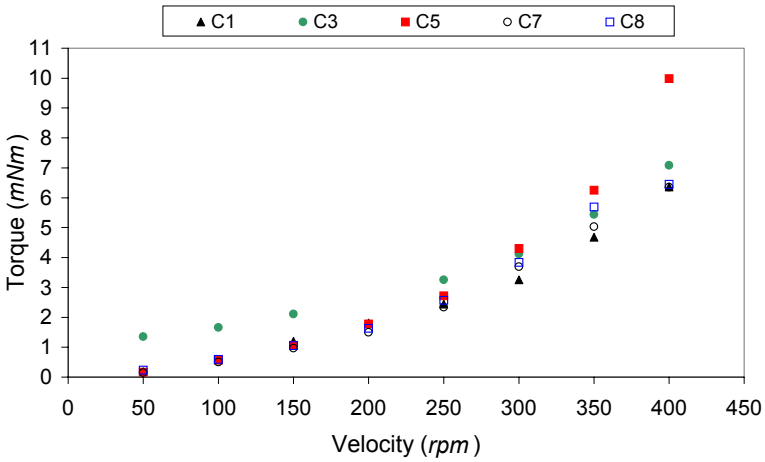

Figure C.2- Torque for the Cávado samples

It can be observed that sample C3 shows a higher torque at low velocities, when compared with other samples. The critical velocity was approximately 250 *rpm* for all samples, corresponding at a critical shear stress of around 0.06 *Pa*. These values are very rough estimates.

The comparison of three estuaries is given in Figure C.3.

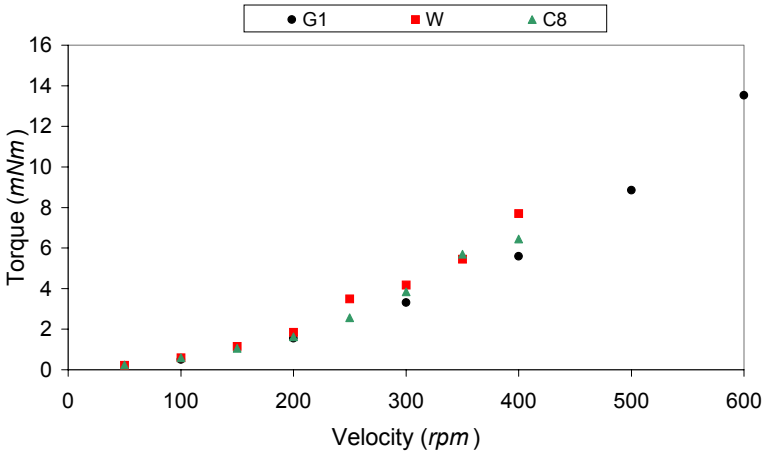

Figure C.3- Torque for the three estuaries

C.2- Fluids characterisation

The sediment laden fluid resulting from erosion tests was characterised for each sample. Figure C.4 shows the viscosity of such fluid for the Cávado samples.

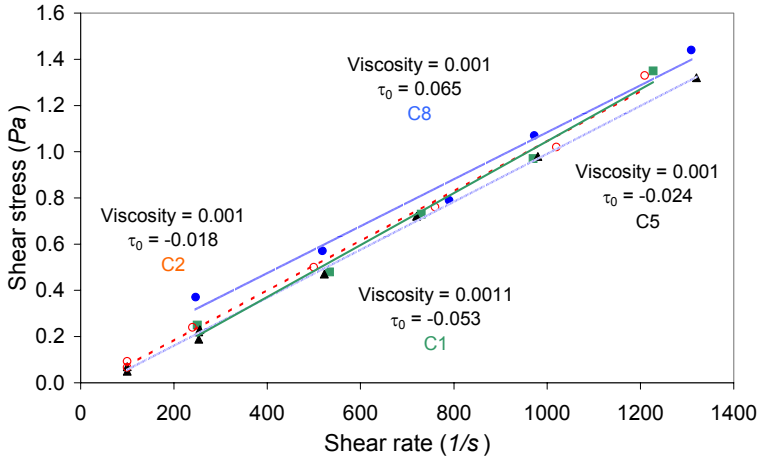

Figure C.4- Fluid viscosity for the Cávado samples

As observed in this graph, the sediment laden fluid has a viscosity very close to that of the water. In addition, it has a Newtonian type fluid behaviour.

The same observations are made for the Westerschelde sample, as shown in Figure C.5.

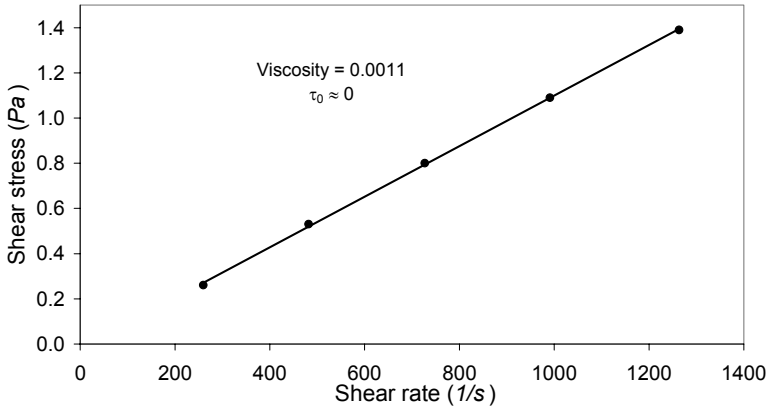

Figure C.5- Fluid viscosity for the Westerschelde sample

However, the fluid from sample G1 (Gironde estuary) has a Bingham type behaviour, such as sample G2, although its viscosity is lower (see Figure C.6).

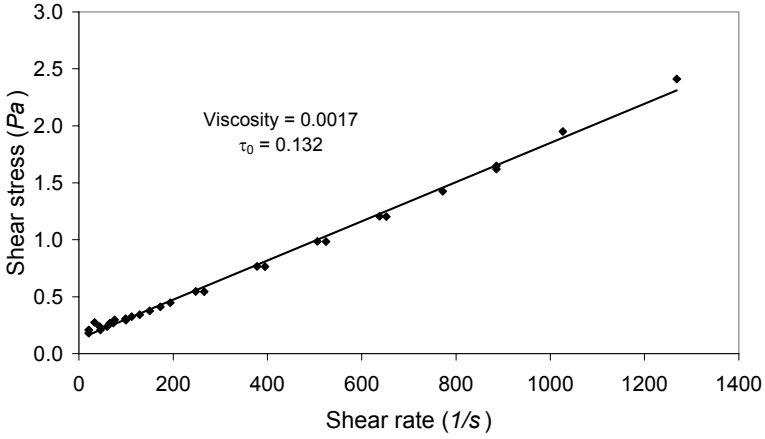

Figure C.6- Fluid viscosity for sample G1

C.3- Mud samples

C.3.1- Chemical composition

The chemical composition for the sediment samples taken from all the three estuaries is compared in Figure C.7.

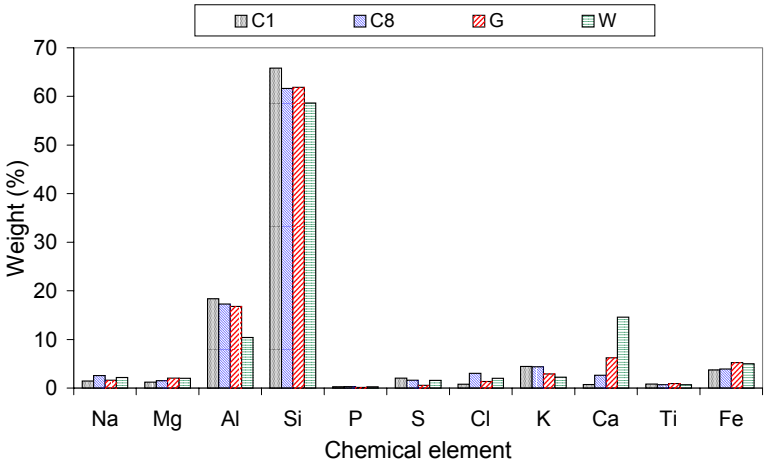

Figure C.7- Chemical composition of the sediments

C.3.2- Particle sizing

The particle sizing results refer to the sediment surface layer (top 2 *mm*), except for some samples from Westerschelde estuary. Figure C.8 presents the particle size distribution for the Cávado samples. A 300 *mm* lens was used for all the samples.

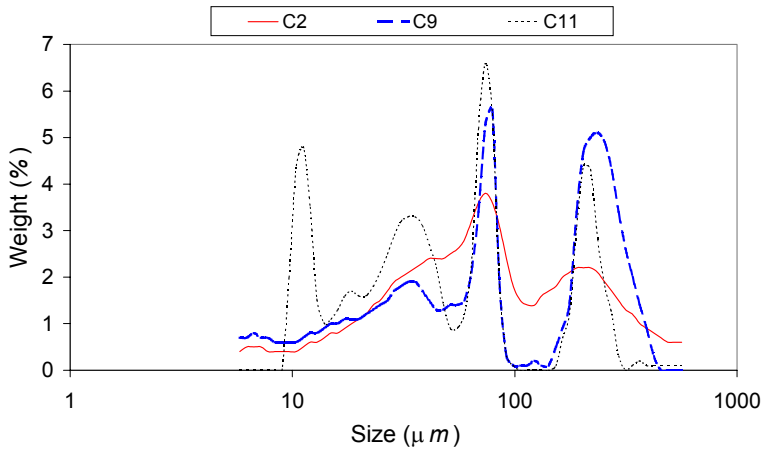

Figure C.8- Particle size distribution in the sediment at Cávado

This figure shows that sample C11 has a higher percentage of small particles, which is not surprising once it was collected away from the water, where a lower content of sand is observed. On the opposite, sample C9 presents a higher content of large particles because of sand.

The Sauter mean diameter is given in Table C.1.

Table C.1- Sauter mean diameter for the Cávado samples

Sample	C2	C9	C11
d_{32} (μm)	33.8	28.76	28.73

In Figure C.9 it is shown the particle size distribution for the samples collected in Gironde in three different positions along a transect: one at 100 *m* from the beach (top shore, using lens 63 *mm*), other at 500 *m* (mid shore, lens 63 *mm*) and other close for the low tide water mark (low shore, lens 600 *mm*).

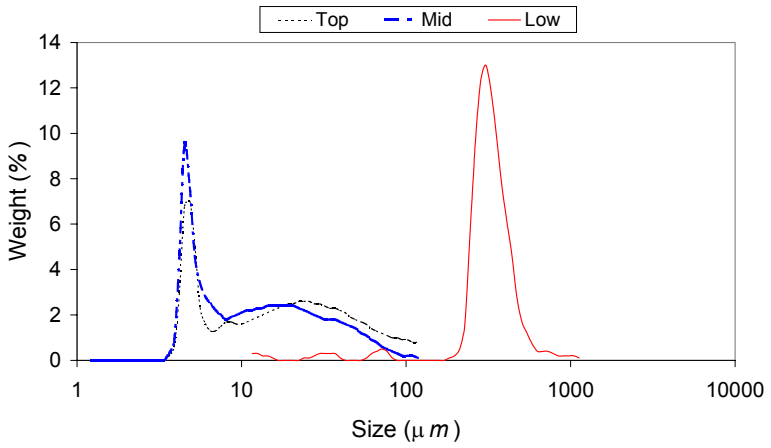

Figure C.9- Particle size distribution in the sediments from the Gironde estuary

Table C.2 presents the Sauter mean diameter for these samples.

Table C.2- Sauter mean diameter to Gironde samples

Sample	Top	Mid	Low
d_{32} (μm)	10.32	8.59	98.92

As it is observed in Figure C.9, the particle size measured at low shore is much higher than for the other two sets. That fact may occur because in that region there was a slope on the ground that favours the transport of finer particles by the tidal flows. This is not surprising because of high tidal current action in the estuary (Dyer, 1998).

Concerning the Westerschelde estuary, Figure C.10 presents the particle size distribution at the surface (corresponding to the first 2 *mm*) and at depths of 4, 6, 8 and 10 *mm*. The samples were collected at top shore site.

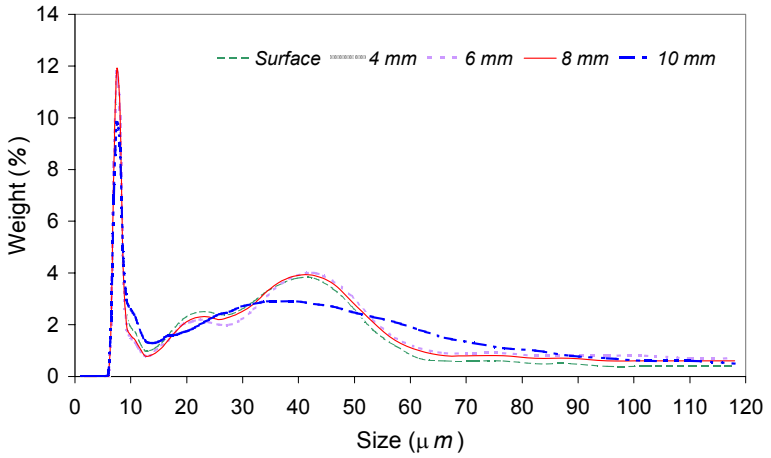

Figure C.10- Particle size distribution in the sediment at Westerschelde

As shown in this graph, the particle size distribution is very similar in depth resulting in similar Sauter mean diameters (Table C.3).

Table C.3- Sauter mean diameter for Westerschelde samples

Sample	Surface	4 *mm*	6 *mm*	8 *mm*	10 *mm*
d_{32} (μm)	12.57	12.87	13.19	13.20	13.44

Finally, a comparison of the three estuaries is presented in Figure C.11.

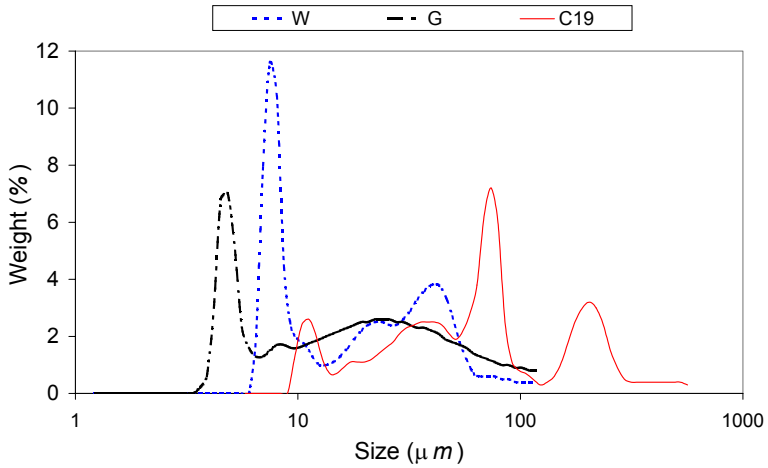

Figure C.11- Particle size distribution for three estuaries

Comparing the top shore results from three estuaries, it is possible to observe that the particles from Cávado have a larger size than those from the other two estuaries. The Gironde particles are the smallest.

The percentage of mud to Gironde and Westerschelde samples is shown in Tables C.4 and C.5, respectively.

Table C.4- Mud percentage for the Gironde samples

Sample	Mud (%)
Top	90
Mid	96
Low	3

Table C.5- Mud percentage to Westerschelde samples

Sample	Mud (%)
Surface	95.5
4 *mm*	89
6 *mm*	92
8 *mm*	93
10 *mm*	91

For this estuary, the percentage of sand (very fine sand) was very low.

C.3.3- Sediment water content

The water content on the sediment for Cávado and Westerschelde estuaries is presented in Figure C.12. Measurements were made at approximately 2 and 4 *mm* in depth from the surface.

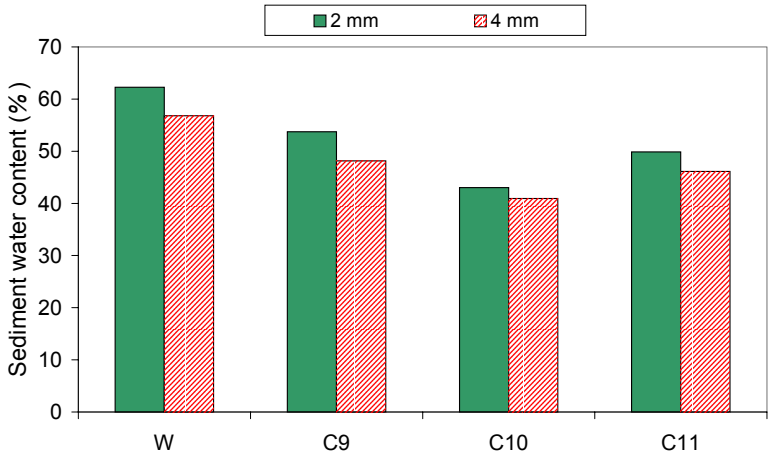

Figure C.12- Sediment water content for Westerschelde and Cávado

ANNEX D - VISCOSITY OF WATER

The viscosity of distilled water is presented in Figure D.1, as a function of the shear rate (velocity), at room temperature.

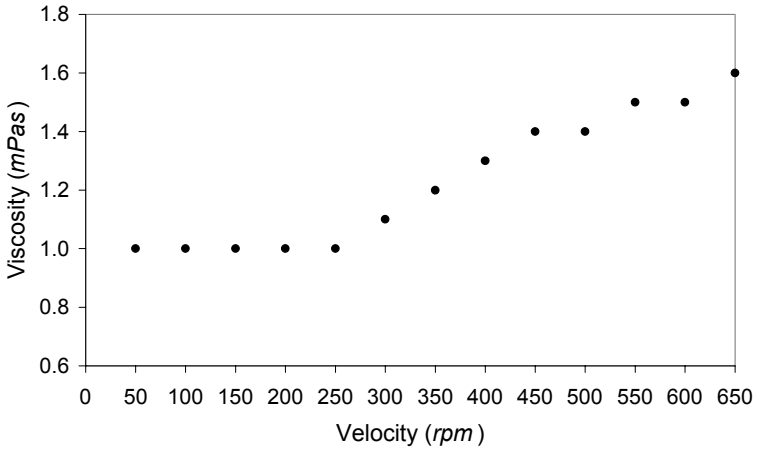

Figure D.1- Viscosity of the water

The water viscosity is 1×10^{-3} *Pa.s*. Values above around 250 *rpm* cannot be considered because secondary flows due to Taylor vortices are induced in the flow. The viscosity is also given in Figure D.2.

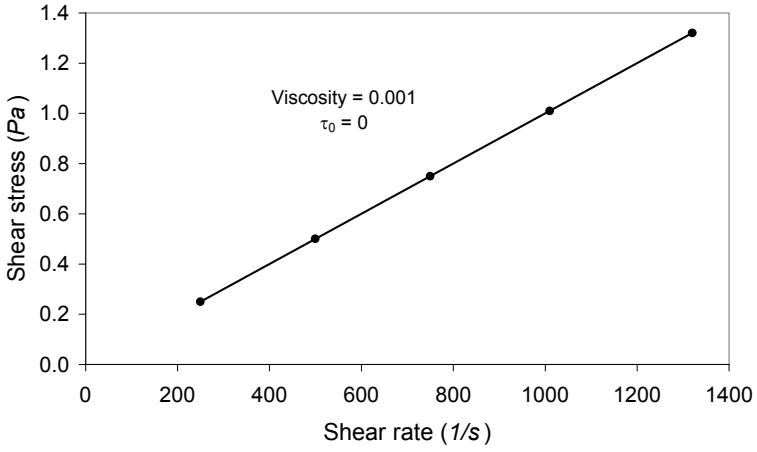

Figure D.2- Shear stress *versus* shear rate

As expected from a Newtonian fluid, $\tau_0 = 0$ *Pa*.

APPENDIX - INFLUENCE OF GAP IN THE FLUME

It is important to evaluate the influence of the gap size (free space filled with fluid) inside the flume, on the velocities profiles and the shear stress. This analysis may be helpful in the interpretation of some results obtained either in artificial or natural beds. It must be stressed that it is not easy to control that gap, due to the process of sediment sample collection.

A set of experiments was carried out, on the mini flume, by varying the gap from the minimum (24 *mm*) up to the maximum (49 *mm*) possible. Measurements were made on a smooth bed, using the standard solution of glycerine, moving up the flat lid after each measurement. The velocity profiles were carried out over a vertical line, at approximately 7.5 *mm* off the outer wall of the flume and at Re = 20,000. For all the experiments, the Reynolds number was kept constant. The mean tangential velocities obtained are shown in Figure 1.

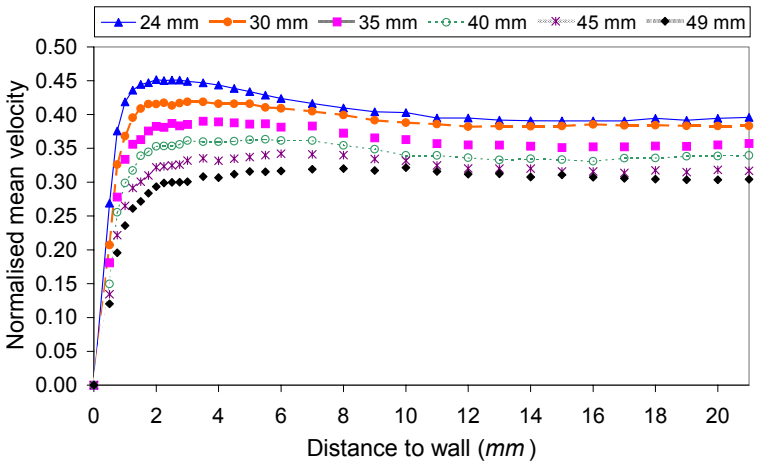

Figure 1- Mean tangential velocity; influence of gap

It is observed a decrease in the velocity when gap increases (the lid velocity is lower). In addition, the wall shear stress is reduced, as observed in Figure 2.

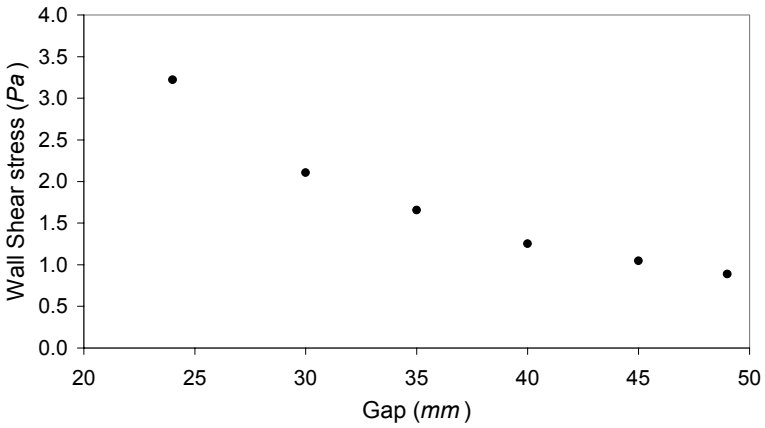

Figure 2- Wall shear stress; influence of gap

It can be concluded that the fluid flow rate is approximately constant for the same Reynolds number, once it is observed that when the cross section decreases, the maximum velocity is increased close to the wall. The turbulence profile is shown in Figure 3. The spread of the data is within the experimental uncertainties and no meaningful and reliable conclusions can be drawn.

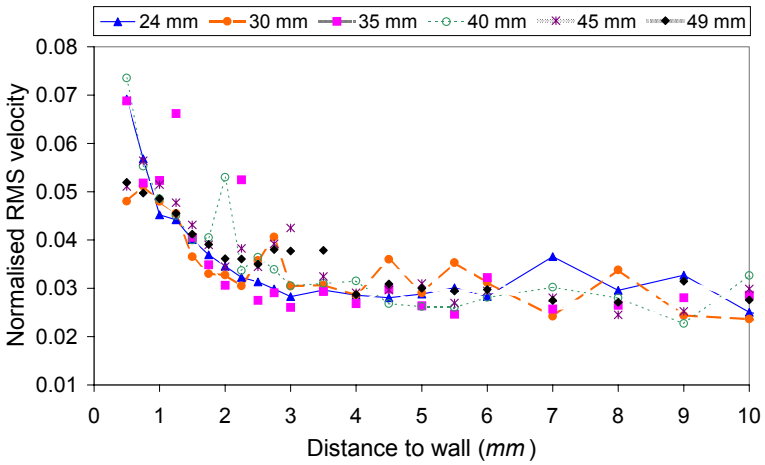

Figure 3- Tangential velocity turbulence; influence of gap

The mean axial velocity is shown in Figure 4.

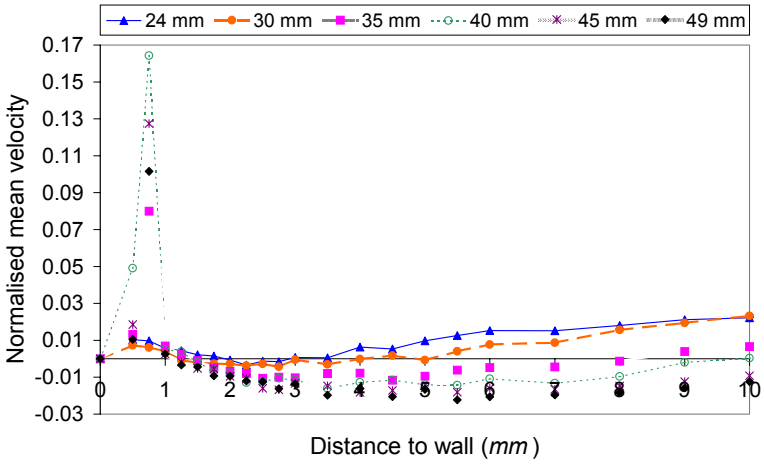

Figure 4- Mean axial velocity; influence of gap

It is observed a strong upward flow (positive velocities) at the distance of 0.75 *mm* from the bottom wall, except for the two smallest gaps tested. The maximum and minimum axial velocities are observed for gaps of 40 and 30 *mm*, respectively. The same behaviour was found for the axial velocity turbulence (Figure 5).

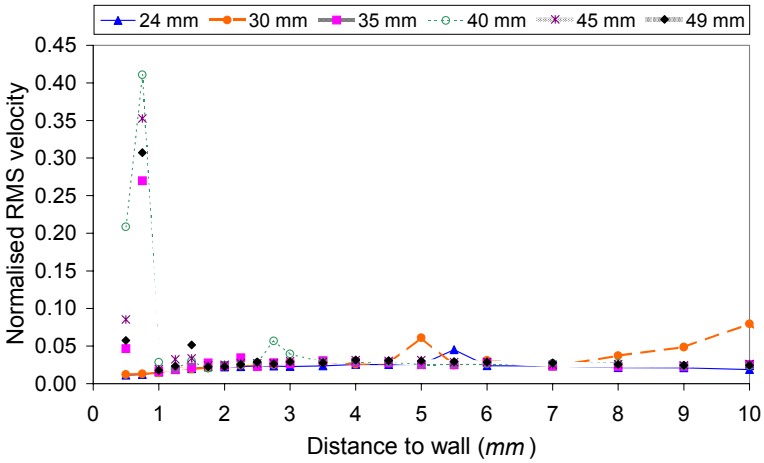

Figure 5- Axial velocity turbulence; influence of gap

It is interesting to compare results obtained in both natural and simulated beds, as a function of the gap size. Thus, looking at Table 5.30, sample C16 presents a gap of 23.7 *mm*, which is similar to the smallest one presented above, for the smooth bed (24 *mm*). In this way, their hydraulic diameters (d_h) were also similar (35 and 35.9 *mm* for the first and the second case, respectively). Although having similar d_h and both tests were carried out at Re = 20,000, because the viscosity of the simulated fluid is around 3 times the water, in this case test took place at a velocity approximately 3 times the experiment in the natural bed (according to Equation 5.27). Thus, although having approximately the same gap and Re, their wall shear stress was completely different (0.119 *Pa* to C16 and 3.222 *Pa* to SB), what is due the sediment bed deformation, as explained before. This means that surface deformation becomes a more important factor than the gap size.

Also, samples C17 and C18 have exactly the same gap, 19 *mm* (Table 5.30), and have very different wall shear stresses for the same Re, as shown in Figure 8.7. This was due the very different sediment composition, as already referred. Thus, sediment composition, which affects the bed deformation, is the main factor to take into account. As a conclusion, gap size effects become particularly important in rigid surfaces.

In *in situ* experiments using an ISIS flume, Williamson and Ockenden (1996) also investigated the gap (distance above the mud bed) influence in the shear stress profiles. Gap measurements were made using ultrasonic probes. They observed that, as the gap becomes smaller, the shear stress becomes more uneven along the radius. Thus, the shear stress increased with flow and decreasing gap. A calibration curve for that instrument was also obtained, consisting in a relationship between the shear stress and the flow gap.

LIST OF REFERENCES

Abernethy, R. B.; Benedict, R. P. and Dowdell, R. B. (1985), "ASME measurement uncertainty", *Transactions of the ASME Journal of Fluids Engineering*, 107, pp 161-164.

Acharya M.; Brounstein, J. and Escudier, M. P. (1986), "Turbulent boundary layers on rough surfaces", *Experiments in Fluids*, 4, pp 33-47.

Albrecht, H. –E.; Borys, M.; Damaschke, N. and Tropea, C. (2003), *Laser Doppler and phase Doppler measurement techniques*, Springer-Verlag, Berlin.

Alvarez-Hernandez, E. M. (1990), *The influence of cohesion on sediment movement in channels of circular cross-section*, PhD Thesis, Department of Civil Engineering, University of Newcastle Upon Tyne.

Amos, C. L.; Daborn, G. R.; Christian, H. A.; Atkinson, A. and Robertson, A. (1992b), "In situ erosion measurements on fine-grained sediments from the Bay of Fundy", *Marine Geology*, 108, pp 175-196.

Amos, C. L.; Droppo, I. G.; Gomez, E. A. and Murphy, T. P. (2003), "The stability of a remediated bed in Hamilton harbour, Lake Ontario, Canada", *Sedimentology*, 50, pp 149-168.

Amos, C. L.; Grant, J.; Daborn, G. R. and Black, K. (1992a), "Sea Carousel - A benthic, annular flume", *Estuarine, Coastal and Shelf Science*, 34, pp 557-577.

Amos, C. L.; Van Wagoner, N. A. and Daborn, G. R. (1988), "The influence of sub-aerial exposure on the bulk properties of fine-grained intertidal sediment from Minas basin, Bay of Fundy", *Estuarine, Coastal and Shelf Science*, 27 (1), pp 1-13.

Andersen, T. J.; Jensen, K. T.; Lund-Hansen, L.; Mouritsen, K. N. and Pejrup, M. (2002), "Enhanced erodibility of fine-grained marine sediments by *Hydrobia ulvae*", *Journal of Sea Research*, 48, pp 51-58.

Antonia, R. A. and Krogstad, P. –A. (2001), "Turbulence structure in boundary layers over different types of surface roughness", *Fluid Dynamics Research*, 28, pp 139-157.

Ariathurai, R. and Arulanandan, K. (1978), "Erosion rates of cohesive soils", *J. Hyd. Div. ASCE*, 104 (HY2), pp 279-283.

Azzopardi, B. J. and Teixeira, J. C. F. (1994), "Detailed measurements of vertical annular two phase flow. Part II: gas core turbulence", *ASME J. of Fluids Engineering*, 116 (4).

Azzopardi, B. J.; Freeman, G. and Whalley, P. B. (1978), "Drop sizes in annular two-phase flow", U.K.A.E.A. Report AERE R-9074.

Baker, R. J. (1974), "The influence of particle seeding on laser anemometry measurements", HL.74/2126, AERE Harwell.

Bates, C. J. and Hughes, T. D. R. (1977), "The effect of both sample size and sampling rate on the statistical fluid flow parameters in a high Reynolds number, low turbulence intensity

flow", *5th Symposium on Turbulence*, Misouri-Rolla, pp 125-131.

Bayvel, L. P. and Jones, A. R. (1981), *Electromagnetic scattering and its applications*, Applied Science Publishers, London.

Belcher, S. E. and Hunt, J. C. R. (1993), "Turbulent shear flow over slowly moving waves", *J. Fluid Mech.*, 251, pp 109-148.

Bennett, S. J. and Best, J. L. (1995), "Mean flow and turbulence structure over fixed, two-dimensional dunes: implications for sediment transport and bedform stability", *Sedimentology*, 42, pp 491-513.

Bennett, S. J. and Best, J. L. (1996), "Mean flow and turbulence structure over fixed ripples and the ripple-dune transition", in: *Coherent Flow Structures in Open Channels*, Ashworth, P. J.; Bennett, S. J.; Best, J. L. and McLelland, S. J. (eds), John Wiley & Sons Ltd, pp 281-304.

Bennett, S. J.; Bridge, J. S. and Best, J. L. (1998), "Fluid and sediment dynamics of upper stage plane beds", *Journal of Geophysical Research*, 103 (C1), pp 1239-1274.

Besley, P. and Delo, E. A. (1990), "The hydrodynamics of the Carousel", Report SR 239, Hydraulics Research Limited, Wallingford, UK.

Best, J. L.; Kostaschuk, R. A. and Villard, P. V. (2000), "Visualization of flow fields associated with sand dunes: results from the laboratory and field", *9th International Symposium on Flow Visualization*, paper number 355.

Bird, R. B; Stewart, W. E. and Lightfoot, E. N. (1976), *Transport phenomena*, John Wiley & Sons, Inc., New York.

Black, K. S. and Paterson, D. M. (1997), "Measurement of the erosion potential of cohesive marine sediments: a review of current in situ technology", *J. Marine Env. Engg*., 4, pp 43-83.

Black, K. S.; Tolhurst, T. J.; Paterson, D. M. and Hagerthey, S. E. (2002), " Working with natural cohesive sediments", *Journal of Hydraulic Engineering*, January Forum, pp 2-8.

Blondeaux, P.; Foti, E. and Vittori, G. (2000), "Migrating sea ripples", *Eur. J. Mech. B-Fluids*, 19, pp 285-301.

Bradshaw, P. (1971), *An introduction to turbulence and its measurement*, First Edition, Pergamon Press Ltd, New York.

BSA/FVA Flow Software Installation & User's guide, DANTEC Measurement Technology A/S (2000), P.O. Box 121, Tonsbakken 18, DK-2740 Skovlunde, Denmark.

Buschmann, M. H. and Gad-el-Hak, M, (2003), "Debate concerning the mean-velocity profile of a turbulent boundary layer", *AIAA Journal*, 41 (4), pp 565-572.

Caywood, C. L. (1999), *Determination of erosion rates of cohesive sediments in the Carson and Truckee Rivers*, Msc Thesis, Civil Engineering, University of Nevada, Reno.

CFX Manual (1997), CFX 4.3, AEA Technology, Oxford, U K.

Chigier, N. (1983), "Drop size and velocity instrumentation", *Prog. Energy Combust. Sci*.,

9 (1-2), pp 155-177.

Clauser, F. H. (1954), "Turbulent boundary layers in adverse pressure gradients", *J. Aero. Sci*., 21, pp 91-108.

Clauser, F. H. (1956), "The turbulent boundary layer", *Adv. Appl. Mech*., 4, pp 1-51.

Coles, D. (1956), "The law of the wake in the turbulent boundary layer", *J. of Fluid Mechanics*, 1, pp 191-226.

Dabron, G. R.; Amos, C. L.; Brylinsky, M.; Christian, H.; Drapeau, G.; Faas, R. W.; Grant, J.; Long, B.; Paterson, D. M.; Perillo, G. M. E. and Piccolo, M. C. (1993), "An ecological cascade effect: migratory birds affect stability of intertidal sediments", *Limnol. Oceanogr*, 38 (1), pp 225-231.

Dade, W. B.; Nowell, A. R. M. and Jumars, P. A. (1992), "Predicting erosion resistance of muds", *Marine Geology*, 105, pp 285-297.

Dankers, P. J. T. (2002), "The behaviour of fines released due to dredging – A literature review", Hydraulic Engineering Section, Faculty of Civil Engineering and Geosciences, Delft University, the Netherlands.

de Brouwer, J. F. C. (2002), *Dynamics in extracellular carbohydrate production by marine benthic diatoms*, PhD Thesis, the Netherlands Institute of Ecology, NIOO-CEMO, the Netherlands.

de Brouwer, J. F. C.; Bjelic, S.; de Deckere, E. M. G. T.; and Stal, L. J. (2000), "Interplay between biology and sedimentology in a mudflat (Biezelingse Ham, Westerschelde, The Netherlands", *Continental shelf Research*, 20, pp 1159-1177.

de Jonge, V. N. and van den Bergs, J. (1987), "Experiments on the resuspension of estuarine sediments containing benthic diatoms", *Estuarine, Coastal and Shelf Science*, 24, pp 725-740.

De Vries, J. W. (1992), "Field measurements of the erosion of cohesive sediments", *Journal of Coastal Research*, 8 (2), pp 312-318.

Doron, P.; Bertuccioli, L. and Katz, J. (2001), "Turbulence characteristics and dissipation estimates in the coastal ocean bottom boundary layer from PIV data", *Journal of Physical Oceanography*, 31 (8), pp 2108-2134.

Droppo, I. G.; Lau, Y. L. and Mitchell, C. (2001), "The effect of depositional history on contaminated bed sediment stability", *The Science of the Total Environment*, 266, pp 7-13.

Durst, F.; Melling, A. and Whitelaw, J. H. (1981), *Principles and practice of laser-Doppler anemometry*, Academic Press, 2nd Edition, London.

Dvorak, F. A. (1969), "Calculation of turbulent boundary layers on rough surfaces in pressure gradient" *AIAA Journal*, 7 (9), pp 1752-1759.

Dyer, K. R. (1998), "The typology of intertidal mudflats", in: *Sedimentary processes in the intertidal zone*, Black, K. S.; Paterson, D. M. and Cramp, A. (eds.), Geological Society, London, Special Publications, 139, pp 11-24.

Dyer, K. R.; Christie, M. C. and Manning, A. J. (2004), "The effects of suspended

sediment on turbulence within an estuarine turbidity maximum", *Estuarine, Coastal and Shelf Science*, 59, pp 237-248.

Engelund, F. (1975), "Instability of flow in a curved alluvial channel", *J. Fluid Mech*., 72, pp 145-160.

Ferziger, J. H. and Perić, M. (1999), *Computational methods for fluid dynamics,* Springer-Verlag, 2nd Edition, Germany.

FiberFlow Installation & User's guide, DANTEC Measurement Technology A/S (1995), Fourth Edition, P.O. Box 121, Tonsbakken 18, DK-2740 Skovlunde, Denmark.

Flemming, B. W. (2000), "A revised textural classification of gravel-free muddy sediments on the basis of ternary diagrams", *Continental Shelf Research*, 20, pp 1125-1137.

French, C. E.; French, J. R.; Clifford, N. J. and Watson, C. J. (2000), "Sedimentation-erosion dynamics of abandoned reclamations: the role of waves and tides", *Continental Shelf Research*, 20, pp 1711-1733.

Friend, P. L. (2001), *Biological influences on the stability of intertidal flat sediments (Arenicola marina)*, PhD Thesis, University of Southampton, UK.

Gallagher, M. W. (1998), *Coherent flow structures over mixed grain sized surfaces and their role in sediment transport*, PhD Thesis, Department of Engineering, University of Aberdeen.

Goldstein, R. J. (1983), *Fluid Mechanics measurements*, Hemisphere Publishing Corporation, Washington DC.

Graham, D. I. (2000), "Turbulence attenuation by small particles in simple shear flows", *Transactions of the ASME Journal of Fluids Engineering*, 122, pp 134-137.

Graham, D. I.; James, P. W.; Jones, T. E. R.; Davies J. M. and Delo, E. A. (1992), "Measurement and prediction of surface shear stress in annular flume", *Journal of Hydraulic Engineering*, 118 (9), pp 1270-1286.

Grant, J. and Daborn, G. (1994), "The effects of bioturbation on sediment transport on an intertidal mudflat", *Netherlands Journal of Sea Research*, 32 (1), pp 63-72.

Grant, W. D.; Boyer, L. F. and Sanford, L. P. (1982), "The effects of bioturbation on the initiation of motion of intertidal sands", *Journal of Marine Research,* 40 (3), pp 659-677.

Grass, A. J. and Ayoub, R. N. M. (1982), "Bed load transport of fine sand by laminar and turbulent flow", *Eighteenth Conf. Coastal Engineering*, pp 1589-1599.

Gust, G. and Southard, J. B. (1983), "Effects of weak load on the universal law of the wall", *Journal of Geophysical Research*, 88 (C10), pp 5939-5952.

Hagiwara, Y.; Murata, T.; Tanaka, M. and Fukawa, T. (2001), "Turbulence modification by the clusters of settling particles in turbulent water flow in a horizontal duct", *4th International Conference on Multiphase Flow*, ICMF 2001, New Orleans, LA, USA.

Hama, F. R. (1954), "Boundary-layer characteristics for smooth and rough surfaces", *Trans. Soc. Naval Arch. Mar. Engrs*., 62, pp 333-358.

Hecht, E. (1991), *Óptica*, Fundação Calouste Gulbenkian , Lisboa.

Hercules Inc., Product data - Aqualon (1995).

Herrmann, H. J. (2002), "Evolution and shapes of dunes", *C. R. Physique*, pp 197-206.

Hinze, J.O. (1987), *Turbulence*, McGraw Hill, 2nd Edition, USA.

Hirsch, C. and Leuckel, W. (1996), "A curvature correction for the *k*-ε model in engineering applications", in: *Engineering turbulence modelling and experiments 3*, Rodi, W. and Bergeles, G. (eds.), Elsevier Science B. V., pp 71-80.

Houwing, E., - J. and van Rijn, L. C. (1995), "In situ determination of the critical bed shear stress for erosion of cohesive sediments", Proceedings of the *24th International Conference on Coastal Engineering*, Kobe, Japan, pp 2058-2069.

Houwing, E., -J. and van Rijn, L. C. (1998), "In situ erosion flume (ISEF): determination of bed-shear stress and erosion of a kaolinite bed", *Journal of Sea Research*, 39, pp 243-253.

Hutchinson, P. and Hewitt, G. F. (1971), "Deposition of liquid or solid dispersions from turbulent gas streams: a stochastic model", *Chemical Engineering Science*, 26, pp 419-439.

Inamuro, T.; Yamaguchi, A. and Ogino, F. (1997), "Fluid flow in a rotating cylindrical container with a rotating disk at the fluid surface", *Fluid Dynamics Research*, 21, pp 417-430.

James, P. W. and Jones, T. E. R. (1992), "The measurement and prediction of surface shear stress induced by Newtonian and non-Newtonian fluids", in: *Theoretical and applied rheology*, Moldenaers, P. and Keunings, R. (ed.), Proceedings of XIth International Congress on Rheology, Brussels, Elsevier Science Publishers B.V., pp 926-928.

James, P. W., Jones, T. E. R. and Stewart, D. M. (1996), "Numerical and experimental studies of annular flume flow", *Appl. Math. Modelling*, 20, pp 225-231.

Jones, C. A. (2000), *An accurate model of sediment transport*, PhD Thesis, Mechanical and Environmental Engineering, University of California, Santa Barbara.

Jones, T. E. R. and Hughes, J. P. (2001), Unpublished information.

Keirsbulck, L.; Labraga, L.; Mazouz, A. and Tournier, C. (2002), "Surface roughness effects on turbulent boundary layer structures", *Journal of Fluids Engineering*, 124, pp 127-135.

Kelly, W. E. and Gularte, R. C. (1981), "Erosion resistance of cohesive soils", *Journal of Hydraulics Division*, Proceedings of the *American Society of Civil Engineers*, 107 (HY10), pp 1211-1224.

Kleinhans, M. G. (2001), "The key role of fluvial dunes in transport and deposition of sand-gravel mixtures, a preliminary note", *Sedimentary Geology*, 143, pp 7-13.

Kline, S. J. (1985), "The purposes of uncertainty analysis", *Transactions of the ASME Journal of Fluids Engineering*, 107, pp 153-160.

Kniskern, T. A. and Kuehl, S. A. (2003), "Spatial and temporal variability of seabed disturbance in the York River subestuary", *Estuarine Coastal and Shelf Science*, 58, pp 37-

55.

Kornman, B. A. and de Deckere, E. M. G. T. (1998), "Temporal variation in sediment erodibility and suspended sediment dynamics in the Dollard estuary", in: *Sedimentary processes in the intertidal zone*, Black, K. S.; Paterson, D. M. and Cramp, A. (eds.), Geological Society, London, Special Publications, 139, pp 231-241.

Kostaschuk, R. A. and Church, M. A. (1993), "Macroturbulence generated by dunes: Fraser River, Canada", *Sedimentary Geology*, 85, pp 25-37.

Kostaschuk, R. A. and Ilersich, S. A. (1995), "dune geometry and sediment transport: Fraser River, British Columbia", in: *River geomorphology*, Hickin, E. J. (ed.), John Wiley & Sons Ltd, pp 19-36.

Kranenburg, C. (1999), "Effects of floc strength on viscosity and deposition of cohesive sediment suspensions", *Continental Shelf Research*, 19, pp 1665-1680.

Krishnappan, B. G. and Marsalek, J. (2002), "Transport characteristics of fine sediments from an on-stream stormwater management pond", *Urban Water*, 4, pp 3-11.

Krogstad, P. –A. and Antonia, R. A. (1999), "Surface roughness effects in turbulent boundary layers", *Experiments in Fluids*, 27, pp 450-460.

Krogstad, P. –A.; Antonia, R. A. and Browne, L. W. B. (1992), "Comparison between rough and smooth wall turbulent boundary layers", *J. Fluid Mech.*, 245, pp 599-617.

Krone, R. B. (1999) "Effects of bed structure on erosion of cohesive sediments", *Journal of Hydraulic Engineering*, 125 (12), pp 1297-1301.

Kuijper, C.; Cornelisse, J. M. and Winterwerp, J. C. (1989), "Research on erosive properties of cohesive sediments", *Journal of Geophysical Research*, 94 (C10), pp 14341-14350.

Lau, Y. L. and Droppo, I. G. (2000), "Influence of antecedent conditions on critical shear stress of bed sediments", *Wat. Res.*, 34 (2), pp 663-667.

Lau, Y. L.; Droppo, I. G. and Krishnappan, B. G. (2001), "Sequential erosion/deposition experiments – demonstrating the effects of depositional history on sediment erosion", *Wat. Res.*, 35 (11), pp 2767-2773.

Laufer. J. (1954), "The structure of turbulence in fully developed pipe flow", NACA report 1174.

Launder, B. E. and Spalding, D. B. (1974), "The numerical computation of turbulent flows", *Computer Methods in Applied Mechanics and Engineering*, 3, pp 269-289.

Launder, B. E.; Priddin, C. H. and Sharma, B. I. (1977), "The calculation of turbulent boundary layers on spinning and curved surfaces", *Transactions of the ASME Journal of Fluids Engineering*, 99, pp 231-239.

Le Hir, P.; Bassoullet, P. and Jestin, H. (2003), "Application of the continuous modelling concept to simulate high-concentration suspended sediment in a macrotidal estuary", in: *Coastal and estuarine fine sediment processes*, Proceedings in Marine Science 3, McAnally, W. H. and Mehta, A. J. (eds.), Elsevier Science, The Netherlands, pp 229-247.

Lee, S. L. and Durst, F. (1979), "On the motion of particles in turbulent flows", State University of New York and Universitat Karlsruhe, W.G.

Lelieveld, S. D.; Pilditch, C. A. and Green, M. O. (2003), "Variation in sediment stability and relation to indicators of microbial abundance in the Okura estuary, New Zealand", *Estuarine, Coastal and Shelf Science*, 56, pp 1-14.

Lick, W. (1982), "Entrainment, deposition and transport of fine-grained sediments in lakes", *Hydrobiologia*, 91, pp 31-40.

Ligrani, P. M. and Moffat, R. J. (1986), "Structure of transitionally rough and fully rough turbulent boundary layers", *J. Fluid Mech.*, 162, pp 69-98.

Lumborg, U. and Windelin, A. (2003), "Hydrography and cohesive sediment modelling: application to the Romo Dyb tidal area", *Journal of Marine Systems*, 38, pp 287-303.

Maa, J. P. –Y.; Lee, C. –H. and Chen, F. J. (1995), "Bed shear stress measurements for VIMS Sea Carousel", *Marine Geology*, 129, pp 129-136.

Maa, J. P.-Y. (1990), "The bed shear stress of an annular sea-bed flume", in: *Estuarine water quality management: monitoring, modelling and research*, Michaelis (ed.), pp 271-275.

Maa, P. –Y. and Mehta, A. J. (1987), "Mud erosion by waves, a laboratory study", *Continental Shelf Research*, 7 (11/12), pp 1269-1284.

Malvern Instruments Ltd, High Performance Systems for Particle Characterization, 2600 Series- User Manual (1991), England.

Martin, P. B.; Pugliese, G. J. and Leishman, J. G. (2000), "Laser Doppler velocimetry uncertainty analysis for rotor blade tip vortex measurements", *AIAA* paper 2000-0263, *38th Aer. Sc. Meeting*, 15 pp.

McLelland, S. J.; Ashworth, P. J.; Best, J. L. and Livesey, J. R. (1999), "Turbulence and secondary flow over sediment stripes in weakly bimodal bed material", *Journal of Hydraulic Engineering*, 125 (5), pp 463-473.

Mehta, A. J. (1981), "Review of erosion function for cohesive sediment beds", Proceedings of the *First Indian Conference on Ocean Engineering*, Indian Institute of Technology, Madras, India, 1, pp 122-130.

Mehta, A. J. (1991), "Review notes on cohesive sediment erosion", in: *Coastal sediments*, Krauss, N. C. *et al.* (ed), 1, pp 40-53.

Mehta, A. J. and Lee, S. –C. (1994), "Problems in linking the threshold condition for the transport of cohesionless and cohesive sediment grain", *Journal of Coastal Research*, 10 (1), pp 170-177.

Melling, A. (1975), *Investigation of flows in non-circular ducts and other configurations by laser Doppler anemometer*, PhD Thesis, University of London.

Mikkelsen, O. A. (2002), "Examples of spatial and temporal variations of some fine-grained suspended particle characteristics in two Danish coastal water bodies", *Oceanologica Acta*, 25, pp 39-49.

Mitchener H. J. and O'Brien, D.J. (2003), "Seasonal variability of sediment erodibility and properties on a macrotidal mudflat, Peterstone Wentlooge, Severn estuary", in: *Coastal and estuarine fine sediment processes*, Proceedings in Marine Science 3, McAnally, W. H. and Mehta, A. J. (eds.), Elsevier Science, The Netherlands, pp 301-322.

Mitchener, H. and Torfs, H. (1996), "Erosion of mud/sand mixtures", *Coastal Engineering*, 29, pp 1-25.

Mohammadi, B. and Pironneau, O. (1994), *Analysis of the k-Epsilon turbulence model*, John Wiley & Sons, England.

Montague, C. L. (1986), "Influence of biota on erodability of sediments", in: *Estuarine cohesive sediment dynamics,* Lecture notes on coastal and estuarine studies, 14, Mehta, A. J. (ed.), Springer-Verlag , Berlin, pp 251-269.

Mouazé, D. and Bélorgey, P. M. (2001), "Internally mounted laser-Doppler-anemometry system for boundary layer measurement", *Experiments in Fluids*, 30, pp 111-114.

Mugele, R. A. and Evans, H. D.(1951), "Droplet size distributions in spays", *Industrial and Engineering Chemistry*, 43 (6), pp 1317-1324.

Nallasamy, M. (1987), "Turbulence models and their applications to the prediction of internal flows: a review", *Computers & Fluids*, 15 (2), pp 151-194.

Nichols, M. M. (1986), "Effects of fine sediment resuspension in estuaries", in: *Estuarine cohesive sediment dynamics*, Lecture notes on coastal and estuarine studies, 14, Mehta, A. J. (ed.), Springer-Verlag , Berlin, pp 5-42.

Nikuradse, J. (1933), "Stromungsgesetze in rauhen rohren, VDI Forschungsheft, nº 361, 1950, English translation, NACA-TM 1292.

Nikuradse, J. (1950), "Laws of flow in rough pipes", NACA Technical memorandum 1292.

Noorany, I. (1984), "Phase relations in marine soils", *Journal of Geotechnical Engineering*, 110 (4), pp 539-543.

Nowell, A. R. M. and Jumars, P. A. (1987), "Flumes: theoretical and experimental considerations for simulation of benthic environments", *Oceanogr. Mar. Biol. Ann Rev.*, 25, pp 91-112.

Parchure, T. M. and Mehta, A. J. (1985), "Erosion of soft cohesive sediment deposits", *Journal of Hydraulic Engineering*, 111 (10), pp 1308-1326.

Paterson, D. (2001), Unpublished information.

Paterson, D. M. (1989), "Short-term changes in the erodibility of intertidal cohesive sediments related to the migratory behaviour of epipelic diatoms*", Limnol. Oceanogr,* 34 (1), pp 223-234.

Paterson, D. M. (1994), "Biological mediation of sediment erodibility: ecology and physical dynamics", Proceedings of the *4th Nearshore and estuarine cohesive sediment transport conference*, INTERCOH-94, Wallingford, UK.

Paterson, D. M.; Tolhurst, T. J.; Kelly, J. A., Honeywill, C.; de Deckere, E. M. G. T.; Huet,

V.; Shayler, S. A.; Black, K. S.; de Brouwer, J. and Davidson, I. (2000) "Variations in sediment properties, Skeffling mudflat, Humber Estuary, UK", *Continental Shelf Research* 20, pp 1373-1396.

Paterson, D. M.; Wiltshire, K. H.; Miles, A.; Blackburn, J.; Davidson, I.; Yates, M. G.; McGrorty, S., and Eastwood, J. A. (1998), "Microbiological mediation of spectral reflectance from intertidal cohesive sediments", *Limnol. Oceanogr*., 43 (6), pp 1207-1221.

Patrick, W. P. (1985), "Error sources in laser velocimeter systems", Technical report, University of Connecticut.

Pedrotti, F. L. and Pedrotti, S. J. (1993), *Introduction to optics*, Prentice-Hall, Inc., 2nd Edition, New Jersey.

Perry, A. E. and Joubert, P. N. (1963), "Rough-wall boundary layers in adverse pressure gradients", *J. Fluid Mech.*, 17, pp 193-211.

Petersen, O. and Krishnappan, B. G. (1994), "Measurement and analysis of flow characteristics in a rotating circular flume", *Journal of Hydraulic Research*, 32, pp 483-494.

Peterson, E. L. (1999) "Benthic shear stress and sediment condition", *Aquacultural Engineering*, 21, pp 85-111.

Petit, F. (1990), "Evaluation of grain shear stresses required to initiate movement of particles in natural rivers", *Earth Surface Processes and Landforms*, 15, pp 135-148.

Pinho, F. T. (1999), "The advantage of double-gap cylinders to minimise the uncertainty of viscosity measurements", Dept. Eng. Mecânica e Gestão Industrial, FEUP, Porto.

Pourahmadi, F. and Humphrey, J. A. C. (1983), "Prediction of curved channel flow with an extended k-ε model of turbulence", *AIAA Journal*, 21 (10), pp 1365-1373.

Prent, M. T. H. and Hickin, E. J. (2001), "Annual regime of bedforms, roughness and flow resistance, Lillooet River, British Columbia, BC", *Geomorphology*, 41, 369-390.

Progelhof, R. C. and Throne, J. L. (1993), *Polymer engineering principles – properties, processes, tests for design*, Hanser (Ed.), Munich.

Rand, B. and Melton, I. E. (1977), "Particle interactions in aqueous kaolinite suspensions I. Effect of pH and electrolyte upon the mode of particle interaction in homoionic sodium kaolinite suspensions", *Journal of colloid and interface science*, 60 (2), pp 308-320.

Rashidi, M.; Hetsroni, G. and Banerjee, S. (1990), "Particle-turbulence interaction in a boundary layer", *International Journal of Multiphase Flow*, 16 (6), pp 935-949.

Raudkivi, A. J. (1997), "Ripples on stream bed", *Journal of Hydraulic Engineering*, 123 (1), pp 58-64.

Ravens, T. M. and Gschwend, P. M. (1999), "Flume measurements of sediment erodibility in Boston harbour", *Journal of Hydraulic Engineering*, 125 (10), pp 998-1005.

Ravisangar, V.; Dennett, K. E.; Sturm, T. W. and Amirtharajah, A. (2001), "Effect of sediment pH on resuspension of kaolinite sediments", *Journal of Environmental Engineering*, 127 (6), pp 531-538.

Rheolab MC 1, Paar Physica, Operating Manual (1998), Germany.

Ridler, E. L. and Sleath, F. A. (2000), "Effect of bed roughness on time-mean drift induced by waves", *Journal of Waterway, Port, Coastal and Ocean Engineering*, 126 (1), pp 23-29.

Riethmüller, R.; Hakvoort, J. H. M.; Heineke, M.; Heymann, K.; Kühl, H. and Witte, G. (1998), "Relating erosion shear stress to tidal flat surface colour", in: *Sedimentary processes in the intertidal zone*, Black, K. S.; Paterson, D. M. and Cramp, A. (eds.), Geological Society, London, Special Publications, 139, pp 283-293.

Roarty, H. J. (2000), *Development of a video technique to study bed load sediment transport*, PhD Thesis, Stevens Institute of Technology, NJ.

Roberts, J.; Jepsen, R.; Gotthard, D. and Lick, W. (1998), "Effects of particle size and bulk density on erosion of quartz particles", *Journal of Hydraulic Engineering*, 124 (12), pp 1261-1267).

Roberts, W.; Le Hir, P. and Whitehouse, R. J. S. (2000), "Investigation using simple mathematical models of the effect of tidal currents and waves on the profile shape of intertidal mudflats", *Continental Shelf Research*, 20, pp 1079-1097.

Rodi, W. (1984), Turbulence models and their application in hydraulics- A state of the art review, University of Karlsruhe, Germany.

Rodi, W. and Scheuerer, G. (1983), "Calculation of curved shear layers with two-equation turbulence models", *Phys. Fluids*, 26 (6), pp 1422-1436.

Römkens, M. J. M., Helming, K. and Prasad, S. N. (2001), "Soil erosion under different rainfall intensities, surface roughness and soil water regimes", *Catena*, 46, pp 103-123.

Rosin, P. and Rammler, E. (1933), "The laws governing the fineness of powdered coal", *Inst. of Fuel*, 7, pp 29.

Ruddy, G.; Turley, C. M. and Jones, T. E. R. (1996), "The influence of microbiology on cohesive sediment dynamics", LISP preliminary results, Black, K. and Paterson, D. (eds.), pp 54-61.

Sabersky, R. H.; Acosta, A. J. and Hauptmann, E. G. (1989), *Fluid Flow, A first course in fluid mechanics*, Macmillan Publishing Company, 3rd Edition, New York.

Schlichting, H. (1979), *Boundary-layer theory*, McGraw-Hill Classic Textbook Reissue Series, 7th Edition.

Schünemann, M., Kühl, H. (1991), "A device for erosion-measurements on naturally formed, muddy sediments: the EROMES-System", GKSS- Forschungszentrum Geesthacht GMBH, Report GKSS 91/ E/ 18, 28 pp.

Sechet, P. and Le Guennec, B. (1999), "The role of near wall turbulent structures on sediment transport", *Wat. Res.*, 33 (17), pp 3646-3656.

Sheng, Y. P. (1989), "Consideration of flow in rotating annuli for sediment erosion and deposition studies", *Journal of Coastal Research*, 5, pp 207-216.

Sloan , D. G.; Smith, P. J. and Smoot, L. D. (1986), "Modeling of swirl in turbulent flow systems", *Prog. Energy Combust. Sci*., 12, pp 163-250.

Soares, A. (2004), Unpublished information.

Soulsby, R. (1997), *Dynamics of marine sands*, Thomas Telford Publications, London.

Staats, N.; de Deckere, E. ; Kornman, B.; van der Lee, W.; Termaat, R.; Terwindt, J. and de Winder, B. (2001), "Observations on suspended particulate matter (SPM) and microalgae in the Dollard estuary, The Netherlands: Importance of late Winter ice cover of the intertidal flats", *Estuarine, Coastal and Shelf Science*, 53, pp 297-306.

Steele, W. G.; Ferguson, R. A.; Taylor, R. P. and Coleman, H. W. (1994), "Comparison of ANSI/ASME and ISO models doe calculation of uncertainty", ISA Transactions, 33, pp 339-352.

Steele, W. G.; Taylor, R. P.; Burrell, R. E. and Coleman, H. W. (1993), "Use of previous experience to estimate precision uncertainty of small sample experiments", *AIAA Journal*, 31 (10), pp 1891-1896.

Sun, H.; Dong, H.; Player, M. A.; Watson, J.; Paterson, D. M. and Perkins, R. (2002) "In-line digital video holography for the study of erosion processes in sediments", *Measurement Science and Technology*, 13, pp L7-L12.

Sutherland, T. F.; Amos, C. L. and Grant, J. (1998), "The erosion threshold of biotic sediments: a comparison of methods", in: *Sedimentary processes in the intertidal zone*, Black, K. S.; Paterson, D. M. and Cramp, A. (eds.), Geological Society, London, Special Publications, 139, pp 295-307.

Swithenbank, J.; Beer, J. M.; Taylor, D. S.; Abbot, D. and McCreath, G. C. (1976), "A laser diagnostic for the measurement of droplet and particle size distribution", Department of Chemical Engineering and Fuel Technology, Sheffield University, Report Nº AD AO21/30.

Tattersall, G. R.; Elliott, A. J. and Lynn, N. M. (2003), "Suspended sediment concentrations in the Tamar estuary", *Estuarine, Coastal and Shelf Science*, 57, pp 679-688.

Tayali, N. E. and Bates, C. J. (1990), "Particle sizing techniques in multiphase flows: A review", *Flow Meas. Instrum.*, 1, pp 77-103.

Taylor, J. R. (1997), *An introduction to error analysis – The study of uncertainties in physical measurements*, 2nd Edition, University Science Books.

Teixeira, J. C. F. (1988), *Turbulence in annular two phase flow*, PhD Thesis, Department of Chemical Engineering, University of Birmingham.

Thais, L. and Magnaudet, J. (1996), "Turbulent structure beneath surface gravity waves sheared by the wind", *J. Fluid Mech.*, 328, pp 313-344.

Tolhurst, T. J.; Riethmüller, R. and Paterson, D. M. (2000b), "In situ versus laboratory analysis of sediment stability from intertidal mudflats", *Continental Shelf Research*, 20, pp 1317-1334.

Tolhurst, T. J.; Black, K. S.; Paterson, D. M.; Mitchener, H. J.; Termaat, G. R. and Shayler, S. A. (2000a), "A comparison and measurement standardisation of four in situ devices for determining the erosion shear stress of intertidal sediments", *Continental Shelf Research*,

20, pp 1397-1418.

Tolhurst, T. J.; Black, K. S.; Shalyer, S. A.; Mather, S.; Black, I.; Baker, K. and Paterson, D. M. (1999), "Measuring the in situ erosion shear stress of intertidal sediments with the cohesive strength meter (CSM)", *Estuarine, Coastal and Shelf Science*, 49, pp 281-294.

Torfs, H. (1995), *Erosion of mud/sand mixtures*, PhD Thesis, Departement Burgerlijke Bouwkunde, Katholieke Universiteit Leuven.

Torfs, H.; Huygens, M. and Tito, L. (1994), "Influence of the cross-section on the erosion criteria for partly cohesive sediments", *Wat. Sci. Tech*., 29 (1-2), pp 103-111.

Torfs, H.; Jiang, J. and Mehta, A. J. (2003), "Assessment of the erodibility of fine/coarse sediment mixtures", in: *Coastal and estuarine fine sediment processes*, Proceedings in Marine Science 3, McAnally, W. H. and Mehta, A. J. (eds.), Elsevier Science, The Netherlands, pp 109-123.

Tritton, D. J. (1988), *Physical fluid dynamics*, 2nd Edition, Oxford Science Publications, New York.

Tsai, C. –H. and Lick, W. (1986), "A portable device for measuring sediment resuspension", *J. Great Lakes Res.*, 12 (4), pp 314-321.

User's guide 57N20/57N35 BSA enhanced, DANTEC Measurement Technology A/S (1991), P.O. Box 121, Tonsbakken 18, DK-2740 Skovlunde, Denmark.

Van der Lee, W. T. B. (2000), "Temporal variation of floc size and settling velocity in the Dollard estuary", *Continental Shelf Research*, 20, pp 1495-1511.

van Driest, E. R. (1956), "On turbulent flow near a wall", *J. Aero. Sci.*, 23, pp 1007.

van Ledden, M..; van Kesteren, W. G. M. and Winterwerp, J. C. (2004), "A conceptual framework for the erosion behaviour of sand-mud mixtures", *Continental Shelf Research*, 24, pp 1-11.

Venditti, J. G. and Bennett, S. J. (2000), "Spectral analysis of turbulent flow and suspended sediment transport over fixed dunes", *Journal of Geophysical Research*, 105 (C9), pp 22,035-22,047.

Versteeg, H. K. and Malalasekera, W. (1998), *An introduction to computational fluid dynamics – The finite volume method*, Longman Group Ltd., England.

Villard, P. and Kostaschuk, R. (1998), "The relation between shear velocity and suspended sediment concentration over dunes: Fraser estuary, Canada", *Marine Geology*, 148, pp 71-81.

Wang, Y. H. (2003), "The intertidal erosion rate of cohesive sediment: a case study from Long Island Sound", *Estuarine, Coastal and Shelf Science*, 56, pp 891-896.

Weast, R. C. (2000), *Handbook of chemistry and physics*, CRC Press, Inc., 1st student Edition, Florida.

White, F. M. (1986), *Fluid Mechanics*, McGraw-Hill International Editions, 2nd Edition, Singapore.

Whitehouse, R. J. S.; Bassoullet, P.; Dyer, K. R.; Mitchener, H. J. and Roberts, W. (2000),

"The influence of bed forms on flow and sediment transport over intertidal mudflats", *Continental Shelf Research*, 20, pp 1099-1124.

Wiberg, P. L. and Smith, J. D. (1987), "Calculations of the critical shear stress for motion of uniform and heterogeneous sediments", *Water Resources Research*, 23 (8), pp 1471-1480.

Widdows, J.; Brown, S.; Brinsley, M. D.; Salkeld, P. N. and Elliott, M. (2000), "Temporal changes in intertidal sediment erodability: influence of biological and climatic factors", *Continental Shelf Research*, 20, pp 1275-1289.

Williams, J. J.; Bell, P. S. and Betteridge, K. F. E. (2002), "Laboratory investigation of sediment resuspension by waves at full-scale", in: *Coastal environment – Environmental problems in coastal regions IV*, Brebbia, C.A. (ed.), WIT Press, UK, pp 203-214.

Williamson, H. J. and Ockenden, M. C. (1996), "ISIS: An instrument for measuring erosion shear stress in situ", *Estuarine, Coastal and Shelf Science*, 42, pp 1-18.

www.cwr.uwa.edu.au/

www.dow.com/glycerine/resources/table12_2140.htm

www.hadlandphoto.com.au/NAC.htm

Yanta, W. J. and Smith, R. A. (1973), "Measurements of turbulence-transport properties with a laser Doppler velocimeter", *AIAA* paper No 73-169, *11th Aer. Sc. Meeting*, 9 pp.

Young, R. N. and Southard, J. B. (1978), "Erosion of fine-grained marine sediments: sea-floor and laboratory experiments", *Geological Society of American Bulletin*, 89, pp 663-672.